

AD-A267 636



AFOSR-90-0308

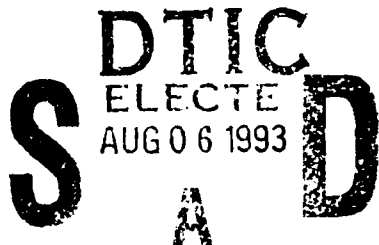
1
AFOSR-90-0308

AFOSR-90-0308

AIR FORCE OFFICE OF SCIENTIFIC RESEARCH

PROJECT MONITOR DR. ALAN ROSENSTEIN

*Microstructure Evolution In The Presence Of
Constraints And Implications On The Properties Of
Mg - Li And Nb - Al Composites.*



ANNUAL REPORT : YEAR 1

PERIOD COVERED : JUNE 1, 1990--MAY 30, 1991

J. A. SEKHAR, L. FABIETTI, L. CANTRELL, C. T. HO, M. G. LAKSHMIKANTHA, N. DEY, R. TRIVEDI & D. CARR

UNIVERSITY OF CINCINNATI
DEPARTMENT OF MATERIALS SCIENCE AND ENGINEERING
CINCINNATI, OH, 45221-0012

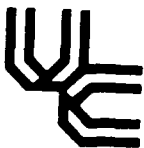
513-556-3105

This document has been approved
for public release and sale; its
distribution is unlimited

H1515⁶ 93-17729

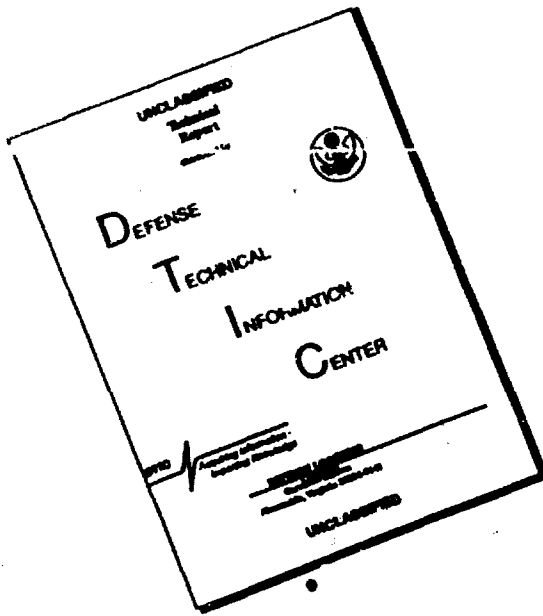


University of Cincinnati



Q 3 R 4 6 7 5

DISCLAIMER NOTICE



**THIS DOCUMENT IS BEST
QUALITY AVAILABLE. THE COPY
FURNISHED TO DTIC CONTAINED
A SIGNIFICANT NUMBER OF
PAGES WHICH DO NOT
REPRODUCE LEGIBLY.**

INDEX

	<u>Page</u>
1.0 INTRODUCTION	11
2.0 EQUIPMENT	16
2.1 UNIDIRECTIONAL SOLIDIFICATION APPARATUS FOR TRANSPARENT MATERIALS	
16	
2.1.1 Heating and Cooling Systems	
2.1.2 Driving System	
2.1.3 Data Acquisition System	
2.1.4 Sample Preparation	
2.1.5 Alloy Preparation	
2.1.6 Cell Preparation	
2.2 HORIZONTAL UNIDIRECTIONAL SOLIDIFICATION APPARATUS FOR MG-LI AND MG-LI COMPOSITES	27
2.2.1 Design of the Specimen Cell	
2.2.2 Velocity Measurement/Calibration	
2.3 HIGH TEMPERATURE UNIDIRECTIONAL SOLIDIFICATION APPARATUS FOR NB-AL AND NB-AL COMPOSITES	35
2.3.1 Temperature Gradient Assembly	
2.3.2 Movement Control	
2.3.3 Argon Cover	
2.3.4 Quench	
2.3.5 Measurement of the Temperature Profiles	
2.3.5.1 Measurement Setup	
2.3.5.2 Optical Fiber Thermometer (OFT) System	
2.3.5.3 Data Acquisition and Treatment	
2.3.6 Experimental Procedure	
2.3.6.1 Heating up and Stabilization	
2.3.6.2 DS-Experiment	
2.3.6.3 Recharge	
2.3.6.4 Control of Temperature Profiles	
2.3.7 Temperature Gradient	
2.3.8 Temperature Profiles and Gradients	
2.3.8.1 Temperature Profiles	
2.3.8.2 Temperature Gradients	

Accesion For	
NTIS	CRA&I
DTIC	TAB
Unannounced	
Justification	
By	
Distribution /	
Availability Codes	
Dist	Avail and/or Special
A-1	

DTIC QUALITY INSPECTED 3

3.0 THEORY DEVELOPMENT FOR PROJECT	50
3.1 GROWTH LIMITS	51
3.1.1 Theoretical Analysis	
3.1.2 Discussion	
3.1.2.1 Effect of Temperature Gradient	
3.1.2.2 Minimum Radius During Unconstrained Growth	
3.1.2.3 Other Microstructure Scales	
3.1.2.4 Non-Equilibrium Effects	
3.2 GROWTH IN CONSTRAINED ENVIRONMENT	58
3.2.1 Microstructures as a Function of Channel Width	
3.2.2 Theoretical Models	
3.2.3 Planar Interface Stability	
3.2.4 Cellular and Dendritic Growth	
3.2.5 Microstructure Map	
3.3 COMBUSTION SYNTHESIS	67
3.3.1 Mathematical Formulation for Combustion Synthesis of an Alloy	
3.3.2 Solution Procedure	
3.3.3 Initial Condition	
3.3.4 Numerical Procedure	
3.3.5 Results and Discussion	
3.3.6 Conclusion	
4.0 TRANSPARENT D/S EXPERIMENTS IN THE PRESENCE OF INERT PARTICLES	85
4.1 EXPERIMENTAL TECHNIQUE	86
4.2 RESULTS	87
4.2.1 Interactions with a Planar Interface	
4.2.2 Particle Trapping Mechanisms	
4.2.3 Morphological Transitions	
4.3 DISCUSSION	89
4.3.1 Interactions Between the Particle and the Interface	
4.3.2 Morphological Transitions	
4.3.2.1 Planar Interface Stability	
4.3.2.2 Cell-Dendrite Transition	
4.3.3 Instability of the Dendrite Tip	
4.3.4 The Effects of Particles on Dendrite Length and Solute Segregation Patterns	
4.3.5 Particle Distribution in the Solidified Material	

4.4 CONCLUSIONS	97
5.0 COMBUSTION SYNTHESIZED NIOBIUM ALUMINIDE - NIOBIUM BORIDE COMPOSITES	99
5.1 EXPERIMENTAL TECHNIQUE	99
5.2 RESULTS	100
5.3 DISCUSSION	101
5.4 CONCLUSION	102
6.0 THERMAL STRESS CRACKING DURING GROWTH OF FACETED MATERIALS	104
6.1 MODEL DESCRIPTION	109
6.1.1 Solidification Model	
6.1.2 Thermal Model	
6.1.3 Stress Model	
6.2 EXPERIMENTAL	115
6.3 RESULT & DISCUSSION	116
6.3.1 Thermal Stresses on the Facets	
6.3.2 Experimental Result and Discussions	
7.0 CONCLUSION AND FUTURE WORK	123
8.0 REFERENCES	124

LIST OF FIGURES FOR SECTIONS 3.0 THROUGH 6.3

Figure 1. Schematic illustrations of various rapid solidification techniques: from reference 1.

Figure 2. Theoretical variation of the dendrite tip radius with interface velocity for non-faceted growth of alumina.

Figure 3. The variation in the minimum dimensionless radius $R_{min}\Delta T_0/2\theta$ with partition coefficient for directional (constrained) growth.

Figure 4. The variation in the dimensionless radius R with dimensionless bath undercooling (unconstrained growth).

Figure 5. The effect of the equilibrium partition function on the dimensionless undercooling at the minimum and intermediate maximum radii from the solute and thermal effects.

Figure 6. The variation of the minimum solutal radius with k (partition coefficient) and C_0 (dimensionless initial concentration).

Figure 7. The scaling of λ_p with VC_0 . λ_p is the distance between the tip and the first side branch. V and C_0 are the velocity of the dendrite tip and the bulk composition, respectively.

Figure 8. A schematic illustration which summarizes experimental observations on the effect of channel width on microstructural development for experimental conditions which would give a stable dendritic array inside a channel of very large width.

Figure 9. The surface tension effect at the channel wall giving rise to instability which is similar to the instability at the grain boundary in a channel of large width. Succinonitrile - 2.5 wt% acetone, $V = 2.0 \mu\text{m/s}$ and $G = 2.36 \text{ K/mm}$.

Figure 10. The effect of contact angle on the instability of a planar interface. The experimental results of the variation in critical velocity for planar interface instability as a function of channel width in impure carbon tetrabromide.⁽¹⁷⁾

Figure 11. A schematic illustration of a cellular interface which defines the Saffman - Taylor width of the cell.

Figure 12. Theoretical prediction of the change in dimensionless undercooling at the tip with channel width.

Figure 13. A schematic illustration of the variation in cell tip temperature with velocity for channels of different widths.

Figure 14. A schematic microstructure map showing regions of planar, cellular and dendritic microstructures in velocity versus relative channel width.

Figure 15. A schematic of the combustion and solidification problem. Q_I is the incident heat flux, BI is the Biot number at the end of the sample which is cooled and V_c is the combustion front velocity. Behind the combustion front is the reacted part of the sample and in front is the unreacted part.

Figure 16. The relevant part of the phase diagram from the Ti-C system.⁽⁴⁴⁾

Figure 17. The plot of the dimensional enthalpy and dimensional temperature during combustion and solidification.

Figure 18. (a) Maximum temperature profiles during combustion for material conditions given in the figure.

Figure 18. (b) Cooling profiles after the combustion process shown in figure 18a. Note that although the cooling boundary condition was incorporated during the combustion process, cooling only began after complete combustion.

Figure 19. Typical thermal and reaction profiles during combustion (low K_o).

Figure 20. Typical thermal and reaction profiles during combustion (high K_o).

Figure 21. The variation of the combustion velocity V and combustion temperature T_c with K_o .

Figure 22. The variation of combustion zone l_r and heat affected zone l_p with K_o .

Figure 23. The variation of combustion velocity V and combustion temperature T_c with the activation energy E .

Figure 24. The variation of combustion velocity V and combustion temperature T_c with the reaction enthalpy Q .

Figure 25. The variation of combustion velocity V and combustion temperature T_c with the thermal conductivity (low K_o).

Figure 26. The variation of combustion velocity V and combustion temperature T_c with the thermal conductivity (high K_o).

Figure 27. The variation of the combustion zone l_r and the heat affected zone l_p with the thermal conductivity (low K_o).

Figure 28. The variation of the combustion zone l_r and the heat affected zone l_p with the thermal conductivity (high K_o).

Figure 29. The variation of combustion velocity V and combustion temperature T_c with the initial substrate temperature, T_0 .

Figure 30. Cooling of a sample heated by a self propagating combustion front (the diameter of the sample $d = 0.0005\text{m}$, the side surface heat transfer coefficient $h = 1000 \text{ w/m}^2\text{K}$).

Figure 31. Temperature-Time profile at a dimensionless distance of $Z = 0.8$ (the diameter of the sample $d = 0.0005\text{m}$, the side surface heat transfer coefficient $h = 1000 \text{ w/m}^2\text{K}$).

Figure 32. The incorporation of a gas bubble into a directionally solidifying planar interface. Bulk composition of the alloy 99.5wt% SCN + water. V (velocity of interface) = $0.8 \mu/\text{s}$ and G (temperature gradient) = 5.5 K/mm . (a)-(d) increasing time.

Figure 33. The incorporation of a system of bubbles and a finite wall into a 5wt% SCN. $V = 0.8 \text{ m/s}$, $G = 5.5 \text{ K/mm}$. (a)-(c) increasing time.

Figure 34. Trapping of low volume fraction small particles by a dendritic interface. $V = 10 \text{ mm/s}$, $G = 5.5 \text{ K/mm}$, $C = 99.5\text{wt\% SCN}$. (a) = 120s, (b) = 132s, (c) = 144s, (d) = 156s, (e) = 312s, (f) = 430s, (g) = 444s. Note that the deformed bubble which now forms the gas porosity begins to travel with a steady state velocity along with the root of the dendrite. Note also the Rayleigh instability in the bubble.

Figure 35. A magnified illustration of dendrite tip splitting by the particles in the experiment described in figure 34. Time: (a) = 252s, (b) = 266s.

Figure 36. Continuation of the sequence of figure 34 and 35 to illustrate the incorporation of particles through a bubble. Note the deformation of the bubble in the interdendritic areas. (a)-(d) increasing time.

Figure 37. Trapping of high volume fraction nickel particles by an initially dendritic interface which changes morphology to a cellular pattern in the presence of the high volume fraction of particles. $G = 5.5 \text{ K/mm}$, $C = 99.5\text{wt\% SCN}$. (a) $V = 10 \text{ mm/s}$, (b) $V = 40 \text{ mm/s}$. Note that a dendritic pattern has appeared at higher velocity.

Figure 38. A schematic illustration of interface perturbation near a particle and the origin of bands around a trapped particle.

Figure 39. A schematic plot of tip radius of a cellular or dendritic interface with and without particles in the liquid ahead of the growing interface.

Figure 40. An illustration of the average and local interface position as a function of the distance solidified for a typical experiment involving the growth of a solidification interface in the presence of particles. The slope of the curve will give the average and local interface velocities.

Figure 41. A typical solidification pattern in a SCN-4% acetone system illustrating the rapid growth of secondary dendrites not far behind the primary dendrite tip.

Figure 42. Possible trapping mechanisms by a dendritic interface.

Figure 43. The calculated theoretical density, measured green density and final fired density for the 7 different compositions. Note that the compositions of 1 and 2% B did not ignite. The theoretical density is calculated on the basis of unrelated constituents.

Figure 44. The combustion temperature profiles for alloys NA4B and NA6B.

Figure 45. The Vickers hardness number and the combustion velocities for 5 different boron contents.

Figure 46. The SEM microstructures of the composites for the alloys (a) NA4B and (b) NA7B.

Figure 47. The variation of volume fraction of porosity for 5 different compositions.

Figure 48. The correlation between the combustion temperatures and the combustion velocities.

Figure 49. The secondary combustion peak noted in the alloy NA6B.

Figure 50. Typical facet interface configuration and cracking phenomenon noted during the bridgeman type growth of a transparent material Salol.

Figure 51. A schematic of the interface configuration and the system. $D = 5 \text{ cm}$ and $L = 3D$.

Figure 52. Magnified portion of the solid liquid interface. Distance between point 'A' and 'C' is the steady state cell spacing and the angle ABC is always constant for a particular direction of growth of the crystal, which in this model has been considered to be the $\langle 111 \rangle$ direction. Positions (1), (2) and (3) are the positions at which the stress calculations will be presented.

Figure 53. Plots of (a) normalized mean hydrostatic stress, σ_m , and (b) normalized equivalent shear stress, τ_e , at various positions defined in figure 52 as a function of cell spacing for a constant average axial temperature gradient of 1.0 K/mm (average local radial temperature gradient is 0.29 K/mm and average local axial temperature gradient is 2.9 K/mm near the interface).

Figure 54. Plots of (a) normalized mean hydrostatic stress, σ_m , and (b) normalized equivalent shear stress, τ_e , at various positions defined in figure 52 as a function of cell spacing for a constant average axial temperature gradient of 5.0 K/mm (average local radial temperature gradient is 1.52 K/mm and average local axial temperature gradient is 14.9 K/mm near the interface).

Figure 55. Plots of (a) normalized mean hydrostatic stress, σ_m , and (b) normalized equivalent shear stress, τ_e , at various positions defined in figure 52 as a function of cell spacing for a constant average axial temperature gradient of 10.0 K/mm (average local radial temperature gradient is 3.09 K/mm and average local axial temperature gradient is 29.9 K/mm near the interface).

Figure 56. Normalized mean hydrostatic stress, σ_m , at various positions defined in figure 52 as a function of square root of interface growth velocity, $(V, \mu\text{m/s})^{1/2}$

Figure 57. Normalized equivalent shear stress, τ_e , at various positions defined in figure 52 as a function of square root of interface growth velocity, $(V, \mu\text{m/s})^{1/2}$.

Figure 58. Contours of (a) radial stress, σ_{rr} , (b) hoop stress, $\sigma_{\phi\phi}$, and (c) equivalent shear stress, τ_e , on a growing facet (which is 0.5^*R away from the center of the crystal) when the cell spacing is $80.69 \mu\text{m}$ and average axial temperature gradient is 1 K/mm . All the stresses are normalized with respect to the $E_{MTM}\alpha/(1-2v)*10^6$.

Figure 59. Contours of (a) radial stress, σ_{rr} , (b) hoop stress, $\sigma_{\phi\phi}$, and (c) equivalent shear stress, τ_e , on a growing facet (which is 0.5^*R away from the center of the crystal) when the cell spacing is $80.69 \mu\text{m}$ and average axial temperature gradient is 10 K/mm . All the stresses are normalized with respect to the $E_{MTM}\alpha/(1-2v)*10^6$.

Figure 60. Contours of (a) radial stress, σ_{rr} , (b) hoop stress, $\sigma_{\phi\phi}$, and (c) equivalent shear stress, τ_e , on a growing facet (which is 0.5^*R away from the center of the crystal) when the cell spacing is $255.2 \mu\text{m}$ and average axial temperature gradient is 1 K/mm . All the stresses are normalized with respect to the $E_{MTM}\alpha/(1-2v)*10^6$.

Figure 61. The interlace shape of the material salol during a imposed growth velocity of $0.1 \mu\text{m/s}$ and in the presence of a positive temperature gradient of 3 K/mm .

Figure 62. Shows the time sequence of events occurring on a single facet during a imposed growth velocity of $5.0 \mu\text{m/s}$ and in the presence of a positive temperature gradient of 3 K/mm . The photographs are taken 5 sec. apart during the growth. (a) Shows a facet with no apparent cracks near the interface. (b) Shows the formation of a sudden crack in a location between the tip and root. (c) Shows the crack being left behind in the crystal during subsequent growth. (d) Shows a fresh crystal facet growing on the cracked face.

Figure 63. Shows the time sequence of events occurring on a single facet during a imposed growth velocity of $5.0 \mu\text{m/s}$ and in the presence of a positive temperature gradient of 3 K/mm . The photographs are taken 5 sec. apart during the growth. (a) Shows a facet with a freshly formed crack. (b) and (c) show crack continually propagating with the interface.

Figure 64. Shows the growth of two macroscopic facets during a imposed growth velocity of $5.0 \mu\text{m/s}$ and in the presence of a positive temperature gradient of 3 K/mm . The photographs are taken 5 sec. apart during the growth. (a) Shows tip splitting occurring on the right facet. (b) Shows crack appearing near the tip (at the new root location) of the right facet.

Title : Microstructure Evolution in the presence of constraints and its implications on the properties of Mg - Li and Nb - Al Composites.

OBJECTIVE : The objective of the research is to gain fundamental knowledge of solidification microstructure evolution in the presence of constraints and to apply this knowledge to the development of relevant metal and intermetallic composites. This work is divided into three parts: (1) critical experimental studies of microstructural development inside channels of different widths and with particles of different sizes and distribution (2) the development of theoretical models to correlate physical concepts with the experimental results, and (3) well-defined experimental studies in metallic and intermetallic systems in presence of fibers and particles to apply fundamental understanding for the mapping of microstructure-processing-property relationships for composite materials made by the solidification route.

The following diagram gives an overview of the project. This is the first year progress report.

Microstructure Evolution in the presence of constraints and its implications on the properties of Mg-Li and Nb-Al Composite

Theoretical Development of Solidification morphology prediction during constrained growth

Limit and scale theory
Constraints

Experimental Apparatus

Transparent Materials

Mg-Li alloys and composites

Nb-Al alloys and composites

Solidification experiments with

Succinonitrile-acetone system

Experiments with Salol

Directional Solidification of Mg-Li alloys

Directional Solidification of Mg-Li Composites

Microstructural Analysis and Modeling

Combustion Synthesis Principles (theory)

Nb-Al alloys made by Combustion Synthesis

Nb-Al - NbB composites made by Combustion Synthesis

Directional Solidification of Nb-Al Alloys

Directional Solidification of Nb- Al- NbB composite alloys

Microstructural Analysis and Modeling

During the first year the following work was completed

- 1) Setting up of high precision transparent directional solidification unit with a fiber optic illumination system. Several experiments were conducted and one paper accepted in the Journal of Materials Science and Engineering.

- 3) Development of Combustion Synthesis Technique for high temperature Nb-Al alloys and Nb-Al Composites. Paper submitted and accepted in the MRS proceedings on High Temperature Ordered Alloys.
- 4) Setting up of directional solidification unit for the Nb-Al composite. Experiments in progress
- 5) Numerical technique for solving for heat flow parameters and microstructure during combustion synthesis of Nb-Al. Paper submitted to Metallurgical Transactions.
- 6) Theoretical Formulation for the scale of microstructure during directional and equiaxed solidification. Paper accepted in the Journal of Crystal Growth
- 7) Numerical Analysis of Cracking Phenomena in Faceted Materials. Paper submitted to Metallurgical Transactions.

During the directional solidification processing of composites, the microstructure formation process can be significantly influenced by the constrained environment of the liquid that is present between the fibers. The solidification microstructure is not only a function of velocity, temperature gradient and composition, but it also depends upon the interfiber spacing. Significant morphological changes can occur when the interfiber spacing becomes of the order of primary cell or dendrite spacing in an unconstrained liquid. Consequently, for solidification processing of fibrous composites, it is possible to design new microstructures which give superior properties by controlling the spacing between the fibers. Results of experimental studies in transparent system, under controlled width of a channel, are presented to characterize the relationship between the microstructural development and the interfiber spacing. Theoretical ideas which become important as the size of the liquid region becomes constrained, are also discussed to quantitatively understand the changes in microstructures from dendritic to cellular to planar front growth as the interfiber spacing decreased. The effect of the width of the channel on these microstructures is represented by a microstructural map which exhibits domains of different single phase morphologies in the growth rate - channel width space.

Similarly a study with particles acting as constraints was carried out. The development of solidification microstructure can be significantly influenced by the presence of inert particles in the liquid during the processing of particulate composites by the solidification techniques. The effect of particles on the microstructural development is characterized through directional solidification experiments in a transparent organic system, succinonitrile, in which the interactions between the particles and the interface can be examined *in situ*. These particle-interface interactions have been examined in

an alloy system in which the long range solute field interactions between the particles and the interface are dominant. These interactions have been found to be significantly different for different interface morphologies, i.e. planar, cellular or dendritic interfaces. The effect of particles on the morphological changes and on the nature of the particle trapping processes are characterized for different particle distributions, particle sizes and interface morphologies. It is shown that the presence of particles in binary alloys can either cause the instability of the interface, such as dendrite tip-splitting, or lead to morphological transitions, such as a dendritic to cellular transition. When the particle density is large, the presence of particles significantly influence the interface shape and thereby alter interface growth characteristics such that an oscillatory behavior of the interface can be obtained under constant externally imposed velocity. Appropriate theoretical ideas are developed to explain the effects of particles on the morphological development of the interface.

The microstructures obtained during the growth in channels and in the presence of fibers are constrained. A similar type of constraint is imposed by the surface energy during rapid solidification. These first need to be understood and the ideas applied to channel and particle constrained growth. There are a wide variety of fascinating microstructures that evolve during rapid growth solidification processing. The microstructural evolution principles of tip stability and transport which control the scale of such microstructures, especially near the limit of absolute stability, are discussed. Theoretical models for predicting the smallest microstructure scale in a binary alloy are discussed for both constrained and unconstrained growth. The effect of the temperature gradient and solute trapping on microstructure evolution at high growth velocities is examined. The results of this study are directly applicable to the growth of microstructures to form composite materials.

A further study was also carried out on faceted materials. Many new materials such as Nickel and Niobium Aluminides may grow with faceted interfaces. These materials are now being composited to increase their fracture toughness. Thermally induced stresses may cause stress to develop on the solid liquid interface of faceted materials. These stresses may be compressive or tensile in nature and may change sign during solidification when traversing from the tip to the root of the dendrite. The tip region is crack free, however the hydrostatic tensile regions may give rise to cracks which are left behind in the sample. A study to model the cracking phenomena was successfully carried out. Simulation with faceted materials growing in channels is expected to be undertaken.

One of the objective of this work is to understand microstructure evolution in Nb-Al composites. These composites were made by combustion synthesis. Results of an experimental study on unidirectional wave combustion synthesized Nb-Al-B composite alloys are described. The effect of

combustion initiation temperature and composition on the microstructural morphology and phases is studied. Correlations with the initial parameters and reaction velocities have been sought to understand the kinetics of the rate controlling step for sustained combustion and for the explanation of the synthesized microstructures. Strategies for controlling the distribution of the reinforcement phases (both ductile and hard) in the composite are discussed. These composites will be directionally solidified. However to make optimum composites, an understanding of the principles of combustion synthesis is required. Therefore, a numerical study of self propagating combustion synthesis is carried out to determine the effect of the heat of reaction (Q), the activation energy (E), the frequency factor (K_0), thermal conductivity (K^*) and initial temperature (T_0) on the combustion velocity and combustion temperature in the presence of cooling at one end. The numerical procedure allows for the formation and solidification of non-stoichiometric combustion products. This includes the phase change of the product through its solidification and eutectic range. Calculations are carried out for the Ti-C system with an objective of predicting solutions which are comparable to previously reported experimentally determined values. Calculations are also compared with the thin zone analytical solution to the combustion problem. The use of low K_0 values to bring the solutions close to the experimentally determined numbers is discussed. Solutions are presented to elucidate the effect of relevant parameters on the thickness of the combustion and pre-heat zones. Conditions where extinction is expected to occur are identified. The effect of the thermal conductivity on the velocity may be to increase or decrease the velocity depending on the value of K_0 . At low K_0 values, an increase in the thermal conductivity may lead to a decrease in the combustion velocity. The effect of the initial temperature on the combustion velocity and temperature is to increase both, however the increase in the combustion temperature may not be proportional to the increase in the initial temperature. E has a pronounced effect on reducing the combustion velocity while not influencing the combustion temperature. The time rate of the solidification process which determines the final microstructure is discussed. These results will now be applied to the Nb-Al-B system.

2.0 EQUIPMENT

Three types of solidification apparatus will be described in this report. The first is the low temperature solidification apparatus for transparent materials, the second is the solidification equipment for Mg-Li alloys and the third is the solidification apparatus for Nb-Al materials. All the three have three main components: a) heating and cooling systems; b) a system for the sample translation in a fixed thermal gradient; c) a data acquisition system. Additionally, a zone refining apparatus built to refine the transparent materials is described.

2.1 UNIDIRECTIONAL SOLIDIFICATION APPARATUS FOR ORGANIC MATERIALS

Several organic materials are transparent and have a melting point close to room temperature making them suitable to be used for "in situ" solidification studies, i.e, the solid-liquid interface morphology may be observed during evolution and information regarding the interface morphology as a function of the solidification variables can be obtained. This information can be then applied to metallic systems. The Figures 1, 2 and 3 show different views of the solidification device. Figure 4 is a schematic of the apparatus showing the principal elements.

2.1.1 Heating and Cooling Systems

The thermal gradient is created between two hollow metallic chambers held at different temperatures. The gap between the chambers is about 5 mm. The temperature of each chamber is fixed by circulating liquid pumped by an electronically controlled thermal bath. The range of temperatures in the system is 0°C to 250°C for the hot chamber and -50°C to 40°C for the cold one. The thermal stability of each system is within $\pm 0.02^\circ\text{C}$.

2.1.2 Driving System

The sample is moved across in the thermal gradient by a combined system of a step motor and a high precision screw. The step motor has 50,000 steps/rev. and it is connected to a precision screw by a pulley. The step motor is activated and controlled by Commodore computer. The actual velocity is obtained through a program which controls the rate of pulses sent to the motor. The system is calibrated using a previously calibrated eyepieces with reticule. Variable parameters in the software are then adjusted until the desired calibration is obtained.

2.1.3 Data Acquisition System

In the unidirectional solidification experiments with organic crystals, three types of information are obtained, a) the record of the interface morphology during the solidification process; b) the interface temperature and c) the temperature gradient.

- a) The solid-liquid interface morphology is recorded in our case using photographic process. Both chambers are mounted in a metallic plate which holds an X-Y stage in the zone adjacent to the gap. The system is mounted on a 1" rubber plate to avoid vibrations. See Fig. 4. An optical microscope is mounted on an X-Y stage. This set-up allows a complete view of the area between the chambers. A light pipe has been attached to the bottom of the gap to increase the illumination. When used as a reflection microscope, a reflecting surface is added to the bottom of the gap and a polarizer and an analyzer can be employed to enhance the contrast. A photographic camera is attached to the top of the microscope. The camera has automatic exposure control. The time between pictures can be automatically fixed when a time sequence record is desired.
- b) The interface temperature measurements are made through a calibrated thermocouple inserted on one side of the sample. The thermocouples are calibrated against thermometers calibrated by the National Bureau of Standards and Technology with a precision of ± 0.05 K. Each thermocouple has its own voltage vs temperature relationship. A microvoltmeter with $\pm 1\mu V$ precision is used to read the thermocouple output.
- c) For the temperature gradient measurements, the thermocouple is connected to a chart recorder and a temperature trace as a function of the position in the gap is obtained by traversing the thermocouple at constant speed through the gap.

2.1.4 Sample Preparation

The purity of the initial components and the care in their processing is a crucial step in the sample preparation. In general there are no commercially available materials with the purity required for our experiments, and therefore purification is always needed.

The materials employed in these experiments go through two purification process : distillation and zone refining.

The material to be purified is first distilled and transferred in a controlled atmosphere to 1200 mm long and 10 mm of internal diameter glass tubes. The tubes are sealed in vacuum and then transferred to the zone refining apparatus.

Zone refining is one of the most important technique in the material purification process. This technique is used in a wide variety of materials such as metals, semiconductors, and organic crystals. The basic idea behind the technique is the fact that when solid and liquid have different composition at the interface, if a small liquid region is moved through the sample at a constant velocity low enough to keep the interface planar, there is net transfer of solute from one end of the sample to the other. If this process is repeated several times a net purification is obtained.

In practice, a set of heaters and coolers are built in series in such a way that in one pass each portion of the sample may go through several cycles. Figure 5 shows the photograph of the zone refining apparatus designed and built at UC. Figure 6 is an schematic of the whole system. In our case the zone refining apparatus was designed to purify materials with melting point up to 300°C. The heaters are Electric Ring heaters provided by Omega and the coolers are aluminium blocks with internal holes for liquid circulation. In our case we use water as a coolant liquid.

Due to the low range of velocities needed in the purification of organic materials, typically in the order of microns per second, an special gear box was built at UC. The gear box has a reduction capability of $\approx 1/50,000,000$. The velocity of the sample during zone refining is about $2 \mu\text{m/s}$.

A typical purification process involves ten passes for the zone refining apparatus that in this case has 10 melting zones.

2.1.5 Alloy Preparation

In our experiments we use the Succinonitrile-Acetone system for the modelling experiments. Alloys in the range of few percents of Acetone are made Therefore the main problem is the purification and handling of Succinonitrile. This material is highly hygroscopic therefore special care was taken to make the alloys in a dry chamber.

2.1.6 Cell Preparation

The material is filled in the gap between two pieces of glass 25 mm width, 1 mm thick and length between 75 mm and 250 mm according to the experimental requirements. The gap size is about $150\mu\text{m}$ and the cell is sealed with an inert epoxy. In case when solidification process is studied within a channel, several strips of Teflon were introduced to obtain that configuration shown in Fig. 6. With this technique, channels with a width lower than $100\mu\text{m}$ may be achieved.

Once the cell is completely sealed, the final concentration is determined as follows. An electric heater with a ring form and with a diameter around 1 cm

is placed on the top of cell in such a way that the thermocouple tip is more or less in the center. The heater is turned on and the condition where there is a small amount of solid at the thermocouple tip surrounded by liquid is noted. This configuration must be kept for a time enough to ensure that the thermal and solute equilibriums have been reached. This condition represents the first solid that is formed that is in equilibrium with liquid, therefore the temperature of the solid represents the liquidus temperature and through the equilibrium diagram.



Figure 1. Unidirectional solidification apparatus general view,

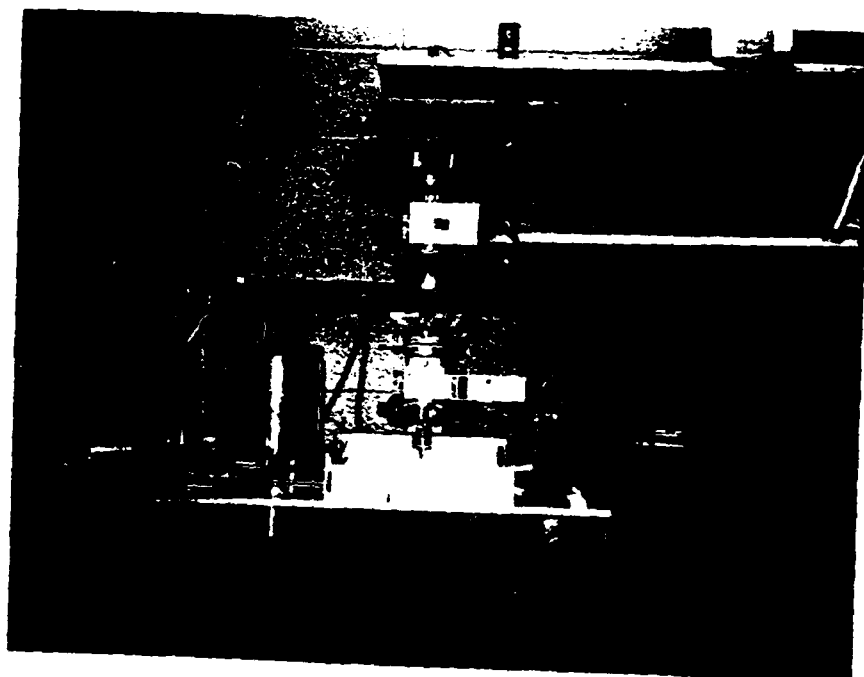


Figure 2. Close up of the directional solidification unit.

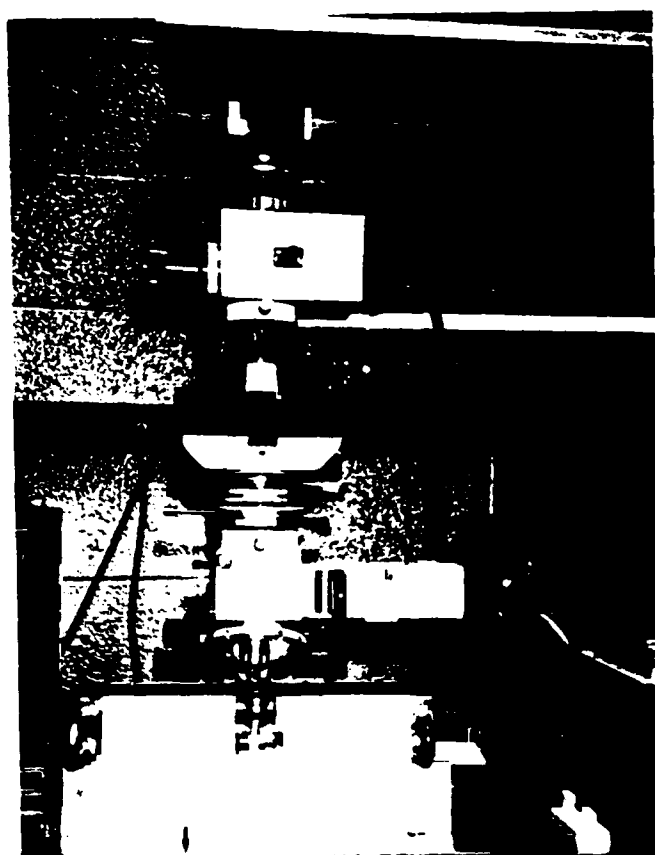


Figure 3. Close up of hot and cold chambers and photographic recording device.

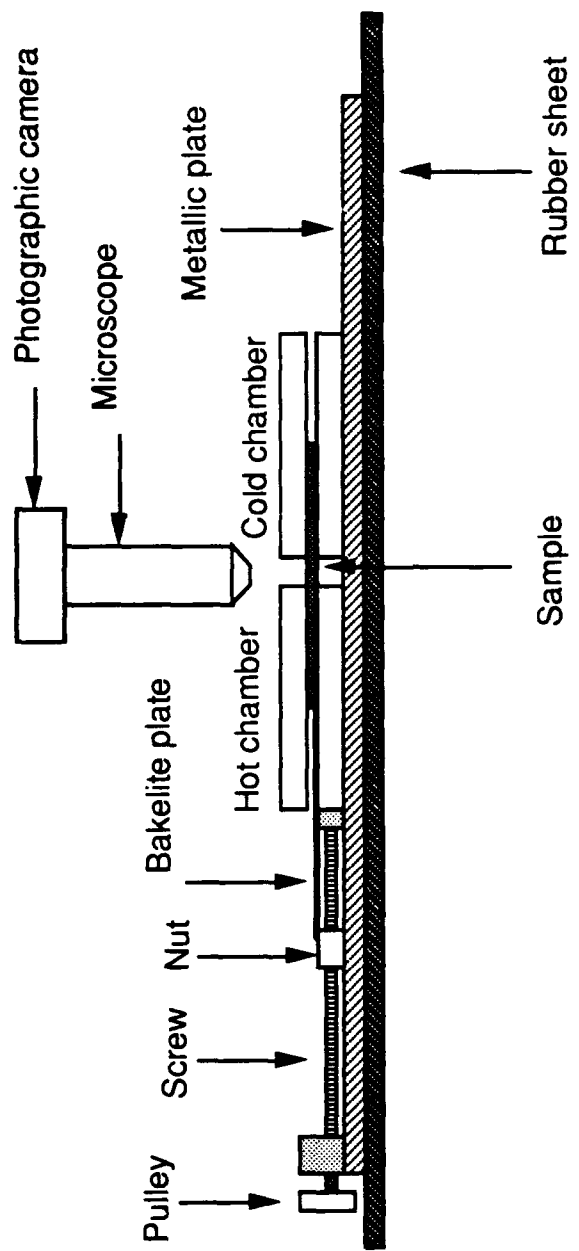


Figure 4. Schematic of the solidification apparatus.

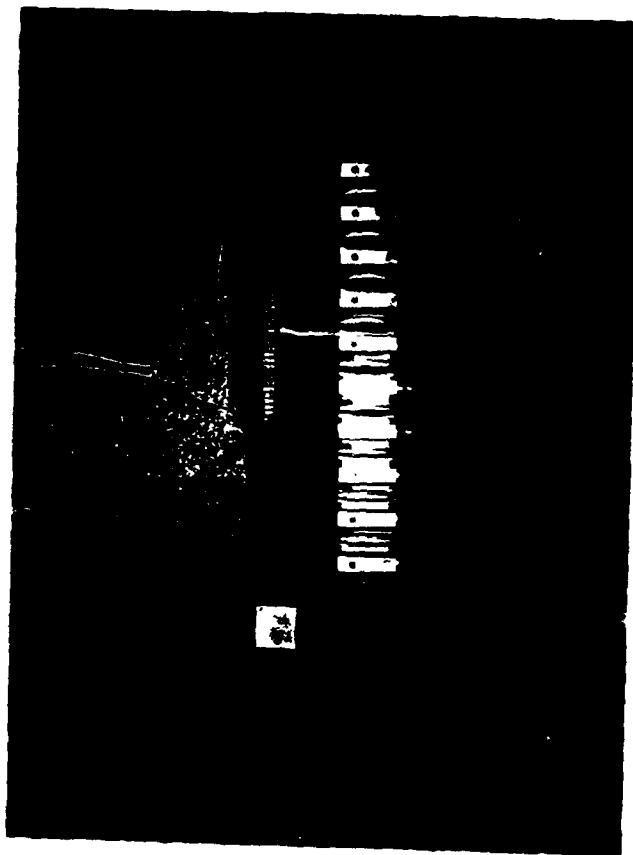


Figure 5. Photograph of the of the zone refining arparatus. From top to bottom the length is 1.20 m.

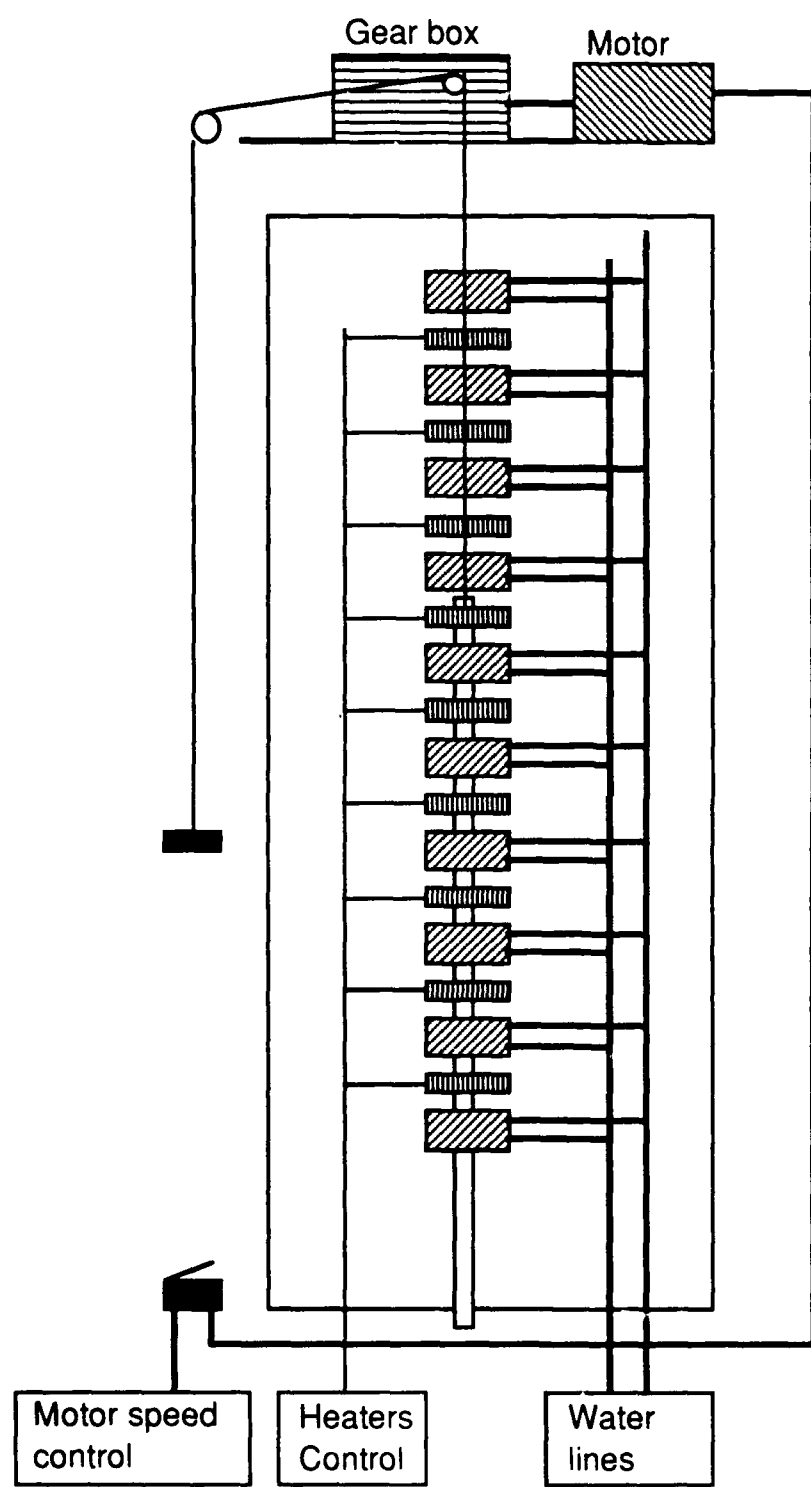
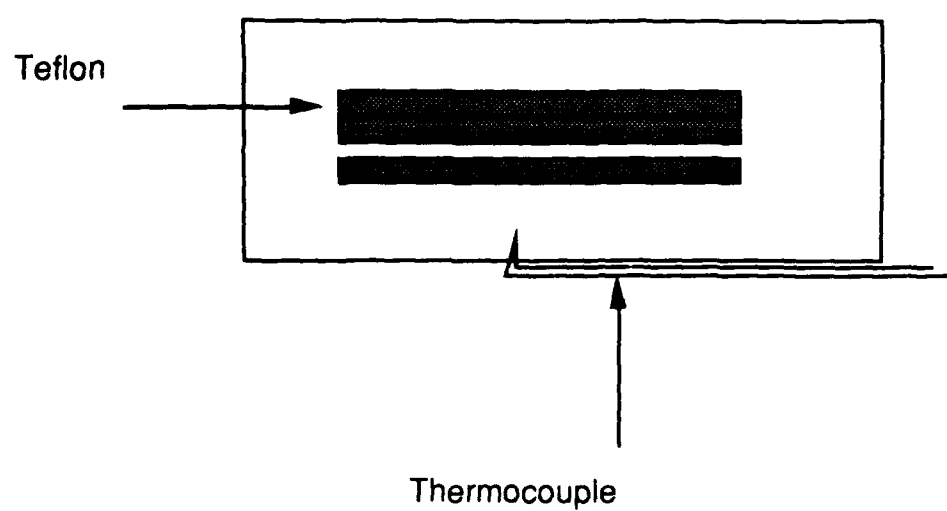
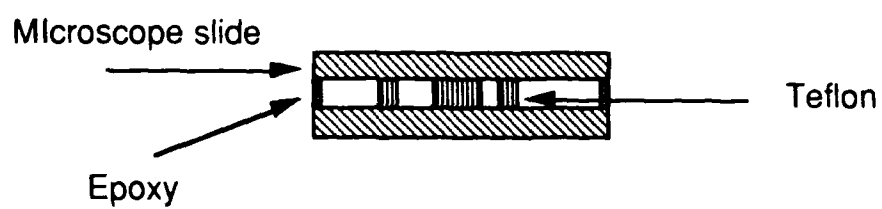


Figure 6. Schematic of the zone refining apparatus.



Top view



Lateral view

Figure 7. Schematic of solidification cells with channels.

2.2 HORIZONTAL UNIDIRECTIONAL SOLIDIFICATION APPARATUS FOR MG-LI AND MG-LI COMPOSITES

Figure 8 illustrates the complete set-up for the experiment. The full length of the experimental chassis is approximately one meter. A cylindrical furnace sits on a stationary platform located on the top of the chassis. The furnace contains a cylindrical hole throughout its length of approximately 3.8 centimeters in diameter. At the ends of the furnace, the cylindrical holes are filled with a solid ceramic cylinder (at the left) and a copper cylinder with a 0.64 centimeter diameter hole (at the right). The copper cylinder has a 0.64 centimeter diameter hollow tube welded around its exterior. The small tube may be used as a cooling device by forcing water through it (the necessity of this water cooling has yet to be determined and will be discussed in a subsequent report). The sample cell (described below) is attached to a holder which moves along the chassis of the apparatus. The movement is caused by the turning of a large screw on which the holder is threaded. The speed of movement is controlled by the velocity controller unit #1 (described below). The movement of the holder causes the sample cell to be withdrawn from the furnace. A thermocouple originating at the temperature controller unit is placed inside the furnace and maintains the furnace at the desired temperature.

The electrical schematic of the temperature controller unit is shown in Fig. 9. The relay acts as a switch for the furnace; which is powered through the temperature control unit and maintains the desired temperature inside the furnace at the position prescribed by the thermocouple.

The schematic of the velocity controller unit #1 is shown in Fig. 10. The range of V.C.U #1 is given in Fig. 11. Due to the limited range of velocities attainable with V.C.U.#1, a second velocity controller has been assembled to be employed for higher velocity experiments.

2.2.1 Design of the Specimen Cell

The specimen cell is designed as illustrated in Fig. 12; which shows a cross-sectional aspect view of the cell. The planar surfaces are constructed of stainless steel (chosen for its low chemical reactivity) 200 micrometers in thickness, 22.86 centimeters in length; and 0.3175 centimeters in width. Between the sheets are placed thin thermocouple wires which are spot-welded to the sheet edges. The best method for attaching the wires to the sheets was found to be by first spot-welding the wires to one sheet along its length and then spot-welding the upper sheet to this arrangement. This procedure guarantees that the wire will be fixed along the edges of the two (upper and lower) sheets without any deviation from the edges. This constitutes one "sandwich". In the completed cell, several sandwiches are

attached together by the same method as described above. It was found that in attaching the additional sandwiches the heat of the spot-welder coupled with gravitational effects caused bending or warping of the final assembled cell. This is a problem because the final cell is to be placed inside of a hollow stainless steel cylinder of 0.439 centimeter in inner diameter (O.D. = 0.515 cm.). If the final cell is too far warped the cell is then constrained inside the cylindrical tube and the possibility of sheet separation of the welds is likely since the force on the sheet is in the direction of sheet separation. To alleviate the problem of warping a special guide device was constructed as shown in Fig. 13. This device helps to hold the sandwiched cell flat during the spot-welding process and eliminates any warping due to gravity effects. The guide does however pose an additional problem of constraining and concealing the loose end of the wire to be welded.

In Fig. 12, a layer of SiC fibers is shown to be attached in sandwich form. In the first cell to be tested this layer is not included due to the cumulative difficulty of combining many layers. In future cells it will be attempted to include this layer on the cell.

2.2.2 Velocity Measurement/Calibration

The measuring device consisted of a metal strip attached to the sample holder on the moving platform. At a given V.C.U. setting movement of the strip was recorded visually using an optical microscope and a scale of 1000 microns in length. The lowest velocity recorded (0.76 microns/sec.) was measured through a distance of 500 microns and the highest velocity recorded (5.47 microns/sec.) was measured through a distance of 1000 microns.

The method of calibration was to take data in intervals of 10 from 30 to 100 on the V.C.U. setting dial in the lo position. 30 was chosen as the lowest dial setting because the gearmotor torque below a setting of 25 was insufficient to supply a constant angular speed to the drive screw of the apparatus. Five separate readings were taken at each setting and were averaged to give the values which appear in the data table and plots.

Due to inaccuracies in timing, visual observation, and small vibrations of the measuring strip due to external causes, an error of +/- 10 sec. was added to each measured time and taken into the calculations. It was confirmed that this time error value is sufficient to account for the maximum error per measurement. Based-on this error, the percent error in the velocity calibrations for the data points taken was found to be $\leq 2\%$.

During a subsequent temperature gradient measurement it was found that over a much longer time period (9:01 hrs.), at the highest velocity controller setting, the actual velocity differed from the calibrated velocity. Specifically,

instead of 5.47 $\mu\text{m/sec}$. which was expected, the velocity was found to be 5.77 $\mu\text{m/sec}$. This is a difference of 5.2% in the velocities. Therefore in future experimental runs, the calibrated velocities will only be used as a rough guide to the actual velocity of the experiment and the velocity will be calculated in each run following a procedure explained elsewhere in this paper.

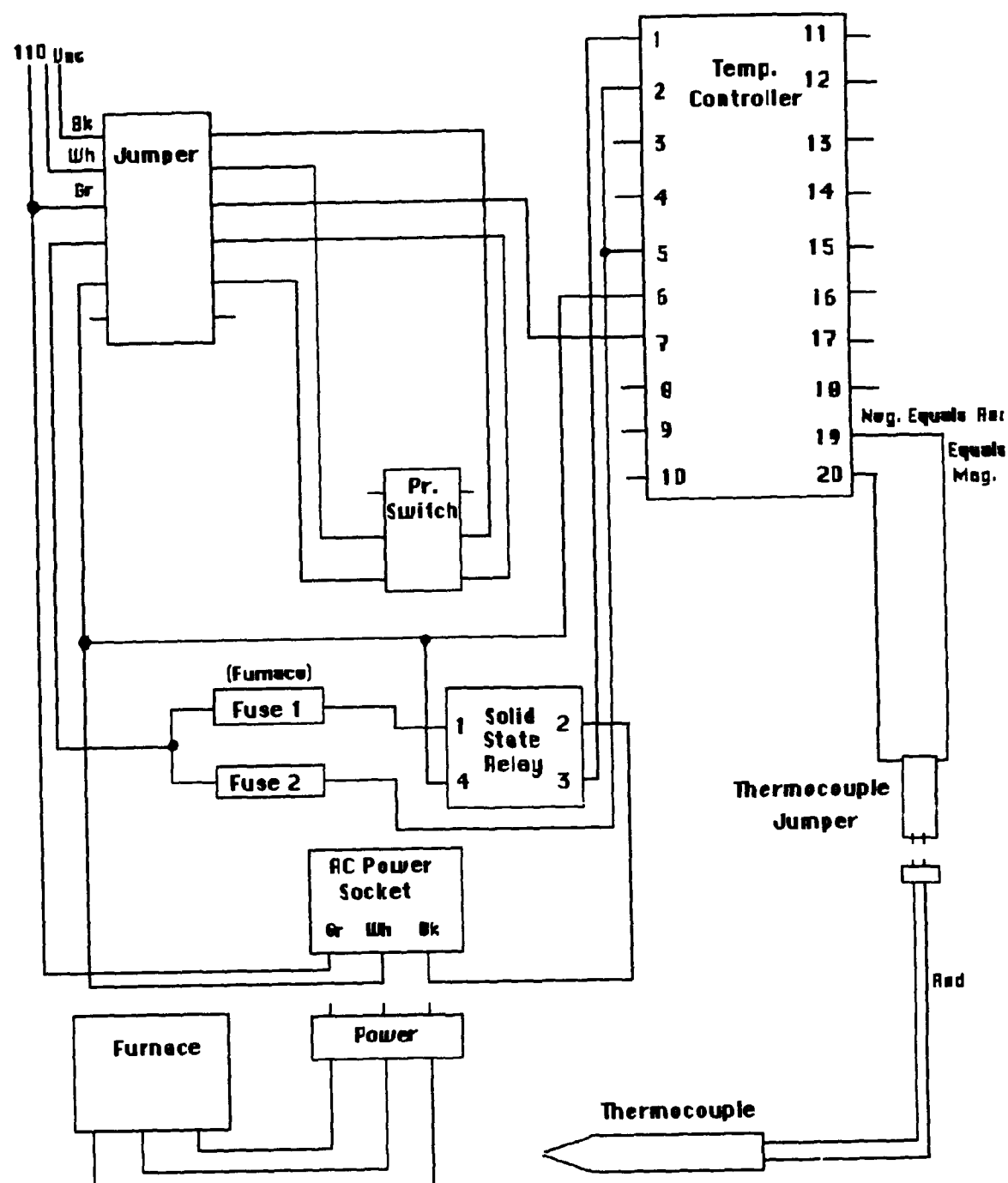
It is noted from the linear fit plot (Fig.11a) that in fitting the data, the actual measurements that were taken are shifted in order to obtain the best fit. This is undesirable since the only data that we are reasonably sure of is altered during the process of analysis. The line plot (Fig.11b) of the data may be more reliable but with so few data points this is uncertain. Therefore, to eliminate some of the uncertainty additional data points will be taken from 25 to 95 on the dial setting in intervals of 10. This will render a 100% increase in the accuracy of the calibration.

The sample cell guide proved useful and necessary to produce an approximately linear, laminated sample cell. If the cell design proves to be effective for the experiment a better guide will be constructed which will eliminate the constraint on the wires.

The sample cell design will hopefully prove useful in that it will allow several lateral constraint distances to be observed simultaneously. These observations may help to determine critical lateral constraint distances for microstructural changes.



Figure 8. Horizontal unidirectional solidification apparatus general view.



Bk. = Line ; Gr. = Ground ; Wh. = Neutral

Figure 9. Schematic of the temperature electrical controller.

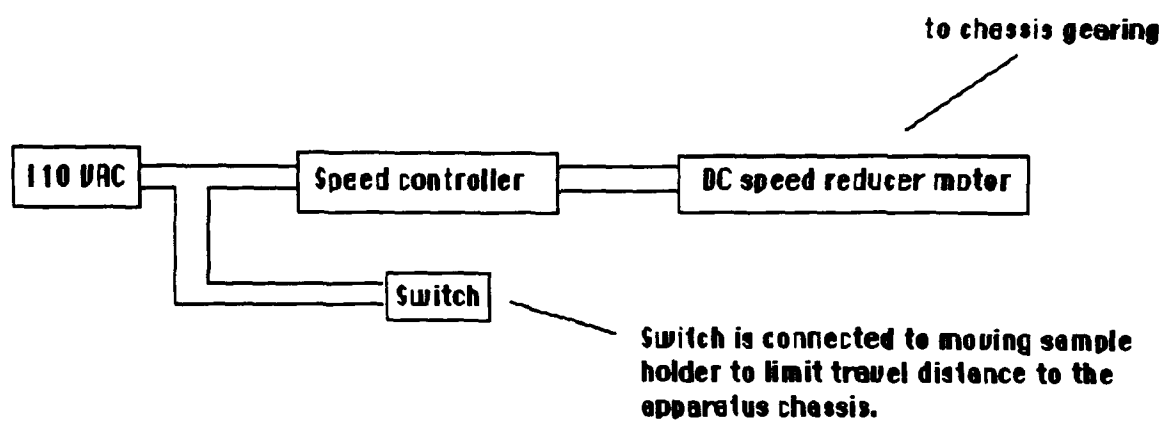


Figure 10. Schematic of the velocity controller

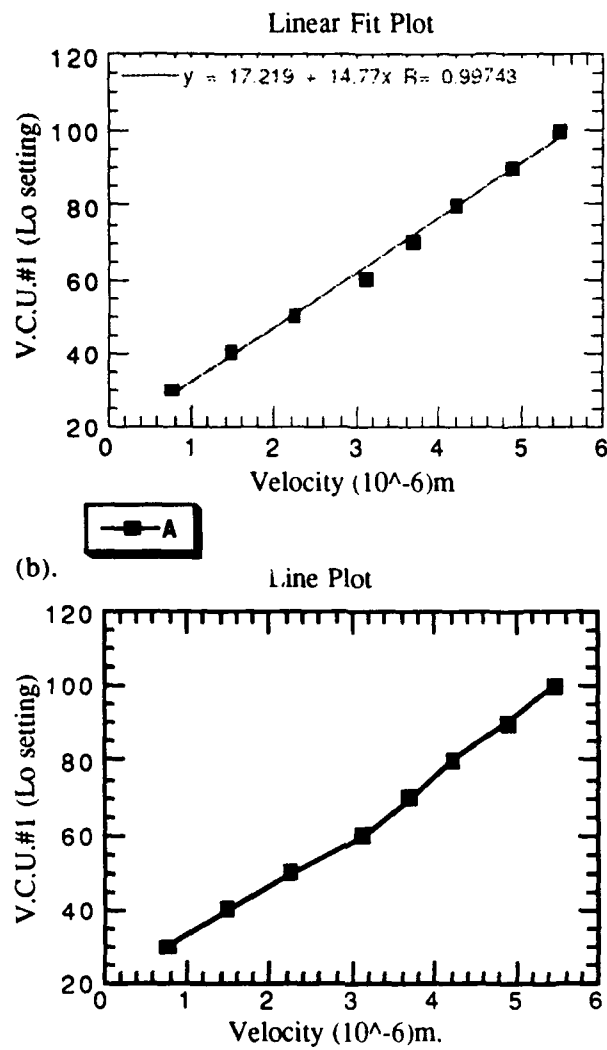


Figure 11. Velocity Control Unit #1 Calibration

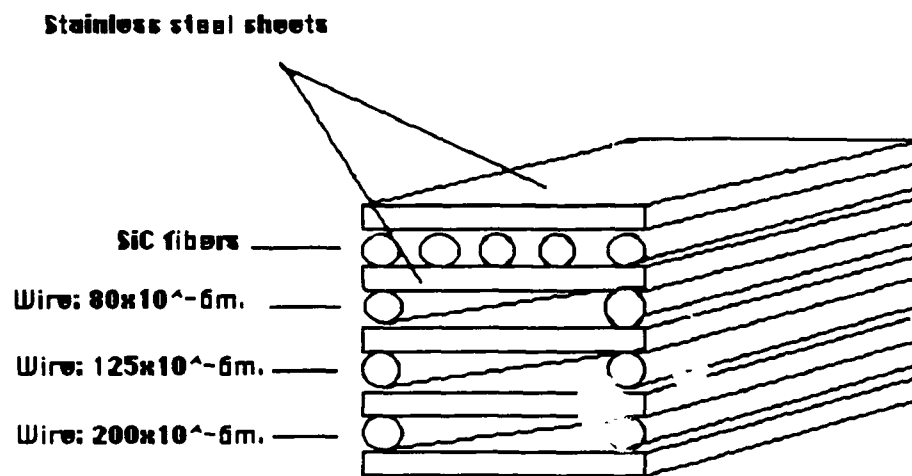


Figure 12. Specimen sample cell.

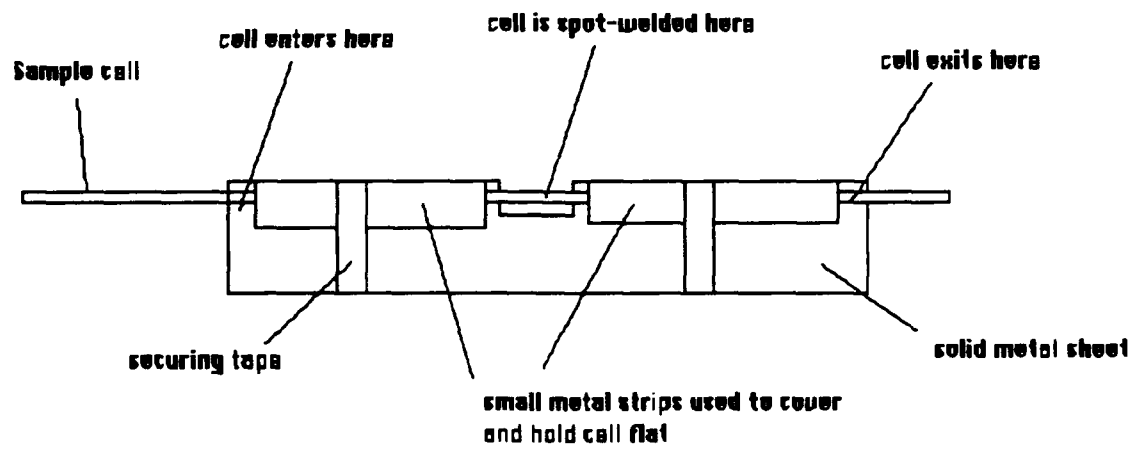


Figure 13. Specimen sample cell guide device.

2.3 HIGH TEMPERATURE UNIDIRECTIONAL SOLIDIFICATION APPARATUS FOR NB-AL AND NB-AL COMPOSITES

Figure 14 shows a general view of the high temperature unidirectional solidification apparatus.

2.3.1 Temperature Gradient Assembly

The directional solidification experiments have been conducted in a system (Figure 15) where the temperature gradient assembly (1) is moved upwards and the ceramic tube containing the sample (2) is held fixed. The temperature gradient assembly consists of a graphite tube (11) held in place by ceramic tube (9,10) and fixed between copper plates (7). The assembly is heated by insulated, water cooled copper induction coils (8). Argon gas is provided separately to the sample (2) and to the graphite (12).

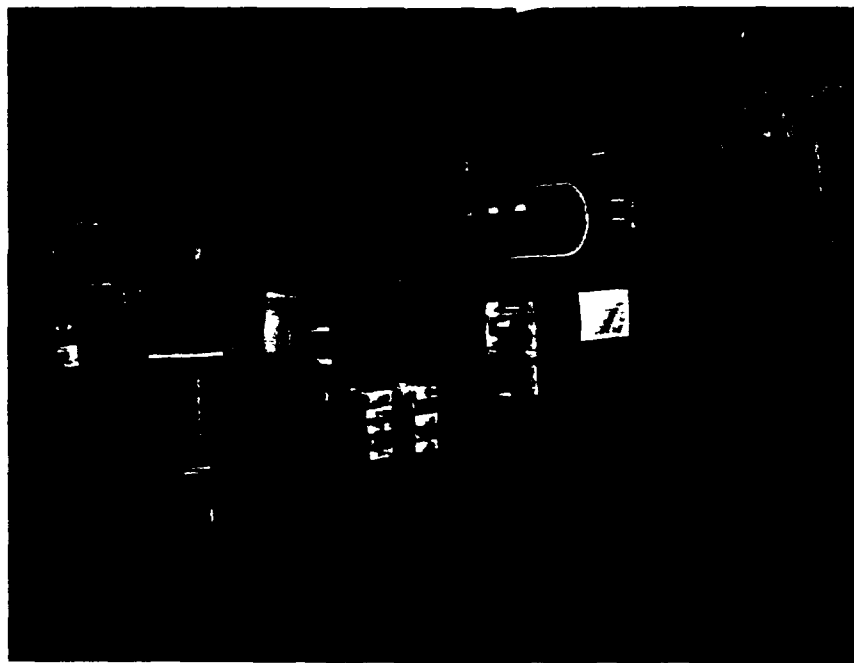


Figure 14. The high temperature Direction Solidification Unit.

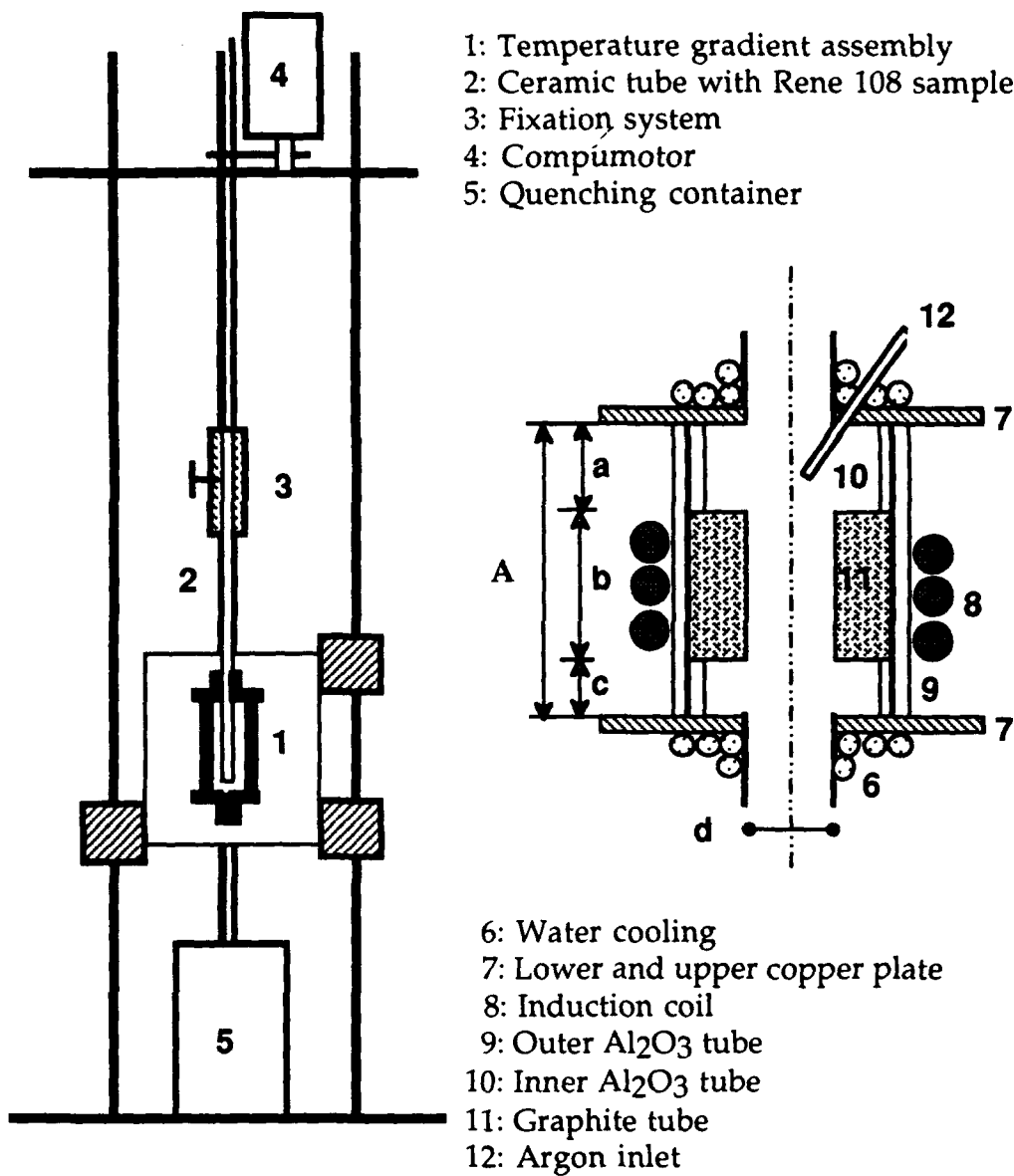


Figure 15. Schematic design of the experimental system (left) and close up view of the cell. The distances (a,b,c,A) of three different temperature gradient assemblies are given in Worksheet I.

2.3.2 Movement Control

The vertical movement of the temperature gradient assembly is controlled by a compumotor (Figure 15 (4)), an electromotor commanded via a computer terminal allowing precise control for way, acceleration and velocity, 12800 steps make 1 rotation. The gears translate the motor movement with a ratio 192/22 to the vertical bar to which the assembly is connected. For instance, 872727 motor steps correspond to 1 cm of vertical displacement. Velocity of the temperature gradient assembly between 0.00015 mm/s to 0.3 mm/s are possible with the installed gears.

2.3.3 Argon Cover

Argon flows directly into the ceramic tube containing the sample (Figure 15 (2)) and into the furnace chamber via the inlet at the upper copper plate (Figure 15 (12)). The flow rate is a compromise between sufficient protection and minimum influence on the sample.

2.3.4 Quench

The tube containing the sample is fixed between two halves of an aluminum cylinder (Figure 15 (3)) pressed against each other by a screw. Turning the wheel connected to the screw releases the ceramic tube which falls down into a water container (Figure 15 (5)).

2.3.5 Measurement of the Temperature Profiles

2.3.5.1 Measurement Setup

Temperature profiles upto a maximum temperature of 1850K have been determined using a molybdenum cylinder instead of a superalloy sample. The cells are now being tested at the higher temperatures required for Nb-Al. The molybdenum cylinder is closed at one end and thus forms a black body into which the lightpipe is "looking" (Figure 16). A sapphire protection tube keeps the lightpipe away from the molybdenum walls (contactless temperature measurement).

2.3.5.2 Optical Fiber Thermometer (OFT) System

The lightpipe itself is a single crystal sapphire tube, polished at one end. It receives the radiation which is conducted through the lightpipe and transmitted to a fiber optical cable.

2.3.5.3 Data Acquisition and Treatment

The Data acquisition unit (Figure 16), translates the received radiation into temperature values knowing the emission factor ($\epsilon = 1.0$) for black body and the calibration factor of the lightpipe (f=1.7930 for sensor #71381). The resolution of the lightpipe is 0.01K. The data is directly transmitted from the OFT-system to a Macintosh computer by a standard RS-232 cable.

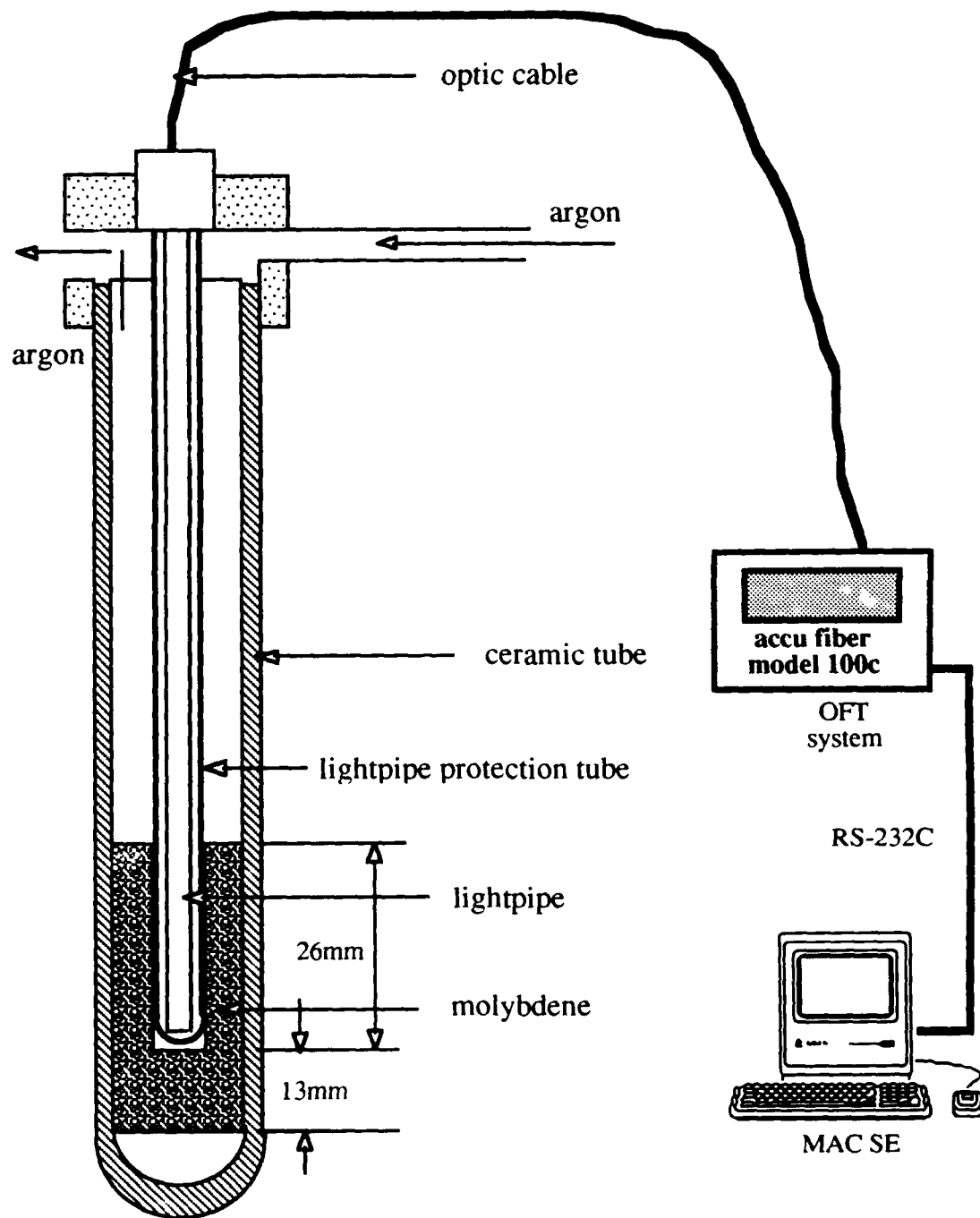


Figure 16 Measurement setup for the determination of temperature profiles within a temperature gradient assembly, by the Optical Fiber Thermometer (OFT) system

2.3.6 Experimental Procedure

2.3.6.1 *Heating up and Stabilization*

The heat up velocity is 10-15 K/min. After reaching the final current set, the assembly is stabilized in temperature for about one hour. Typing heating up and stabilization data is shown in Worksheet III for temperatures upto 1850K.

2.3.6.2 *DS-Experiment*

After the stabilization period, the assembly is moved upwards with a constant velocity. At the quench-position, the fixation wheel (Figure 15(3)) is turned and the ceramic tube is allowed to fall into the water container. The compumotor is stopped, position and time are taken .

2.3.6.3 *Recharge*

After the first sample has been quenched, the assembly is recharged with a previously aligned ceramic tube containing a new sample and another experiment is run. In this way, several experiments can be performed the same day. The advantages of recharging are:

- saving time and energy
- Minimizing graphite consumption
- Uniform conditions for all the sample

2.3.6.4 *Control of Temperature Profiles*

Despite the argon protection, there is a certain graphite consumption. However, the temperature profile is not affected during a 20 hour period of directional solidification experiments at 1850K as shown in Figure 19

2.3.7 Temperature Gradient

The temperature profiles of the three temperature gradient assemblies have been measured. The mean temperature gradient in the mush zone G_M has been determined as in Worksheet IV between temperature (1769K) and (1705K). The temperature gradient at 1769K is also given (Table 2).

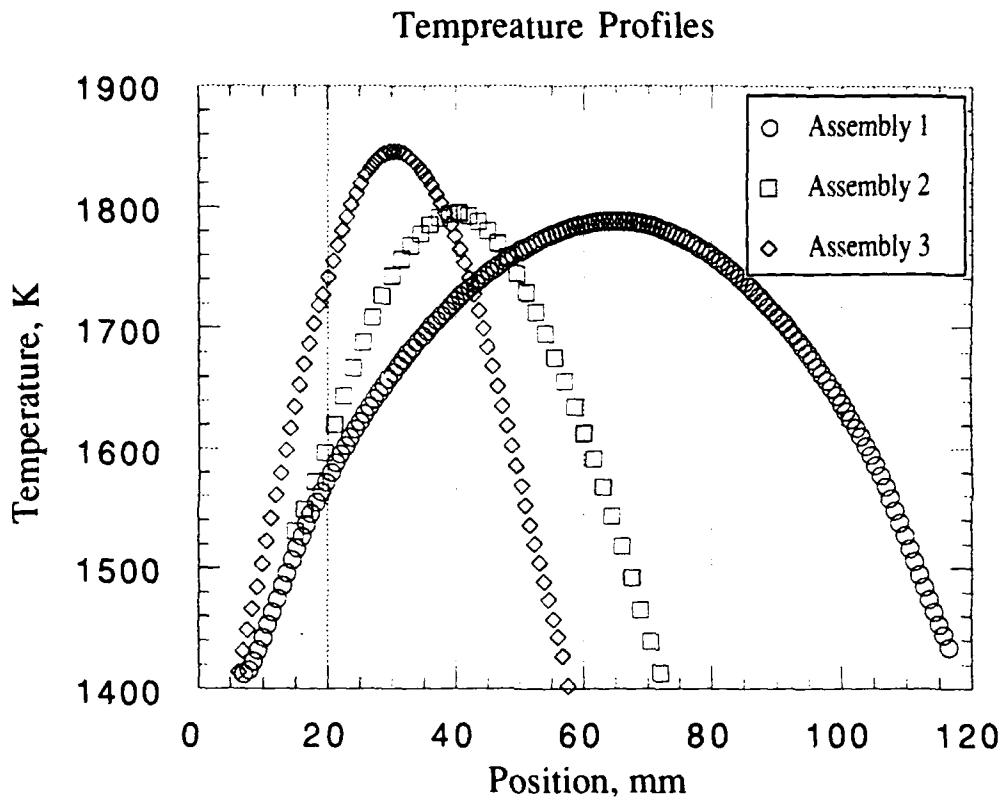


Figure 17. Temperature profile measured inside the three solidification cells at a vertical velocity (upwards) of $V=75 \mu\text{m/s}$ with the OFT system

	G_M (K/mm)	$G(1769)$
Assembly 1	4.6	4.2
Assembly 2	9.9	9.5
Assembly 3	17.5	17.1

Table 2. Mean temperature gradient G_M and $G(1769)$.

The temperature profiles have been measured at two different velocity $v=9.4 \mu\text{m/s}$ and $75 \mu\text{m}$ in opposite directions (upwards and downwards). Figure 18 shows a superposition of these profiles. The effect of graphite consumption on the temperature profile has also been investigated

(Figure 19) by making measurements before and after a complete set of experiments for assembly 3 where the effect is expected be most pronounced.

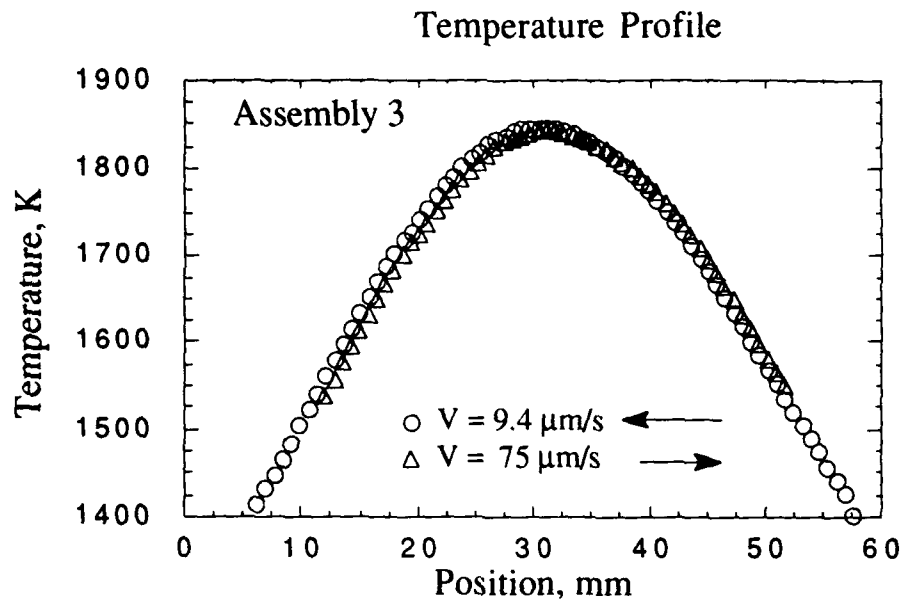


Figure 18. Temperature profile of assembly 3 measured at 2 different velocities upwards with $V=75 \mu\text{m/s}$ and downwards with $V=9.4 \mu\text{m/s}$.

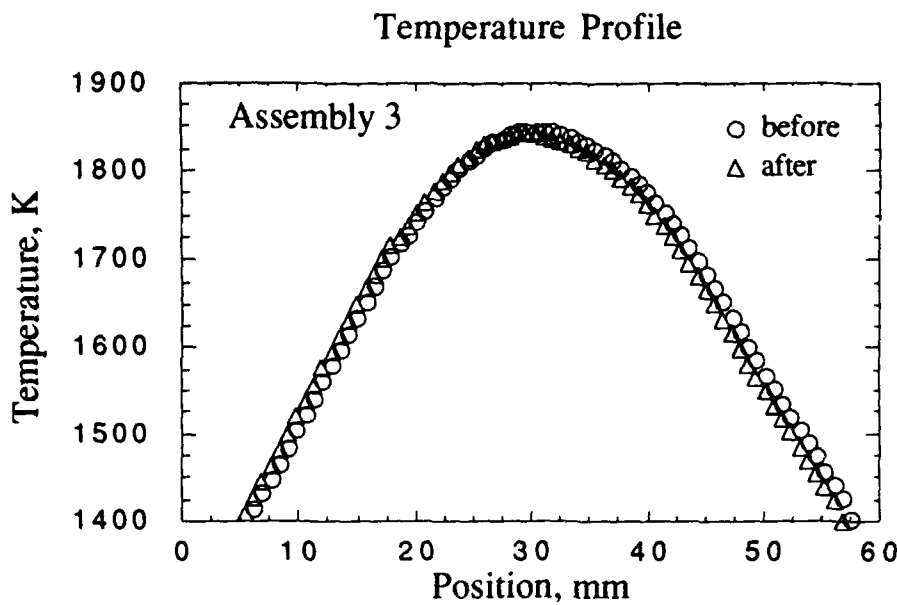


Figure 19 Temperature profiles measured in assembly 3 before and after a complete set of directional solidification experiment.

2.3.8 Temperature Profiles and Gradients

2.3.8.1 *Temperature Profiles*

The temperature profiles have been measured at two different velocity (Figure 18) similar to the ones to be used for the experiments. The two experiments were with upward and downward motion of the solidification cell. Upwards motion was at $75 \mu\text{m}$ and downwards was at $9.4 \mu\text{m/s}$. As no significant difference was found between the two profile, it may be concluded that in this velocity range, the measurement velocity and direction has no significant influence on the profile.

The maximum temperature of the two profile are identical (Figure 18) which mean that the assembly has reached a stable temperature, so that heat up and stabilization procedures described in Worksheet III could be used with confidence.

The temperature profiles measured predict correctly the position of the solid/liquid interface which can be verified by analyzing the quench interface. A small difference in the coil position or in the current set of the transformation can modify the profile and change the temperature gradient. For example, a little modification of the coil position of assembly 2 after the

initial measurement changed the temperature profile. Remeasuring the profile after all experiments will then give a profile with a correct interface position.

The temperature profiles are reproducible even after a whole set of experiments (Figure 19) which shows that the graphite consumption that exists despite of the argon protection does not affect the profile of assembly 3 where the effect of graphite consumption should be most pronounced. This will be tested again at the planned higher temperatures.

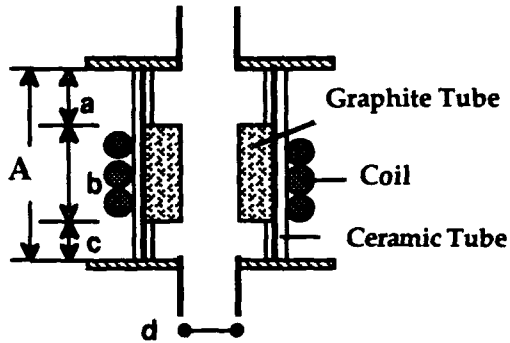
2.3.8.2 *Temperature Gradients*

The temperature gradient at 1769K has been determined by fitting a polynomial to the temperature profile, deriving the polynomial and taking its value at the liquidus temperature (1769K). The values are given in table 2.

The mean temperature gradient, G_M , may be determined by a linear regression of the temperature values between the liquidus temperature and the solidus temperature. Worksheet IV shows linear regressions made at the lower temperatures. These will be extended to the higher temperatures.

WORKSHEET IGeometric Characteristics of the Temperature Gradient Assemblies

The following table contains the values of A,a,b, and c which are indicated in Figure 15 ($d=12\text{mm}$ for all 3 assemblies). Also given are the outer diameter (OD) and the inner diameter (ID) of all tubes, the position of the heating coils and the number of windings for each assembly.



		Assembly 1	Assembly 2	Assembly 3
Outer Ceramic Tube	OD	32mm	32mm	32mm
	ID	27mm	27mm	27mm
	A	104mm	133mm	61mm
Inner Ceramic Tube	OD	26mm	26mm	26mm
	ID	21mm	21mm	21mm
	a	47mm	6mm	27mm
Graphite Tube	OD	26mm	26mm	26mm
	ID	12mm	12mm	12mm
	b	30mm	120mm	14mm
Coil Position Limits	lower	20mm	30mm	15mm
	upper	60mm	110mm	35mm
Number of Coil Winding		5	5	3

WORKSHEET II

Velocity Range and Calibration

The velocity was calculated by following formula from which the velocity range can be list as Table 1.

motor velocity Vm [rot/s]	vertical velocity Ve [$\mu\text{m}/\text{s}$]
0.001	0.15
0.002	0.29
0.004	0.59
0.008	1.17
0.016	2.35
0.032	4.69
0.064	9.39
0.128	18.8
0.256	37.5
0.152	75.1
1.024	150

Vertical displacement : x [mm]

$$V_e = \frac{x \text{ [mm]} * 10^3 \frac{\text{mm}}{\text{mm}}}{t \text{ [s]}}$$

Rotations per second : Vm

$$= \frac{10^3 * x * V_m}{n}$$

Motor unit : $z = x * \text{ratio} * 10^4$

$$= \frac{10^3 * x * V_m * 12800}{z}$$

Number of rotation : $n = z / 12800$

$$= \frac{10^3 * x * V_m * 12800}{x * \text{ratio} * 10^4}$$

Total time required : $t = n / V_m$

$$= \frac{12800 * V_m \frac{\text{mm}}{\text{s}}}{\text{ratio}}$$

Effective Velocity (Ve)

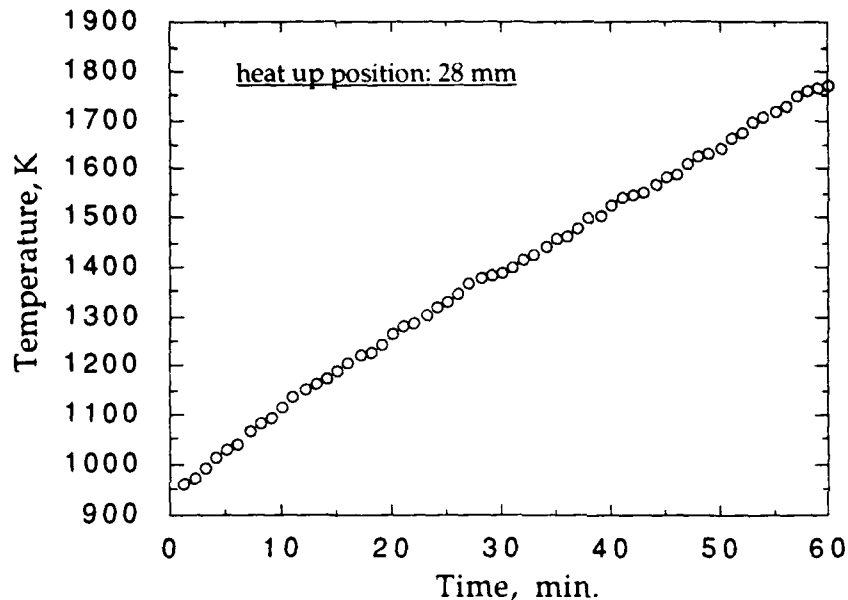
$$V_e = 146.7 \text{ Vm}$$

WORKSHEET III

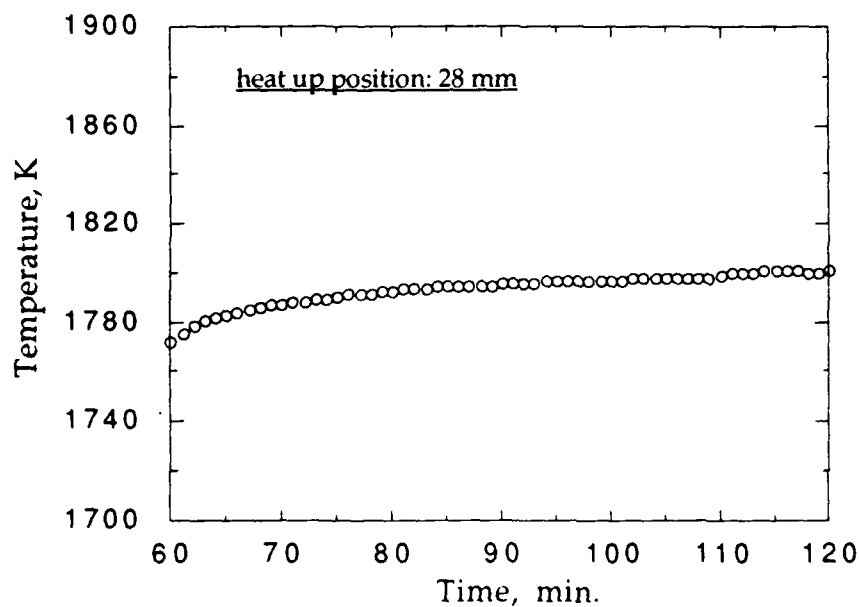
Heating and Stabilization Procedures for the Experiment

Heating up and stabilization are measured with the lightpipe in what is supposed to be the hottest position of the assembly.

Heating up of assembly 3



Stabilization of assembly 3



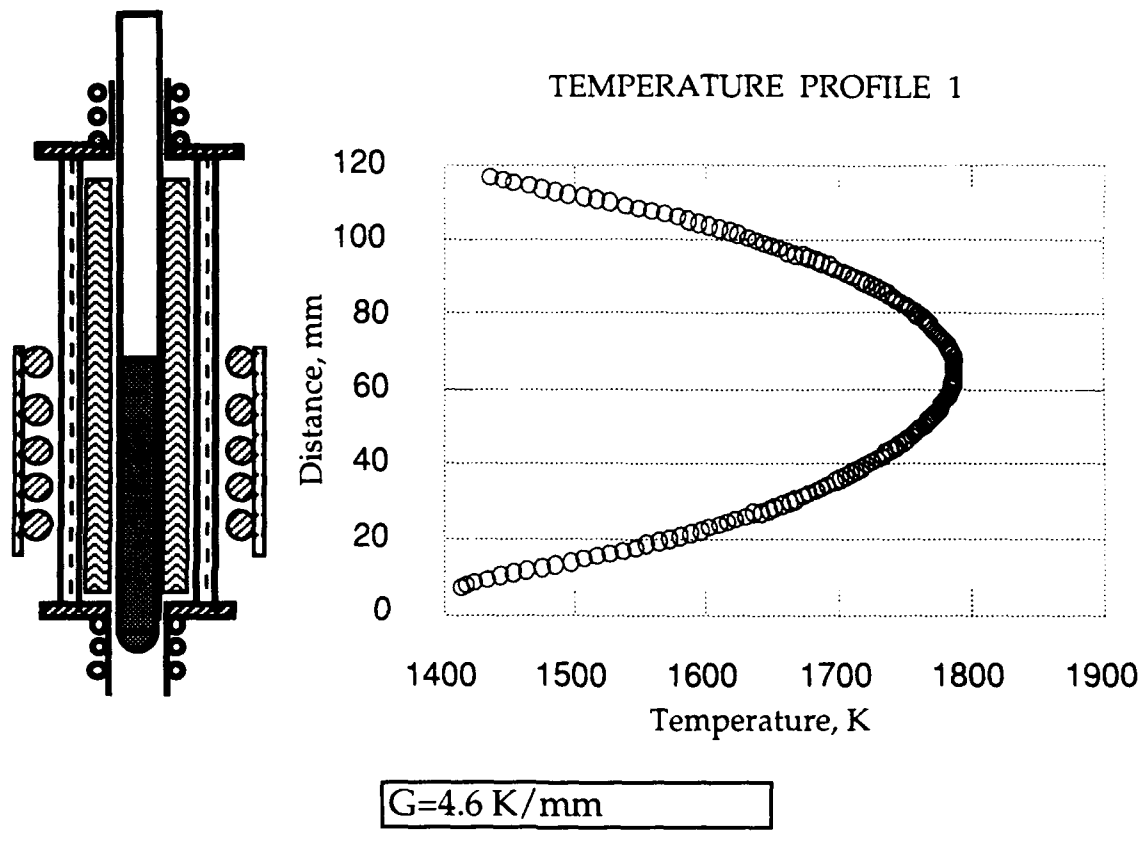
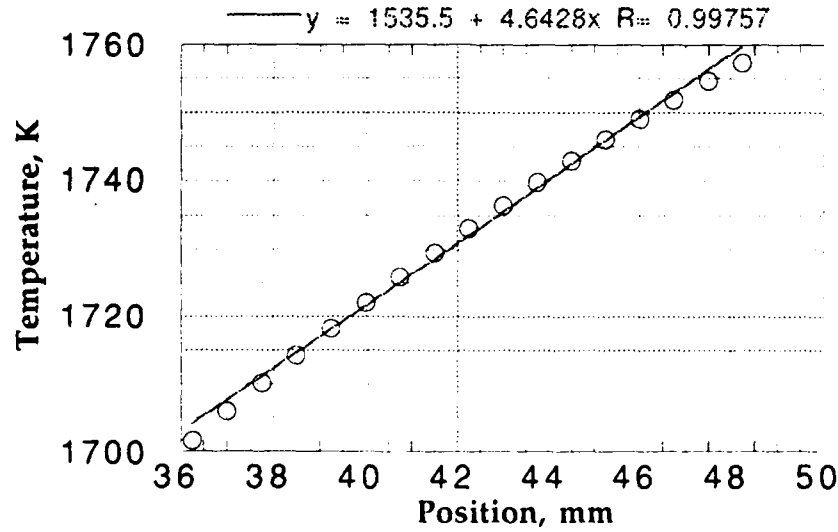
WORKSHEET IVDetermination of the Temperature Gradients in the Mush ZoneTemperature Gradient Assembly 1

Figure IV.1 Determination of the mean temperature gradient of assembly 1

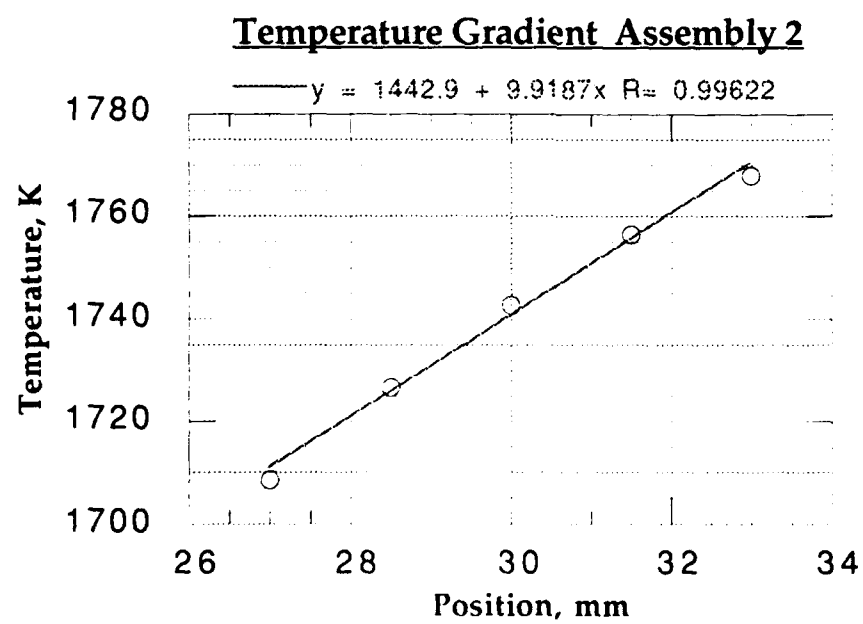
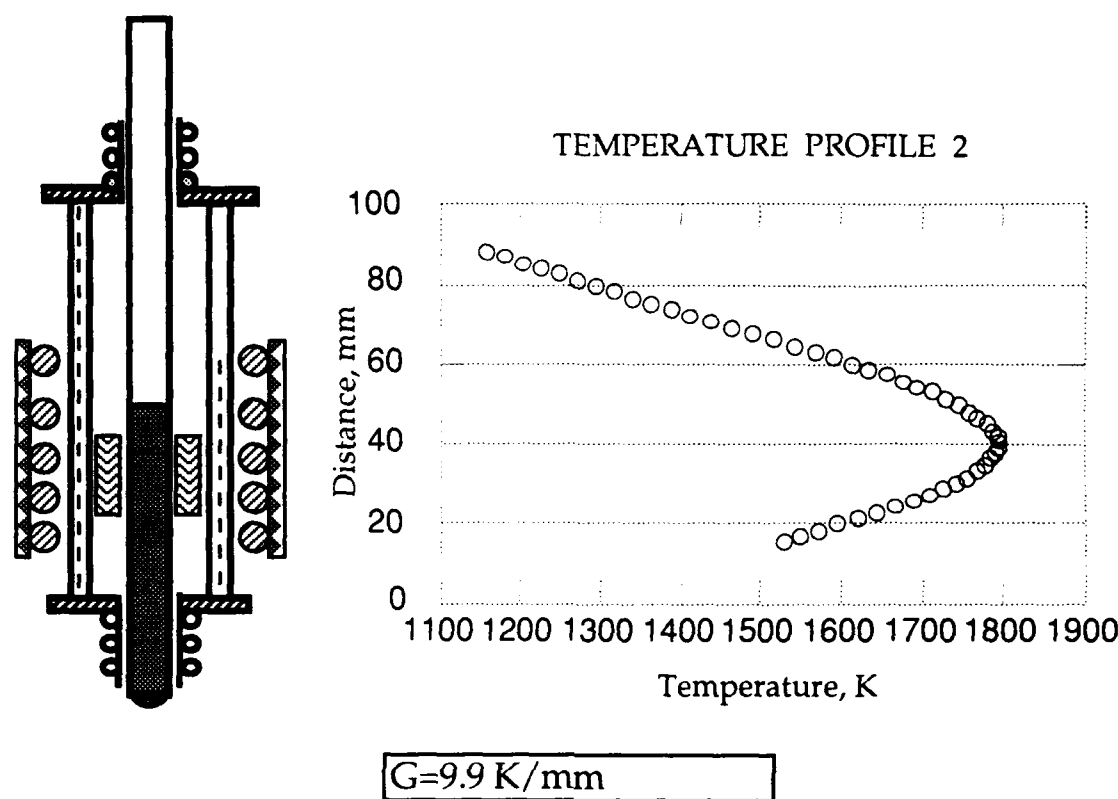


Figure IV.2 Determination of the mean temperature gradient of assembly 2

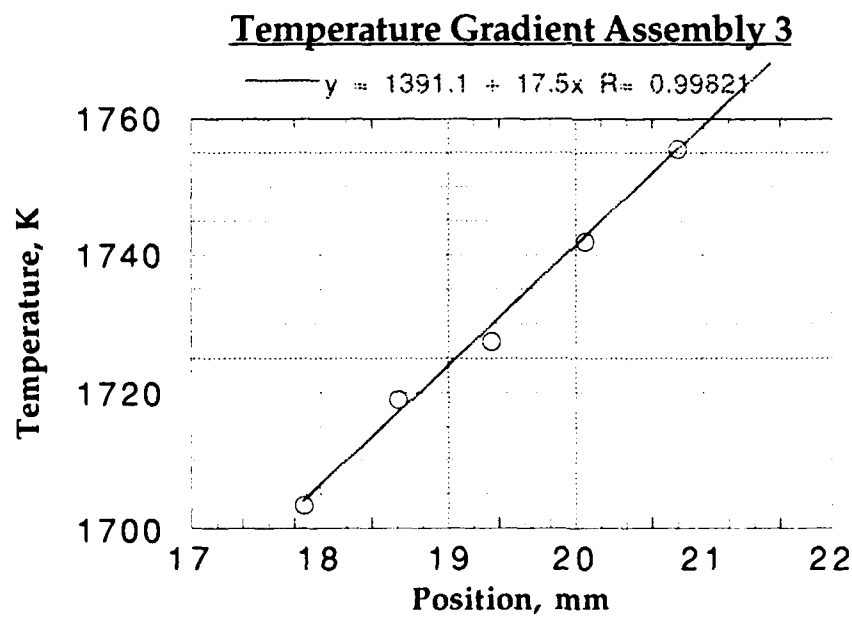
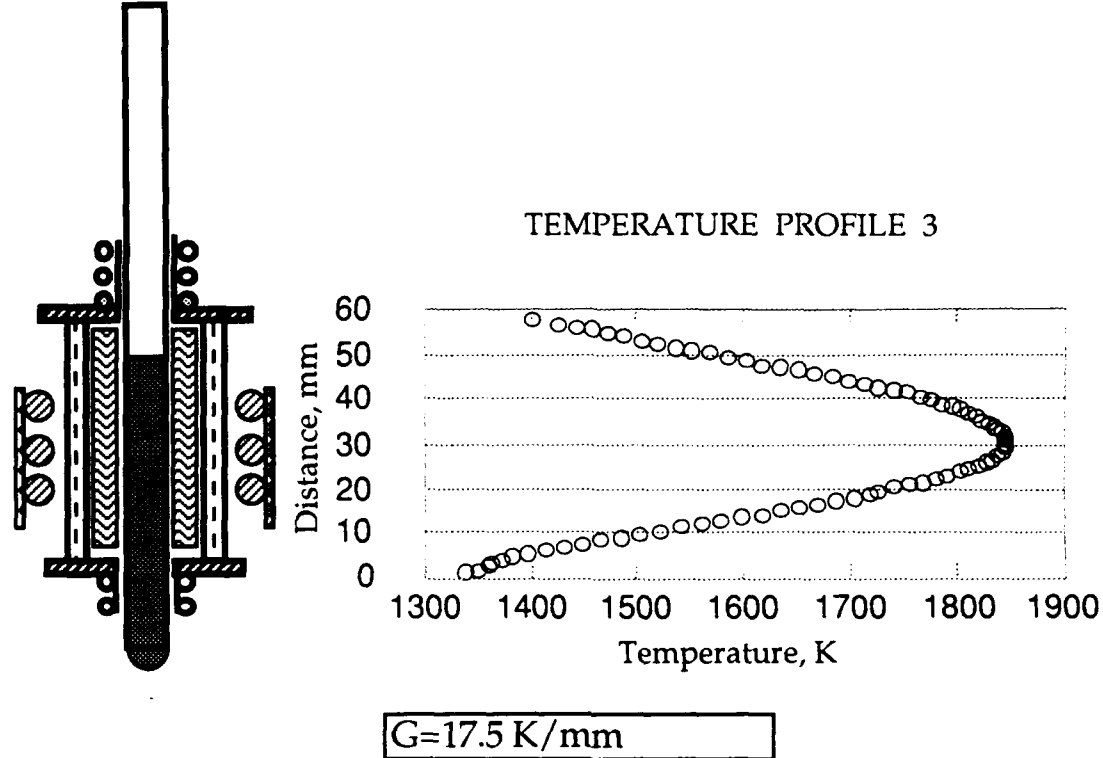


Figure IV.3 Determination of the mean temperature gradient of assembly 3

3.0 THEORY DEVELOPMENT FOR PROJECT

NOMENCLATURE FOR THE FOLLOWING CHAPTER (GROWTH LIMITS)

a_0 = a length scale of the order of the interatomic distance

α = thermal diffusivity (m^2/s)

C_0 = alloy concentration wt%

C_0 = dimensionless alloy concentration = $C_0 m/\theta$

c_p = specific heat (assumed to be constant and equal for solid and liquid)

$d_0 = \Gamma/\theta$ (m)

D = diffusion coefficient (m^2/s)

G = weighted temperature gradient K/m

G = dimensionless temperature gradient = GR/θ

G_c = concentration gradient in liquid at the interface wt%/m

G_c = dimensionless concentration gradient in liquid at the interface $mG_c R/\theta$

ΔH = volumetric heat of fusion (J/m^3)

k_v = velocity dependent partition coefficient

k = equilibrium partition coefficient

m = slope of liquidus line (K/wt%)

P_c = solutal peclet number = $VR/2D$

P_t =thermal peclet number = $VR/2\alpha$

R = dimensionless dendrite tip radius = R/d_0

R_{min} = minimum dimensionless radius = R_{min}/d_0

ΔT_0 = equilibrium freezing range

ΔT_0 = dimensionless freezing range = $\Delta T_0/\theta$

ΔT_{abs} = dimensionless absolute temperature = $\Delta T_{abs}/\theta$

$v_{dim}=\eta\varepsilon V$

V = growth velocity (m/s)

V = dimensionless growth velocity = $Vd_0/2\alpha$

$\varepsilon=a_0/d_0$

Γ = Gibbs Thompson parameter (Km)

$\theta = \Delta H/c_p$ (K)

η = ratio of thermal / solute diffusivity = α/D

λ_1 = primary dendrite arm spacing during constrained growth.

λ_2 = the first side branch spacing.

λ_p = the distance between the tip and the first side branch.

3.1 GROWTH LIMITS

Growth limits are set by plane front growth and the growth observed during rapid solidification. Rapid solidification techniques fall into two broad categories⁽¹⁾: (1) the chilling techniques; and (2) the undercooling techniques. These techniques are illustrated in figure 1. The sequence of events leading to the solidified microstructure, regardless of the technique, are: the melting of the constituents, cooling of the liquid, nucleation or epitaxy, and the growth/coarsening of the initially solidified material. The scale of the final microstructure that forms during rapid solidification is controlled by the number of nucleation events and mainly by the growth process. Growth can occur with a positive temperature gradient (constrained growth) or with a negative temperature gradient (unconstrained growth) in front of the solidifying material. In very broad terms, the two categories of rapid solidification as shown in figure 1 follow this distinction. In this report we examine a few features of the the scale of the microstructure that evolve under rapid solidification conditions for both constrained and unconstrained growth. We consider the solidification of a binary alloy of such a composition that a dendritic morphology establishes itself during the early stages of solidification.

For both types of growth an increase in the solidification interface velocity leads to the dendrite tip becoming finer until a stabilizing influence, first discovered by Mullins and Sekerka,⁽²⁾ causes the tip to blunt to an extent that a plane front re-emerges at high growth velocities. The transition from fine dendritic to plane front happens continuously during constrained growth through an intermediate microcellular structure.⁽³⁾ Microcellular patterns have also been observed during unconstrained growth.

An absolute stability criterion is available for both types of growth. Under most conditions this criterion is independent of the temperature gradient felt by the interface. For constrained and unconstrained growth the criteria are, respectively,^(2,4)

$$V_{abs} = D\Delta T_0/\Gamma k \quad (1)$$

$$V_{abs} = D\Delta T_0/\Gamma k + \alpha_l \theta / \Gamma \quad (2)$$

(see list of symbols, bold italics are dimensionless quantities)

In this report we examine the conditions which determine the finest tip radius that is allowed by a material and process under conditions of rapid solidification.

3.1.1 Theoretical Analysis

Theoretical models for the microstructure development in the dendritic region are based on the solution of the solute and thermal fields and the determination of the operating point of the dendrite tip (considered to be a paraboloid of revolution). For constrained growth of a dendrite growing at constant velocity, V, i.e., at $G > 0$, Kurz et al.⁽⁵⁾ have shown that

$$aV^2 - bV + G = 0 \quad (3)$$

$$a = \Gamma / 4\sigma^* P_c D^2 \quad (4)$$

$$b = \xi_c \theta_c / D \quad (5)$$

$$\xi_c = 1 - (2k / \{2k - 1 + (1 + 1/\sigma^* P_c)^{1/2}\}) \quad (6)$$

σ^* is the stability constant and has a constant value for a given material.⁽³⁾ The value of σ^* is taken to be 0.025 in this report.

$$\theta_c = k\Delta T_0 / [1 - (1-k)Iv(P_c)] \quad (7)$$

$Iv(P_c)$ is the Ivantsov function of the solutal Peclet number P_c .

Equations (3)-(7) can be solved to obtain a unique value for the radius of the dendrite tip. A typical solution is shown for the Al_2O_3 -1wt% MgO system⁽⁶⁾ in figure 2. Assumed values for the calculation are $D = 9 \times 10^{-11} m^2/s$, $k = 0.118$, $G = 3 \times 10^6 K/m$, $k\Delta T_0 = 11.8 K$. Note that the tip radius can vary over several orders of magnitude and that a minimum tip radius is observed. We are interested in this minimum value of the radius, R_{min} . The governing condition for this has been developed earlier⁽³⁾ and is given by

$$1 + [d \ln \theta_c / d \ln P_c] + [d \ln \xi_c / d \ln P_c] = 0 \quad (8)$$

Following Trivedi et al.⁽³⁾ the value of $R_{min}\Delta T_0 / 2\theta$ as a function of the partition coefficient is given in figure 3.

For unconstrained growth ($G < 0$) of an isolated dendrite tip growing with a constant velocity, V, and tip radius, R, into a bath with a fixed undercooling ΔT , Lipton et al.⁽⁷⁾ have shown that a restricted solution exists and is given by

$$\Delta T = Iv(P_t) + C_0(A-1) + 2\sigma^* PtF(A), \quad (9)$$

where $Iv(Pt)$ is the Ivantsov function of the thermal Peclet number, Pt

$$A = \theta_c / k\Delta T_0 \quad (10)$$

$$F(A) = \xi_t + 2\xi_c \eta C_0 A (1-k) \quad (11)$$

$$\xi_t = 1 - 1 / (1 + 1/\sigma * Pt)^{1/2} \quad (12)$$

$$\eta = \alpha / D \quad (13)$$

Only η values which are typical for metals ($\eta = 10^4$) are considered in this report. A plot of ΔT vs R is shown in figure 4. Note that the graph shows two minima corresponding to solutal and thermal control of the radius.⁽⁷⁾ The dimensionless radius R is given from the stability criteria⁽³⁻⁵⁾ as

$$R = [\sigma * Pt F(A)]^{-1}. \quad (14)$$

Substituting equation (14) in equation (9), we get

$$R = 0.5 [\Delta T - Iv(Pt) - C_0 (A-1)]^{-1}, \quad (15)$$

and the condition for the minimum radius becomes

$$1 - d Iv(Pt) / d \Delta T - C_0 dA / d \Delta T = 0. \quad (16)$$

Equations (8) and (16) describe the condition for the minimum radius during growth and may be used to determine the finest microstructure that is allowed.

The onset of the absolute stability and corresponding planar structure occurs according to equations (1) and (2). In reality the equations for the paraboloid tip will breakdown as the tip blunts and plane front is approached. However it is interesting (for order of magnitude calculations) to push the model to this limit to see what type of predictions are made for the pecllet number close to the onset of absolute stability. For unconstrained growth we can combine equation (2) and (9) to get ΔT_{abs} . Assuming that

$$\Delta C_0 (1-k) / \eta k^2 \ll 1, \quad (17)$$

we get Pt for absolute stability as ~ 6.81 . Obviously this prediction is not entirely correct because the cellular tip interacts with neighboring cells for constrained growth and the gradient becomes steeper as a cell tip replaces a

the more sharper dendrite tip. Similarly the gradient would become steeper as tip blunting begins to occur for unconstrained growth and equation (17) is not appropriate. However the Pt value may be considered as typical value where tip blunting can occur.

All the necessary conditions for obtaining the scale of the microstructure close to the absolute stability condition during rapid solidification are now available from equations (1), (2), (8) and (16).

3.1.2 Discussion

3.1.2.1 *Effect of Temperature Gradient*

Although the influence of the imposed temperature gradient during constrained growth is expected to be negligible near the limit of absolute stability,⁽²⁾ there is a small effect on the minimum tip radius as shown in reference 3 especially when considering dilute solutions. For unconstrained growth, once again the temperature gradient term is absent at the conditions of absolute stability, equation (2). The gradient during unconstrained growth, for the calculations described above, is set during the growth by the bath undercooling conditions. The temperature gradient term becomes important at large Peclet numbers if $G_c \xi_c$ is of the same order as $G \xi_t$. The parameter $F(A) \cdot G$ is a measure of this. $F(A)$ is seen from numerical calculations to remain $>>1.0$ for most conditions studied in this report when measured at the limit of the solutal minimum of velocity, but diminishes considerably when approaching thermal minimum closer to the absolute stability conditions.

3.1.2.2 *Minimum Radius During Unconstrained Growth*

Increasing the bath undercooling ΔT leads to an increase in the velocity and the Peclet number. From figure 4 we note that the radius first decreases with undercooling, reaches a minimum corresponding to the solute effect, then increases to correspond to the thermal control, and the further shows the thermal minimum close to the onset of absolute stability.

The effect of composition on the radius has been described earlier⁽⁷⁾ clearly highlighting the influence of the equilibrium partition function especially at low concentrations. For the same dimensionless undercooling the dimensionless radius increases with dimensionless concentration for solute concentration C_0 greater than 0.1⁽⁷⁾.

Figure 5 shows the effect of the equilibrium partition function on the dimensionless undercooling at the minimum and intermediate maximum radius from the solute and thermal effects. The three curves refer to the solutal minimum, the maximum radius between the solutal minimum and

thermal minimum, and the thermal minimum. The undercooling required to obtain the solutal minimum diminishes with the decreasing partition coefficient, however, the undercooling to obtain the thermal minimum remains high (there is a small influence of k on this value and occurs numerically on account of the formulation equation (9)). The minimum radius value ($R_{min} \approx 6.3$) is generally that obtained at the thermal minimum. However, with decreasing k and increasing C_0 , the solutal minimum can be smaller than the thermal minimum. Figure 6 shows the variation of the minimum solutal radius with k and C_0 .

3.1.2.3 Other Microstructure Scales

The other microstructural scales that are necessary to be characterized are the λ_1 (the primary dendrite arm spacing during constrained growth), λ_2 (the first side branch spacing) and λ_p (the distance between the tip and the first side branch). For unconstrained growth, λ_2 /radius is known to lie between 2 and 3 for isotropic materials.⁽⁸⁾ For constrained growth⁽⁹⁾ the ratio is closer to 2. The parameter λ_p , which is important for equiaxed growth, also scales with the tip radius (5 to 10 times tip radius⁽⁸⁾). For constrained growth, data from Somboonsuk and Trivedi⁽¹⁰⁾ indicates that λ_p scales with VC_0 . This relationship is shown in figure 7. Other scaling laws have also been developed for λ_p .⁽¹⁰⁾ λ_1 is more difficult to predict. Recent experiments⁽³⁾ also indicate that λ_1 may not have a unique value in the high growth regime and will reduce significantly if being studied near the dendrite-microcellular transitions.

3.1.2.4 Non-Equilibrium Effects

At high growth velocities non equilibrium effects become important. For example the partition function may increase with velocity. A widely accepted model of solute trapping^(11,12) gives the following relationship between the partition function and velocity

$$k_v = (k + (a_0 V / D)) / (1 + ((a_0 V / D))). \quad (18)$$

Rewritten in dimensionless⁽¹³⁾ form by defining $v_{dim} = \eta \epsilon V$ equation (18) becomes

$$k_v = (k + 2v_{dim}) / (1 + 2v_{dim}) \quad (19)$$

where ϵ is the ratio a_0/d_0 .

The transition from the velocity independent k to the velocity dependent k_v occurs between $v_{\text{dim}}=10^{-2}$ to 10^2 as discussed in reference 13. The transition from k to k_v causes the solution to approach the pure thermal solution at an undercooling value lower than that obtained by using the velocity independent k . This effect will change the scale of the microstructure; specifically the minimum in the solutal tip radius will increase significantly as seen in figure 6 when considering the curve for the variation in the minimum tip radius with k . The present analysis can easily accommodate these effects by incorporating equation (18), into equations (8) and (16). A good estimate is also available from figure 6 and using the partition coefficient calculated from equation (19). This calculation is left to future publications. However it should be noted that the effect on the radius R_{\min} can be substantial, e.g if k increases from 0.1 to 0.8 during high velocity growth and C_0 is 0.1, then from figure 6 we note that R_{\min} can increase by two orders of magnitude i.e. \sim from $10-10^3$. Thus it is important to incorporate non-equilibrium effects especially when k is small.

THIS IS A BLANK PAGE

3.2 GROWTH IN CONSTRAINED ENVIRONMENT

We shall first discuss the main features of the experimental results developed prior to this project, and then develop appropriate models to examine the effect of finite width of the channel on the stability of planar, cellular and dendritic structures. Finally, we shall use the results of experimental study and the predictions of theoretical models to develop a microstructure map which correlates microstructures with the magnitude of the width of the channel.

3.2.1 Microstructures as a Function of Channel Width

For experimental conditions of velocity, temperature gradient and composition which will give a dendritic microstructure in a channel of very large width, the dendritic structure becomes unstable inside a narrow channel. Depending on the size of the channel, the stable structures inside the channel can be cellular, half dendritic, half cellular or planar. One possible sequence of microstructure transitions as a function of channel width is shown schematically in figure 8.

The key parameter that alters the microstructure inside the channel is the ratio d/λ . The large or the small size of the channel is dictated by the ratio d/λ . The condition $d/\lambda=1$ implies that the dendritic structure inside a narrow channel will be the same as the dendritic structure in a very large channel. This is because any dendrite in an array can be thought of as growing in a channel of width λ because of the no flux condition across the planes half way between the dendrites. If d/λ is smaller than one, one may first consider an array of dendrites in a large channel, and then examine what would happen if these dendrites are brought closer together. In this case the solute fields of the neighboring dendrites will overlap which may stabilize the interface with respect to sidebranch instabilities so that a cellular structure can result. This solute field interaction can thus cause dendritic structures to transform to half dendritic, cellular or planar structure inside the channel as the value of d/λ is decreased. Sekhar and Trivedi⁽¹⁴⁾ have also shown that a cellular structure inside a large channel width would become dendritic if d/λ is little larger than one. This can again be explained by first considering a steady state cellular array in a large channel and then visualizing what would happen if the spacing between the cells is increased. In this case the increased spacing will reduce the solute interaction between the cells so that the concentration gradient at the side of the cell will increase and cause sidebranch instability to give rise to a dendritic structure.

3.2.2 Theoretical Models

In this section we shall develop some basic theoretical ideas which will give some insight into the reasons why microstructures are altered significantly inside a channel when the channel width becomes very small. Initially the conditions for the planar interface stability inside a small channel will be examined. Next, a theoretical model will be proposed to evaluate the effect of narrow channel on the stability of cellular and dendritic microstructures. The presence of narrow channel modifies microstructures due to two major effects: (i) The channel walls act as a barrier to the solute diffusion field thereby decreasing the lateral diffusion. This may give rise to morphological transitions, i.e. a nonplanar interface may change to a planar interface. (ii) The requirement to satisfy surface energy balance among the wall, solid and liquid at the triple points causes the interface to acquire curvature. The presence of curvature would: (a) enhance lateral solute transport and thus destabilize a planar interface near the triple point regions or (b) increase the surface energy which will stabilize the interface.

3.2.3 Planar Interface Stability

The stability of a planar interface inside a narrow channel of width d is essentially analogous to the stability of a planar interface for a small grain of width d . This is because the surface energy balance constraint at the wall is equivalent to the surface energy balance at a grain boundary. In the case of a channel, the grain boundary energy is simply replaced by the wall-solid energy. When the velocity of a planar interface is increased, the first instability occurs at the grain boundary. A similar perturbation would be observed inside a small channel at one of the walls. In fact, if the wavelength of perturbation is smaller than the channel width, then the perturbation inside a channel and that at the grain boundary will be very similar. This is shown in figure 9 in which the velocity of a planar interface is increased to destabilize the interface near a grain boundary. Note that the perturbation at the grain boundary on the left of the channel resembles the perturbation inside the channel. Also, the position of the tip of the perturbation near the boundary and inside the channel are exactly the same indicating that the leading segment of these perturbations have the same temperature as long as the perturbation width is smaller than the channel width.

We shall first consider a simpler case in which the contact angle at the wall is 90° so that the interface inside the channel can remain planar at low velocities. The steady-state growth of such a planar interface inside and outside the channel will be precisely the same. The stability of the interface, however, will be different for the interface that is constrained to grow inside the channel. This is because the instability of the interface with respect to long wavelength perturbation is not possible since the possible wavelengths of perturbations are restricted by the width of the channel. Thus, when the channel becomes very narrow, it will tend to increase the stability of a planar interface.

The result of figure 9 shows that the stability of a planar interface inside a channel can be understood by examining the planar interface stability for a grain of finite width. The latter problem has been studied in detail by Unger and Brown.⁽¹⁵⁾ Instead of varying velocity under constant temperature gradient, Unger and Brown examined the stability of a planar interface as a function of temperature gradient under constant growth rate condition. Since the planar interface stability condition is largely determined by the ratio G/V , the results of Unger and Brown can be readily transferred to the constant temperature gradient condition. There are two important aspects of grain boundary instability. First, as the velocity is increased, the grain boundary groove deepens. This grain boundary groove deepening, and the increase in amplitude at the hump around the groove is a slowly varying function of velocity. On the other hand, when the interface becomes unstable, the amplitude of the hump increases sharply. Consequently, by examining the rate of change of amplitude with velocity, it is possible to define the condition at which the planar interface becomes unstable near the grain boundary. Through a detailed numerical analysis Unger and Brown⁽¹⁵⁾ have shown that the critical temperature gradient required for the rapid amplification of grain boundary perturbation increases as the width of the grain decreases or the contact angle at the boundary increases. consequently, for our experiments with constant temperature gradient, the critical velocity for the planar interface instability will decrease as the width of the channel decreases.

A theoretical model for the planar interface stability in finite width samples has also been proposed by Caroli et al.⁽¹⁶⁾. They found that the critical velocity decreases as the thickness of the sample decreases. Figure 10 shows the basis of the Caroli et al. model in which the finite width of the sample results in the development of interface curvature which influences the planar interface stability condition. Also shown are the experimental results of de Cheveigne et al.⁽¹⁷⁾ in impure carbon tetrabromide on the variation in the critical velocity for planar interface instability as a function of the thickness of the sample. It is apparent that the destabilizing effect of interface curvature on the solute gradient is significantly larger than the stabilizing effect of capillarity so that the critical velocity decreases as the width of the channel decreases.

3.2.4 Cellular and Dendritic Growth

The formation of cellular and dendritic structures inside a narrow channel will now be examined. The basic model for cellular growth in a channel is shown in figure 11, and the solution of this model requires the solution of diffusion equation in the liquid around the cellular interface. Since the growth rate in cellular regime is very small, the diffusion distance, D/V , is much larger than the scale of cellular microstructure. Thus the diffusion field is essentially governed by the Laplace equation:

$$\Delta C = 0 \quad (20)$$

where Δ is the Laplacian operator. The concentration on the interface is given by:

$$C = (C_0/k) + z(G/m) + (\Gamma/m)K \quad (21)$$

where K is the curvature of the interface and Γ is capillarity constant which is the ratio of the interfacial energy to the melting entropy per unit volume. z is the coordinate in the direction of growth and the origin of the coordinate system is taken to correspond to the location corresponding to the planar interface condition. The normal gradient of concentration at the interface is determined by the flux balance condition at the interface:

$$(\partial C / \partial n) = - (V/D) \cos \theta C_I (1 - k) \quad (22)$$

where θ is the angle between the interface normal and the growth direction, and C_I is the concentration along the interface. The boundary condition at the wall are given by:

$$\partial C / \partial y = 0, \quad \text{at } y = +d/2 \text{ and } -d/2. \quad (23)$$

where y is the coordinate is perpendicular to the growth direction.

In order to take into account the imposed constant temperature in the liquid, we now define a concentration variable, C' , such that

$$C' = C - (C_0/k) - z(G/m) \quad (24)$$

where C_0 is the alloy composition, k the solute distribution coefficient, G the temperature gradient and m the slope of the liquidus which is assumed to be constant. In this coordinate system the tip of the cell will be located at a distance z_0 . With this variable the diffusion equation becomes:

$$\Delta C' = 0 \quad (25)$$

with the boundary conditions:

$$C' = (\Gamma/m)K, \quad (26)$$

$$\partial C' / \partial n = - [C_I (1 - k)(V/D) + (G/m)] \cos \theta, \quad (27)$$

and

$$\partial C'/\partial y = 0 \quad \text{at } y = +d/2 \text{ and } -d/2. \quad (28)$$

The solution of equations (25) to (28) is complicated due to the fact that the shape of the interface is not known, but it must be calculated such that the the solutions of the above equation are self-consistent. Pelcé and Pumir⁽¹⁸⁾ and Karma and Pelcé⁽¹⁹⁾ have shown that the above set of equations can be solved if one assumes that the concentration variation near the tip region is small. In this case the problem is analogous to the Saffman-Taylor problem of viscous fingering in which the concentration field C' is analogous to the pressure field. The solution to the viscous fingering in a Hele-Shaw cell has been obtained by McLean and Saffman⁽²⁰⁾ and Vanden-Broeck,⁽²¹⁾ and they found a discrete set of solutions. Kessler and Levine⁽²²⁾ have subsequently shown that only the fastest growing cell is stable with respect to tip-splitting instability. This analogy between the Saffman-Taylor fingers and cellular growth has been developed by Pelcé and Pumir⁽¹⁸⁾ and Karma and Pelcé⁽¹⁹⁾ to obtain a self-consistent solution for cellular growth in a channel of width d . The solution obtained by Karma and Pelcé⁽¹⁹⁾ can be rewritten in the following form that is suitable for calculations of cellular growth in a channel:

$$d^2 = \left[\frac{\Gamma \Delta T_0}{|m|G} \right] \left[\frac{V_c}{V} \right] \left[\frac{50.8 \Lambda}{2\Lambda - 1} - 47.93 \right] \left[\frac{1 - (1 - k)\Lambda}{k \{ 1 - (V_c/V) \}} \right] \quad (29)$$

$$\frac{\Delta T}{\Delta T_0} = \frac{k\Lambda + (1 - \Lambda)(V_c/V)}{1 - (1 - k)\Lambda} \quad (30)$$

where ΔT and ΔT_0 are cell tip undercooling and the equilibrium freezing range of the alloy, respectively. The parameter $\Lambda = \Lambda'/d$ is the relative width of the cell near the tip, and the physical interpretation of Λ' is shown in figure 11. The parameter Λ can be eliminated from the simultaneous solution of equations (29) and (30) so as to obtain a relationship between the cell tip undercooling and the width of the channel.

Equations (29) and (30) have been solved for the succinonitrile-acetone system, and the results are shown in figure 12. The dimensionless undercooling, $\Delta T/\Delta T_0$, is found to increase rapidly as the width of the channel is decreased. Note that when the dimensionless undercooling becomes unity, a planar interface is stabilized. As the width of the channel is increased, the dimensionless undercooling decreases so that the cellular interface approaches the condition for a dendritic growth. The results of this

theoretical model explain the effect of finite width channel on microstructural transitions, as observed in our experimental study.

Figure 12 shows that the interface temperature in a small channel will be lower than that in a large channel, and this is observed experimentally, as shown previously.⁽²²⁾ For a channel whose width is equal to λ , the tip temperature will be identical to that obtained in experiments carried out in unconstrained liquid, and the tip temperature will vary with velocity, as shown schematically in figure 13. The effect of finite size channel will be to alter the tip temperature. The tip temperature will decrease as the channel width decreases, whereas it will increase for d greater than λ . The effect of finite size channel width on the tip temperature of cell is also shown schematically in figure 13.

The assumptions in the model that the concentration variation in the tip region is small and that the diffusion field is governed by the Laplace equation restricts the application of the model to the cellular regime. A detailed model which is valid close to the planar/cellular and cellular/dendritic transitions needs to be developed to understand quantitatively the microstructural transitions in finite width channels.

When a dendritic structure forms in a channel, the walls of the channel significantly influence the diffusion field behind the dendrite tip region. The major effect is to reduce the concentration gradient as the width of the channel becomes narrow. This reduction in solute gradient will tend to stabilize the interface against sidebranch formation. When sidebranches do form, the amplification rate of these sidebranches would be reduced significantly in narrow channels which will tend to increase the secondary branch spacings. These coarser sidebranch spacings are not the result of surface energy driven coarsening, but they arise from the dampening effect caused by the walls on the amplification of these branches.

3.2.5 Microstructure Map

The theoretical ideas discussed above show very clearly the reasons why morphological transitions may occur as the width of the channel is decreased. The critical velocity for the stability of planar interface is decreased with the decrease in the channel width. The transitions between cellular and dendritic structures have been found to depend on the channel width in a more complicated manner in that it is controlled not by the width of the channel, but by the relative width of the channel, i.e. d/λ . For a very narrow channel, where d/λ is small, a dendritic structure will tend to become cellular as the relative width is decreased. However, if the relative width is just greater than one, then a cellular structure in a large channel will become dendritic as the relative width becomes larger than one.

The basic ideas on the morphological transitions in narrow channels can be summarized in a microstructure map, shown in figure 14. For very large channel width, the planar, cellular and dendritic structures depend upon velocity in a manner indicated at the right hand side of the diagram. When the relative width of the channel is very small, the cellular regime is expanded since both the planar and dendritic structures will transform to cellular structures. The dendritic regime will be extended to lower velocities when the relative width is little larger than unity. For clarity, we have not shown the regimes of half dendritic and half cellular in this figure.

NOMENCLATURE FOR THE FOLLOWING CHAPTER (COMBUSTION SYNTHESIS)

A_c	A parameter which accounts for initial particle contact
$\Delta P^0 AP$	Finite difference coefficients
Bi	Biot Number = $h H_s / K^*$
C_p	Specific heat, (J/kgK)
C_{PR}	Specific heat of reacted product, J/kgK
C_{PU}	Specific heat of unreacted product, J/kgK
C_{PRL}	Specific heat of reacted liquid product, J/kgK
d	Diameter of the substrate sample, m
E	Activation Energy, J/mole
f_L	Fractional liquid content
f_E	Fractional eutectic content
H	Enthalpy, J/kg
h	Surface heat transfer coefficient, (W/m ² K)
H_s	Length of specimen, m
ΔH_{SL}^*	Latent-heat of fusion of the product phase, J/kg
ΔH_{SE}^*	Latent-heat of fusion of the eutectic, J/kg
K	Non-dimensional thermal conductivity
K^*	Dimensional thermal conductivity, W/mK
K_o	Frequency factor, Sec ⁻¹
K_s	Dimensional thermal conductivity of solid, W/mK
K_l	Dimensional thermal conductivity of liquid, W/mK
K_c	Equilibrium partition coefficient
Q	Heat of reaction, J/kg
t	Dimensional time, sec
T	Temperature, K
T_E	Eutectic temperature, K
T_L	Liquidus temperature, K
T_M	Melting temperature, K
T_f	Ambient temperature, K
V_f	Volume fraction of diluent
Z	Non-dimensional co-ordinate
Z^*	Dimensional co-ordinate, m
ρ	Density, kg/m ³
\emptyset	Non-dimensional enthalpy
θ	Non-dimensional temperature
θ_f	Non-dimensional ambient temperature
τ	Non-dimensional time
η	Non-dimensional fraction of reacted product

Superscripts

n New time level
o Old time level

Subscripts

n Northern side of control volume
N Northern control volume
P Center of current control volume
s Southern side of control volume
S Southern control volume

3.3 COMBUSTION SYNTHESIS

Most of the alloys and composites of the Nb-Al type will be made by combustion synthesis. It is therefore important to understand this process theoretically. The recent interest in the development of new materials through combustion synthesis has highlighted the importance of the phase change phenomena during combustion and the subsequent solidification process. Few papers have dealt with the complete numerical solution of the heat conduction process in materials prepared by combustion synthesis.⁽²³⁻²⁷⁾ Several important problems have not yet been tackled or need further addressing. These relate to the physics of the combustion process and the macro-micro models of synthesis from condensed initial constituents. The aim of the macro-micro models should be to relate the final microstructure to the combustion process. This report is a first report in this direction.

Anderson et al.⁽²³⁾ have solved for the steady state and transient solutions for the spontaneous ignition problem with the Frank-Kamenetskii parameter as a incremental loading variable using the Galerkin Finite element method. Numerical prediction of the modes of flame front propagation and stability phenomena in condensed single-phase systems (i.e., no melting) has been reported by Shkadinsky et al.⁽²⁴⁾ The steady state and oscillating regimes of combustion regimes have been obtained numerically by Holt et al.⁽²⁶⁾, although numerical solutions have not been discussed in detail. A detailed analysis and modeling of exothermic solid-solid noncatalytic reactions has been carried out by Puszynski et al.⁽²⁷⁾ Puszynski et al.⁽²⁷⁾ developed the criteria for stable, unstable and degenerated combustion, as well as the approximate relations for the velocity of a steady state profile as a function of the heat-transfer coefficient, which was applied arbitrarily to all nodes of their numerical scheme. A recent review by Margolis⁽²⁸⁾ has shown that several oscillatory modes of combustion may manifest during condensed phase combustion process

No detailed numerical investigation of the phase change heat conduction problems and subsequent solidification process have been reported for combustion synthesis. Margolis⁽²⁹⁾ has however considered the case of a phase change leading to a change in the combustion kinetics during the melting of a reactant phase. The aim of the present report is to deal with the numerical investigation of the various parameters involved in the solution of the phase change problem in the combustion synthesis process through a one dimensional analysis. The essential influence of the long range variables like thermal conductivity can also be easily elucidated through a one dimensional analysis.

Exothermic reaction processing circumvents difficulties encountered in conventional methods of time and energy intensive sinter processing and is

being extensively studied for the creation of ceramic and intermetallic compounds.⁽³⁰⁻⁴⁰⁾ The heat transfer during the combustion process is highly non-linear on account of both the combustion reaction as well as the solidification process. It is therefore not immediately apparent what the products and microstructure in the combusted product will be. However various experimental studies have been reported where the combustion microstructures temperatures and velocities have been measured.⁽³⁰⁻⁴⁰⁾ The resultant microstructure in a combustion synthesized solid is determined by the reaction, thermal history and the nature of microstructure evolution determined by the cooling conditions and the constraints imposed on the solute diffusivity. There is a similarity of this process with the solidification process in the presence of constraints.^(14,41,42) In this report combustion conditions are considered for the formation of non-stoichiometric TiC for which the values of velocity, temperature and reaction products are available.⁽³⁴⁾ Additionally a method to incorporate a heat source to start the combustion process is presented in this report.

3.3.1 Mathematical Formulation for Combustion Synthesis of an Alloy

A first-level model for the self-propagating combustion synthesis of composite materials is developed in this report. The model has the following features:

- (1) Formation and solidification of non-stoichiometric combustion products. This includes the phase change of the product through its solidification and eutectic range.
- (2) Initial heating by a surface heat source or ignition by bringing a portion of the uncombusted material to an ignition temperature.
- (3) Calculation of pertinent synthesis parameters that will allow for prediction of final microstructure.
- (4) Versatility in incorporating thermal effects on account of porosity formation and liquification.

The one-dimensional numerical model assumes the following sequence of events: (a) Powders of combustible material and diluents are pressed together, (b) these are ignited by a surface heat source, (c) the combustion front propagates in the compact, (d) There is a cooling source at one end (opposite surface as shown in figure 15). External cooling may be present at the side walls because of radiative or convective cooling. For the problem discussed in this report, the combustible mixture is formed out of Ti and C. The final product is non-stoichiometric TiC and the product obtained from non-equilibrium cooling of the liquid is governed by the section of phase diagram⁽⁴³⁾ shown in figure 16.

The energy equation for transient heat conduction, which includes the source term containing heat release due to the reaction is given by

$$\rho \frac{\partial H}{\partial t} = \frac{\partial^2 (K^* T)}{\partial Z^*^2} - \frac{4 * h}{d} (T - T_f) + \rho Q K_0 (1 - V_f) A_c \exp\left(\frac{E}{RT}\right) \quad (31)$$

In the equation, the first term on the right hand side is the conduction heat transfer term, the second term is the surface heat loss parameter and the third term gives the heat release on account of the reaction. See nomenclature for an explanation of symbols. In this analysis we have assumed that the reaction is homogeneous and contact limited. The model leads itself to different physics of the combustion problem by changing equation (36) given below. We now define the following non dimensional parameters

$$\theta = \frac{C_{PR}(T - T_E)}{\Delta H_{SL}^*}, \quad \emptyset = \frac{H - H_{SE}^*}{\Delta H_{SL}^*},$$

$$H_{SE}^* = C_{PR}(T_E - T_0) \quad K = \frac{K^*}{K_S}, \quad Z = \frac{Z^*}{H_S}, \quad \tau = K_O t$$
(32)

Using the above non dimensional parameters, the above equation may be recast as

$$\frac{\partial \emptyset}{\partial \tau} = \gamma \frac{\partial^2 (K\theta)}{\partial Z^2} - \alpha(\theta - \theta_f) + (1 - V_f) A_c v \exp\left(\frac{-N}{1 + \beta\theta}\right)$$
(33)

where

$$\gamma = \frac{K_S}{\rho H_S^2 C_{PR} K_O}, \quad v = \frac{Q}{\Delta H_{SL}^*}, \quad N = \frac{E}{RT_E}, \quad \beta = \frac{\Delta H_{SL}^*}{C_{PR} T_E}, \quad \alpha = \frac{4h}{d\rho K_0 C_{PR}}$$
(34)

The unreacted fraction of the specimen ($1 - \eta$) contributes to the heat of reaction from the combustion. This may be incorporated into equation (33) to give:

$$\frac{\partial \emptyset}{\partial \tau} = \gamma \frac{\partial^2 (K\theta)}{\partial Z^2} - \alpha(\theta - \theta_f) + (1 - V_f)(1 - \eta) A_c v \exp\left(\frac{-N}{1 + \beta\theta}\right)$$
(35)

where η = Reacted fraction.

The above equation is solved simultaneously with the following mass balance equation (first order reaction)

$$\frac{\partial \eta}{\partial \tau} = A_c (1 - \eta) \exp\left(\frac{-N}{1 + \beta\theta}\right)$$
(36)

The product microstructure may be determined from the solidification conditions of the liquid of composition C_0 that forms during the combustion process. The composition C_0 is predetermined in the analysis. In this report thermophysical constants and phase diagram that is considered is the Ti-C phase diagram.⁽⁴³⁾ The relevant portion of this phase diagram is shown in figure 16.

The composition C_0 melts at a liquidus temperature T_L . Subsequent solidification follows the Scheil distribution or the linear distribution of fraction solid with temperature.⁽⁴⁴⁾ The product additionally contains a volume fraction of eutectic f_E which is calculated from the Scheil condition as $C_E/C_0 = f_E^{(k-1)}$. During the combustion process there is no formation of the mushy or eutectic zone and this need not be considered. However to maintain a strict balance of enthalpy, it is assumed in this report, that all phases are also present during the heat up combustion cycle. Figure 17 is a plot of the non dimensional enthalpy and non dimensional temperature during combustion and solidification. The derivation of this relationship is given below. The various η values represent the changes in this relationship as combustion proceeds. Table 1 shows the average thermophysical constants used in this report. The non-dimensional relationship between enthalpy and temperatures (i.e., $\phi-\theta$ relation) is derived in the manner given below. The analysis is similar to the relationships for solidification derived by Sekhar et al.^(44,45) following the approach for an enthalpy-temperature type solution of the Stefan problem proposed by Shamsunder and Sparrow.⁽⁴⁶⁾

CASE 1

When $\eta = 1$ i.e., constituents are fully reacted.

SOLID PHASE: ($T < T_E$)

$$\phi = \theta = \frac{C_{PR}(T-T_E)}{\Delta H_{SL}^*}, \quad T < T_E, \quad \phi < 0 \quad (37)$$

EUTECTIC REGION: ($T = T_E$)

$$\theta = 0 \quad \phi = f_{LE} \frac{\Delta H_{SE}^*}{\Delta H_{SL}^*} \quad (38)$$

$$0 \leq f_{LE} < f_E, \quad \text{and} \quad 0 \leq \phi \leq f_E \frac{\Delta H_{SE}^*}{\Delta H_{SL}^*} \quad (39)$$

MUSHY REGION: ($T_E < T < T_L$)

$$\theta = \frac{C_{PR}(T-T_E)}{\Delta H_{SL}^*}, \quad \phi = \frac{C_{PR}(T-T_E)}{\Delta H_{SL}^*} + f_L \quad (40)$$

$$\therefore \theta = (\emptyset - f_L) \frac{C_{PR}}{C_{PRL}} \quad (41)$$

where $f_E < f_L \leq 1.0$:
 $K = K_S (1-f_L) + K_L f_L$

Where f_L is the liquid fraction and is given by the following linear relation⁽⁴⁰⁾

$$f_L = f_E + \left(\frac{T - T_E}{T_L - T_E} \right) (1 - f_E) \quad (42)$$

$$f_L = f_E + \theta \left(\frac{\Delta H_{SL}^* (1 - f_E)}{C_{PR}(T_L - T_E)} \right) \quad (43)$$

$$\therefore \frac{\Delta H_{SE}^*}{\Delta H_{SL}^*} f_E < \emptyset \leq 1 + \frac{C_{PR}(T_L - T_E)}{\Delta H_{SL}^*} \quad (44)$$

$$\therefore \emptyset = R_1 \theta + R_2 \quad (45)$$

$$\text{where } R_1 = \frac{C_{PRL}}{C_{PR}} + \frac{\Delta H_{SL}^*}{C_{PR}} \left(\frac{1 - f_E}{T_L - T_E} \right)$$

$$R_2 = f_E$$

LIQUID PHASE: ($T < T_L$)

$$\emptyset = 1 + \frac{C_{PRL}(T - T_E)}{\Delta H_{SL}^*}, \quad \theta = \frac{C_{PR}(T - T_E)}{\Delta H_{SL}^*} \quad (46)$$

$$\therefore \theta = \frac{C_{PR}}{C_{PRL}} (\emptyset - 1) \quad (47)$$

$$\emptyset > 1 + \frac{C_{PRL}(T_L - T_E)}{\Delta H_{SL}^*}, \quad (48)$$

CASE 2

When $\eta=0$ i.e., constituents are still unreacted

$$\theta = \frac{C_{PR}(T-T_E)}{\Delta H_{SL}^*}, \quad \emptyset = \frac{C_{PU}(T-T_O) - C_{PR}(T_E-T_O)}{\Delta H_{SL}^*} \quad (49)$$

where

$$R_1 = \frac{C_{PR}}{C_{PU}}, \quad R_2 = \frac{(C_{PR}-C_{PU})(T_E-T_O)C_{PR}}{C_{PU}\Delta H_{SL}^*} \quad (50)$$

CASE 3

When $0 < \eta < 1$, i.e., partial combustion has occurred

$$\text{define } \emptyset_R = \frac{H_R - H_{SE}^*}{\Delta H_{SL}^*}, \quad \emptyset_U = \frac{H_U - H_{SE}^*}{\Delta H_{SL}^*} \quad (51)$$

$$\text{We have } \emptyset = (1-\eta)\emptyset_U + \eta\emptyset_R. \quad (52)$$

SOLID ZONE:

$$\emptyset = (1-\eta) \left[\frac{C_{PR}(T-T_O) - H_{SE}^*}{\Delta H_{SL}^*} \right] + \eta \left[\frac{C_{PU}(T-T_O) - H_{SE}^*}{\Delta H_{SL}^*} \right] \quad (53)$$

$$\theta = \frac{C_{PR}(T-T_E)}{\Delta H_{SL}^*} \quad (54)$$

$$\therefore \theta = R_1\emptyset + R_2 \quad (55)$$

where

$$R_1 = \frac{C_{PR}}{(1-\eta)C_{PU} + \eta C_{PR}}, \quad R_2 = \frac{(C_{PR}-C_{PU})(T_E-T_O)(1-\eta)C_{PR}}{\Delta H_{SL}^*((1-\eta)C_{PU} + \eta C_{PR})} \quad (56)$$

LIQUID PHASE

$$\emptyset = (1-\eta)\emptyset_U + \eta\emptyset_R \quad (57)$$

where

$$\emptyset_R = \frac{C_{PRL}(T-T_O) - C_{PR}(T_E-T_O) + \Delta H_{SL}^*}{\Delta H_{SL}^*} \quad (58)$$

$$\emptyset_U = \frac{C_{PU}(T-T_0) - C_{PR}(T_E-T_0)}{\Delta H_{SL}^*} \quad (59)$$

$$\theta = \frac{C_{PR}(T-T_E)}{\Delta H_{SL}^*} \quad (60)$$

The relationship between \emptyset and θ can be written as

$$\theta = \emptyset S_1 + S_2 \quad (61)$$

where

$$S_1 = \frac{C_{PR}}{\eta C_{PU} + (1-\eta)C_{PRL}} \quad (62)$$

$$S_2 = \frac{C_{PR}(T_E-T_0)(C_{PR}-\eta C_{PRL}-(1-\eta)C_{PU})}{\Delta H_{SL}^*(\eta C_{PU} + (1-\eta)C_{PRL})} \quad (63)$$

AT MELTING POINT

$$\theta = \frac{C_{PR}(T_M-T_E)}{\Delta H_{SL}^*} \quad (64)$$

$$\frac{C_{PR}(T_M-T_E)}{\Delta H_{SL}^*} < \emptyset < \frac{C_{PRL}(T_M-T_E)}{\Delta H_{SL}^*} + \frac{(T_E-T_0)(C_{PRL}-C_{PR})}{\Delta H_{SL}^*} + 1 \quad (65)$$

3.3.2 Solution Procedure

On integrating the energy equation over a volume element ($dV = dZ$), the finite difference equation is obtained for the control volume P. Notation is kept as close as possible to variables defined in the previous publications.(44,45) Assuming that $V_f=0$ i. e there are no diluents we may write

$$[AP^0\emptyset_p^n + \theta_p^n AP - RHS] = v(1-\eta) \text{EXP} \left[\frac{-N}{1+\beta\theta_p^n} \right] \quad (66)$$

where $RHS = d_N\theta_N^n + d_S\theta_S^n + AP^0\emptyset_p^0 - \alpha\theta_f$

$$d_S = \frac{K_S\gamma}{(Z_n-Z_S)(Z_p-Z_S)} \quad d_N = \frac{K_N\gamma}{(Z_n-Z_S)(Z_N-Z_p)} \quad (67)$$

$$AP = d_S + d_N - \alpha$$

$$AP^0 = \frac{1}{dt}$$

The finite difference equations are solved by the Gauss-Seidal iterative method. Once t solution at the old time level(o) is obtained, the initial solution of the new time level(n) is set equal to that of the old one, and the transient iteration is started.

CASE 1

When $\eta=1$ i.e., fully reacted

SOLID PHASE:

$$\phi_p^n < 0, \quad \theta_p^n = \phi_p^n \quad (68)$$

$$\phi_p^n = \frac{\text{RHS}}{(AP^0 + AP)} \quad (69)$$

EUTECTIC REGION:

$$\theta_p^n = 0 \quad (70)$$

$$\phi_p^n = \frac{\text{RHS}}{AP^0} \quad (71)$$

MUSHY PHASE:

$$\phi_p^n = R_1 \theta_p^n + R_2 \quad (72)$$

$$\theta_p^n = (\phi_p^n - f_L) \frac{C_{PR}}{C_{PRL}} \quad (73)$$

$$AP^0 \phi_p^n + AP \theta_p^n - RHS = 0 \quad (74)$$

The above equations can be combined to form:

$$\phi = \frac{RHS \cdot R_2 + AP \cdot R_1}{(AP + AP^0 R_2)} \quad (75)$$

LIQUID PHASE:

$$\phi_p^n > 1 + \frac{C_{PRL}(T_L - T_E)}{\Delta H_{SL}^*} \quad (76)$$

$$\phi_p^n = \frac{\left(RHS + AP \cdot \frac{C_{PR}}{C_{PRL}} \right)}{\left(AP^0 + AP \cdot \frac{C_{PR}}{C_{PRL}} \right)} \quad (77)$$

$$\theta_p^n = \frac{C_{PR}}{C_{PRL}} (\phi_p^n - 1) \quad (78)$$

CASE 2

When $\eta=0$ i.e., unreacted

We have

$$\theta_p^n = \phi_p^n \cdot R_1 + R_2 \quad (79)$$

$$AP^0 \phi_p^n + AP\theta - RHS - v \exp\left(\frac{-N}{1 + \beta\theta_p^n}\right) = 0 \quad (80)$$

Combining the above two equations, we get

$$(A_1 \cdot \phi_p^n + A_3) + A_6 \cdot \exp\left(\frac{-A_7}{A_4 + A_5 \cdot \phi_p^n}\right) = 0 \quad (81)$$

$$\text{where } A_1 = AP^0 + R_1 \cdot AP, \quad A_3 = AP \cdot R_2 - RHS, \quad A_6 = \sqrt{1-\eta} \quad (82)$$

$$A_4 = N + \beta R_2, \quad A_5 = \beta R_1 \quad A_7 = N \quad (83)$$

CASE 3

When $0 < \eta < 1$ i.e., partial combustion

SOLID ZONE:

$$\theta_p^n = \emptyset_p^n \cdot R_1 + R_2 \quad (84)$$

$$[AP^O \emptyset_p^n + \theta_p^n AP - RHS] = v(1-\eta) \exp \left[\frac{-N}{1 + \beta \theta_p^n} \right] \quad (85)$$

Combining these two, we get

$$(A_1 \cdot \emptyset_p^n + A_3) + A_6 \cdot \exp \left(\frac{-A_7}{A_4 + A_5 \cdot \emptyset_p^n} \right) = 0 \quad (86)$$

where $A_1 = AP^O + R_1 \cdot AP$, $A_3 = AP \cdot R_2 - RHS$, $A_6 = v(1-\eta)$ $\quad (87)$

$$A_4 = N + \beta R_2, \quad A_5 = \beta R_1 \quad A_7 = -N \quad (88)$$

LIQUID ZONE:

We have $\theta_p^n = \emptyset_p^n \cdot S_1 + S_2$ $\quad (89)$

$$[AP^O \emptyset_p^n + \theta_p^n AP - RHS] = v(1-\eta) \exp \left[\frac{-N}{1 + \beta \theta_p^n} \right] \quad (90)$$

Combining these two equations, we get

$$A_1 \cdot \emptyset_p^n + A_3 + A_6 \exp \left(\frac{A_7}{A_4 + A_5 \cdot \emptyset_p^n} \right) = 0 \quad (91)$$

where $A_1 = AP^O + R_1 \cdot AP$, $A_3 = AP \cdot R_2 - RHS$, $A_6 = v(1-\eta)$ $\quad (92)$

$$A_4 = (1 + \beta \cdot S_2), \quad A_5 = \beta S_1 \quad A_7 = -N \quad (93)$$

3.3.3 Initial Condition

Initial condition for ignition at the first point of the sample could be both by starting the solution with a predetermined initial temperature as well as by the incorporation of a surface heat flux as shown in figure 15. The heat flux was incorporated in the following fashion. When the boundary condition is given in terms of heat flux, the additional equation for the calculation for temperature at the boundary is obtained by integrating the differential equation over the 'half' control volume adjacent to the boundary. The pertinent equation after the integration is given by

$$[AP^0\theta_P^n + \theta_P^n AP - RHS] = \sqrt{1-\eta} \exp\left[\frac{-N}{1 + \beta\theta_P^n}\right] \quad (94)$$

Where if P=First node, then

$$AP = \frac{2K\gamma}{dZ^2} \quad (95)$$

$$RHS = AP^0\theta_1^0 + \left(\frac{2C_1}{dZ} + \frac{2K\theta_2^n}{dZ^2} \right) \quad (96)$$

$$C_1 = \frac{QI * HS * C_{PR}}{\Delta H_{SL}^* * K_S} \quad (97)$$

if P=Last node, then

$$AP = \frac{2\gamma}{dZ} \left[\frac{K}{dZ} + Bi \right] \quad (98)$$

$$RHS = AP^0\theta_P^0 + \frac{2\gamma}{dZ} \left[Bi * \theta_f^n + \frac{K}{dZ} \theta_{P-1}^n \right] \quad (99)$$

3.3.4 Numerical Procedure

The Gauss Sidel iteration is used for solving the equations. First, the initialization of temperatures and enthalpies at all nodes is done using the proper initial and boundary conditions. The number of nodes taken for the calculation is 1201 per mm length of the sample i.e., length of each division is 0.85 microns for all the solutions. The time step used in problems ranged from 10E-4 to 10E-5 seconds depending on the K_o value of the problem. At a given time, the reacted fraction of the current iteration is found using the values of the reacted fraction and temperature of the earlier iteration. Based on the value of the reacted fraction and the enthalpies, the calculations are performed at the appropriate zones. In each zone, the exponential source

term is calculated using the enthalpies of the earlier iteration. The convergence criteria used to ascertain whether the solution at each time level is converged or not is obtained when the relative error, i.e,

$$\left| \frac{\phi^{m+1} - \phi^m}{\phi^m} \right| \text{ for all nodes} \leq \epsilon$$

The value of ϵ used for checking convergence is 0.001.

Table 1. Thermophysical values used in the calculations

PARAMETERS	VALUES
ΔH_{SL}^*	1.395E+06 J/kg
ρ	4900 kg/m ³
C_{PU}	858.42 J/kg/K
C_{PR}	909.3 J/kg/K
C_{PRL}	1116.7 J/kg/K
T_f	300 K
T_L	3373 K
T_M	3423 K
T_E	1918 K
H_S	0.001 m

3.3.5 Results and Discussion

The solutions given below correspond to the combustion and solidification of a material which follows the Ti-C phase diagram. Thermophysical constants are chosen to be representative of this system. Solutions are provided for the variation of velocity and combustion temperatures by varying thermophysical constants while holding other constants at values which are found in the Ti-C system. It is assumed that the reaction product is Ti-C of stoichiometric composition of 42 atomic % Ti. The liquidus for this composition is 3373K, the eutectic forms at 1918K ($\theta = 0$) and the volume of eutectic calculated from the Scheil equation is 8.099%. For the calculations presented in this report, the thermal conductivities and densities of all phases are assumed to be equal and independent of temperature. The main reason to do this is to achieve confidence in the solutions prior to the next step of making the program more versatile. This is achieved by comparing the solution obtained in this work to the thin zone combustion solution⁽²⁴⁾

$$U^2 = 1.1 \left(\frac{K^* K_0}{\rho^* Q} \right) \frac{RT_C^2}{E} \exp \left(\frac{-E}{RT_C} \right) \quad (100)$$

It is also an objective of this report to test the validity of the widely used equation (100).

Although the problem has been developed in dimensionless form, the results will be presented with both dimensional and dimensionless conditions to illustrate key effects. Figure 18(a) and (b) illustrate the different time scales of the problem when considering combustion and solidification from one end. Figure 18a is a plot of the temperature profile during combustion for the material conditions given in the figure. The combustion interface is sharp and propagation in the sample occurs within 4.5×10^5 dimensionless time (corresponds to 45 milliseconds). When compared to this speed, the heat removal from the cooled end of the specimen (figure 15) is relatively slow even with high Bi numbers imposed on the surface. This is seen in figure 18b where, after combustion, the end begins to cool (Bi = 10.0). In a dimensionless time of 8×10^5 , only 10% of the specimen has experienced the surface cooling effect.

Figure 19 illustrates the thermal and reaction profiles obtained during combustion. l_r and l_p refer to the zone in which the reaction takes place and the zone in which there is heating prior to the reaction, respectively. Also shown is the eutectic temperature above which some liquid forms and below which there is complete solid. The l_r and l_p zones can be considerably

narrower as shown in figure 20, where K_o is now increased by two orders of magnitude.

The combustion velocity and combustion temperature T_c are dependent on K_o , E, Q and the thermal conductivity. The variations of V and T_c with K_o are shown in figure 21. The velocity is seen to increase with K_o ; however, the combustion temperature T_c is seen to reach a steady value with an increased in K_o . Similarly, l_r and l_p decrease with K_o as shown in figure 22.

The activation energy E has a dramatic effect on the velocity as shown in figure 23. We note that an increase in E beyond 2×10^5 J/mole leads to extinction, and a lower value of E below 2×10^5 J/mole leads to an exponential increase in velocity. The combustion temperature T_c , on the other hand, is relatively insensitive to a lowering of E and remains at $\theta = 0.49$ for $E = 1.0 - 2 \times 10^5$ J/mole. Very low values of E lead to conditions for spontaneous ignition in the sample. In the regions of self propagation, it was immaterial to the solution whether the initial condition was heat flux or set initial temperature. The data in figure 23 fit a curve of $V = 965 * \exp(-3.3 \times 10^5 E)$. The effect of the enthalpy of combustion Q, is to increase both T_c and V as shown in figure 24. Below a minimum value, self sustained front propagation is not possible. This is seen for example at $Q=2.08 \times 10^6$ in figure 24.

Values of velocity and combustion temperature for TiC have been reported in reference 34. We have found that these values are difficult to match at high K_o values. If K_o is high the the velocity as shown in figure 21 becomes very high. This velocity may be lowered by choosing a high E value. However a high value for E leads to a condition where extinction may take place. Clearly the use of equation (36) and the fact that the contact conditions are taken to be ideal in this report seems to be inadequate for accurate prediction and matching with reported experimental values. If an area of contact expression had been properly incorporated then A_c , [see equation (31)] would be less than one. In effect this is similar to reducing K_o . The K_o calculated from transition state theory is of the order of 10^{13} s^{-1} .⁽⁴⁸⁾ The values chosen for the calculations in this report are from $10^8-10^{10} \text{ s}^{-1}$. Such low value of K_o have previously been used for matching experiments and calculations for the devolatilization of pulverized coal.⁽⁴⁹⁾ In the reference 49 additionally the choice of low K_o values for first order reactions has been discussed vis-a-vis the real complexity of the reaction.

Figures 25 and 26 show the variations of V and T_c with thermal conductivity. The thermal conductivities may be changed by ie initial compaction pressure and the final porosity of the product. In addition the thermal conductivity may be influenced by any form of pressure application during combustion. At low K_o (figure 25), the velocity is first seen to increase with

K^* . Beyond 44 J/msk, extinction takes place. Also shown in the plot is the variation of T_c which initially falls only marginally up to a thermal conductivity value of 25./msk and then falls rapidly before becoming constant at 2360 K prior to extinction with a further increase in the thermal conductivity. Figure 27 shows the l_r and l_p values. We note that the variation in l_p is similar (although opposite in sense) to T_c . Also plotted in figure 25 is a plot of equation (100) with the T_c values obtained from the numerical program. We note that the equation is predictive even though l_r may be relatively large as compared to the value obtained from figure 20. Figure 26 shows the variation of velocity and combustion temperature with the thermal conductivity at a high K_0 value. The increase in velocity is now proportional to $K^{1/2}$ as predicted by equation (100). The combustion temperature is relatively constant (falls only from 2665K to 2605K). The equation (100) is seen to be again predictive. Several experimental measurements⁽³⁰⁻⁴⁰⁾ have been used to calculate activation energy from a measurement of velocity and combustion temperature and equation (100). We note that numerical solutions obtained by us even at large l_R values match reasonably with the analytical value, thus giving credibility to the reported values of activation energy. However the sensitivity of the solutions to E is noted from figure 23 and we note that the solutions from equation (100) may be 20% in error. It is therefore imperative to obtain activation energy values only by matching with detailed numerical calculations using the formulation which includes the phase change effects and different values of the thermophysical constants for different zones in both reacted and unreacted portions of the sample. In the next phase of work we expect to make the model versatile to input individual thermophysical values of reactants and diluents. There is no close analytical expression in such cases. Figure 28 shows the l_r and l_p values corresponding to the solution in figure 26. It is to be noted that these values are an order of magnitude lower than those shown in figure 27 (i.e., at the lower K_0).

The effect of the initial temperature of the compacts prior to ignition has an effect on the combustion velocity and temperature. Both increase with an increase in the initial temperature as shown in figure 29. Note however that increase in temperature is not additive towards determining the final combustion temperature i.e a 200K increase in initial temperature does not lead to a corresponding increase in the combustion temperature. This occurs because of two factors (a) the specific heat of the product is higher than that of the reactants and (b) the effect of thermal conductivity on the solution is enhanced because of the steeper temperature gradients.

The versatility in the current formulation lies in the fact that cooling which results in solidification is tackled along with the combustion problem. Figure 30 shows the cooling of a sample heated by a self propagating combustion front. Cooling is affected by both heat transfer from the sides as well as the end as shown in figure 15. The thermal history of a point at

$Z=0.8$ is shown in figure 31 (a plot of dimensionless temperature and time). Note the flat region after the rapid heat up and the subsequent rapid drop in temperature. The applied heat transfer coefficient along the sides was 10^3 W/m²sK. This is a value that incorporates both the radiative as well as convective cooling.⁽²⁷⁾ The Biot number at the end was taken to be 10 (this gives a end heat transfer coefficient of 10^6 W/m²sK). Clearly the cooling from the sides has had little or no impact on the solution, cooling is predominantly from the end only.

3.3.6 Conclusion

A numerical formulation for self propagating combustion synthesis of a system that forms a non-stoichiometric alloy has been developed. The formulation incorporates both the kinetics of combustion as well as the kinetics of the solidification process during and subsequent to the combustion process.

The variation of the combustion velocity and combustion temperature with the heat of reaction (Q), the activation energy (E), the frequency factor (K_0), thermal conductivity (K^*) and initial temperature (T_0) has been studied. Results when compared to a commonly employed analytical formulation, equation (100), show that the approximate analytical solution although in reasonable agreement with the numerical solution may be in error by more than 20%. The effect of the thermal conductivity on the velocity may be to increase or decrease the velocity depending on the value of K_0 . At low K_0 values, an increase in the thermal conductivity may lead to a decrease in the combustion velocity. The effect of the initial temperature on the combustion velocity and temperature is to increase both, however the increase in the combustion temperature may not be proportional to the increase in the initial temperature. E has a pronounced effect on reducing the combustion velocity while not influencing the combustion temperature. Extinction conditions are approached with decreasing Q and increasing E .

THIS IS A BLANK PAGE

4.0 TRANSPARENT D/S EXPERIMENTS IN THE PRESENCE OF INERT PARTICLES

Microstructural development during the directional solidification of materials are generally studied under controlled processing conditions for samples whose cross-section is uniform and the dimensions of the sample are several orders of magnitude larger than the length scales of the microstructure. In many important solidification processing techniques of commercial importance such ideal situations are not always present. For example, in directionally solidified castings, the changes in the cross-section of the object will significantly alter the microstructure.^(14,50) In the solidification processing of composite materials in presence of fibers, the liquid freezes in a narrow channel, and the solidification microstructures in such constrained regions have been found to be significantly different than those predicted on the basis of large sample width.^(14,42,51-53) In this report we shall consider another technologically important problem which deals with the processing of composites in the presence of inert particles in the liquid. These particles can significantly influence the morphologies that develop during the solidification process,⁽⁴¹⁾ and these morphological changes will alter the microsegregation profiles. Thus, it is possible to design critical size and distribution of particles, and characterize processing conditions of growth rate, composition and temperature gradient to obtain an optimum microstructure which can produce a composite material with superior properties. In this report, our aim is to examine the fundamental phenomena which critically control the microstructural evolution during the directional solidification of alloys when the liquid, prior to freezing, has inert particles dispersed in it.

Short range interactions between the particle and the interface have been emphasized in previous studies,⁽⁵⁴⁻⁵⁹⁾ and these interactions would be important for the solidification of pure materials. These earlier studies have shown that there exists a critical velocity which determines whether a foreign particle in front of a solid liquid interface will be entrapped or pushed. The trapping or engulfing of particles by the interface has been thought to depend on the balance of forces between the repulsion at the interface and difficulty in pushing the particle (including displacing the liquid in front of the particle) through the medium in front of the interface. Furthermore, experimental studies have been carried out in transparent materials like salol⁽⁵⁴⁾ which have high entropy of fusion so that they grow with a faceted interface even when small impurities are present. The kinetic effects present in these systems tend to stabilize the planar interface with respect to local perturbations in the shape of the interface. Most metals, on the other hand, have nearly isotropic interface properties which allow the solid/liquid interface to readily deform its shape to conform to the shape dictated by the local solute gradient at the interface.

The main aim of this report is to examine the following two important aspects of solidification microstructural development in presence of particles. (1) Most important materials for particulate composites are alloys in which solute diffusion plays a dominant role in establishing the morphology of the interface. These solute fields are long range in nature so that the solute field interaction would be significantly more important than the short range interaction forces that are considered in the earlier models. (2) The alloys used for composite materials are generally concentrated alloys so that under most practical growth conditions the microstructure will be either cellular, dendritic or eutectic. The interactions between particles and the nonplanar interface will be significantly different than those for the planar interface. In order to examine how the particles alter the morphology of the interface, and the mechanism by which particles are trapped or pushed at the interface, experiments have carried out in a transparent system where the interface configurations can be examined *in situ*, and the particle interactions with cellular and dendritic interfaces can be observed precisely. The microstructural changes observed in these experiments will be presented in this report and the results will be analyzed through the discussion of appropriate theoretical models.

4.1 EXPERIMENTAL TECHNIQUE

In order to observe the particle - interface interactions *in situ*, directional solidification experiments have been carried out in a model transparent system with succinonitrile (SCN) as the major component. Succinonitrile has a low entropy of fusion which allows one to use it as a model analog for metallic systems. The directional solidification cell was prepared by first taking two glass plates, separated by a distance of about $150\mu\text{m}$, which were fused on all sides by using a low melting point glass. Prior to the fusing of the glass cell, a calibrated thermocouple was introduced in the cell to quantitatively measure the temperature profile during the directional solidification run. Two large openings were cut on two sides of cell, and the mixture of succinonitrile and particle was introduced through one of the openings in a controlled environmental chamber in presence of dry inert gas so as to avoid the contamination of the sample. After the liquid was rapidly frozen in the cell, the openings were sealed with an epoxy.

Three types of particles were used with liquid succinonitrile to examine the effect of particles with different thermal conductivities on the particle - interface interactions. They were: 1) nickel powder (-600 mesh), 2) polishing grade alumina powder ($0.03\text{-}0.5\mu\text{m}$), and 3) coarse cobalt powder ($\sim 100\mu\text{m}$). In addition to the particles, the interaction of gas bubbles with the interface was also examined. The distribution of particles obtained inside the the cell was similar to that mixed into the bath except when the volume fraction exceeded about 30%. Above this volume fraction the particles were found to coagulate

and form a cellular network in the liquid inside the sample cell. Some experiments were also carried out by introducing fine bubbles of inert gas in the liquid to characterize the differences in interactions for bubbles and inert particles.

Directional solidification studies were carried out using a temperature gradient stage as described earlier by Hunt et al.⁽⁶⁰⁾ and by Mason and Eshelman.⁽⁶¹⁾ For the directional solidification experiments described in this report, as received succinonitrile of 99.5% purity was used and the temperature gradient was kept constant at 5.5K/mm. The critical interface breakup velocity for this composition and temperature gradient was experimentally determined to be 1.8 $\mu\text{m}/\text{s}$. Thus, experimental studies were carried out over the external velocity range of 0.5 - 20 $\mu\text{m}/\text{s}$ so as to obtain an initially planar, cellular or dendritic interface. The interactions between these interfaces and the particles were then observed *in situ* under a microscope and photographed at one second interval.

4.2 RESULTS

Experimental results on the interaction between a planar interface and particles will be described first. Next, the mechanisms by which particles are trapped by a cellular and dendritic interface will be examined. Finally, the experimental results on the morphological transitions caused by the presence of particles will be presented.

4.2.1 Interactions with a Planar Interface

The interactions of a planar interface in presence of particles or bubbles were examined. Figure 32(a-d) illustrates the change interface shape as it approaches gas bubbles. As the interface approaches a large bubble, it deforms and forms a depression. This interaction begins when the particle is significantly away from the interface. The interface segment below the bubble is initially slowed down and the rest of the interface continues to move at the imposed rate. The depressed segment of the interface thus is undercooled more so that it subsequently advances rapidly and engulfs the particle. This acceleration of the interface leaves behind a region of higher solute, as shown in figure 33a. When the bubble size is small, the deformation of the interface is quite small so that the interface appears to go around the bubble without significant change in solute field over the rest of the interface.

The presence of large bubbles or particles can also cause a planar interface to become nonplanar, as seen in figures 33a and 33b. This morphological transition occurs since the interface region close to, but not just below the particle, accelerates due to the possibility of some sidewise solute distribution as the interface becomes curved. This increase in velocity can cause the planar

interface to become unstable and form cellular structure. In addition, the acceleration of the interface gives rise to distinct banded regions in the solidified material, figure 33c.

4.2.2 Particle Trapping Mechanisms

The interactions between the particles and the nonplanar interface are shown in figures 34-36. In all cases the particles were observed to be trapped readily into the solid when the interface was nonplanar. On a microscopic scale, the trapping mechanism is dictated by the solute field interaction with the particle and it is analogous to that for the particle trapping by a planar interface, as described above.

When a dendritic interface interacts with particles, different trapping mechanisms are found to be operative. The most important variable which determines the trapping mechanism is the relative size of the particle compared to the scales of dendrite tip radius and primary spacing. The volume fraction of the particles also plays an important role in choosing the trapping mechanism. The growth of dendrites in a low nickel powder particle concentration in succinonitrile is illustrated in figure 35. The dendritic interfaces in all the photographs are growing at $10 \mu\text{m/s}$ ($G=5.5\text{K/mm}$), i.e. at $(V/V_c) = 5.56$. The particles have been observed to incorporate into the dendrites by the following mechanisms:

- 1) The particles incorporate into the solid through the local deformation of the interface which is analogous to the particle trapping for the planar and cellular fronts, figure 34.
- 2) The particle trapping occurs between the secondary dendrites close to the dendrite tip, figure 35. When trapping occurs by secondary dendrites (i.e. in the secondary dendrite interstices) the particles are trapped very close to the first few side branches; very rarely does a particle travel to the root of the primary dendrite before it is trapped. Note that when these secondary branches grow further, the trapped particle appears close to the dendrite axis.
- 3) The particle causes the dendrite tip region to become unstable and give rise to a tip - splitting phenomenon. The mechanism of tip splitting of the primary dendrite by a correctly placed particle is illustrated in figure 35. Such tip-splitting also occurs when the particle is attached to a gas bubble and it interacts with the dendrite tip, as shown in figure 36a. Note that the particles, which enter the solid while attached to a gas bubble, remain attached to the bubble even though the bubble eventually deforms and aligns with the interdendritic space of the primary dendrite, as shown in figure 36b.

4.2.3 Morphological Transitions

At higher volume fraction of the particles, a morphological transition of the dendrite to a quasi-steady state cellular configuration occurs. Such a transition is illustrated in figure 37 which shows the interface structure at an imposed velocity of $10\mu\text{m/s}$. At this velocity, when the fraction of particles is small, a dendritic structure has been found to be present (see figures 35 and 36). When the volume fraction of particles is increased, a cellular structure appears as shown in figure 37. When the velocity is increased further to $40\mu\text{m/s}$, a dendritic pattern is found to form. In addition to the large volume fraction of particles, the dendrite to cell transition was also observed when particles of large radii were present in the liquid.

4.3 DISCUSSION

The solidification microstructure that develops when an alloy is directionally solidified in presence of inert particles depends not only on the processing parameters such as the growth rate and the temperature gradient, but it is also significantly influenced by the size and the density of particles.⁽⁴¹⁾ The influence of particles on the solidification microstructure will now be discussed in three parts to examine : (a) the long range interaction between the particle and the interface, (b) the changes in morphologies due to the presence of particles, and (c) the effect of particles on the stability of the interface

4.3.1 Interactions Between the Particle and the Interface

Several forms of particle - interface interactions have been considered in the literature. A theoretical model of particle-interface interaction was first developed by Uhlmann et al.,⁽⁵⁴⁾ in which they developed a differential equation which describes the diffusional process in a region between the particle and a planar interface. The deformation of the interface due to the solute field interaction with the particle was not considered in their model. Bolling and Cisse⁽⁵⁵⁾ considered the deformation of the interface. However they assumed that the shape of the interface was invariant with time in the regime where particle interactions with the interface were significant. Other forces which become effective as the particle comes close to the interface have also been considered in several models.⁽⁵⁶⁻⁵⁸⁾ However, these forces are only short range forces which become effective only when the interface is within few atomic distances from the particle. In binary alloys, the interaction between the interface and the particle begins when the particles are comparatively at larger distances away from the interface. This long range interaction becomes dominant since the presence of particles perturb the diffusion field in the liquid ahead of the interface. This perturbed diffusion field alters the concentration gradients at different segments of the interface

so that the shape of the interface changes with time. The distance at which the interaction begins is of the order of the diffusion distance, which is characterized by D/V . For succinonitrile, the diffusion coefficient is $1.27 \times 10^{-5} \text{ cm}^2/\text{s}$, so that the diffusion distance will vary from 12.7 mm at $V=0.1 \mu\text{m}/\text{s}$ to 0.127 mm at $V=10 \mu\text{m}/\text{s}$. The thermal fields on the other hand are seen not to be affected in these experiments by the particles. The glass cover conducts the heat rapidly and in the absence of high connectivity between the particles the amount of heat conducted by the system per unit area and time is relatively unaffected i.e the thermal gradient is set by the experimental system. These interaction distances are so large compared to the small range forces that become important when the interface is close to the particle that the solute effect will be dominant during the solidification of alloys in presence of particles.

The solute field interaction between the particle and the interface can be visualized by considering a particle that is present ahead of the interface. When the interface approaches the particle within the distance D/V , the particle act as a barrier to the diffusion field which leads to solute rejection between the particle and the interface. This additional solute pile up will cause the concentration gradient at the interface to decrease and thereby slow down the growth of the interface segment that is just below the particle, as shown in figure 38a. Note that as this interface segment is slowed down the rest of the interface which does not see the particle barrier will continue to move at the imposed rate so that a depression of the interface is formed just below the particle. The interaction between the particle and the planar interface is somewhat analogous to the interaction between a dislocation and a particle, the interaction of the stress field for the dislocation being replaced by the solute field interaction for the solidification process. As the interface grows between the particles, it acquires a curvature (figure 38b), which will allow lateral diffusion of solute so that the interface tends to accelerate. However, under the conditions of a planar interface growth, the leading part of the interface is soon decelerated due to the presence of significant temperature gradient that is present in the liquid. This allows the rest of the interface to catch-up with the leading segment of the interface. In this process of acceleration, a solute rich region is left behind which surrounds the particle, figure 38c. In the present experiment the initial impurity content was quite small and the single phase region quite large so that only solute bands around the particle were observed. In concentrated alloys, it is possible that a eutectic or a second phase may form at the particle interface because of the extensive solute pile up. For planar interface growth, the velocities are small so that the interaction distance will be large. On the other hand, dendritic interfaces have smaller interaction distances since the solute is rejected laterally into the interdendritic region. Thus the deformation of the interface will be smaller for a dendritic interface compared to that for a planar interface.

The deformation of the interface in presence of particles depends upon the solute build up between the particles and the interface. The initial long range interactions are governed by the diffusion distance which is characterized by the processing conditions. However, as the interface approaches the particles, the solute field interaction will be governed by the size of the particles (radius r_p) and the volume fraction of particles, f_p . When the size or the density of particles is large, the barrier to solute field becomes large so that the concentration gradient at the interface is altered significantly. These changes in concentration gradients at the interface will significantly influence not only the stability of the interface but it will also alter the scales of microstructures that develop in presence of particles. In order to examine the effect of f_p we now consider two extreme cases. First consider r_p or f_p to be very large so that the particles essentially form a complete barrier to the diffusion field. In this case the interface, as it approaches the barrier, slows down. Since the external velocity is constant, the interface continues to become highly undercooled, so that at some point the driving force becomes sufficiently large for the interface to penetrate small regions of liquid between the particles. Alternately, the liquid on the other side of the particles become highly undercooled so that new crystals will nucleate there. When the particles are fine and the density of particles is low, the change in the solute gradient at the interface due to the presence of particles is small so that the solute field interaction between the particle and the entire interface is negligible. In this case short range interactions may become important.

4.3.2 Morphological Transitions

When inert particles are present in the liquid, the changes in solute gradient at the interface will influence the conditions for morphological transitions. The conditions for planar to cellular and cellular to dendritic transitions will be altered in presence of particles.

4.3.2.1 Planar Interface Stability

The planar interface instability condition, in absence of particles, is given by Mullins and Sekerka⁽²⁾ as

$$mG_C\xi_C - G = \Gamma/\sigma^* \lambda^2 \quad (101)$$

where Γ is the capillarity constant which is the ratio of solid-liquid interfacial energy to the melting entropy per unit volume, m is the slope of the liquidus, G_C is the solute gradient in the liquid at the dendrite tip, G is the conductivity-weighted average temperature gradient at the interface, and σ^* is a constant equal to 0.025. The function ξ_C accounts for the effect of velocity on the concentration gradient term that governs the stability of the interface.⁽⁴⁾ The

function ξ_c is unity for small velocities, whereas it approaches zero when the velocity becomes very large. For all experimental conditions used in this work, the velocities are sufficiently small so that $\xi_c=1$.

The general stability condition of the interface depends upon three factors: (1) the concentration gradient at the interface, (2) the conductivity weighted average temperature gradient at the interface, and (3) the surface energy effect. The surface energy contribution comes from the increase in area of the perturbed interface and it tends to stabilize the interface. For a general sinusoidal perturbation of the interface, this term is not influenced by the presence of particles. The temperature gradient term is also not influenced significantly by the presence of particles since in the directional solidification the temperature field is controlled by the external hot and cold sources, and the latent heat contribution is negligible for small growth rates that are used in the present studies. Furthermore, the thermal conductivities in the solid and in the liquid are equal for succinonitrile, so that the conductivity weighted average temperature gradient is the same as the temperature gradient in the liquid. Experimental measurements of temperature profiles in presence of particles also confirmed that the temperature gradient in the liquid remained unchanged as the velocity or the particle density was altered. The major effect of particles on the stability of the interface thus comes from the influence of particles in altering the concentration gradient at the interface.

If we define ξ_p as the function that characterizes the influence of particles on the solute gradient at the interface, then the planar interface stability criterion can be written as:

$$mG_c\xi_p - G = \Gamma/\sigma^*\lambda^2 \quad (102)$$

In the above equation G_c is the concentration gradient in the liquid at the unperturbed interface for the steady state growth in absence of particles. ξ_p is a function that characterizes the effect of particles on the concentration gradient at the interface. Thus $G_c\xi_p$ is the actual solute concentration gradient that is present at the interface in presence of particles in the liquid. The function ξ_p will be unity when no particles are present in the liquid, and it will approach zero when the particle density or the radius of particles becomes very large. In general the value of ξ_p will be a function of f_p and r_p , and it will vary from one to zero as the volume fraction or the radius of particles increases.

The surface energy effect is generally negligible for the planar interface stability condition at low velocities, so that the surface energy term in equation (102) can be neglected. The value of the composition gradient in

presence of particles, $G_c \xi_p$, can now be obtained from the flux balance equation at the interface, which gives:

$$G_c = (V_I/D) \{C_0(1-k)/k\}/\xi_p, \quad (103)$$

where V_I is the actual velocity of the interface. Substituting the above value of the concentration gradient in equation (105), we obtain

$$V_{Ic} = \{GD/\Delta T_0\}/\xi_p \quad (104)$$

Since the function ξ_p varies from zero to one, the critical velocity, V_{Ic} , for the planar interface stability in presence of particles will be larger than that in absence of particles. Consequently, the processing conditions which give a cellular interface in absence of particles can become a planar interface when significant volume fraction of particles are present in the liquid. Also, when the interface accelerates between the particles, a planar interface can acquire sufficient velocity to become nonplanar.

4.3.2.2 Cell-Dendrite Transition

Experimental studies show that a dendritic to cellular transition can occur in presence of high density of particles. When particles are encountered ahead of the advancing interface, solute accumulation occurs between the particle and the interface which gives rise to a shallower solute gradient in front of the interface. As discussed earlier, this decrease in the solute gradient at the interface will slow down the growth of dendrites and thus increase the dendrite tip radius. The dendrite tip radius, under steady-state condition, is experimentally shown⁽⁹⁾ to be controlled by the marginal stability criterion first proposed by Langer and Müller-Krumbhaar.⁽⁶²⁾ One also obtains precisely the same result for succinonitrile when the solvability condition is used for the stability of dendrite tip.⁽⁶³⁾ The dendrite tip selection criterion has been extended by Kurz, Giovanola and Trivedi⁽⁵⁾ for the directional solidification of alloys. According to this criterion, the dendrite tip radius, R , is given by:

$$R = [\Gamma D / \sigma^*(m G_c \xi_c - G)]^{0.5} \quad (105)$$

The effect of particles is to alter the concentration gradient at the interface, and for small velocities one may modify the above equation to include the solute field interaction parameter, ξ_p , which gives for the dendrite tip radius the expression :

$$R = [\Gamma D / \sigma^*(m G_c \xi_p - G)]^{0.5}, \quad (106)$$

where G_C is the solute gradient in the liquid at the dendrite or cell tip in absence of particles. When the dendritic interface is far from the particle, the steady-state dendrite exhibits the radius value, given by equation (104) in which the term ξ_p is unity. When the interface approaches the particle within the diffusive interaction regime, the interaction will cause the solute gradient at the interface, given by $\xi_p G_C$ to decrease, so that the radius will tend to increase, as seen from equation (104). If the interaction is large, the radius will increase sharply. If the dendrite growth conditions are not too far from the cell-dendrite transition conditions, then this increase in radius will cause dendrites to become cells, as discussed by Kurz et al.⁽⁵⁾

When large number of particles are present, the interface which would be dendritic in absence of particles can become cellular. Also once a cellular interface is formed, and the interface traps the particles, the interface may not readily change to a dendritic interface because the time required to readjust the diffusion field can be large. Somboonsuk and Trivedi⁽⁶⁴⁾ and Seetharaman et al.⁽⁶⁵⁾ have carried out detailed experimental studies to examine the dynamics of cellular and dendritic growth by varying the velocities of the interface. They have shown that the cell to dendrite transition is quite sluggish and the cellular structure persists for some time after the velocity is increased. In the case where particles are present, the interface will also encounter additional particles before a dendritic pattern can be reestablished so that a quasi-steady state cellular pattern can replace a dendritic pattern. A schematic plot of tip radius vs. velocity is shown in figure 39. The tip radius increases with increasing volume of particles. The dotted and the solid lines show the cellular and the dendritic regimes, respectively. Note that the effect of particles is very analogous to the decrease in alloy composition, since lower alloy compositions decrease the concentration gradient at the interface which is qualitatively analogous to the decrease in the concentration gradient at the interface due to the interaction between the particles and the dendrite or cell tips.

Although the local interface velocity varies considerably to accommodate the trapping of particles, the average interface velocity remains equal to the imposed velocity if the imposed velocity is not very large. Figure 40 is a semi-quantitative plot of the average and local interface position variations during a given experiment. The fluctuations in the interface position, and thus in local velocity of the interface give rise to solute bands as the local velocity is altered due to the presence of particles. The positions where particles are trapped and where solute banding will occur on account of local interface accelerations are also shown schematically in figure 40.

4.3.3 Instability of the Dendrite Tip

Our experimental results have shown that a particle when it approaches the dendrite tip can cause the dendrite tip to split. This tip-splitting behavior can be understood if we examine the dendrite tip stability model. The dendrite tip stability theory predicts a unique stable tip radius value under given experimental conditions when no particles are present in the liquid. The stabilizing factor for the dendrite tip is the capillarity effect and a stable dendrite tip radius exists for which the destabilizing effect due to the solute gradient is balanced by the stabilizing effect due to capillarity. If the radius is slightly higher than that predicted by the stability condition, then the capillarity effect is reduced, which in turn may cause the dendrite tip to split. Note that the presence of a particle ahead of the dendrite tip also reduces the concentration gradient at the interface which tends to stabilize the interface. Thus, the presence of particles does not always cause dendrite tips to split. If the effect of particles on solute gradient is large compared to that on the capillarity effect, then the dendrite will tend to increase the radius and it may become cellular. This condition would indeed be satisfied for particles that are larger than the dendrite tip radius. However, if the particles are very fine, then the dendrite tip curvature is reduced significantly compared to the decrease in the solute gradient, and in this case, a tip-splitting would occur. Our experimental studies confirm these predictions since in presence of large particles or large particle densities, tip radius was found to increase. In contrast, when particles were very fine and few, i.e. of the order of dendrite tip radius or smaller, then the concentration gradient was influenced less than the change in the curvature of the tip and the dendrite tip was found to undergo the tip-splitting phenomenon.

4.3.4 The Effects of Particles on Dendrite Length and Solute Segregation Patterns

During the solidification of alloys, a two phase region, called the mushy zone, is generally present. The extent of this mushy zone determines solute segregation profiles and the possible formation of the second phase. The freezing process in the mushy zone is thus critical in the development of the final microstructure and the properties of the solidified material. The presence of particles in the liquid can significantly influence the extent of the mushy zone.

The length of the mushy zone is equal to $(T_{\text{tip}} - T_{\text{base}})/G$, where T_{tip} and T_{base} are temperatures at the tip and the base of a dendrite or cell, respectively, and G is the average temperature gradient in the two-phase region. For dendrites, T_{base} corresponds to the eutectic temperature if the system exhibits a eutectic, whereas for a cell T_{base} is below the solidus temperature if the diffusion in solid is not negligible. The major influence of

particles in the liquid on the mushy zone length comes from the change in the dendrite or cell tip temperature. The solute field interaction between the dendrite or cell and the particle causes the tip temperature to decrease, and this decrease in temperature becomes appreciable when dendrites undergo a transition to cells in presence of high density of particles. Thus, the extent of mushy zone, and the resultant microsegregation, is reduced when the alloy is solidified in presence of particles. The reduction in the mushy zone will be significant when high volume fraction of particles are present in the liquid. This change in mushy zone length will also impact the heat flow and the time for solidification.⁽⁴⁵⁾

4.3.5 Particle Distribution in the Solidified Material

The distribution of particles in the resulting solid may or may not follow the distribution in the liquid. The actual distribution of particles that one obtains in the solidified material will largely depend upon the morphology of the interface that is present under given experimental conditions. When particles are trapped by a plane front or cells, the distribution remains similar to that present in the liquid prior to solidification. On the other hand, when a dendritic structure is present during solidification, then the distribution of particles in the solid can be significantly different from that in the liquid. Although more work needs to be carried out for a conclusive analysis, our preliminary results seem to suggest that an alignment of particles can occur if the solidification mode remains dendritic and if most of the particles are trapped by the secondaries close to the dendrite tip. The trapping of particles between dendrites usually occurs just behind the tip, within the first ten secondary branches. This is because of the fact that secondary branches close to the dendrite tip have small amplitudes, whereas this amplitude increases sharply after the first few branches, as shown in figure 41. Note that the secondary branches from a given dendrite and from a neighboring dendrite essentially block the particles from going to the base of the dendrite. The particles which are trapped between the branches close to the tip will remain between these branches as the dendrite grows. The particles that have been trapped a few branches behind the tip may appear to be trapped at the base of the dendrite in metallic systems when one observes these particles after the alloy is quenched.

In the experimental study presented here, the solidification was carried out in thin samples to minimize convection effects so as to isolate the particle-interface interactions. In the actual production of metal-matrix composites, convection effects present in the interdendritic region can cause particle motion in the liquid, and this may significantly alter the distribution of particles in the solid.

4.4 CONCLUSIONS

In order to examine the interactions of particles with the solidifying interface, in situ observation of particle interactions with various interface morphologies have been carried out in a transparent organic system. It is shown that, in binary systems, the effect of particles on the solute field can be dominant. The presence of particles alter the solute gradient at the interface which can give rise to significant changes in the morphology of the interface. Several important effects of this solute field interactions on the morphological changes of the interface have been presented and discussed in this report.

The long range interaction between the particle and the interface occurs when an interface approaches the particles within the diffusive interaction regime. The solute gradient at the interface segment facing the particle is thus reduced which causes a perturbation in the shape of the interface. The trapping of the particle occurs as the interface segments away from the particle grow out and envelope the particle. The interface facing the particle is initially lagging from the rest of the interface. However, after the particle is trapped, it advances rapidly, thereby giving rise to a solute band in the vicinity of the particle.

The long range particle-interface interaction is shown to prevent the interface from moving uniformly at a constant rate. Consequently, steady-state conditions are not present at the interface. The interface, in fact, exhibits an oscillatory behavior. Consequently, most of the models which exist in the literature for steady-state interface growth, with short range interaction effects, need to be extended to the case where the velocity of the interface is not constant, but it oscillates in presence of particles.

The perturbation in the solute field due to the presence of particles has been shown to change the dendrite tip radius and the dendrite tip temperature. These effects give rise to dendrite to cellular transition as the density of particles is increased. Also the length of the dendrite is reduced in presence of particles. It is important to emphasize that a high density of particles can cause dendrite to cellular transition so that one can still solidify the material at higher velocities and obtain a cellular structure with smaller microsegregation profiles. When fine particles of lower densities are present, the particle approaching the dendrite tip is found to give rise to a tip-splitting phenomenon.

The interactions between the particle and the interface have been found to depend upon the volume fraction of the particles and the size of the particles. These interactions, as observed in the present experimental study, are summarized in figure 42.

Theoretical ideas on the stability of the planar interface and the dendrite tip radius have been discussed and appropriate modifications in these effects due to the presence of particles in the liquid have been discussed.

5.0 COMBUSTION SYNTHESIZED NIOBIUM ALUMINIDE - NIOBIUM BORIDE COMPOSITES

Niobium aluminide-based intermetallic matrix composites are potential high temperature aircraft engine materials. Of the several techniques available to synthesize such composites, combustion synthesis (CS) may offer an efficient and economical route for the manufacture of these composites. Microstructures of Nb-Al-B composites made from the CS technique are examined in this report. Exothermic reaction processing circumvents difficulties encountered in conventional methods of time and energy intensive sinter processing and is being extensively studied for the creation of ceramic and intermetallic compounds.^(30-37,40) In this report we examine the features of the final microstructure after combustion synthesis of Nb-Al-B composites and relate the same to the initial selection of constituents and to the kinetics of the combustion reaction.

5.1 EXPERIMENTAL TECHNIQUE

The reactants used in this research consisted of elemental powder Niobium, Aluminum, and amorphous Boron. Nb, Al and B powders were -325 mesh. The purity of Nb, Al, and B was 99.8%, 99.55% and 92% respectively. Reactant powders were weighed based on the weight pct of boron in the stoichiometric Nb_3Al mixture. The compositions of this study are listed in Table 2.

Table 2. The Compositions of Boron- Nb_3Al mixture and the phases after combustion. The question mark adjacent to a phase indicates that these phases were not always noted in all the samples of the same designation.

No	Boron, wt%	Nb, Al in the stoichiometry of Nb_3Al , wt%	phases noted after combustion
NA1B	1	99	*
NA2B	2	98	*
NA3B	3	97	$\text{Nb}, \text{NbB}, \text{Nb}_2\text{Al}, \text{NbAl}_3$
NA4B	4	96	$\text{Nb}, \text{NbB}, \text{Nb}_2\text{Al}, \text{NbAl}_3$
NA5B	5	95	$\text{Nb}, \text{NbB}, \text{Nb}_2\text{Al}, \text{NbAl}_3 ?$
NA6B	6	94	$\text{NbB}, \text{Nb}_2\text{Al}, \text{NbAl}_3 ?$
NA7B	7	93	$\text{NbB}, \text{Nb}_2\text{Al}, \text{NbAl}_3 ?$

* sample did not ignite

Powders were mixed by mixing in a glass jar for 8 hours. Pellets were made from this powder in a tensile-bar die by applying 15000 psi pressure for 1 minute. The theoretical and green densities were calculated and measured, respectively. Densities are shown in figure 43. Subsequently, the compacted pellets were placed in a controlled furnace set at a temperature 600°C. A flowing Ar gas cover was maintained over the samples. Samples were next ignited with a welding torch. Both temperature and velocity of the combustion wave were monitored with W26%Re-W5%Re thermocouples firmly embedded in the sample. The measured density after combustion is also show in figure 43 and indicates that the samples shrink on combustion.

For preventing oxidation, a 5 psi argon gas cover was continuously applied during the heating stage and cooling stage. The temperatures in the sample as well as in the furnace were monitored and recorded by connecting to a 8-channel analog input data acquisition system. X-ray diffraction from the reacted samples was obtained with Cu K α radiation and scanning was from $2\theta=14-85^\circ$. Optical micrographs were obtained after polishing and etching with a solution made up from glacial acetic acid 50ml, nitric acid 20ml, hydrofluoric acid 5ml. The samples contained porosity. The volume fraction of this porosity was measured from micrographs taken at 200x and digitally processed to obtain volume fraction information.

5.2 RESULTS

Of the seven compositions listed in Table 2, the two with the lower boron content, 1 and 2 wt. pct, did not ignite at the initial temperature of 600 C. The rest of the samples sustained an ignition front which passed across the sample. Two different temperature profiles were noted during the sample cooling stage, subsequent to the passage of the combustion wave. Figure 44 shows the continuous cooling curves. The high boron content samples (6 and 7 wt. pct) showed the profile with the plateau region during solidification. Figure 45 shows the measured combustion velocities with different boron contents. The combustion temperature increases with increasing boron content and was measured to be from 1990 K to 2478 K. X-ray analysis indicated the presence of Nb₂Al, NbB, Nb, and NbAl₃ as shown in Table 2. Also shown in figure 45 is the average Vickers hardness for the final product after combustion. Note the similarity of the hardness and velocity profiles shown in figure 45.

Figure 46(a)-(b) show the SEM microstructures for the alloys NA4B and NA7B. Note the uniform dispersion of the NbB particles in a Nb₂Al/NbAl₃ matrix. The volume fractions of porosity for 5 different compositions are plotted in figure 47 as a function of the boron content.

5.3 DISCUSSION

It is apparent from the micrographs of figure 46 that combustion synthesis may be successfully employed to obtain a uniform microstructure with well dispersed NbB particles in a Nb₂Al/NbAl₃ matrix. The hardness values are extremely high indicating that beneficial use of these composites is possible. However the alloys are brittle, although the brittle particles were clearly seen to arrest crack propagation during testing for Vickers hardness. Compositions NA4B and NA5B additionally contain unreacted Nb which may act as a ductile toughening agent. Properties of the composites may be optimized by a careful selection of the microstructure. Hence it is of importance to understand the evolution of the microstructure.

Heat is generated during the formation of NbB, and makes the reaction self sustaining. Assuming that the reaction zone is narrow, the velocity of the combustion wave may be written as,⁽⁶⁶⁾

$$u^2 = \sigma_n \alpha \frac{C_p R T_c}{Q E} K_0 \exp\left(-\frac{E}{R T_c}\right) \dots \quad (107)$$

where u is the wave velocity, σ_n a constant, α the thermal diffusivity, C_p the heat capacity, R the gas constant, Q the heat of the reaction, T_c the combustion temperature, and K_0 the pre-exponential constant for the reaction.

Equation (107) may be rewritten to give a relationship between $\ln u/T_c$ and $1/T_c$, such that values of E may be obtained. This value may be expected to reflect the rate limiting step for the synthesis.⁽³⁴⁾ When comparing with the experimental results the implicit assumption is that the presence of excess Nb and Al does not influence significantly the relationship between u and T_c expressed in equation (107). Figure 48 is a plot of $\ln u/T_c$ & $1/T_c$, and shows two distinct linear regions similar to a previous observation in Ti-C mixtures.⁽³⁴⁾ The measured activation energies in the two regions are 38 KJ and 247 KJ/mole. The activation energies may be compared to that reported in reference 67 for the diffusion of B in NbB at high and low temperature respectively. A comparison indicates that at low temperatures the kinetics of the combustion synthesis process may be controlled by the diffusion of B through NbB layer to the reaction front. Microstructural analysis reveals that at low boron contents needle shaped reinforcements are seen in the matrix (figure 46a). At the higher temperatures the calculated activation energy is small and there may be melting of constituents prior to combustion. An examination of the transition temperature in figure 48 indicates that the temperature is close to the melting points of both boron and niobium and local melting close to the reaction zone may have

occurred. Typical microstructures shown for example in figure 46b reveal large (1-3 μm) NbB plates. The aluminum is always molten at temperatures above 933.4K and the influence of this on the CS reaction is being explored.

The average particle size of the NbB particles in the high boron content alloys is 1-3 μm which is much smaller than the average particle size of the reactant powder (-325 mesh). Thus it is likely that unreacted B and Nb may be left behind after combustion. The amount of hard phase increases with boron content as shown in figure 46. The variation of the hardness and velocity with boron content (figure 45) are similar. For the low boron content compositions, both the velocity and the hardness increase with the boron content. This is an indication that the extent of reaction and fraction of hard phase increase with boron addition. For the high boron content compositions, a tapering of the hardness and only a gradual rise in velocity with increasing boron are noted. This observation may indicate that the reaction is no longer contact limited and that the number of hard particles may remain the same although the size of the particles may change.

The formation of the matrix microstructure should now involve (a) the melting and mixing of residual Nb, Al and B and (b) the formation of Nb-Al compounds by an exothermic reaction between the Nb and Al. A secondary peak in the temperature profile shown in figure 49 is often noted indicating the possibility of a second exothermic reaction.

With an increase in B and consequent formation of NbB, the amount of Nb left for alloying with Al is reduced, however the local temperatures increase as shown in figure 44 and mixing of the constituents is more uniform. With an increase in the B content beyond 6 wt. pct (Table 2), free Nb is no longer noted. The solidification sequence from the phase diagram indicates that non-equilibrium solidification of the alloy may lead to the presence of the Nb₂Al-NbAl₃ eutectic. A lamellar eutectic is noted in composition of Nb-Al combusted without B.⁽⁶⁸⁾ However no lamellar eutectic is seen in the alloys reported in this work, which may be an indication that the presence of particles influence the eutectic morphology.⁽⁶⁸⁾ Such a morphology change has been previously reported in dendritic alloys.⁽⁴¹⁾

5.4 CONCLUSION

Combustion Synthesis is a viable method of making niobium aluminide composites containing NbB as the hard reinforcing phase and Nb as the ductile reinforcing phase.

The diffusion of B in NbB appears to be the rate controlling step in the synthesis reaction at a low boron content. At high boron contents the calculated activation energy of the CS reaction is low.

A secondary exothermic reaction also occurs between Nb and Al. The bulk matrix microstructure consists of Nb_2Al and NbAl_3 .

Careful processing by selection of the sizes of the initial constituents may be used as a versatile technique for making engineered niobium aluminide composites containing both hard and soft high temperature phases.

6.0 THERMAL STRESS CRACKING DURING GROWTH OF FACETED MATERIALS

The type of defects and defect distribution in crystals grown from melt depend on numerous factors like the plastic strain produced by thermal stresses, inheritance of defects from the seed, type of solid-liquid interface, growth variables, the shape of the phase boundary, the thermal conditions, the purity of the liquid and the die construction.⁽⁶⁹⁻⁷²⁾ During growth from the melt, crystals are subjected to stresses which arise on account of non-linear temperature gradients and chemical factors. Sometimes, stresses also arise from structural changes. When non-linear temperature gradients with or without any structural constraints are experienced by a growing crystal, thermal stresses develop within the crystal. Thermal stresses may also develop with a linear temperature gradient, if the growing crystal experiences structural constraints against free thermal expansion or compression. These stresses can be either compressive or tensile. Defects such as low-angle boundaries⁽⁷³⁾ in the crystal manifest often when these stresses exceed the yield strength of the material. These boundaries may cause deviation in the optical path through a crystal in an anisotropic material such as ruby or in a material like LiNbO₃ which has very little plastic range of deformation. Exceeding the yield stress may also cause brittle cracking.⁽⁷³⁾ The crystal growth axis is also often critical. In a uniaxial crystal such as LiNbO₃, the tendency for cracking is increased considerably if the crystal is grown on orientation other than the main symmetry axis because the crystal has different expansion properties in different crystal direction. In order to find out the most optimum velocity and temperature distribution for defect free crystal growth, it is important to know the mechanical and thermal properties of the crystals and also the variation of these properties with temperature.

Solidification conditions critically affect the interface morphology during growth. During the directional solidification of an alloy or pure material, two distinctly different growth behaviors may be obtained.^(6,74-78) depending on whether the interface is faceted or non faceted. Both of these interface types are expected to respond differently to the imposed solidification condition for the generation of defects and cracks in the crystal and at the solidification interface. In this report we examine thermal stresses and cracking conditions for faceted growth of an interface type that forms distinct macroscopic facets. Figure 50 shows a typical facet interface configuration and cracking phenomena noted during the bridgman type growth of a transparent material salol.

A critical velocity for transitions to non faceted growth exists for all faceted interfaces.^(6,76,77) In this report we assume only those conditions where the interface remains faceted Bridgman type growth is considered. The

Bridgman technique is known to overcome the intrinsic problem associated with the Czochraski technique.⁽⁷⁹⁻⁸⁸⁾ The outstanding results obtained with vertical Bridgman growth of large diameter GaAs and InP samples⁽⁸⁹⁾ demonstrates the potential of the Bridgman technique. There is, therefore, a need for analyzing and optimizing the growth parameters of a crystal in the Bridgman configuration. The Bridgman configuration is also popular for the morphological studies on the faceted solid liquid interface with transparent materials.^(47,90-92)

In recent years several thermal analyses and thermal stress analysis of the Bridgman-type crystal growth system have been reported in the literature. These analyses can be broadly divided into two types: (a) models developed to predict the temperature field in the growing crystal and the melt during crystal growth in Bridgman configuration⁽⁹³⁻¹⁰⁷⁾ and (b) models developed to predict both the temperature field and thermal stress generation in the solidified crystal during growth in the Bridgman configuration.^(112,113,115-117) Only the combined thermal and stress problems are discussed.

Several authors⁽¹⁰⁸⁻¹¹¹⁾ have contributed towards an understanding of the origin of stresses in crystals grown by the Czochralski method. A good review of these studies has been presented by Brice.⁽¹⁰⁹⁾ However there seems to be only little available literature for crystals grown by Bridgman method.^(112,113,115-117) Stresses arises during crystal growth because of the non-linear temperature and composition distribution in the crystal during growth. It has been shown in several studies^(97,100-103) that non-linear temperature distribution is generated near the growth interface. This part of the crystal is the most critical region for the thermal stress generation. It is generally believed that the macroscopic interface shape strongly influences the generation of defects during directional solidification. Control of the interface growth morphology and stress is affected by many factors⁽¹¹⁷⁾ like the presence of the crucible, velocity of growth, differences in the thermal conductivity between crystal and its melt, temperature gradient in solid and liquid at the interface, and the release of the latent heat of solidification.⁽¹¹⁷⁾

There is debate about which stress has the most importance influence on the quality of crystal. Huang et al.⁽¹¹²⁾ report that the shear stress (Tresca stress) has the most important influence on the crystal. Giarandet et al.⁽¹¹³⁾ on the other hand calculate the Von-Mises stresses and their dependence on growth parameters. Jordan et al.⁽¹¹⁴⁾ determined the excess stress field from the elastic stress field so as to relate the quality of the crystals to its growth parameters. In this method the radial, tangential and axial principal stress generated by the non-uniform temperature distribution are transformed into 12 resolved shear stress components for the {111}, <110> slip system, prevalent in most semi-conductor crystals. If the <100> is considered as the crystal growth direction, it can be shown that five of the 12 resolved shear

stress components σ_i ($i = I, II, \dots, V$) are linearly independent. It is postulated that the major mechanism by which dislocations are first generated in the growing crystal is by crystallographic glide caused by the excessive thermal stress. According to Schmid's law the absolute value of any or all of the σ_i must exceed the critical resolved shear stress, σ_{crss} , for slip to occur. Since the dislocation density is proportional to the glide strain, it is also taken as proportional to excess shear stress sum σ_e , defined by

$$\sigma_e = 4\sigma_I^e + 2(\sigma_{II}^e + \sigma_{III}^e + \sigma_{IV}^e + \sigma_V^e) \quad (108)$$

$$\text{where } \sigma_i^e = |\sigma_i| - \sigma_{crss} \quad \text{for } |\sigma_i| > \sigma_{crss} \quad (109)$$

$$\text{or } \sigma_i^e = 0 \quad \text{for } |\sigma_i| \leq \sigma_{crss}. \quad (110)$$

A drawback with such analysis is that, the initial stress calculation in the crystal starts with the thermoelastic stress calculation, but does not account for the fact that the generation of dislocations modifies the prevailing stress patterns.

Garandet⁽¹¹⁵⁾ have presented an exact analytic solution of the thermal stress generation in a crystal grown by the Bridgman technique. The crystal was considered to be a solid cylinder with constant thermal and mechanical properties. Two idealized, very simple, cases which were considered are (a) in which the crystal can fully accommodate the thermal gradient. The condition for the temperature field for the "zero-stress" solution can therefore be derived and (b) the case where the crucible prevents radial expansion of the crystal. For the analysis of the first case, the derived temperature field for "zero-stress" solution is of the form

$$T = T_0 + gz \quad (111)$$

where T_0 is the reference temperature, g is any constant, and z is the axial distance. For the zero stress condition to prevail, Garandet⁽¹¹⁵⁾ showed that there should not be any temperature gradient in the radial direction, i.e., all the isotherms should be parallel to the radial axis and, in the axial direction, the temperature should be constant or that it should have linear gradient ($= g$). Taking $z = 0$ at the bottom end of the sample and T_0 as a reference temperature it was determined that

$$T = gz \quad (112)$$

gives the temperature field condition for zero stress condition. The axial and radial displacement as a function of z and r for the zero stress condition to prevail for the above-mentioned temperature field was calculated to be to be

$$u = \alpha g y z, \quad w = \alpha g \left(\frac{z^2 - r^2}{2} \right) + c \quad (113)$$

where α = coefficient of thermal expansion
 g and c are constants.

According to this result, it may be postulated that there should be enough room in the crucible for the crystal to expand radially in the course of elaboration for the retention of stress free conditions. However the melt will always be stress-free, so the correct boundary conditions should have been $z = 0$ at the solid-liquid interface and T_0 , the freezing point temperature for the correct evaluation of the thermal strain. If this process is followed, the displacement at the solid-liquid interface will be

$$u = 0 \quad \text{and} \quad w = c \quad (114)$$

and at any point below solid-liquid interface u and w are given by equation (114)

Therefore for $z < 0$, $u < 0$ and $\alpha = +ve$, the crystal will contract radially during its elaboration. In other words the design of the crucible to make room for crystal expansion during elaboration need not be the most critical factor for stress free growth. The main problem to be tackled for attaining near zero stress condition at the interface is therefore the control of the crystal growth morphology and thermal conditions such that the radial fluxes are minimized. Additionally, a provision for a linear temperature gradient in the axial direction in the solidified portion of the crystal is required.

Huang et al.^(112,116) solved the two-dimensional heat transfer problem during crystal growth in the Bridgman configuration using a finite element technique to obtain the temperature distribution in the system. The radius of the crystal chosen for this analysis was varied from 0.5 to 25 mm, and the height was kept at a value of 0.8 times the radius to eliminate the end effects. Temperature distribution in the sample was calculated by assuming a temperature distribution at the surface of the melt-solid body. Convection in the melt was neglected and the growth rate of the crystal was assumed to be zero (i.e., system was considered to be under a steady-state condition), and hence the effect of the latent heat, density of the material and specific heat of the material were neglected. It was found that, if $K_s = K_L$ (K_s = conductivity of solid, K_L = conductivity of the melt) and the imposed temperature gradient on the surface of the melt-solid body is uniform, then the shape of the interface is planar. But, if $K_s < K_L$ with uniform temperature gradient, then the interface shape is concave. It was also found that, if $K_s > K_L$, then the interface shape can be made convex or less concave by increasing the

temperature gradient in the solid as compared to that in the liquid near the interface. In the thermoelastic stress calculation, they assumed E (elastic modulus) remains constant up to the melting point. They found that the interface shape affects the temperature distribution in the solid and high maximum shear stresses are associated with convex interface shapes, rather than concave, and even on the planar interface (where there should not be any radial temperature gradient at the interface). Since linear axial or radial temperature gradient cannot generate any thermal stresses,⁽¹¹⁵⁾ the stresses during the planar interface may have been due to non-linear axial temperature distribution in the solidified portion of the crystal. However the results of Huang et al.^(112,116) do not indicate a non-linearity in the axial temperature gradient, making their solution the first to indicate a stress in the crystal even in the presence of a linear axial temperature gradient and zero radial temperature gradient.

Motakef⁽¹¹⁷⁾ investigated the influence of growth rate and furnace axial temperature gradients on the solid-liquid morphology and the stress associated with it in 5 and 7.6 cm diameter GaAs crystal grown by the VGF method. The analysis was done for a constant diameter portion of the crystal, and so the effect of various parameters during the early and final stages of solidification was neglected. In this analysis, he considered the crystal and melt contained in a crucible of a fixed internal diameter and thickness. The outer surface of the crucible was considered to be in radiative interaction with a constant axial gradient and thermal environment, which was translated axially at a uniform rate. It was assumed that the rate of translation of the furnace gradient equaled the crystal growth rate. The temperature field in the charge and ampoule, as well as the shape of the solid-liquid interface was obtained by finite-element solution of the using ABAQUS.⁽¹²⁰⁾ Once the temperature field was obtained, the elastic stress distribution in the crystal was obtained by the numerical solution of the linear thermo-elastic equation using ABAQUS. From the calculated radial, tangential and axial stress, the excess stress was calculated as described in reference 114. Some interesting results of the solution are: (i) Maximum stresses are seen to occur close to the growing interface. (ii) Results indicate that the interface shape changes (becomes more concave) during the early stages of growth, and reaches a nearly constant value after three crystal radii of constant diameter growth. (iii) With increasing growth rate, the release of latent heat of crystallization results in increased concavity of the growth interface. This concavity decreases asymptotically towards the zero growth rate limit with increasing axial gradient in the furnace. (iv) The average excess stresses near the growth surface (which is calculated as the average of excess stresses at the centerline and the periphery of the crystal) are seen to increase with increasing furnace gradient. At identical growth rate conditions, the excess stress for 7.6 cm diameter crystal is nearly twice as large as those in the 5 cm diameter crystal. In general, it is noted that the stresses increases with furnace gradients and growth rate but it is also seen that, for the 7.6 cm diameter at the higher

growth rates of 0.5 and 1.0 cm/h, a reduction of furnace gradients to below a critical value leads to an increased excess stress state.

In all the calculations available in the literature, there has been little or no emphasis placed on the morphological state of the interface. The curvatures of the interface in the previous solutions were thermally induced on account of the imposed mold conditions. It is however well known that the interface, during the directional growth of an alloy may assume severely convoluted morphologies^(91,92) during growth on account of stability problems. Cells (faceted and non faceted) and dendrites may result. These morphologies may then cause local radial temperature gradients in addition to solute gradients in the growing crystal. The effect of this on the stresses needs to be critically examined. In this report an attempt is made to study the effect of thermal stress on the growth of a faceted cellular interface.

6.1 MODEL DESCRIPTION

To solve for the stresses, a solidification model, a thermal model and a stress model are required.

6.1.1 Solidification Model

Shangguan and Hunt⁽¹¹⁸⁾ have numerically modelled dynamical pattern formation of faceted cellular array growth. They found that the cellular interactions were either transient or persistent, depending on the growth condition. The range of stable cell spacing for a given growth condition could be calculated by using four different models. Three of these models which do not invoke solute rejection are described below.

(a) Model I. The main assumption in this model is that the solute undercooling is negligible ($\Delta T_S = 0$) and that nucleation rate per unit area is proportional to the local kinetic undercooling at the nucleation site. A linear kinetic law is assumed which gives

$$R_i \text{ (nucleation rate per unit area)} = B_i \Delta T_K \quad (115)$$

where

B_i = nucleation coefficient

ΔT_K = kinetic undercooling

following these assumptions

$$\lambda \approx V^{1/2} \quad (116)$$

λ = facet cell spacing
 V = steady state growth rate.

(b) Model II - The nucleation rate was proportional to the exponential of $-1/\Delta T_K$ (Two dimensional nucleation)

$$R_2 = \beta_2 \exp(-K/\Delta T_K) \quad (117)$$

where

R_2 = nucleation rate per unit area (Model II)

β_2 = nucleation coefficient (Model II)

K = kinetic coefficient

For this model, (118)

$$V = 2\beta_2 K / (\sin^2 \alpha G) [\Gamma - 1.2 K \tan \alpha / (G \lambda)] \quad (118)$$

where

Γ = incomplete Gamma function.

G = temperature Gradient

α = angle subtended by the facets and

λ = cell spacing

(c) Model III - In this model, they replaced the two-dimensional nucleation with the screw dislocation mechanism, which gives

$$\lambda_{max} = 2 \tan \alpha (\sin \alpha / \beta_3)^{1/2} V^{1/2} G \quad (119)$$

λ_{max} = maximum cell spacing

β_3 = kinetic coefficient (Model III).

According to this model, the maximum kinetic undercooling along a facet is at the base of the facet, so two neighboring facets share the same growth rate and, therefore, no interaction occurs until the separation reaches the value λ_{max} . The cell tip cannot extend beyond the melting isotherm which is an upper limit for growth.

In the present study, finite element analysis was used to calculate the temperature distribution and the thermal stress associated with a crystal with a faceted zig-zag solid-liquid interface grown by Bridgman method. The analysis was done for the constant diameter portion of the crystal and the

time when the cell interaction has stopped and a stable cell spacing is reached (steady state conditions). The effect of various parameters during the early and final stages of growth is not investigated.

Stable cell spacing was determined by using the equation for model III. In this analysis, a constant cell spacing was taken to be equal to λ_{\max} . Material data for nickel is used for the study. There are two reasons for selecting this material for our analysis (a) the mechanical and thermal properties of nickel at all temperatures, especially near melting point are documented,⁽¹¹⁹⁾ (b) the yield stress of nickel is high, therefore for the thermal stress calculation, a linear elastic analysis can be made by avoiding the complexities of non-linear stress analysis. This linear analysis is capable of giving information on the relative magnitude and pattern of stress distribution in the growing crystal as a function of different growth parameters and temperature distribution. This information may be used to identify the parameters which are more critical for the generation of thermal stresses or detrimental to the properties of the growing crystal. Thermophysical properties of nickel used in this analysis are given in Table 3.

This analysis can be divided into two parts, (a) thermal modelling and (b) stress modelling. In the thermal modelling, the temperature distribution in the growing crystal is determined, which is then input into the stress model to calculate the associated stress generation.

6.1.2 Thermal Model

A schematic of the system under consideration is given in figure 51. The diameter of the crystal used for this analysis is 5 cm. Steady state conditions are assumed for the calculations.

Table 3

Table 3. MATERIAL PROPERTIES FOR NICKEL (MELTING POINT 1726K) reference 119

Temperature, K	Modulus, N/m ²	E Thermal conductivity J/msK	Density Kg/m ³	Poisson's ratio	Coefficient for therm expansion, K ⁻¹
298	2.11E11	88.5	8900	0.33	13.3E-06
630	1.84193E11	88.5	8900	0.33	13.3E-06
1725	9.89812E10	88.5	8900	0.33	13.3E-06
1726	9.89034E10	88.5	8900	0.33	13.3E-06

As shown in figure 51, the crucible wall is assumed to be a perfectly adiabatic surface and the tip of the zig-zag interface (points like B as shown in figure 52) is assumed to be at the melting temperature. Our intention in this study is to find out the effect of zig-zag interface on the interface temperature distribution when the thermal conductivity of the melt and solid is different (when thermal conductivity is same, then at low growth velocity there will be no local radial temperature gradient in the vicinity of the cell tip and, hence, no thermal stress generation). It is assumed in the calculations given below that the thermal conductivity of liquid is far less than that of solid, and so negligible. Since the aim here is to observe the trends and not actual values, assuming the thermal conductivity of the melt to be very small is a one way of reducing the amount of computer time required to solve this problem without sacrificing the objective of the study. The slanting faces of the facet cells were therefore considered to be adiabatic in the thermal model. With this assumption a parabolic temperature profile develops along the facet edge. Calculations were also performed with non-equal thermal conductivities in the liquid and solid. Once again a parabolic profile was seen to exist along the facet face thus giving rise to confidence in the general thermal solution as being representative of the true case.

The temperature field in the charge was obtained by solving the partial differential equation for the heat conduction namely

$$K \frac{\partial^2 T}{\partial r^2} + \frac{K_r}{r} \frac{\partial T}{\partial r} + K_z \frac{\partial^2 T}{\partial Z^2} + Q = V_g \rho C \frac{\partial T}{\partial t} \quad (120)$$

Where

T = temperature

r = radius

K_r, K_z == thermal conductivities in the r and z directions

Q = heat generated within the body

V_g = growth rate

ρ = density

C = Specific heat

Since the temperature distribution in a Bridgman system is an axisymmetric problem, the three-dimensional problem reduces to a two-dimensional problem. As shown in figure 51, only half of the two-dimensional section needs to be taken into account in calculations because the symmetry about the vertical axis.

In addition to the above assumption, the following additional assumptions were also incorporated

- (a) The system is in a steady state condition (i.e., $\partial T / \partial t = 0$).
- (b) The thermal conductivity, density, and heat capacity are the same in the solid and are independent of temperature and orientation.
- (c) The rate of liberation of latent heat of fusion is negligible compared with other heat fluxes (i.e., $Q = 0$).
- (d) The system is assumed to grow with very low growth rate so the heat carried by any convection term due motion is considered to be negligible as compared due to the heat flux transport due to thermal conductivity (i.e., $V g \rho C \partial T / \partial Z \approx 0$).

With these assumptions, the equation (120) becomes

$$K \frac{\partial^2 T}{\partial r^2} + \frac{K}{r} \frac{\partial T}{\partial r} + K \frac{\partial^2 T}{\partial Z^2} = 0 \quad (121)$$

The surface tension effects of the crucible-crystal-melt tri-junction could potentially influence the melt-solid interface shape in the region close to the crucible. This phenomenon is difficult to quantify and the effect is neglected in the present study.

As a result of symmetry, only 15 cm (= L) by 2.5 cm (= D/2) area with a pointed end at the top (as shown in figure 51) was taken as the domain in our finite element analysis. For the thermal analysis, the domain was sub-divided using a two-dimensional 8-noded, iso-parametric element. The temperature field was obtained by a finite element solution of the energy equation using ANSYS.(120)

The temperature distribution for the crystal was calculated for various values of T_0 (as shown in figure 51, which gives different values of average temperature gradient in the crystal) and various values of cell spacing. The Length AC is the repeat distance for the facets as shown in figure 52. The angle LABC is kept constant at value $\alpha/2 = 54^\circ 44'$,

6.1.3 Stress Model

Non-linear axial, and radial temperature gradients in a growing crystal generate thermal stress. Having found the temperature distribution, the stresses are calculated by writing the constitutive law for the material as

$$\epsilon_{rr} = \frac{1+v}{E} \sigma_{rr} - \frac{v}{1+v} \sigma_{xx} \delta_r + \alpha (T - T_{ref}) \delta_{rr} \quad (122)$$

where

ϵ_{ij} = strain tensor

σ_{ij} = stress tensor

δ_{ij} = Kronecker delta tensor

E = Young's Modulus (the variation with temperature is given in Table 3)

ν = Poisson ratio

α = thermal expansion coefficient

T_{ref} is taken as the melting point temperature = 1726°K.

Traction free boundaries were assumed. The stress was determined using the finite element package ANSYS.⁽¹²⁰⁾ The same grid was used for both the stress and temperature computation. In the stress calculation the domain was discretized using a two dimensional eight noded isoparametric solid element. At the facets, to fit into the zig-zag shape a six-noded triangular element was used. A triangular shaped element was formed by defining the same node number for three nodes of the eight noded isoparametric element. $\sigma_{\gamma\gamma}$ (= radial stress), $\sigma_{\theta\theta}$ (= hoop stress) and σ_{zz} (= axial stress) were computed at four integration points for the eight noded elements and at three integration points for the six noded triangular elements.

Once these stresses are calculated, other stress parameters were determined namely

(a) Hydrostatic tension σ_m defined by

$$\sigma_m = (\sigma_{\gamma\gamma} + \sigma_{\theta\theta} + \sigma_{zz})/3. \quad (123)$$

(b) The equivalent shear stress τ_e which is defined by

$$\tau_e = \sqrt{S_{ij}S_{ij}/2} \quad (124)$$

where S_{ij} is the stress deviator,

$$S_{ij} = \sigma_{ij} - \sigma_{KK}\delta_{ij}/3 \quad (125).$$

where $\sigma_{KK} = \sigma_1 + \sigma_2 + \sigma_3 / 3$

Under a state of pure hydrostatic tension and compression, i.e., when

$$\sigma_{\gamma\gamma} = \sigma_{\theta\theta} = \sigma_{zz} = \sigma$$

$\sigma_m = \sigma$ and τ_e will vanish.

Under conditions of pure shear σ_m will vanish and τ_e will be equal to shear stress. τ_e gives the value of that part of the stress component which causes dislocation slip and, hence, the material to yield, and σ_m gives the measure of the stress triaxiality at that point. Once the various stresses at the integration points are calculated, element nodal stresses are calculated using extrapolation of the integration point stresses in the element natural coordinate system. For the triangular elements the stress variation are assumed to be of the form

$$a + b s + c t \quad (126)$$

and for quadrilateral elements the stress variation are assumed to be of the form

$$a + b s + c t + d s t \quad (127)$$

where

a, b, c, d = Coefficients
s, t = Element Coordinates

Once the various stresses at all the nodes are calculated the stresses at the nodes where more than one element meet are averaged by summing up the stress values at a particular node contributed by all the elements having this common node and dividing this value by the number of elements meeting there. All the stress components obtained are measured in the unit of $E_m \alpha T_m / 10^6 \cdot (1-2\nu)$. This averaging method leads to the stresses being calculated right up to the interface in the solid.

6.2 EXPERIMENTAL

Directional solidification experiments on SALOL were carried out using an apparatus described by Mason and Eshelman.⁽⁶¹⁾ Thin glass cells were prepared by fusing the glass slides on three sides such that the gap between the slides was maintained at a constant level of 150 mm. The cells were filled with Salol by capillary action and then the cells were sealed with non-reactive epoxy.

The cells were directionally solidified in the temperature gradient stage at an imposed velocity of 5.0 mm/s. The hot and cold chambers were maintained at 325 ± 0.2 K and 283 ± 0.2 K respectively. The temperature gradient across the solid-liquid interface was estimated to be 3 K/mm. The experiments were carried out by starting from a planar interface and continuing the runs until steady state conditions were established. In all the runs the experiments were

started with a very low defect density interface. This was achieved by holding the interface stationary for nearly 12 hours and allowing for coarsening and elimination of defects.

6.3 RESULT & DISCUSSION

The model developed in the previous section was applied to determine the temperature and associated thermal stress distribution near the solid - liquid interface during the directional solidification of nickel with a zig-zag interface in the Bridgman type growth configuration . The simulation was conducted for conditions prevailing during the period when the length of the solidified crystal had reached three times the diameter. Once the crystal length reached two times its diameter it was observed that there was no significant variation of stresses near the interface with further growth.

The calculation of temperature distribution and the associated thermal stresses was done for the various average axial temperature gradients and velocity of growth of the solid - liquid interface. (In the bridgman type growth configuration, these two parameters can be varied independently). For a particular pair of values of interface growth velocity and average temperature gradient the steady state cell spacing (λ) was calculated using equation (119). Table 4 shows all the various combinations of average temperature gradient and interface growth velocities for which calculations were performed.

The thermal model indicates that on account of differences in the thermal conductivities between the solid and the liquid and the zig-zag shape of the interface, radial temperature gradients arise in regions close to the solid - liquid interface. The radial temperature gradient near the interface is periodic in nature, in the sense that as shown in figure 52 the temperature at the point 'A' and 'C' are equal. However there is variation in temperature as we move from 'A' to 'C'. This temperature distribution is symmetrical about a point midpoint between 'A' and 'C' (i.e., as we move from the point 'A' towards the point 'C' the temperature increases until we reach the midpoint between 'A' and 'C' and then it starts decreasing). We define the average local radial temperature gradient near the interface as the difference in temperature between positions (3) and (2), as shown in figure 52, divided by the distance between these positions. It should be noted that the radial temperature gradient decreases as we move away from the interface and becomes zero after a certain distance from the interface. After this, the temperature distribution becomes one dimensional with only the axial temperature gradient being present.

The radial temperature gradient near the interface distorts the otherwise linear axial temperature gradient. We may also define the average local axial temperature gradient near the interface as the difference in temperature between position (1) and position (3), as shown in figure 52, divided by the

distance between these two points. The axial temperature gradient becomes equal to average axial temperature gradient imposed on the growing crystal in the region far away from the interface. The average local radial temperature gradient and average local axial temperature gradient for the different values of average axial temperature gradient and cell spacings are tabulated in Table 4.

Thermal stresses are generated on the account of the two dimensional variation of temperature near the interface and the jagged shape of the interface. From Table 4 we note that the magnitude of the average local radial temperature gradient and average local axial temperature gradient is a linear function of the average axial temperature gradient but independent of cell spacing (λ), (i.e, for $\lambda > 0$). For $\lambda = 0$ the shape of the interface will become planar and the radial temperature gradient will become zero everywhere and there will be no thermal stress generation.

6.3.1 Thermal Stresses on the Facets

On account of the axisymmetry of the crystal the only non-zero stresses are σ_{rr} , $\sigma_{\theta\theta}$ and σ_{zz} . The solution for the mean hydrostatic tension σ_m and the equivalent shear stress τ_e , both normalized with respect to the quantity $\alpha EMT/(1-2v)*10^6$ are presented in figures 53-55 for the position (1), position (2) and position (3) respectively for the facet in figure 52. Figure 53a, figure 54a and figure 55a show the variation of normalized σ_m at the above mentioned positions with the cell spacing at a constant average axial temperature gradient of 1K/mm, 5K/mm and 10K/mm respectively. Figure 53a shows that at a constant axial temperature gradient of 1K/mm, the normalized σ_m is tensile in nature for the position (2) and position (3) and that they are nearly equal. The σ_m becomes more tensile in magnitude at these position as the cell spacing increases. Note also that the variation of σ_m with cell spacing is linear. At position (3) the normalized σ_m is compressive in nature and becomes more compressive in magnitude as the cell spacing increases. Note that for this case also, there is a linear variation of normalized σ_m with cell spacing.

Figure 54a and figure 55a show similar variation at a constant axial temperature gradient of 5K/mm and 10K/mm respectively. When comparing figure 53a, figure 54a and figure 55a, it should be noted that the absolute values of the normalized σ_m increases with increasing the average axial temperature gradient for the same value of the cell spacing, or in other words the absolute value of the slope of curve of the variation of the

normalized σ_m with cell spacing increases with an increase in average axial temperature gradient

Figure 53b, figure 54b and figure 55b show the variation of the normalized τ_e (equivalent shear stress) with cell spacing at a constant average axial temperature gradient of 1K/mm, 5K/mm and 10K/mm respectively. Figure 53b shows that at a constant axial temperature gradient of 1K/mm, the variation of normalized τ_e with cell spacing is linear for all the three positions but that the normalized τ_e is always higher at position (1) than at positions (2) and (3). For all the values of the cell spacings, the slope of the curve for position (1) is higher than that of positions (2) and (3). Figure 54b and figure 55b show similar variation at a constant axial temperature gradient of 5 K/mm and 10 K/mm respectively. Comparing the figures it may be noted that as the average axial temperature gradient increases, the slope of the curve of the variation of normalized τ_e with cell spacing also increases for all the three positions. For a particular set of growth parameters used for the calculations the values of the stresses on all the facets are equal when calculated between 0.1R to 0.9R (where R is the radius of the crystal). Very close to the boundaries there is a slight difference in the magnitude of stresses experienced by the facets. The result described above refer to the region of the crystal between 0.1 and 0.9 R.

The stress model predicts that during the growth of a crystal with a zig-zag interface at a constant velocity the tip of the facet experiences a compressive mean hydrostatic stress whereas the root of the facet experiences a tensile mean hydrostatic stress. It also predicts that the equivalent shear stress τ_e experienced by the tip of the facet is higher than that experienced by the root of the facet. Since τ_e is the measure of that part of the stress tensor which causes plastic deformation by dislocation slip, it may be inferred that during the growth of a crystal, the tip of the facet will undergo plastic deformation before the root.

A new parameter may be introduced which allows us to collapse the six graphs figures 53-55 into two graphs such that the result may be presented more efficiently. This new parameter ' Ω ' is given by

$$\Omega = G_{\lambda} / \lambda^{\lambda_{\max}} \quad (128)$$

Plots of Ω versus σ_m and τ_e indicate that σ_m and τ_e scale linearly with Ω . From equation (119), which gives the relationship between the steady state maximum cell spacing (λ_{\max}) and the velocity of the growth and the axial temperature gradient, we find that

$$G_{AV,A} * \lambda_{max} \propto V^{1/2} \quad (129)$$

Therefore σ_m and τ_e should scale linearly with $V^{1/2}$. This relationship is shown in figure 56 and figure 57.

Assuming that the model for growth i.e., equation (119) is representative of the actual conditions, then for a particular system the above relationship predicts that the velocity of growth of the interface determines the magnitude of the various stresses generated on the facet. If the axial temperature gradient is decreased, keeping the velocity of the interface growth constant then the steady state cell spacing of the jagged interface increases to maintain the stress level. It may therefore be concluded that while growing a crystal with a zig-zag interface (in a bridgman growth configuration), in spite of having two controlling parameters which may be varied independently viz. the growth velocity and axial furnace temperature gradient, fixing the velocity of the growth fixes the magnitude of the various stresses which are generated on the facets independent of the imposed axial temperature gradient.

Figures 58a, 58b and 58c show the contour plots of normalized σ_{rr} (radial stress), $\sigma_{\phi\phi}$ (hoop stress) and τ_e (equivalent shear stress) on a facet which is 0.5 R distance away from the centre of the crystal. These contours plots are for the condition when the cell spacings of the facets are $80.69\mu m$ and average axial temperature gradient is $1 K/mm$. Contours plots of σ_{zz} (axial stress) are not shown because the traction free solid-liquid interface boundary (i.e., no constrain on the solid-liquid interface in the axial direction) makes these stresses very small. Thus the axial stress values near the solid-liquid interface are negligible when compared to that of radial and hoop stresses. Consequently σ_m in this region is determined by the values of the radial and hoop stresses.

As can be noted in figures 58a and 58b the radial stress and the hoop stress are highly compressive in nature near the tip of the facet and their magnitude decreases as we move towards the root of the facet. In the region between 'F' and 'G' as shown in figure 58a the radial stress changes from a compressive state to a tensile state and between 'G' and 'H' as shown in figure 58b the hoop stress changes from a compressive state to tensile state. It may be therefore be concluded that this is also the region where σ_m changes its nature from compressive to tensile.

As shown in figure 58c the contour plots of τ_e show that the value is maximum at the tip and decreases monotonically as we move towards the

root of the facet. Since the equivalent shear stress gives the value of only that part of the stress which causes dislocation slip and hence yielding of the material, it may be inferred that these high equivalent shear stresses near the tip of the facet will cause plastic deformation in this region. Dislocations will move along their slip planes and will pile up at any obstacle (e.g. the obstacle may be due to the formation of sessile dislocations). The acting on the slip plane squeezes the dislocations together. At some critical value of the stress the dislocations at the head of the pile-up are pushed so close together that they may coalesce into a wedge crack or cavity dislocation. This is equivalent to micro crack nucleation. Thus the crack may grow by plastic deformation so long as the dislocation source continues to force dislocations into the pile-up. It should be noted that only equivalent shear stresses are involved in forcing the dislocations together and hydrostatic stresses are not involved in the microcrack nucleation process. However, hydrostatic stresses influences crack propagation. Compressive hydrostatic stresses act to close these small microcrack and generally will make the crack propagation process more difficult. Tensile hydrostatic stresses help in the propagation of these deformation induced microcracks. Tensile hydrostatic stresses help in the opening of these microcracks and in the propagation of these microcracks to form large cracks in the material.

On examination of the contour plots of figure 58a, figure 58b and figure 58c we may infer that in spite of having a very high equivalent shear stresses near the tip, no crack will be seen forming in this region because of the high compressive hydrostatic stress in this region. As the facet grows the material at the tip (containing the microcracks) will pass through a region of decreasing compressive hydrostatic stress and ultimately pass through regions of tensile hydrostatic stress. (Note that in this region also equivalent shear stresses are quite high in magnitude). On passage through the region of tensile hydrostatic stress the microcracks will propagate and cracks will be seen forming in the material. Therefore in figure 58a the cracks should start propagating between the region 'F' and 'G'.

Figures 59a, figure 59b, and figure 59c show the contour plots of normalized radial stress, hoop stress and equivalent shear stress when the cell spacing of the facet are $80.69\mu\text{m}$ and average axial temperature gradient of 10K/mm is imposed. It may be noted that due to the ten fold increase in the average axial temperature gradient the absolute magnitude of all the stresses has increased by nearly 10 times but the region where they change their nature from compressive to tensile is located as before. Figures 60a, 60b and 60c show the same contour plots when the cell spacing of the facets is $255.2\mu\text{m}$ and average axial temperature gradient is 5K/mm . Note again that the absolute values of all the stresses has increased but the region where they change from compressive to tensile is nearly the same as described before.

6.3.2 Experimental Result and Discussions

Experiments were conducted in directionally growing Salol to examine the onset of cracking. Figure 61 shows the interface shape during a imposed growth velocity of $0.1 \mu\text{m/s}$ and in the presence of a positive temperature gradient of 3 K/mm . Note the similarity of the interface configuration to that shown in figure 52. Growth was initiated as discussed above by imposing a constant velocity of growth on the Hele - shaw cell . Salol is known to grow by the screw dislocation mechanism.^(121,122)

Figure 62 shows the time sequence of events occurring on a single facet during growth. The photograph are taken 5 seconds apart during growth. Figure 62a shows a facet with no apparent cracks near the interface . As growth progresses, a crack suddenly appears as shown in figure 62b and extends from the interface to the interior of the facet. Note that this crack appears in a location between the tip and the root of the facet. From the observations made in the previous section this may be the region where the tensile hydrostatic stress are felt. Figure 62c shows the crack now left behind in the crystal during subsequent growth. Also noted is a fresh crystal facet which starts on the cracked face and grows as shown in figure 62d. The cracking phenomena discussed in this sequence was common to all the facets, however the growth of a new facet from the crack region was seen only occasionally.

Figure 63 shows a similar sequence i.e., no crack in 63a and the crack appearing in 63b and 63c. However in this case the crack was seen to continuously propagate with the interface. The propagation however, was noted to be jerky. It was also not apparent whether the crack grew with the interface or whether the larger crack on the facet was joined by fresh crack forming on the solidification interface.

As noted above, cracking was only prevalent at some distance away from the tip of the facet. However in a few special cases the crack could appear at the tip. One of these cases is shown in figure 64. For the growth of a facet which has reached the liquidus at the tip, tip splitting is required for further growth. Figure 64 shows the growth of two macroscopic facets. Figure 64b is taken 5 seconds after figure 64a. Of the two tips shown in figure 64b, the one on the right splits and the one on its left does not. The splitting process is seen to leave behind a crack. One possible explanation for this phenomenon is that when the splitting takes place, a root type region is suddenly created. Once again, the material which was in a high compressive state under high equivalent shear stress, now is in a region of hydrostatic tension. This may lead to the cracking phenomenon noted in the figure.

The experimental result shown in the sequences of figures 62, 63 and 64 indicate that cracking occurs behind the tip or in regions which are a root to the facet. A comparison with the numerical results discussed above indicate that the observations are similar to those expected from the calculations. Some caution is in order because the calculation relate to an isotropic material whereas the experimental observations relate to SALOL which is orthorhombic.⁽¹²³⁾ It is not entirely clear how solute distribution may have influenced the experimental observations. Although the Salol was purified, a certain amount of solute is always present. Even small amounts of solute may cause cracking. Nevertheless, the results of the numerical work and the experimental study are consistent.

7.0 CONCLUSION AND FUTURE WORK

All the work has proceeded on schedule. Most of the theoretical and experimental framework for the project has been established during the first year. The working team for the next year is also in place. Several important techniques for modeling and generation of the Mg-Li composites and the Nb-Al composites have been developed. Several papers have been sent for publication based on the first years work. A possible patent application is being considered for filing as an invention disclosure.

Further work will now concentrate on (i) clinching the key aspects of the transparent work and extending the same to microsegregation in constrained environments (ii) performing the directional experiments on the Mg-Li alloys and composites and (iii) performing the directional experiments on the Nb-Al and Nb-Al composites made by combustion synthesis.

8.0 REFERENCES

1. J. A. Sekhar, Current Science, vol. 54, no. 18 (1985) 904-911.
2. W. W. Mullins and R. F. Sekerka, J. Appl. Phys., vol. 35 (1964) 444-51.
3. R. Trivedi, J. A. Sekhar and V. Seetharaman, Metall Trans., vol. 20A (1989) 769-778.
4. R. Trivedi and W. Kurz, Acta Metall., vol. 34 (1986) 1663-1620.
5. W. Kurz, B. Giovanolla and R. Trivedi, Acta Metall., vol. 34 (1986) 823-30.
6. J. A. Sekhar, A. Bharti and R. Trivedi, unpublished results. See also ibid vol. 20A (1989) 2191-2194.
7. J. Lipton, W. Kurz and R. Trivedi, Acta Metall., vol. 35 (1987) 957-964. See also J. Lipton, M. E. Glicksman and W. Kurz, Mater. Sci. and Engng., vol. 65 (1984) 57.
8. S. C. Huang and M. E. Glicksman, Acta Metall., vol. 29 (1981) 701-705.
9. R. Trivedi and K. Somboonsuk, J. Mater. Sci. Engng., vol. 65 (1984) 65.
10. K. Somboonsuk and R. Trivedi, Scripta Metall., vol. 18 (1984) 1283-1286.
11. M. J. Aziz, J. Appl. Phy., vol. 53 (1982) 1158.
12. K. A. Jackson, G. H. Gilmer and H. J. Leamy, Sym. Mater. Res. Soc., Academic Press, New York (1980).
13. R. Trivedi, J. Lipton and W. Kurz, Acta. Metall., vol. 35 (1987) 965-970.
14. J. A. Sekhar and R. Trivedi, J. Mat. Sci. Eng., vol. A114 (1989) 133-146.
15. L. H. Unger and R. A. Brown, Phys. Rev. B, vol. 30 (1984) 3933-3999.
16. B. Caroli, C. Caroli and B. J. Roulet, J. Cryst. Growth, vol. 76 (1986) 31-49.
17. S. de Cheveigné, C. Guthman and M. M. Lebrun, J. Cryst. Growth, vol. 73 (1985) 242.
18. P. Pelcé and A. Pumir, J. Cryst. Growth, vol. 73 (1985) 337-342.
19. A. Karma and P. Pelcé, Phys. Rev. A, vol. 39 (1989) 4162-4169.

20. J. W. McLean and P. G. Saffman, *J. Fluid. Mech.*, vol. 102 (1981) 445.
21. M. Vanden-Broek, *Phys. Fluids*, vol. 26 (1983) 2033.
22. D. Kessler and H. Levine, *Phys. Rev. Lett.*, vol. 57 (1986) 3069-3072; see also Solidification of Metal Matrix Composites, ed. by P. Rohatgi, The Minerals, Metals & Materials Society, 1990, pp. 26-27.
23. C. A. Anderson and O. C. Zienkiewicz, *Journal of Heat Transfer*, (August 1974) 398-404.
24. K. G. Shkashinsky, B. I. Khaikin and A. G. Merzhanov, *Combustion, Explosion and Shock Waves*, vol. 7 (1971) 15-22.
25. A. G. Merzhanov and B. I. Khaikin, *Prog. Energy Combust. Sci.*, vol. 14 (1988) 1-98.
26. J. B. Holt and Z. A. Munir, *Journal of Materials Science*, vol. 21 (1986) 251-259
27. Jan Puszynski, Jan Degreve, and Vladimir Hlavacek, *Ind. Eng. Chem. Res.*, vol. 26 (1987) 1424-1434.
28. S. B. Margolis, *Progress in Energy and Combustion Science*, vol. 17, no. 2 (1991) 135-162.
29. S. B. Margolis, *Combustion Sci. and Technology*, vol. 43 (1985) 197-215.
30. W. R. Wrzesinski and J. C. Rawers, *J. Mat. Sci. Let.*, vol. 9 (1990) 432.
31. L. L. Wang, Z. A. Munir and J. B. Holt, *Metall. Trans. B*, vol. 21 (1990) 567.
32. H. C. Yi and J. J. Moore, *J. Mat. Sci. Let.*, vol. 8 (1989) 1182 ; *J. Mat. Sci.*, vol. 24 (1989) 3449, vol. 24 (1989) 3456; vol. 25 (1990) 1159; *J. Metals*, vol. 8 (1990) 31.
33. Z. A. Munir, *Ceram. Bull.* vol. 67, (1988) 342.
34. S. D. Dunmead, D. W. Redey, C. E. Semler and J. B. Holt, *J. Am. Ceram. Soc.*, vol. 72, no. 12, (1989) 2318.
35. D. M. Bowden, P. J. Meschter, L. H. Yu, M. A. Meyers and N. N. Thadhani, *J. Metals*, vol. 40 (1988).

36. R. A. Perkins and K. T. Chiang, *Scripta Metal.*, vol. 22 (1988) 419 .
37. D. M. Bowden, *Mater. Manufact. Proc.*, vol. 4, no. 1 (1989) 85.
38. C. T. Ho and J. A. Sekhar, *MRS Publication on Ordered Intermetallic Alloys*, 1991 (in press).
39. H. P. Li, S. B. Bhaduri and J. A. Sekhar, *Metallurgical Transactions* 1991 (in review).
40. Y. M. Chiang, J. S. Haggerty, R. P. Messner and C. Demetry, *Ceram. Bull.*, vol. 68, no. 2 (1989) 420.
41. J. A. Sekhar and R. K. Trivedi, *Solidification of Metal Matrix Composites*, TMS, Warrandale, (1990) 39-50.
42. R. K. Trivedi , S. H. Han, and J. A. Sekhar, *Solidification of Metal Matrix composites*, TMS, Warrandale, (1990) 23.
43. M. Hansen, Constitution of Binary Alloys, McGraw Hill, New York, 1958 p. 384.
44. J. A. Sekhar, S. Kou and R. Mehrabian, *Metallurgical Transactions A*, vol. 14A (June 1983) 1169-1177.
45. B. Basu and J. A. Sekhar, *Metallurgical Transactions A*, vol. 20A (September 1989) 1833-1845.
46. N. Shamsunder and E. M. Sparrow, *J. Heat Transfer, Trans. ASME*, vol. 97 (1975) 97-105.
47. M. C. Flemings, Solidification Processing, McGraw-Hill, New York, NY, 1974, pp. 160-63.
48. S. W. Benson, Thermochemical Kinetics, John Wiley and Sons, 1968, p. 75.
49. D. B. Anthony, J. B. Howard, H. C. Hottel and H. P. Meissner, *Proceedings of the Fifteenth Symposium (International) on Combustion*, The Combustion Institute, 1975, pp. 1303-1317.
50. L. M. Fabietti, V. Seetharaman and R. Trivedi, *Metall Trans.*, vol. 21A (1990) 1299 .
51. A. Mortensen, J. A. Cornie and M. C. Flemings, *Metall. Trans.*, vol. 19A (1988) 709.

52. A. Mortensen, J. A. Cornie and M. C. Flemings, *J. Met.*, vol. 60 (1988) 12.
53. A. Mortenson in Solidification of Metal-Matrix Composites, ed. by P. Rohatgi, The Metallurgical Society, Warrendale, PA (1990), p. 1.
54. D. R. Uhlman, B. Chalmers and K. A. Jackson, *J. Appl. Phys.*, vol. 35 (1964) 2986.
55. G. F. Bolling and J. Cisse, *J. Cryst. Growth*, vol. 10 (1971) 56.
56. A. A. Chernov and A. M. Mel'nikova, *Soviet Physics Cryst.*, vol. 10 (1966) 666.
57. P. K. Rohatgi, R. Asthana and S. Das, *Int. Metal. Review*, vol. 31 (1986) 115.
58. D. M. Stefanescu, B. K. Dhindaw, A. S. Kacar and A. Moitra, *Metall. Trans.*, vol. 19A (1988) 2847.
59. R. Shashikumar, T. R. Ramamohan and B. C. Pai, *Acta Metall.*, vol. 37 (1989) 2085.
60. J. D. Hunt, K. A. Jackson, and H. Brown, *Rev. Sci. Instr.*, vol. 37 (1966) 805.
61. J. T. Mason and M. A. Eshelman, Rep. IS-4906, 1986 (Ames Laboratory, Ames, IA).
62. J. S. Langer and H. Müller-Krumbhaar, *Acta Metall.*, vol. 26 (1978) 1681.
63. P. Pelce and Y. Pomeau, *Studies in Appl. Math.*, vol. 74 (1986) 245-54.
64. K. Somboonsuk and R. Trivedi, *Acta Metall.*, vol. 33 (1985) 1051.
65. V. Seetharaman, L. M. Fabietti and R. Trivedi, *Metall. Trans.*, vol. 20A (1989) 2567.
66. A. G. Merzhanov, *Arch. Procesow Spalania* vol. 5, no. 1, (1974) 17.
67. G. V. Samsonov and O. P. Epik, *Fiz. Metal. i Metalloved.*, vol. 14 (1962) 479; also see *Phys. Metals Metallog. [USSR]*, vol. 14, Nr. 3 (1962) 144; *Dopovidi Akad. Nauk Ukr. RSR* (1964) 67.
68. C. T. Ho and J. A. Sekhar, submitted for publication.

69. R. E. Novak, R. Metzl, A. Dreeben, et al., *J. Cryst. Growth*, vol. 50, no. 1, (1980) 13-150.
70. K. Wada and K. Hoshikawa, "Growth and characterization of sapphire ribbon crystals," *J. Cryst. Growth*, vol. 50, no. 1 (1980) 151-159.
71. S. E. Azoyan, L. P. Egorov, L. M. Zatulovskii, et al., "Making sapphire tubes from the liquid by Stepanov's method and examination of their properties and use in production of high-pressure sodium lamps," *Izv. Akad. Nauk SSSR, Ser. Fiz.*, vol. 43, no. 9 (1979) 1953-1962.
72. R. E. Novak and K. M. Kim, "Dislocations in {1012} sapphire ribbons grown by the EFG process," *J. Cryst. Growth*, vol. 50, no. 1 (1980) 330-334.
73. B. Cockayne, "Developments in Melt-Grown Oxide Crystals," *J. Cryst. Growth*, vol. 3 (1968) 4.
74. W. K. Burton, N. Cabrera and F. C. Frank, *Philos. Trans. R. Soc. London*, vol. A243 (1951) 299-358.
75. K. A. Jackson, *Mat. Sci. & Engg.*, vol. 65 (1974) 7-13.
76. J. W. Cahn ; *Acta Metall.*, vol. 8 (1960) 554-562.
77. K. N. Rao and J. A. Sekhar, *Scripta Metall.*, vol. 21 (1987) 805-810.
78. R. S. Fidler, M. N. Crocker and R. W. Smith, *J. Cryst. Growth*, vol. 13-14 (1972) 739-746.
79. C. R. Abernathy, A. P. Kinsella, A. S. Jordan, R. Caruso, S. J. Pearton, H. Temkin and H. Wade, *J. Crystal Growth*, vol. 85 (1987) 106-115.
80. A. S. Jordan, A. R. Von Neida and R. Caruso, *J. Crystal Growth*, vol. 76 (1986) 243.
81. A. G. Elliot, C.-L. Wei, R. Farroro, G. Woolhouse, M. Scott and R. Hiskes, *J. Crystal Growth*, vol. 70 (1984) 169.
82. Urban Ekhult and Torbjorn Carlberg, *J. Crystal Growth*, vol. 76 (1986) 317-322.
83. H. M. Mobgood, R. N. Thomas, D. L. Barrett, G. W. Eldridge, M. M. Sopira and M. C. Drice, in Semi-Insulating III-V Materials, Kah-nee-ta, 1984, eds. D. C. Look and T. S. Blakemore (Shiva, Nantwich, 1984), p. 149.

84. T. Inoue, S. Nishine, M. Shibata, T. Matsumoto, S. Voshitake, Y. Sato, T. Shimoda and K. Fujita, in Proc. 12th Intern. Symp. on GaAs and Related Compounds, Karuizawa, 1985, Inst. Phys. Conf. Ser 79, ed. M. Fujimoto (Inst. Phys., London-Bristol, 1986), p. 7.
85. J. D. Garrett, M. N. Iyer and J. E. Greedan, J. Crystal Growth, vol. 41 (1977) 225.
86. D. S. Robertson and I. M. Young, J. Mater. Sci., vol. 17 (1980) 1729.
87. M. Adachi, Japan J. Appl. Phys., vol. 24, Suppl. (1985) 24-3.
88. FAN Shi-Ji, SHEN Guan-Shun, WANG Wen, LI Jin-Long and LE Xiu-Hong, J. Crystal Growth, vol. 99 (1990) 811-814.
89. W. A. Gault, E. M. Monberg and J. E. Clemans, J. Crystal Growth, vol. 74 (1986) 491.
90. W. Kurz and D. J. Fisher, "Fundamentals of Solidification," Trans Tech Publication, 1989.
91. K. Somboonsuk, Ph.D. Thesis, Iowa State University, 1984.
92. D. J. Fisher, EPFL, Ph.D. Thesis, No. 301, 1978.
93. T. W. Clyne, J. Crystal Growth, vol. 50 (1980) 684-690.
94. T. W. Clyne, J. Crystal Growth, vol. 50 (1980) 691-700.
95. D. M. L. Bartholomew and A. Hellawell, J. Crystal Growth, vol. 50 (1980) 453-460.
96. T. Jasinski, W. M. Rohsenow and A. F. Witt, J. Crystal Growth, vol. 61 (1983) 339-354.
97. S. Sen and W. R. Wilcox, J. Crystal Growth, vol. 28 (1975) 36.
98. R. J. Naumann , J. Crystal Growth, vol. 58 (1982) 554-568.
99. R. J. Naumann , J. Crystal Growth, vol. 58 (1982) 569-584.
100. Chong E. Chang and W R. Wilcox, J. Crystal Growth, vol. 21 (1974) 135-140.
101. Ta-Wei FU and William R. Wilcox, J. Crystal Growth, vol. 48 (1980) 416-424.

102. T. Jasinski, A. F. Witt and W. M. Rohsenow, *J. Crystal Growth*, vol. 67 (1984) 173-184.
103. T. Jasinski and A. F. Witt, *J. Crystal Growth*, vol. 71 (1985) 295-304.
104. C. L. Jones, P. Capper and J. J. Gosne, *J. Crystal Growth*, vol. 56 (1982) 581-590.
105. C. L. Jones, P. Capper, J. J. Gosney and I. Kenworthy, *J. Crystal Growth*, vol. 69 (1984) 281-290.
106. Lawrence Rozier Holland, *J. Crystal Growth*, vol. 96 (1989) 577-583.
107. M. J. Crochet, F. Dupret, Y. Ryckmans, F. T. Geiling and E. M. Monberg, *J. Crystal Growth*, vol. 97 (1989) 173-185.
108. A. S. Jordan , R. Caruso , A. R. Von Neida and J. W. Nielsen, *J. Appl. Phys.*, vol. 52 (1981) 3331.
109. J. C. Brice, *J. Crystal Growth*, vol. 42 (1977) 427.
110. J. C. Brice, *Acta Electron*, vol. 16 (1973) 291.
111. E. Billig , *Brit. J. Appl. Phys.* vol. 7 (1956) 375.
112. C. E. Huang, D. Elwell and R. S. Feigelson, *J. Crystal Growth*, vol. 69 (1984) 275-280.
113. J. P. Garandel, T. Duffar and J. J. Favier, *J. Crystal Growth*, vol. 96 (1989) 888-898.
114. A. S. Jordan, A. R. Von Neida and R. Caruso, *J. Appl. Phys.*, vol. 52 (1981) 3331.
115. J. P. Garandel, *J. Crystal Growth*, vol. 96 (1989) 680-684.
116. C. E. Huang, D. Elwell and R. S. Feigelson, *J. Crystal Growth*, vol. 64 (1983) 441-447.
117. Shahryar Motakef, *J. Crystal Growth*, vol. 98 (1983) 711-720.
118. D. K. Shangguan and J. D. Hunt, *J. Crystal Growth*, vol. 96 (1989) 856-870.
119. Harold J. Frost and Michael E. Ashby, Deformation - Mechanism Maps, Pergamon Press , 1982.

120. ANSYS Users Manual. Gabriel J. DeSalvo and Robert W. Gorman, Swanson Analysis Systems , Inc.
121. G. Chadwick, Sheffield Univ., Met Soc. J., vol. 9 (1970) 15.
122. U. Duerig, J. H. Bilgram and W. Kaenzig, Phys. Rev A, vol. 30, no. 2 (1984) 946-59.
123. J. H. Bilgram, U. Duerig, M. Waechter and P. Seiler, Journal of Crystal Growth, vol. 57, no. 1 (1982) 1-5.

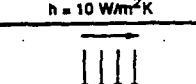
Table (4)

Velocity of interface growth ($\mu\text{m/s}$)	Average axial temperature gradient $1 \times 10^{-2} (\text{K}/\mu\text{m})$	Average axial temperature gradient $5 \times 10^{-3} (\text{K}/\mu\text{m})$	Average axial temperature gradient $1 \times 10^{-3} (\text{K}/\mu\text{m})$
1.0	$\lambda_{\max} = 2.551 \mu\text{m}$	$\lambda_{\max} = 5.104 \mu\text{m}$	$\lambda_{\max} = 25.518 \mu\text{m}$ * $0.29 \times 10^{-3} (\text{K}/\mu\text{m})$ ** $2.99 \times 10^{-3} (\text{K}/\mu\text{m})$
10.0	$\lambda_{\max} = 8.069 \text{ mm}$ * $3.09 \times 10^{-3} (\text{K}/\text{mm})$ ** $29.96 \times 10^{-3} (\text{K}/\text{mm})$	$\lambda_{\max} = 16.139 \text{ mm}$ * $1.52 \times 10^{-3} (\text{K}/\text{mm})$ ** $14.96 \times 10^{-3} (\text{K}/\text{mm})$	$\lambda_{\max} = 80.696 \text{ mm}$ * $0.30 \times 10^{-3} (\text{K}/\text{mm})$ ** $2.96 \times 10^{-3} (\text{K}/\text{mm})$
50.0	$\lambda_{\max} = 18.044 \text{ mm}$ * $3.09 \times 10^{-3} (\text{K}/\text{mm})$ ** $29.89 \times 10^{-3} (\text{K}/\text{mm})$	$\lambda_{\max} = 36.088 \text{ mm}$ * $1.51 \times 10^{-3} (\text{K}/\text{mm})$ ** $14.92 \times 10^{-3} (\text{K}/\text{mm})$	$\lambda_{\max} = 180.442 \text{ mm}$ * $0.26 \times 10^{-3} (\text{K}/\text{mm})$ ** $2.94 \times 10^{-3} (\text{K}/\text{mm})$
100.0	$\lambda_{\max} = 25.518 \text{ mm}$ * $3.00 \times 10^{-3} (\text{K}/\text{mm})$ ** $29.89 \times 10^{-3} (\text{K}/\text{mm})$	$\lambda_{\max} = 51.036 \text{ mm}$ * $1.52 \times 10^{-3} (\text{K}/\text{mm})$ ** $14.89 \times 10^{-3} (\text{K}/\text{mm})$	$\lambda_{\max} = 255.184 \text{ mm}$ * $0.29 \times 10^{-3} (\text{K}/\text{mm})$ ** $2.90 \times 10^{-3} (\text{K}/\text{mm})$

'*' represents Average local radial temperature gradient near the interface.

''**' represents Average local axial temperature gradient near the interface.

CHILLING TECHNIQUES

 $h = 10^2 \text{--} 10^6 \text{W/m}^2\text{K}$	CONDUCTION HEAT REMOVAL SPLAT COOLING, PLANAR FLOW CASTING, DOUBLE ROLLER QUENCHING, INJECTION CHILLING, PLASMA SPRAY DEPOSITION.
 $h = 10^2 \text{--} 10^5 \text{W/m}^2\text{K}$	CONVECTIVE HEAT REMOVAL. VARIOUS FORMS OF ATOMISERS (GAS & WATER) UNIDIRECTIONAL ATOMISER, CENTRIFUGAL ATOMISER, ROTATING CUP PROCESS PLASMA SPRAY.
 $h = 10 \text{ W/m}^2\text{K}$	RADIATIVE HEAT REMOVAL ELECTROHYDRODYNAMIC PROCESS, VACUUM PLASMA PROCESS.
 $h \rightarrow \infty$	DIRECTED AND CONCENTRATED ENERGY TECHNIQUES. CONDUCTION: HEAT REMOVAL LASERS (PULSED AND CONTINUOUS) ELECTRON BEAM.

UNDERCOOLING TECHNIQUES

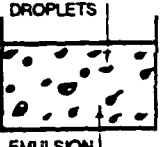
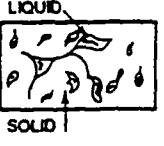
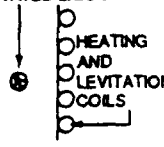
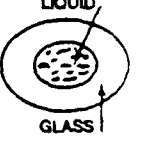
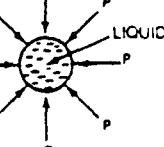
 METAL LIQUID DROPLETS EMULSION	DROPLET EMULSION TECHNIQUE
 LIQUID SOLID	EQUILIBRIUM MUSHY ZONE TECHNIQUE
 LEVITATED LIQUID HEATING AND LEVITATION COILS	LEVITATION TECHNIQUE LEVITATION MAY BE GAS JET OR INDUCTION CURRENT TYPE
 LIQUID GLASS	NUCLEANT FLUXING TECHNIQUE
 LIQUID P P P P P P	RAPID PRESSURE APPLICATION TECHNIQUE

Figure 1. Schematic illustrations of various rapid solidification techniques: from reference 1.

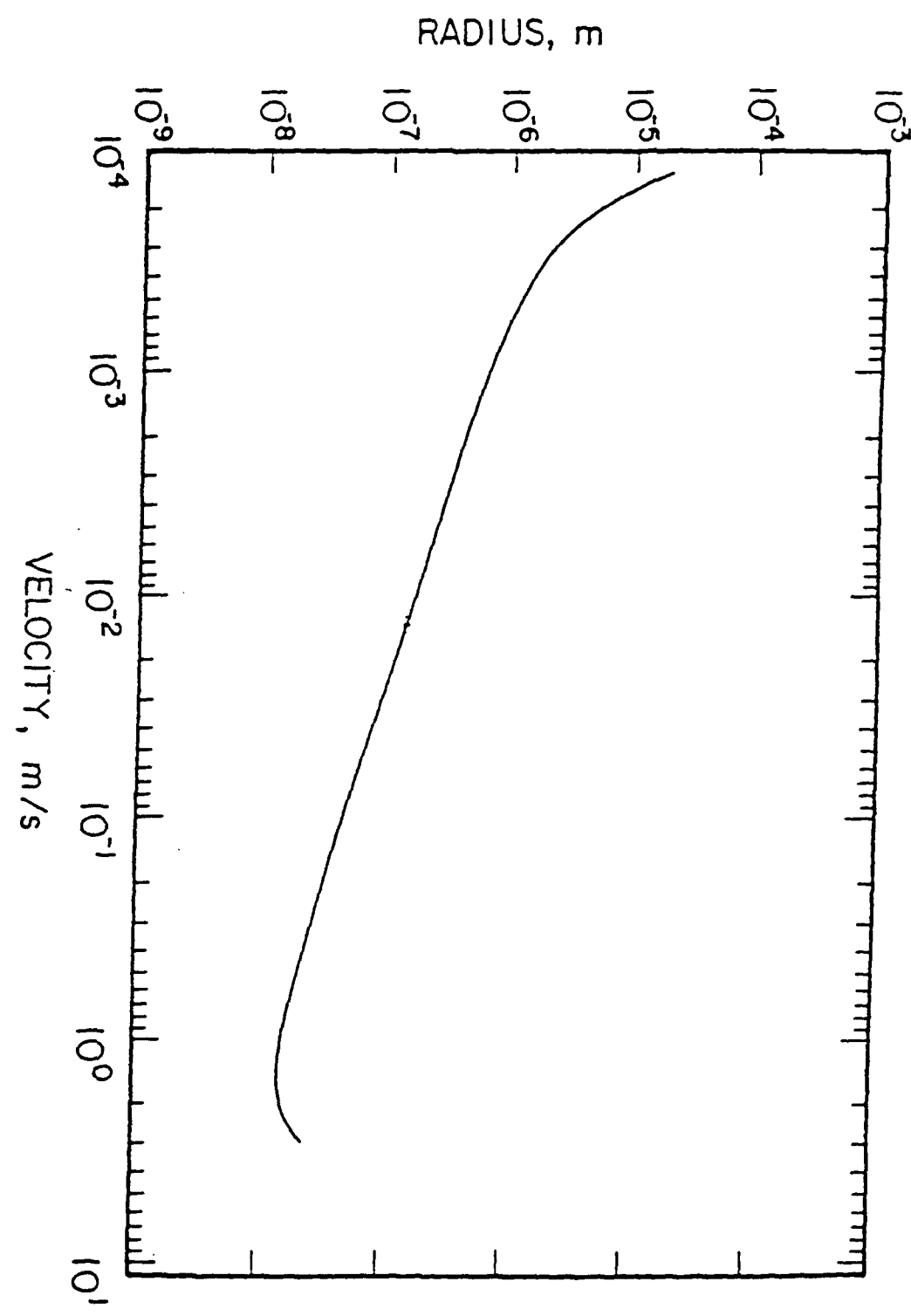


Figure 2. Theoretical variation of the dendrite tip radius with interface velocity for non-faceted growth of alumina.

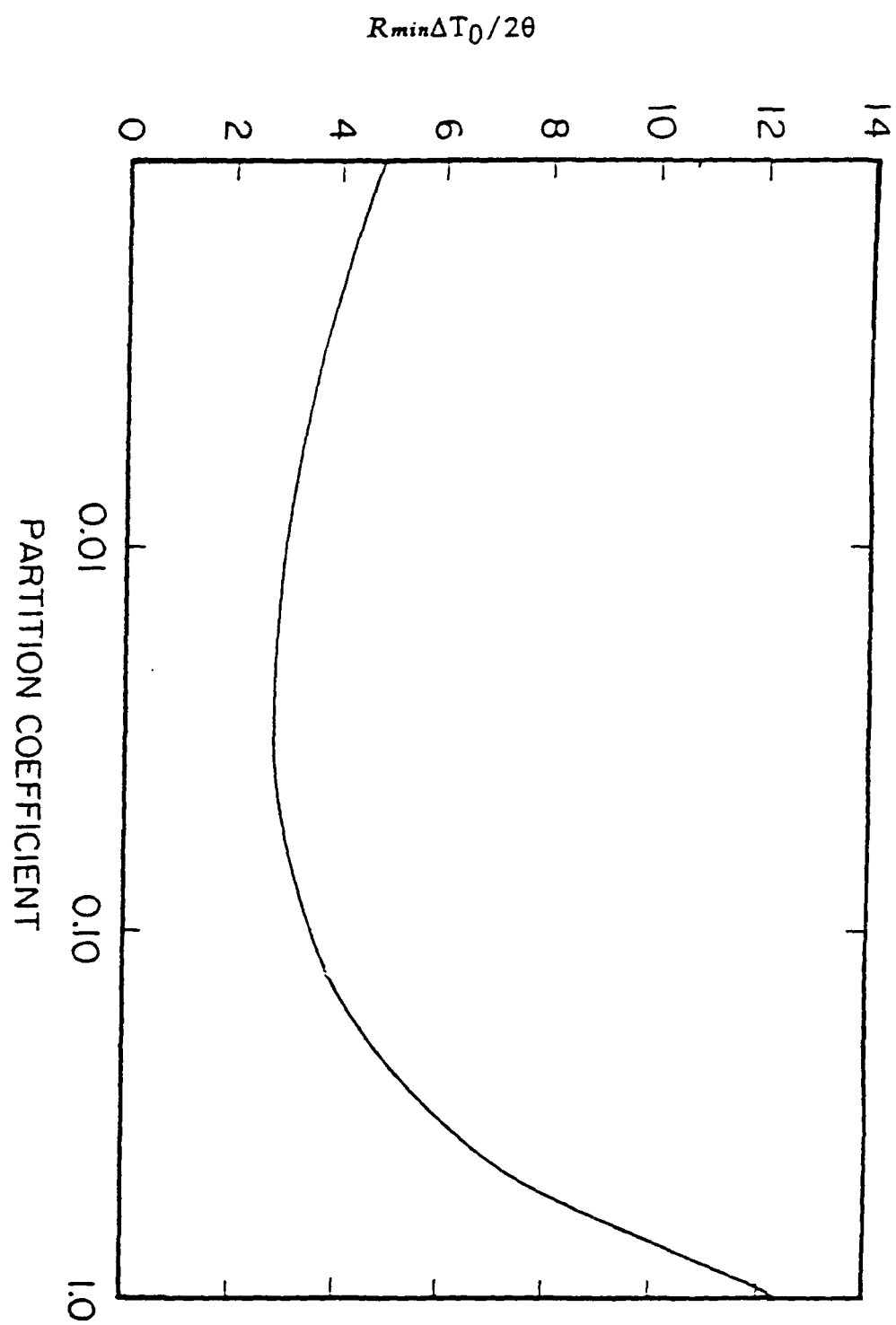


Figure 3. The variation in the minimum dimensionless radius $R_{min}\Delta T_0/2\theta$ with partition coefficient for directional (constrained) growth.

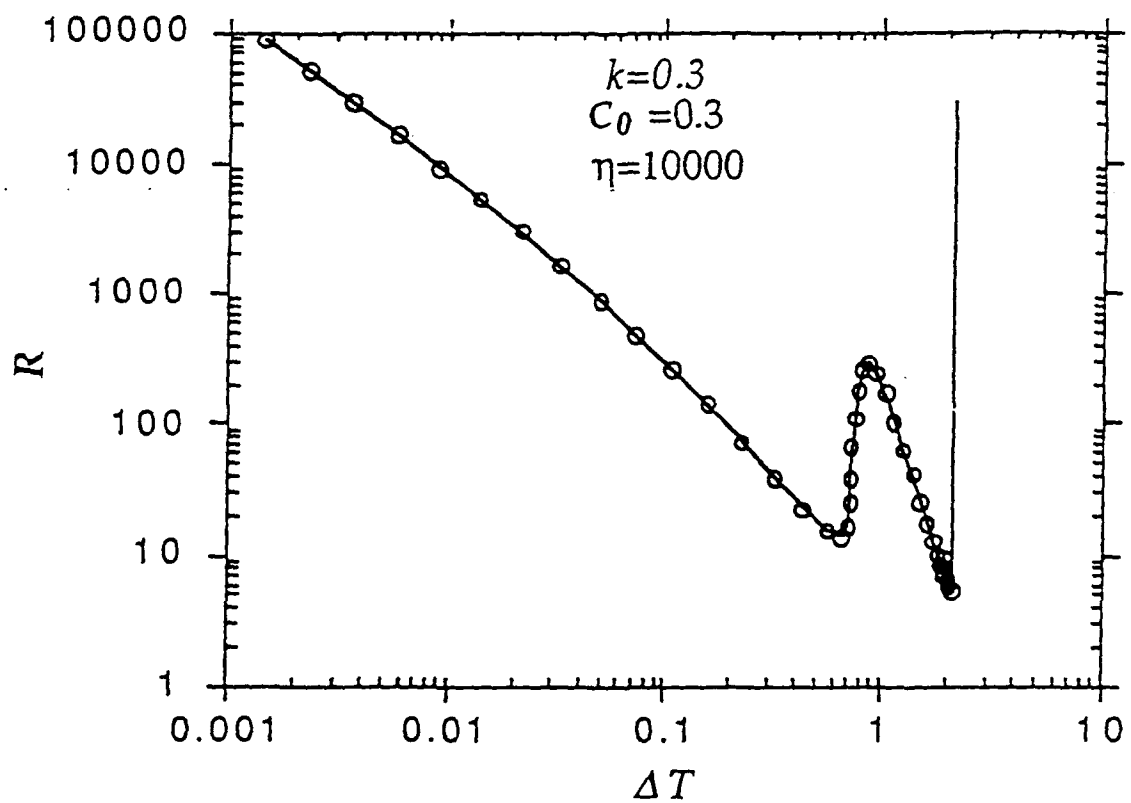


Figure 4. The variation in the dimensionless radius R with dimensionless bath undercooling (unconstrained growth).

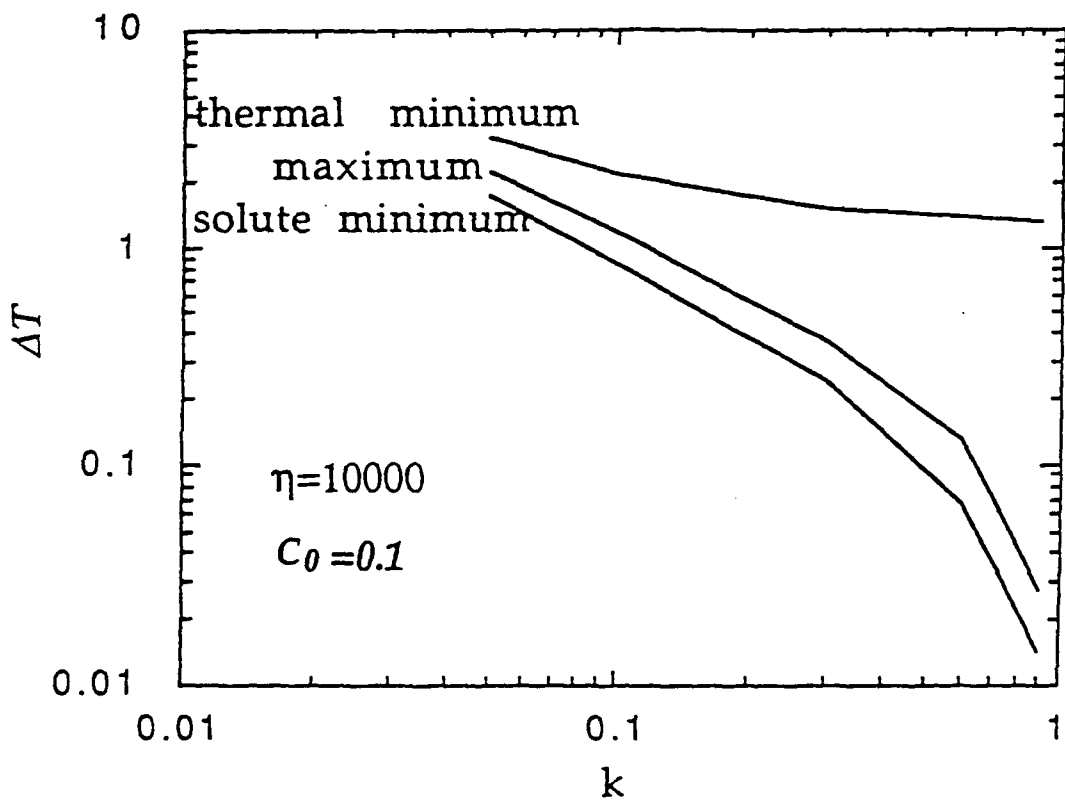


Figure 5. The effect of the equilibrium partition function on the dimensionless undercooling at the minimum and intermediate maximum radii from the solute and thermal effects.

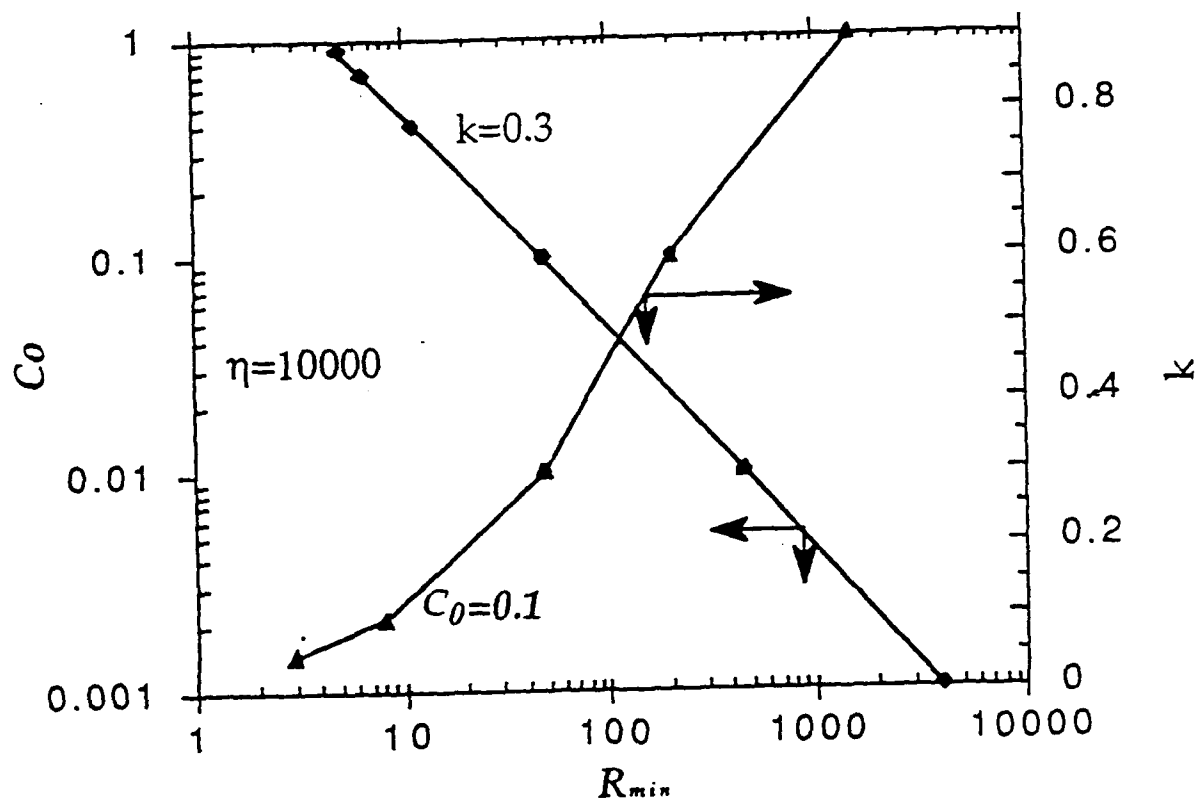


Figure 6. The variation of the minimum solutal radius with k (partition coefficient) and C_0 (dimensionless initial concentration).

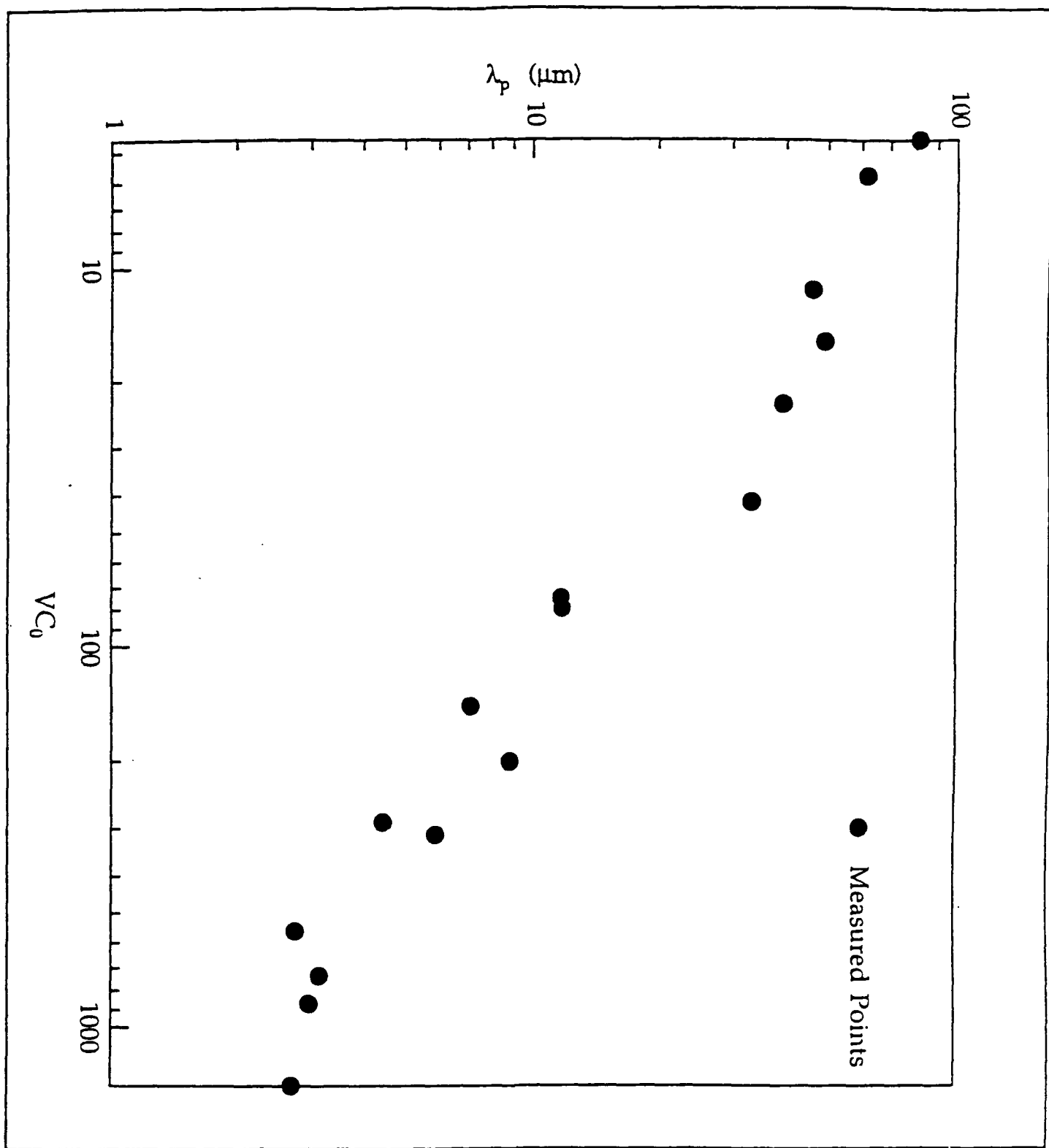


Figure 7. The scaling of λ_p with VC_0 . λ_p is the distance between the tip and the first side branch. V and C_0 are the velocity of the dendrite tip and the bulk composition, respectively.

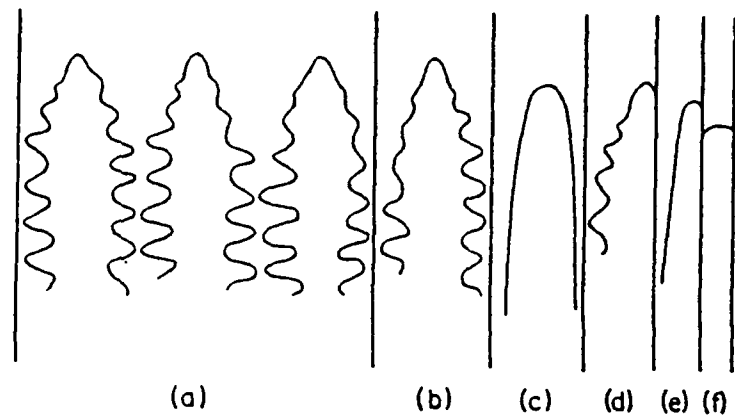


Figure 8. A schematic illustration which summarizes experimental observations on the effect of channel width on microstructural development for experimental conditions which would give a stable dendritic array inside a channel of very large width.

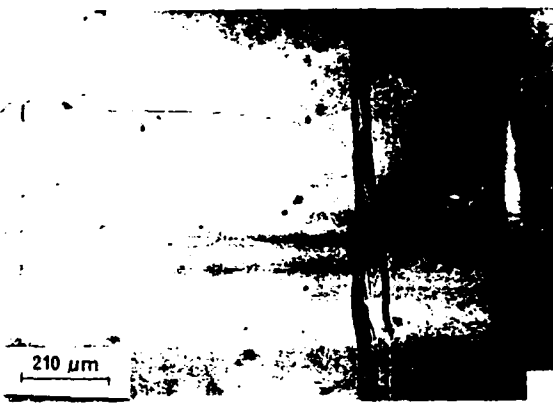


Figure 9. The surface tension effect at the channel wall giving rise to instability which is similar to the instability at the grain boundary in a channel of large width. Succinonitrile - 2.5 wt% acetone, $V = 2.0 \mu\text{m}/\text{s}$ and $G = 2.36 \text{ K/mm}$.

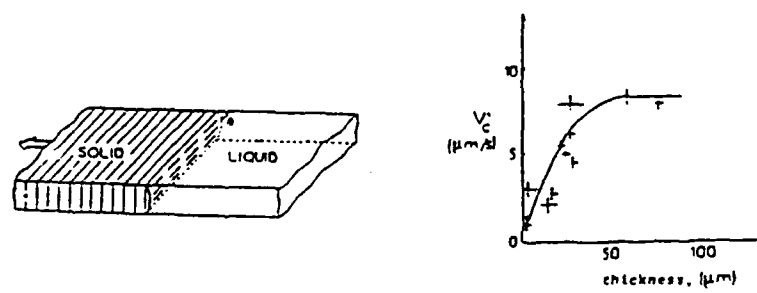


Figure 10. The effect of contact angle on the instability of a planar interface. The experimental results of the variation in critical velocity for planar interface instability as a function of channel width in impure carbon tetrabromide.⁽¹⁷⁾

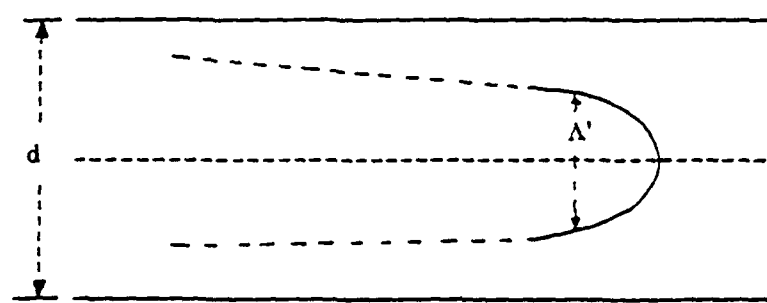


Figure 11. A schematic illustration of a cellular interface which defines the Saffman - Taylor width of the cell.

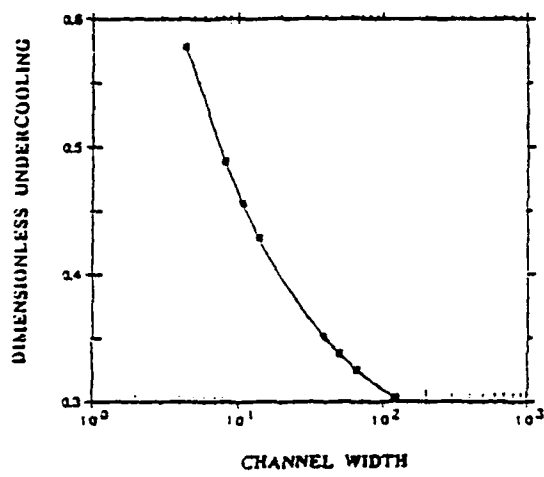


Figure 12. Theoretical prediction of the change in dimensionless undercooling at the tip with channel width.

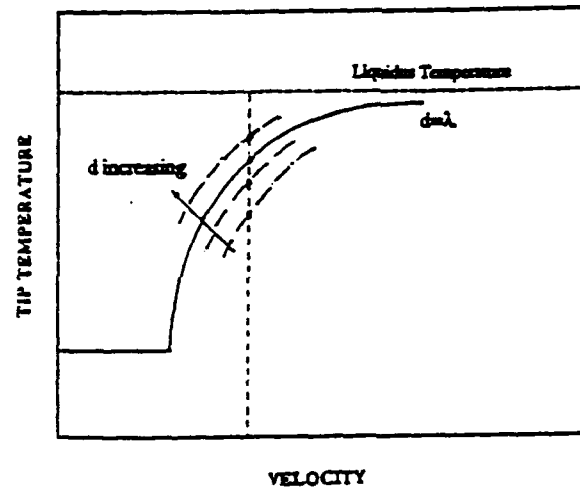


Figure 13. A schematic illustration of the variation in cell tip temperature with velocity for channels of different widths.

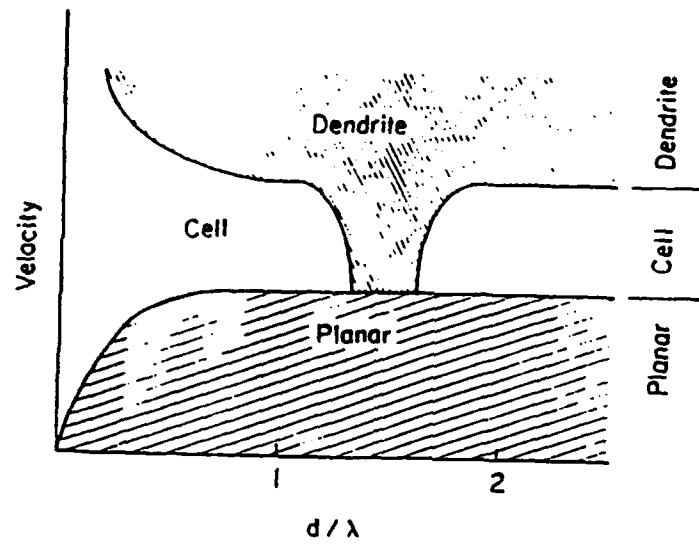


Figure 14. A schematic microstructure map showing regions of planar, cellular and dendritic microstructures in velocity versus relative channel width.

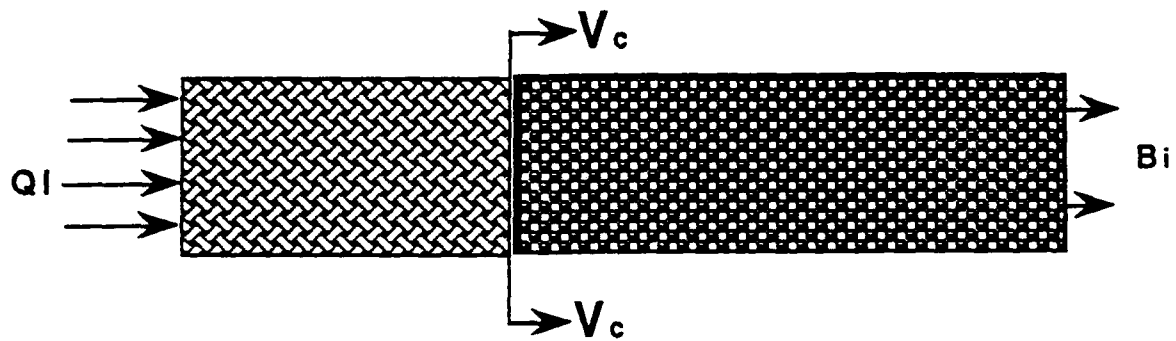


Figure 15. A schematic of the combustion and solidification problem. Q_I is the incident heat flux, Bi is the Biot number at the end of the sample which is cooled and V_c is the combustion front velocity. Behind the combustion front is the reacted part of the sample and in front is the unreacted part.

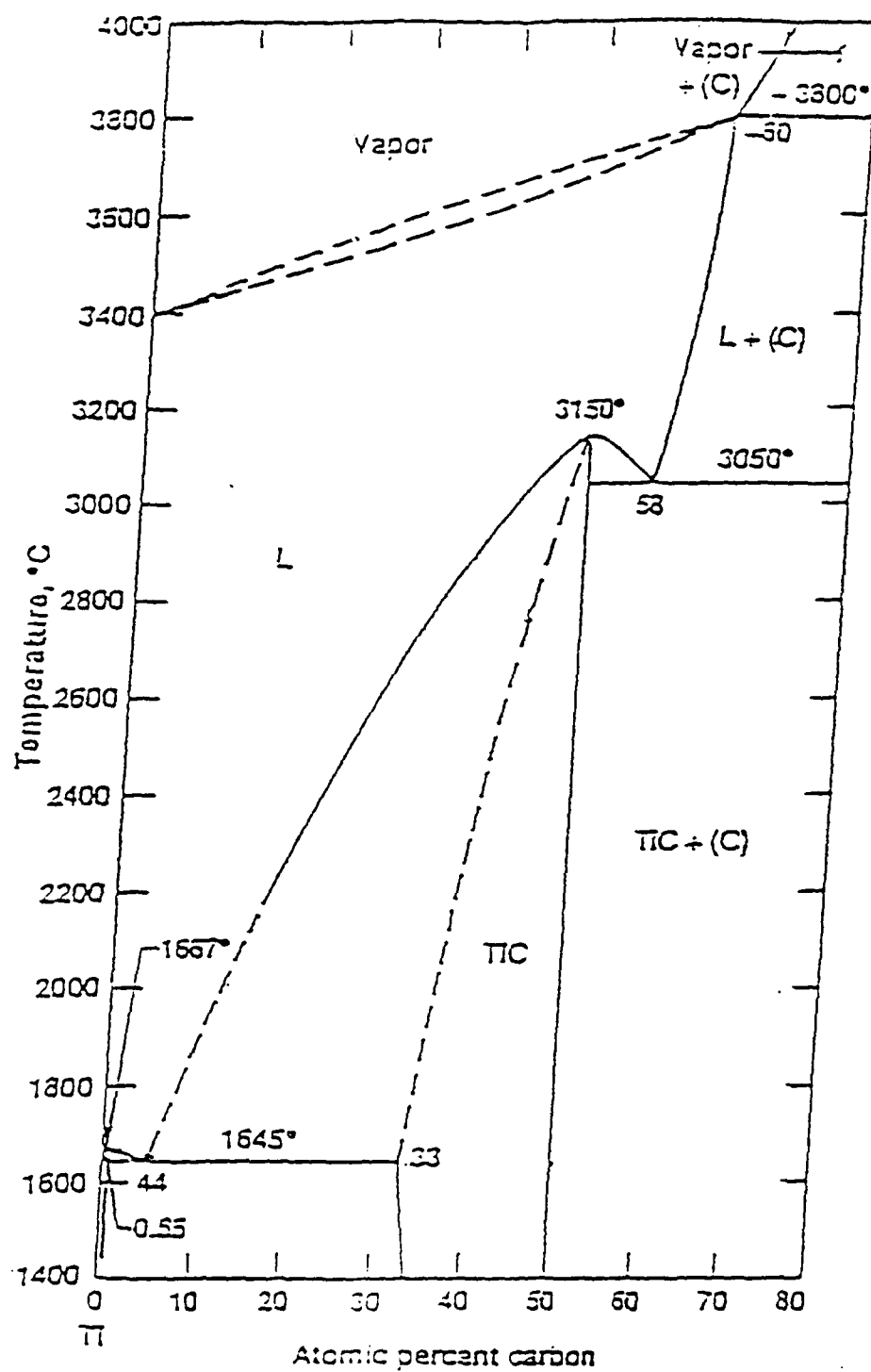


Figure 16. The relevant part of the phase diagram from the Ti-C system.⁽⁴⁴⁾

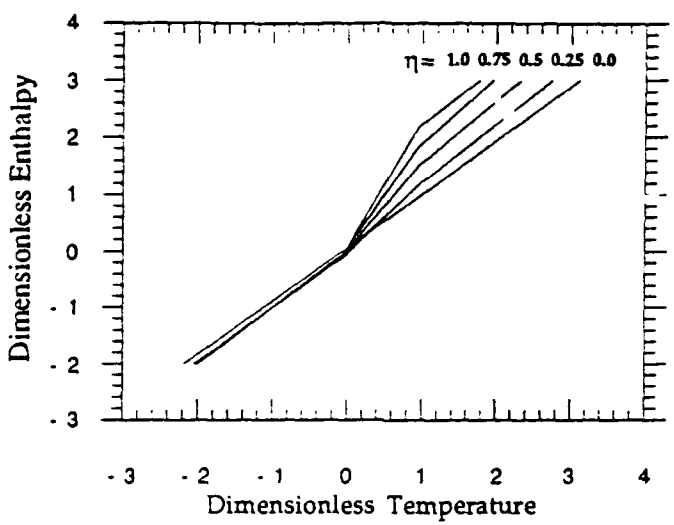


Figure 17. The plot of the dimensional enthalpy and dimensional temperature during combustion and solidification.

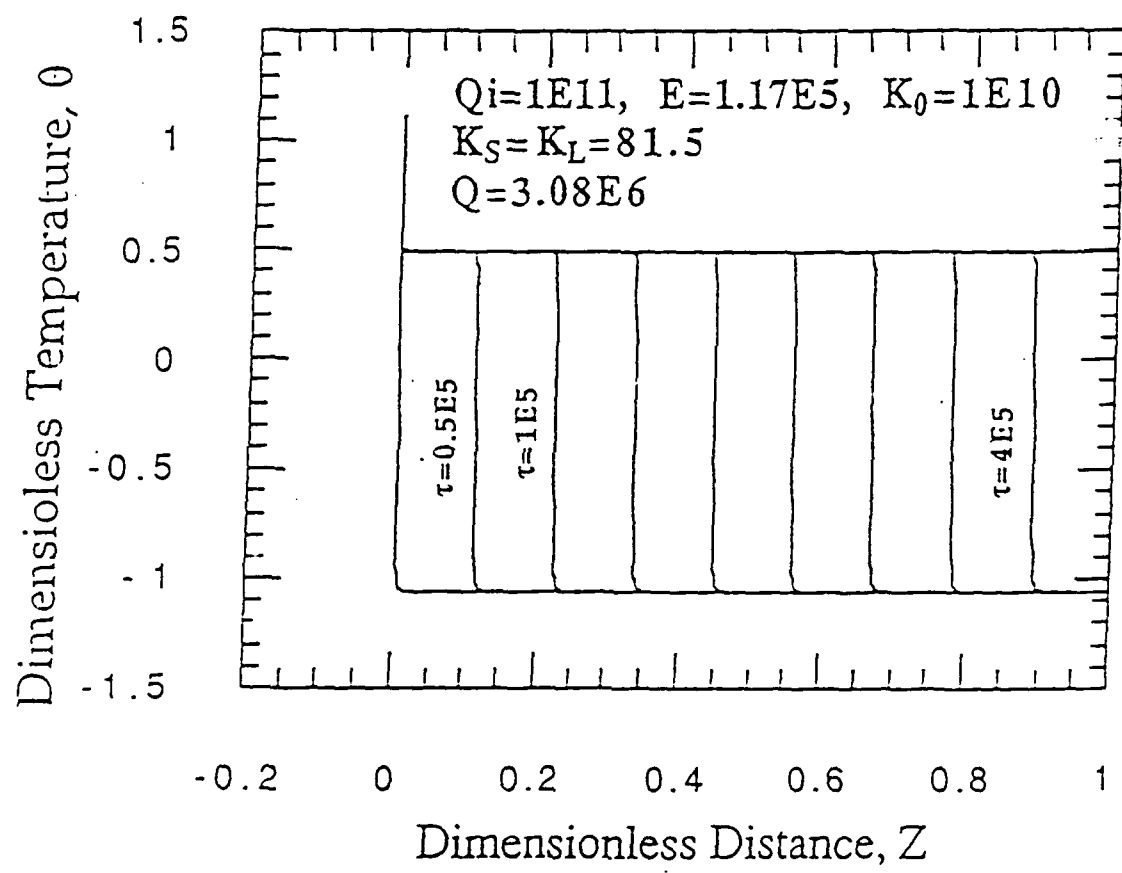


Figure 18. (a) Maximum temperature profiles during combustion for material conditions given in the figure.

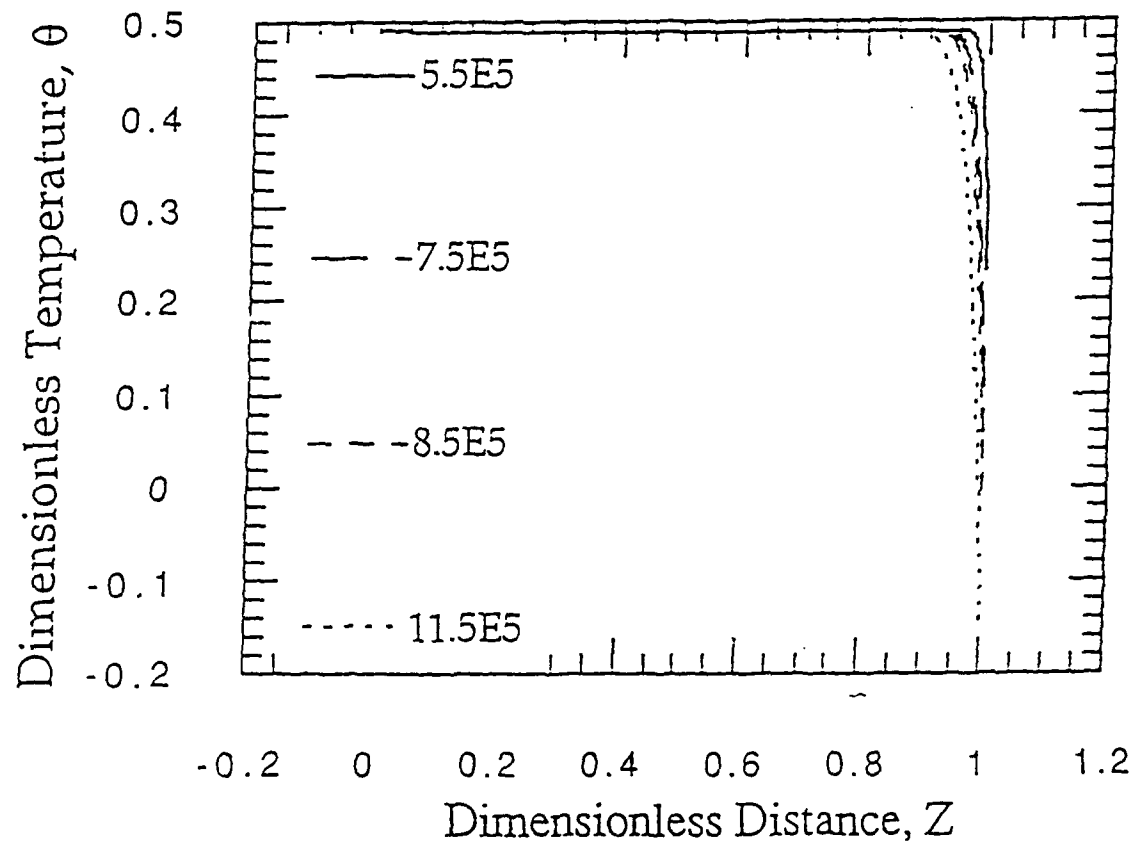


Figure 18. (b) Cooling profiles after the combustion process shown in figure 18a. Note that although the cooling boundary condition was incorporated during the combustion process, cooling only began after complete combustion.

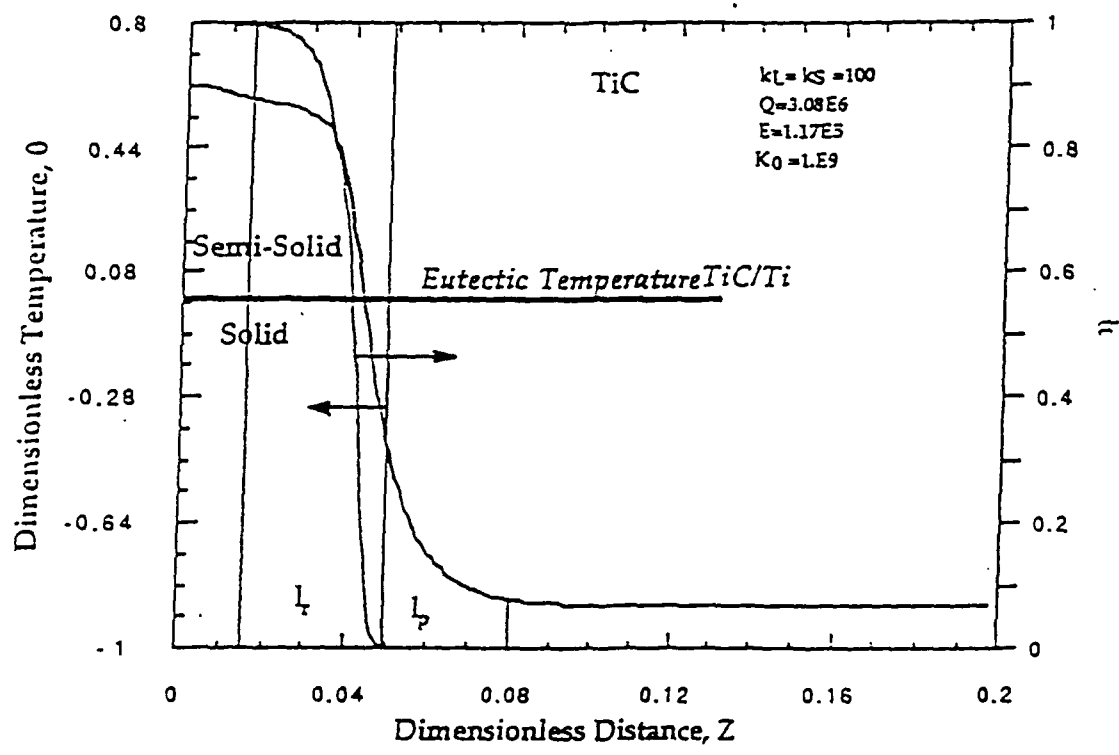


Figure 19. Typical thermal and reaction profiles during combustion (low K_0).

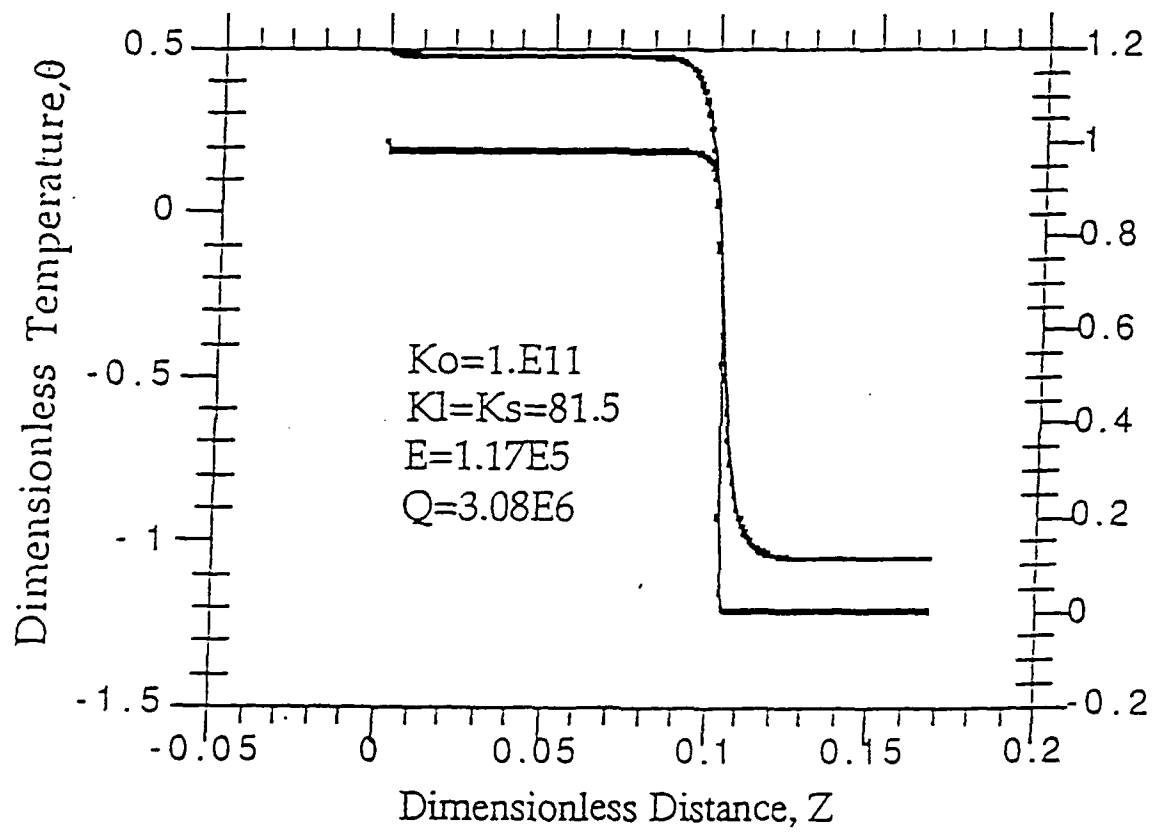


Figure 20. Typical thermal and reaction profiles during combustion (high K_o).

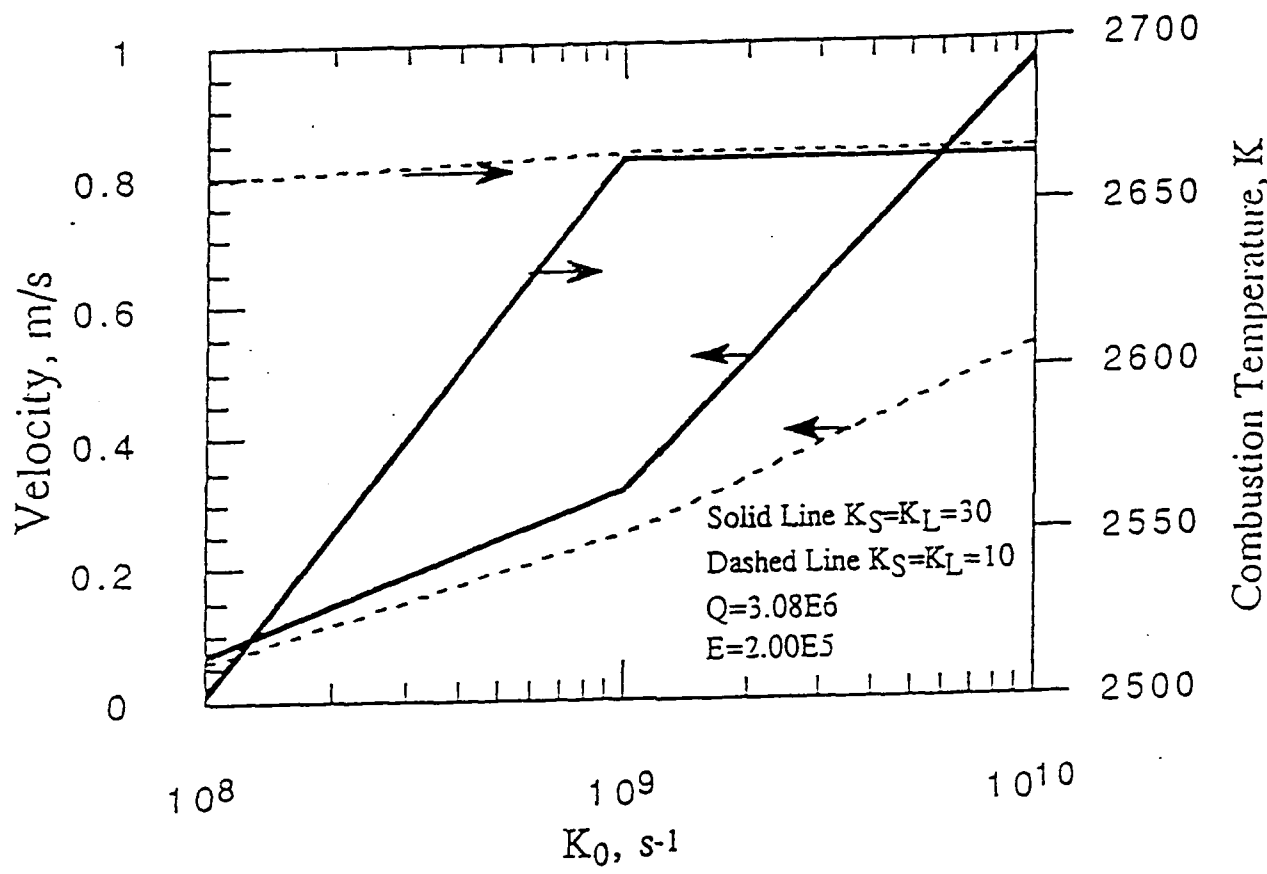


Figure 21. The variation of the combustion velocity V and combustion temperature T_c with K_0 .

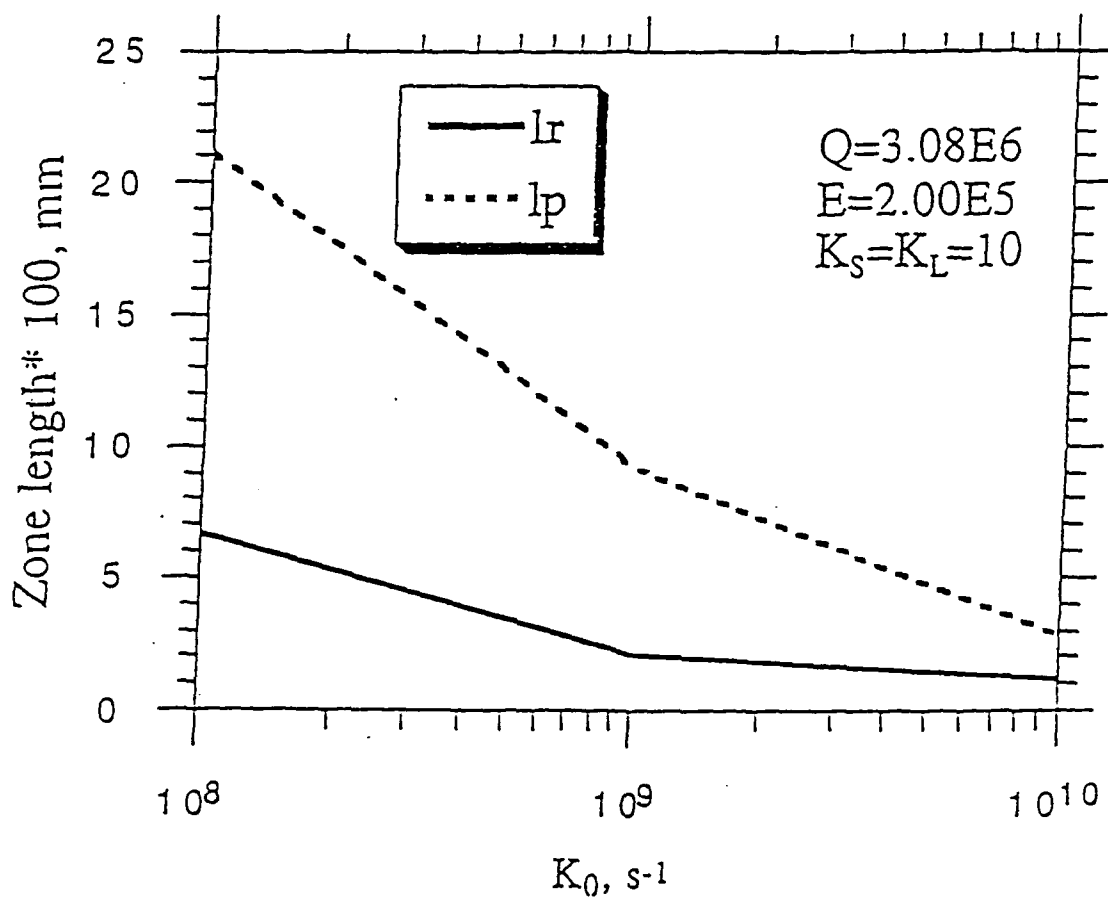


Figure 22. The variation of combustion zone l_r and heat affected zone l_p with K_0 .

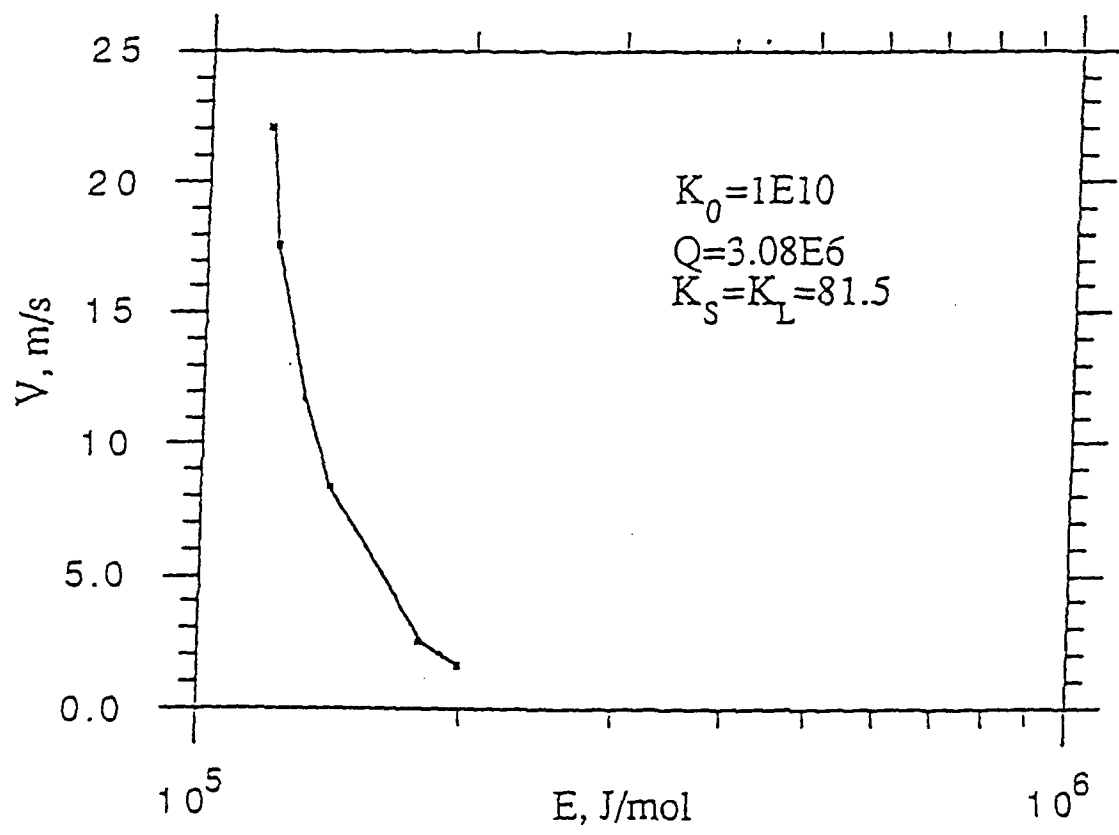


Figure 23. The variation of combustion velocity V and combustion temperature T_c with the activation energy E .

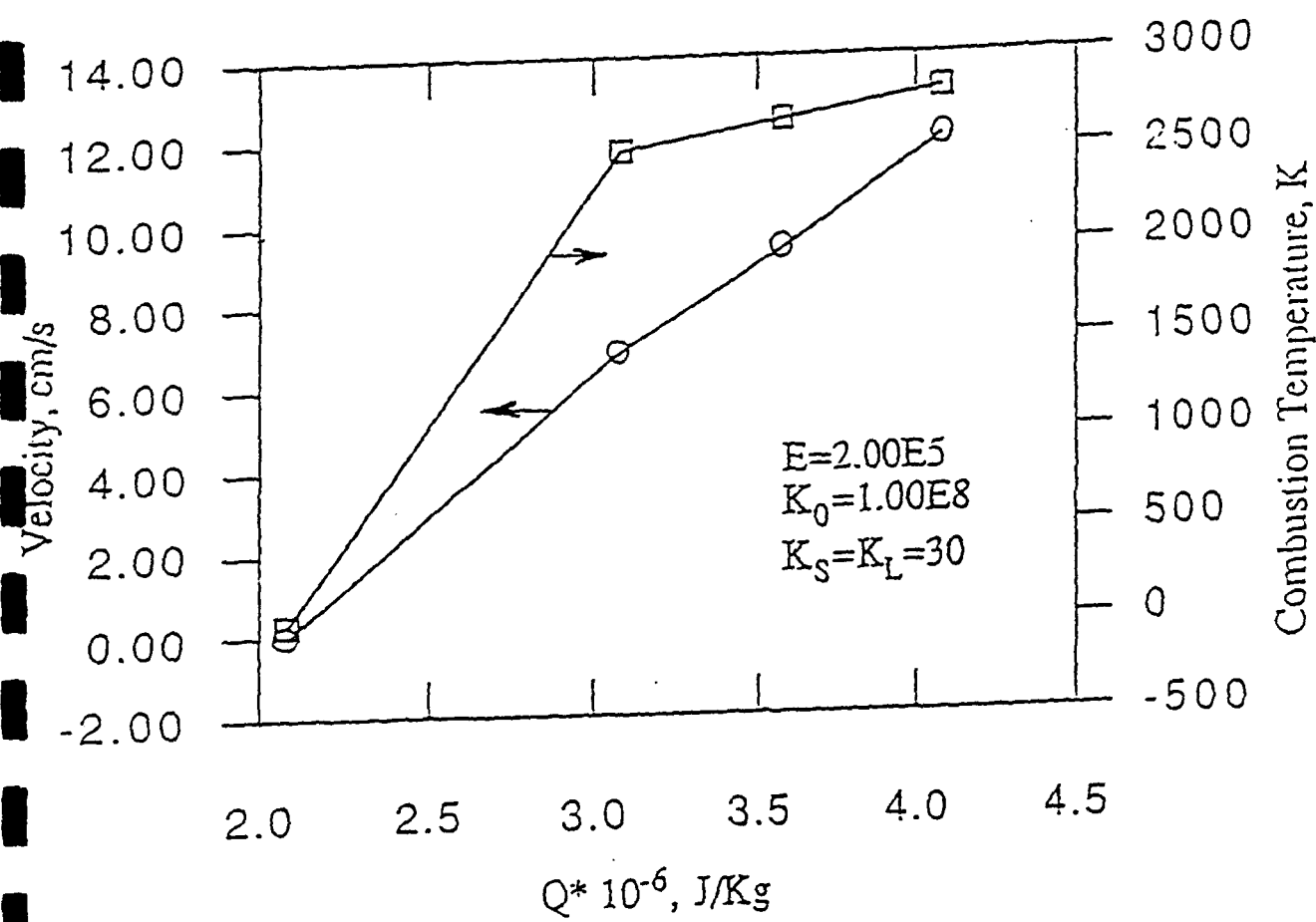


Figure 24. The variation of combustion velocity V and combustion temperature T_c with the reaction enthalpy Q .

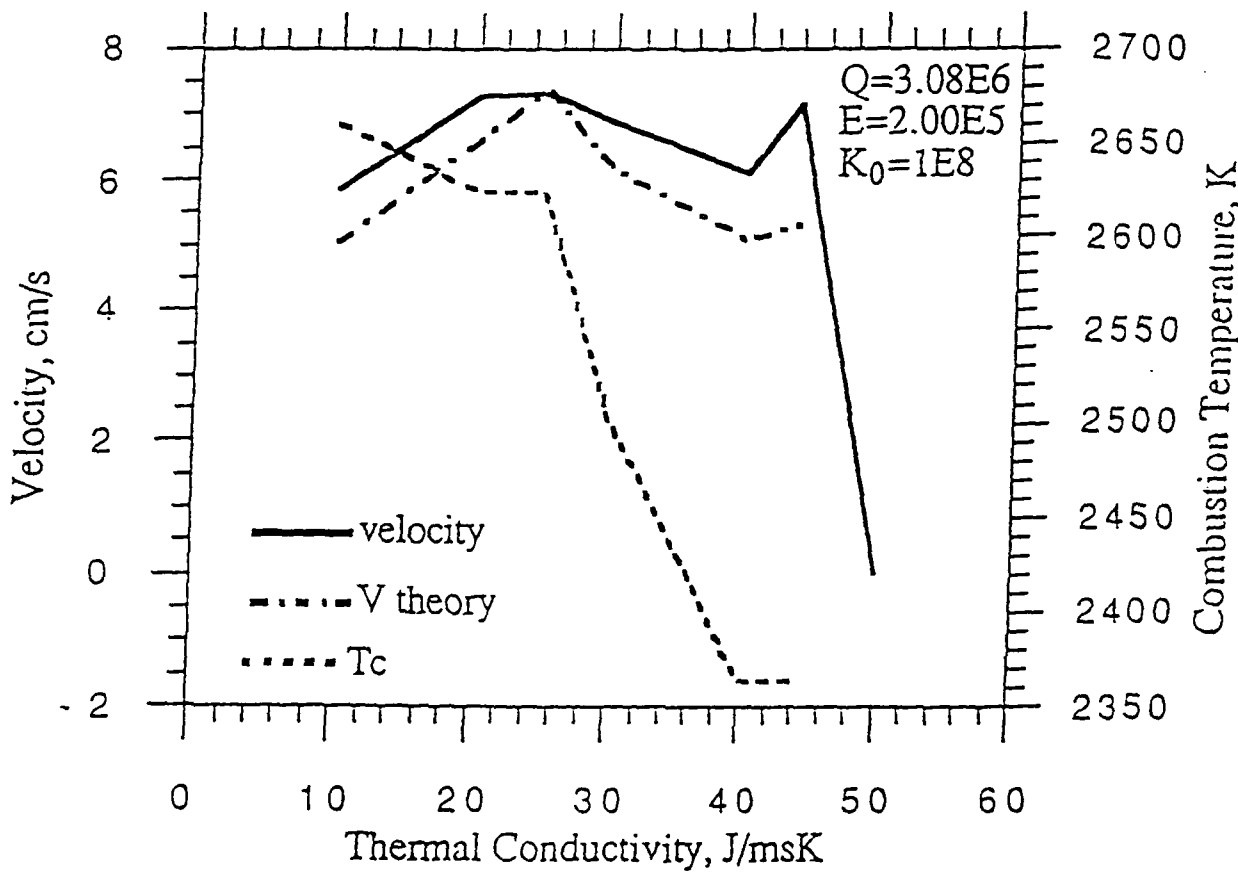


Figure 25. The variation of combustion velocity V and combustion temperature T_c with the thermal conductivity (low K_0).

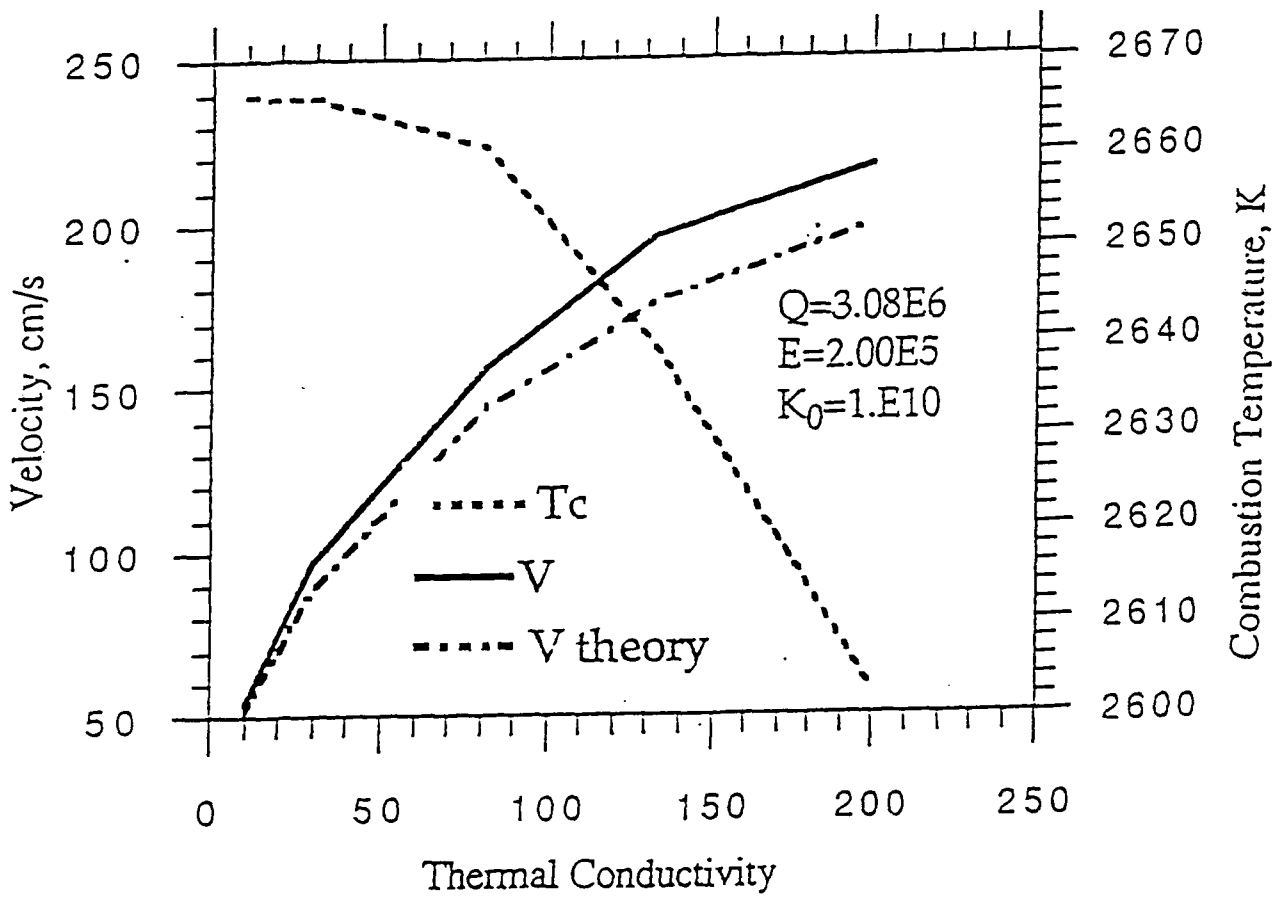


Figure 26. The variation of combustion velocity V and combustion temperature T_c with the thermal conductivity (high K_0).

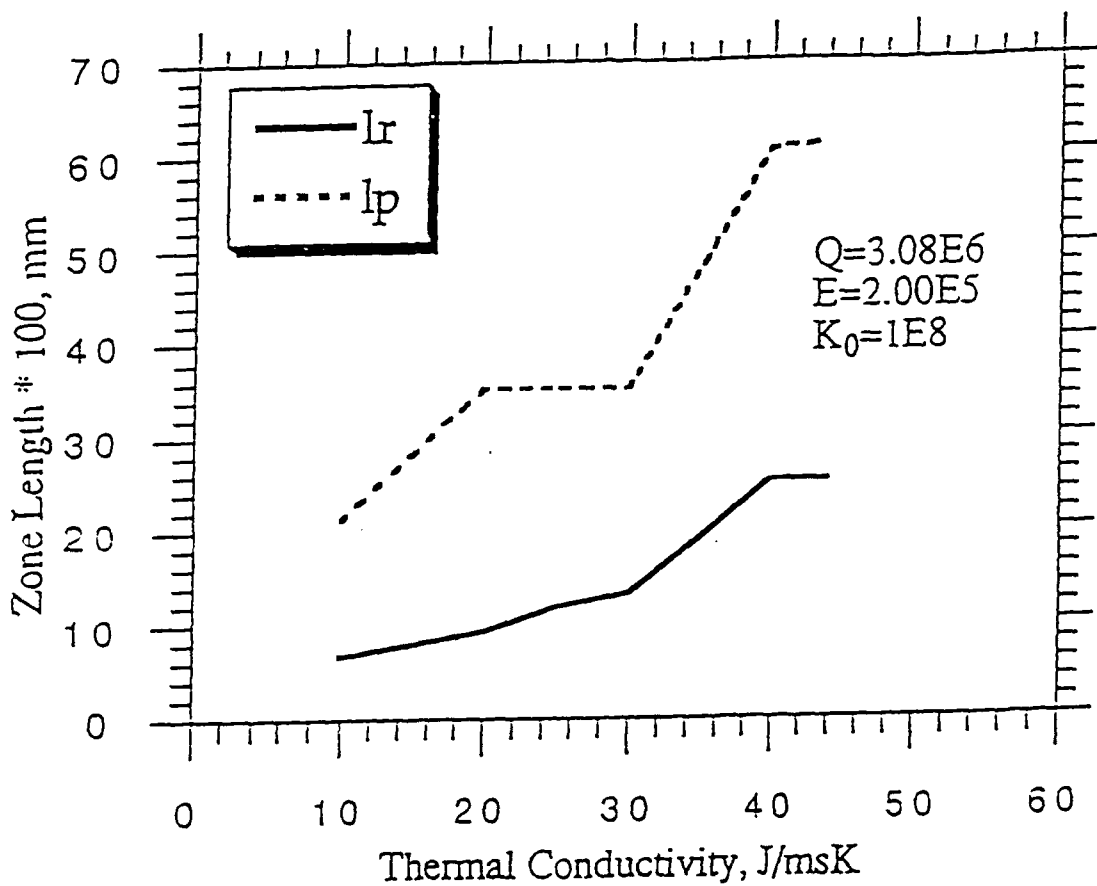


Figure 27. The variation of the combustion zone l_r and the heat affected zone l_p with the thermal conductivity (low K_0).

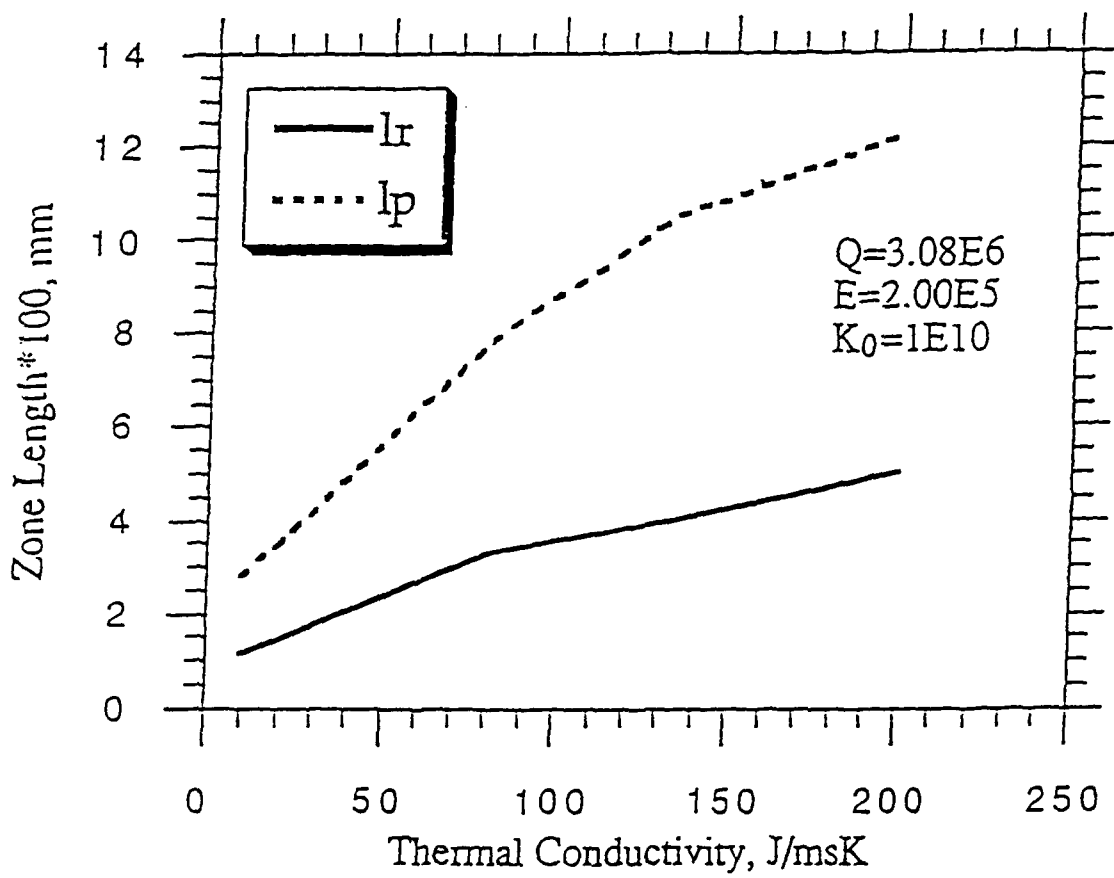


Figure 28. The variation of the combustion zone l_r and the heat affected zone l_p with the thermal conductivity (high K_0).

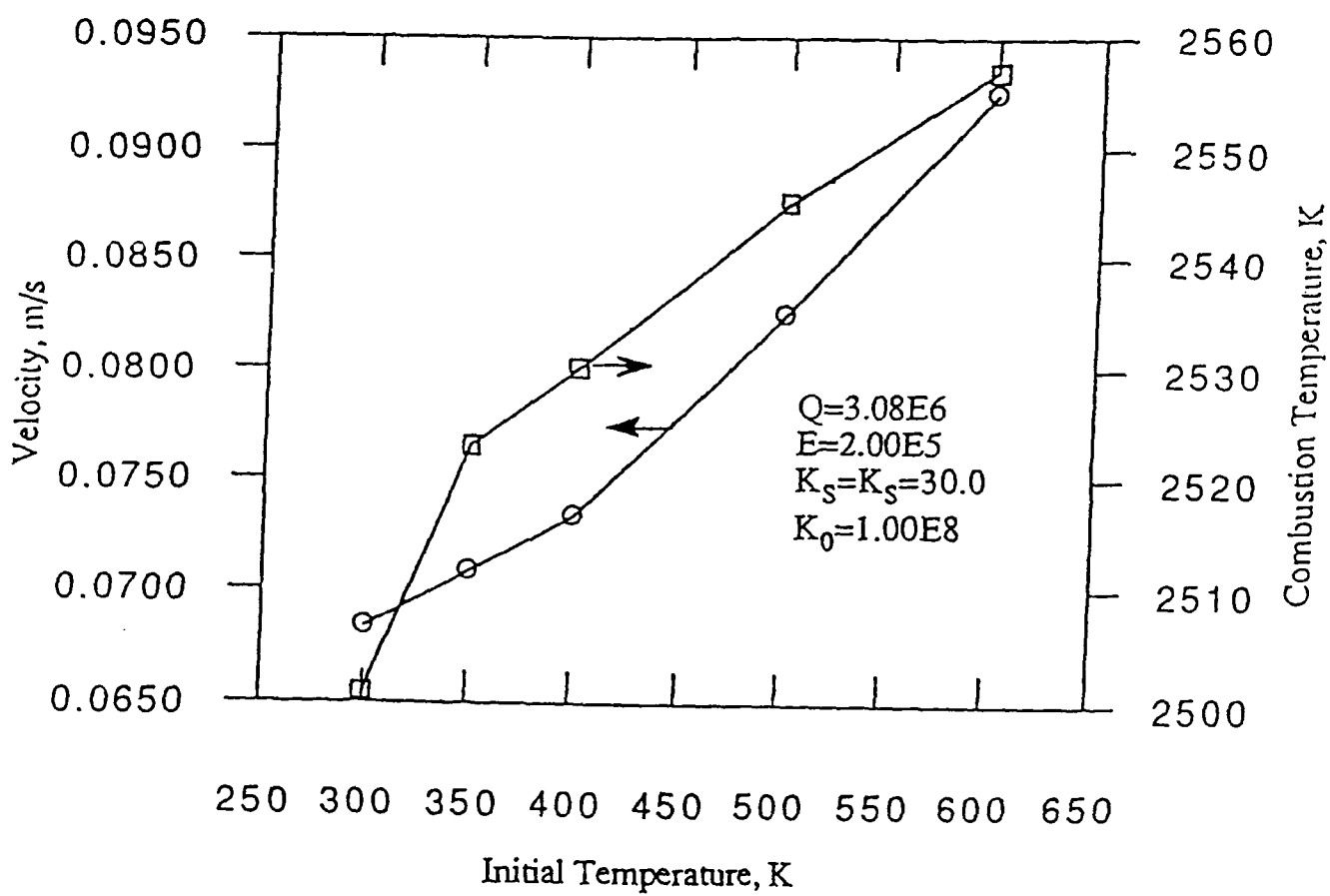


Figure 29. The variation of combustion velocity V and combustion temperature T_c with the initial substrate temperature, T_0 .

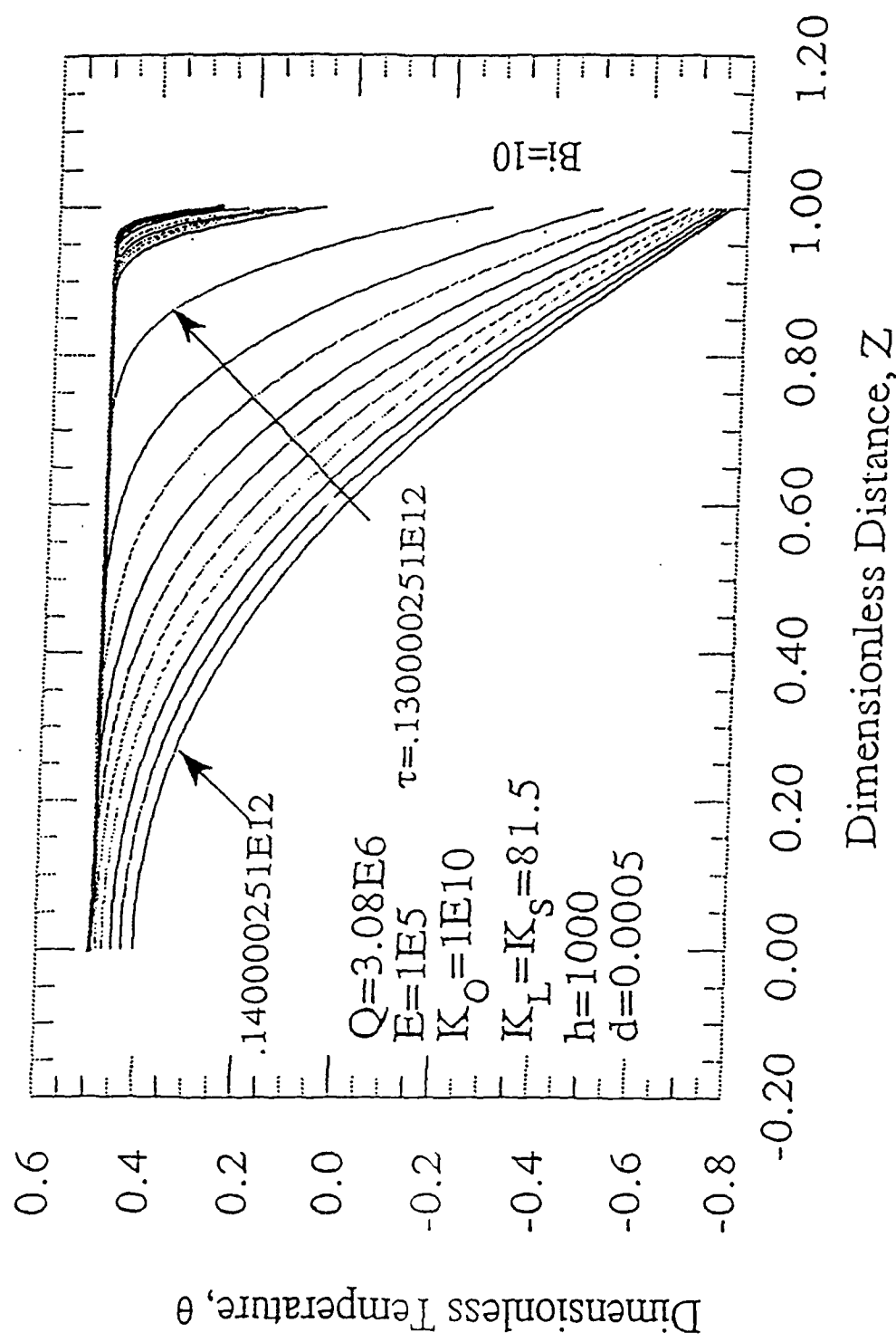


Figure 30. Cooling of a sample heated by a self propagating combustion front
 (the diameter of the sample $d = 0.0005\text{m}$, the side surface heat
 transfer coefficient $h = 1000 \text{ w/m}^2\text{K}$).

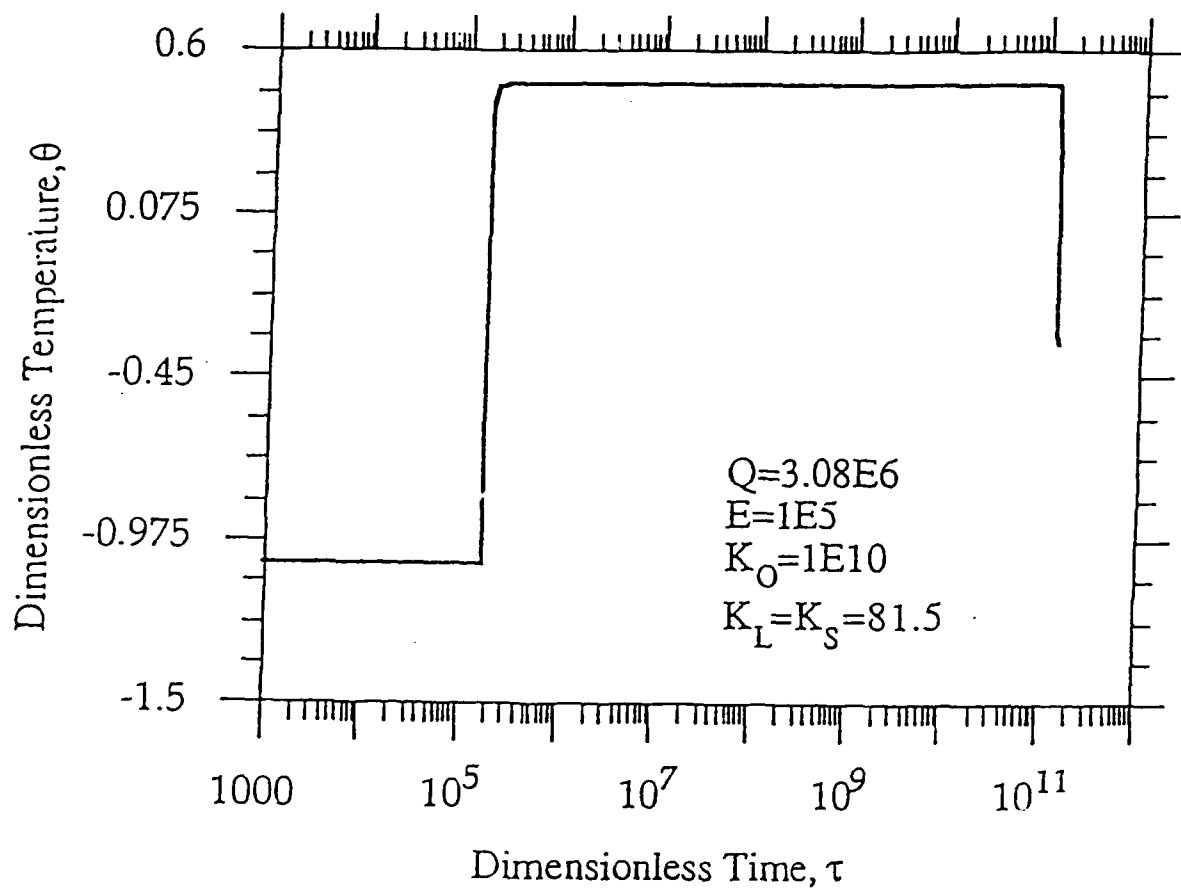
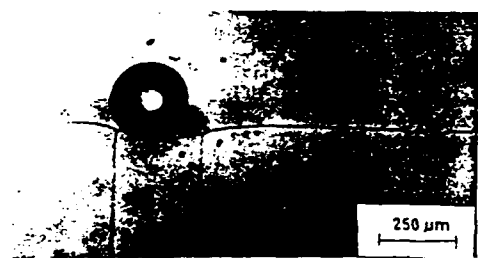
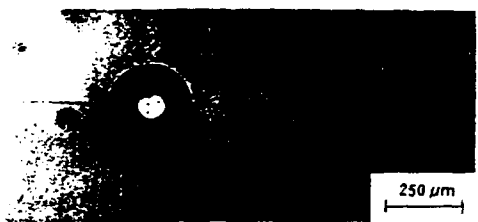


Figure 31. Temperature-Time profile at a dimensionless distance of $Z = 0.8$ (the diameter of the sample $d = 0.0005\text{m}$, the side surface heat transfer coefficient $h = 1000 \text{ w/m}^2 \text{ K}$).



(a)



(b)

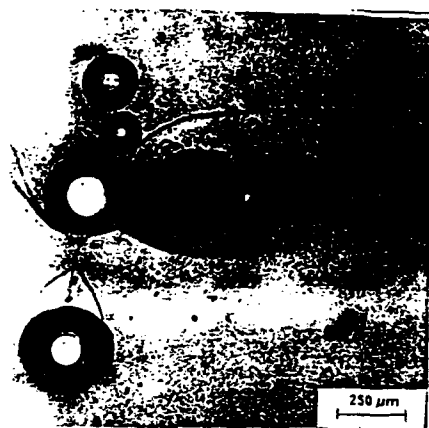


(c)

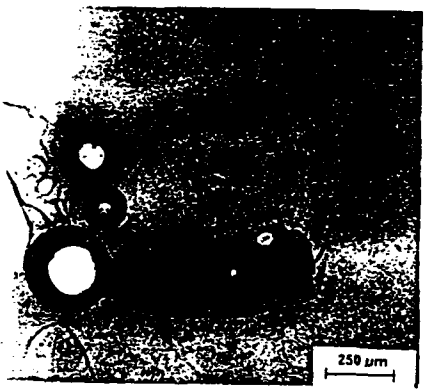


(d)

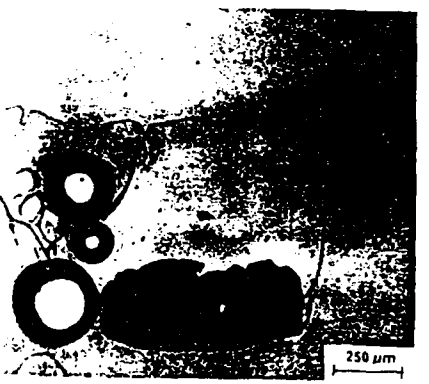
Figure 32. The incorporation of a gas bubble into a directionally solidifying planar interface. Bulk composition of the alloy 99.5wt% SCN + water. V (velocity of interface) = $0.8 \mu\text{m/s}$ and G (temperature gradient) = 5.5 K/mm . (a)-(d) increasing time.



(a)



(b)



(c)

Figure 33. The incorporation of a system of bubbles and a finite wall into a 5wt% SCN. $V = 0.8 \text{ m/s}$, $G = 5.5 \text{ K/mm}$. (a)-(c) increasing time.



(a)

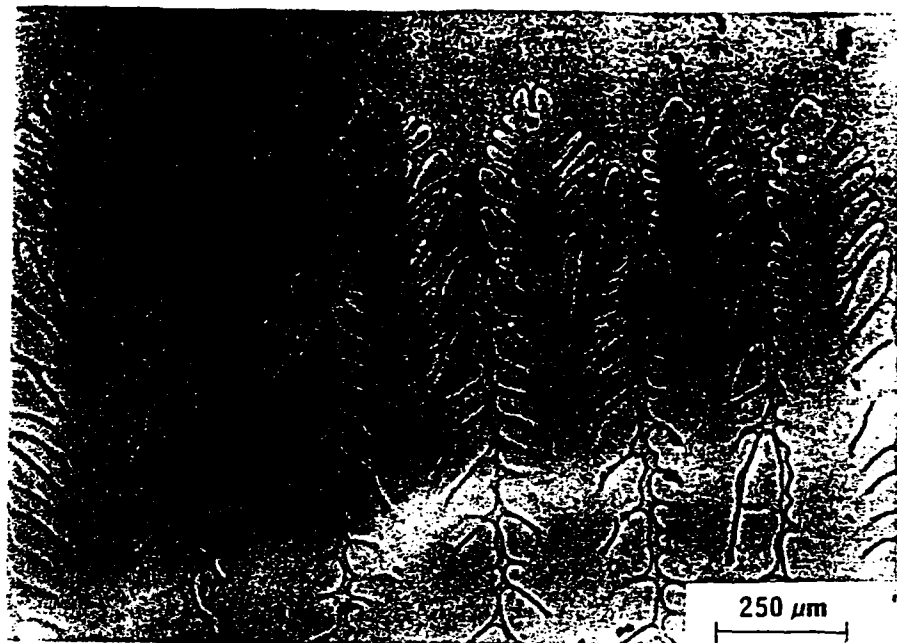


(b)

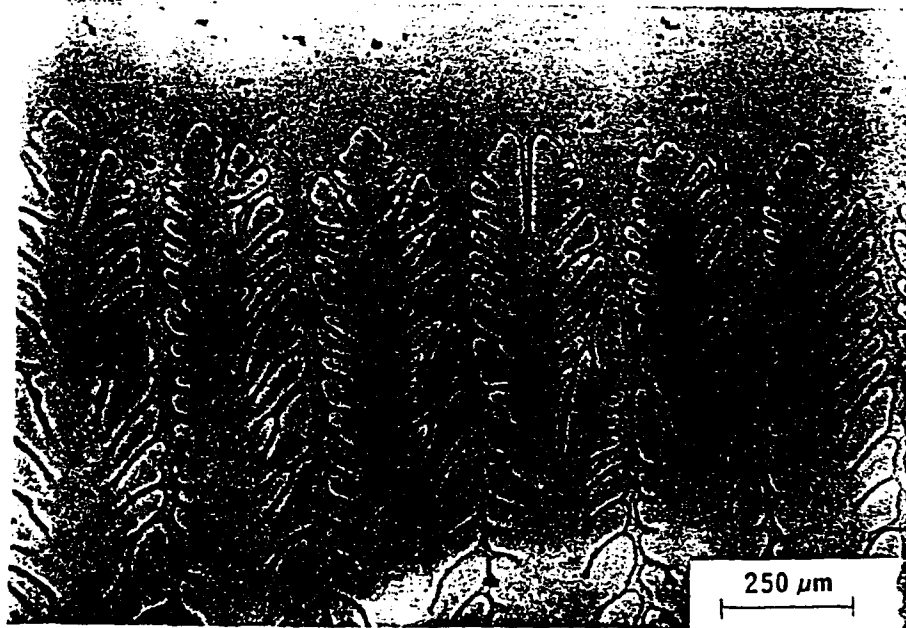


(c)

Figure 34. Trapping of low volume fraction small particles by a dendritic interface. $V = 10 \text{ mm/s}$, $G = 5.5 \text{ K/mm}$, $C = 99.5\text{wt\% SCN}$. (a) = 120s, (b) = 132s, (c) = 144s, (d) = 156s, (e) = 312s, (f) = 430s, (g) = 444s. Note that the deformed bubble which now forms the gas porosity begins to travel with a steady state velocity along with the root of the dendrite. Note also the Rayleigh instability in the bubble.



(a)

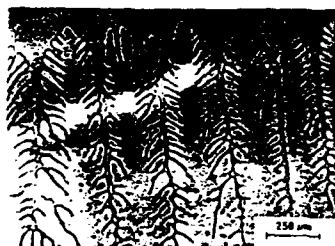


(b)

Figure 35. A magnified illustration of dendrite tip splitting by the particles in the experiment described in figure 34. Time: (a) = 252s, (b) = 266s.



(a)



(b)

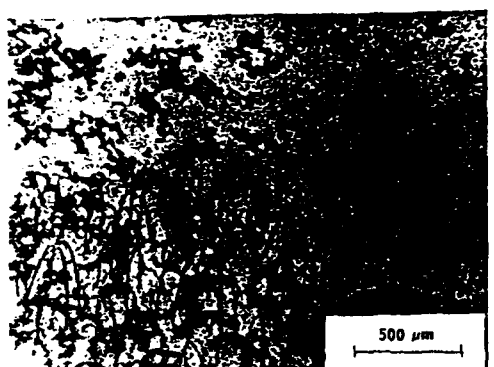


(c)



(d)

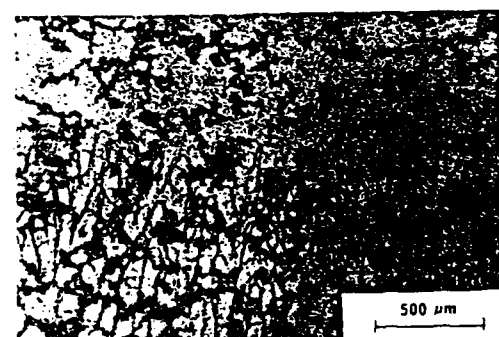
Figure 36. Continuation of the sequence of figure 34 and 35 to illustrate the incorporation of particles through a bubble. Note the deformation of the bubble in the interdendritic areas. (a)-(d) increasing time.



(a)



(b)



(c)

Figure 37. Trapping of high volume fraction nickel particles by an initially dendritic interface which changes morphology to a cellular pattern in the presence of the high volume fraction of particles. $G = 5.5 \text{ K/mm}$, $C = 99.5\text{wt\% SCN}$. (a) $V = 10 \text{ mm/s}$, (b) $V = 40 \text{ mm/s}$. Note that a dendritic pattern has appeared at higher velocity.

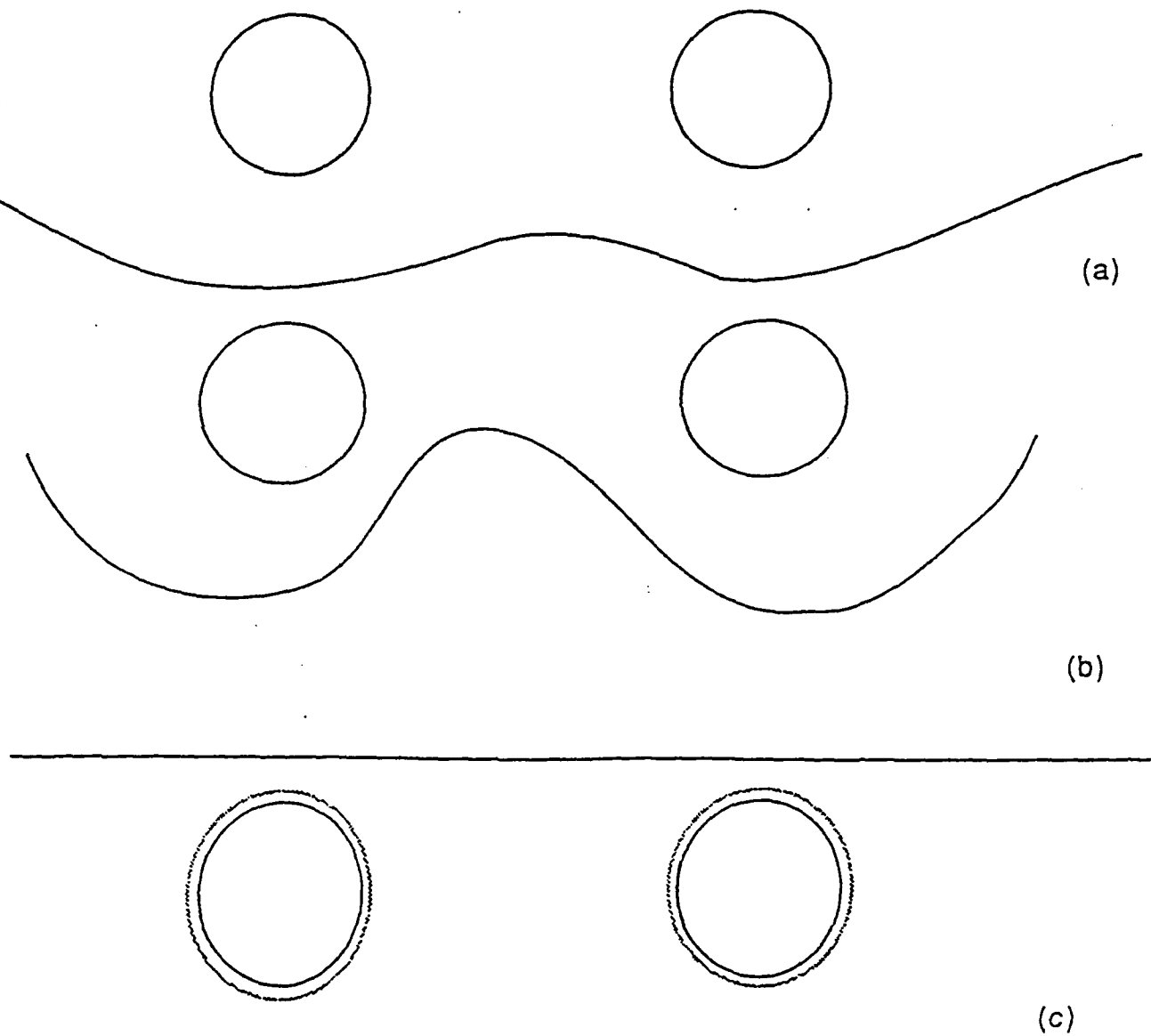


Figure 38. A schematic illustration of interface perturbation near a particle and the origin of bands around a trapped particle.

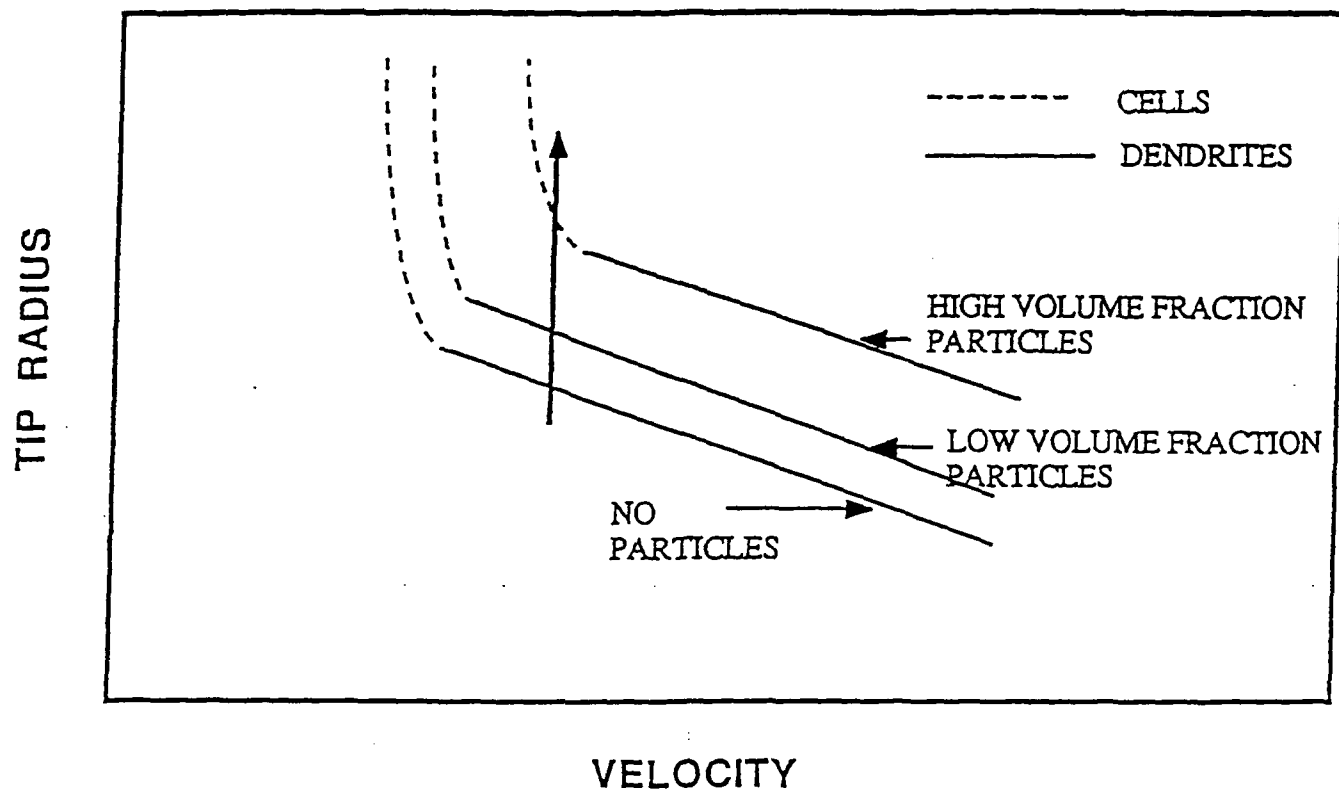


Figure 39. A schematic plot of tip radius of a cellular or dendritic interface with and without particles in the liquid ahead of the growing interface.

DISTANCE

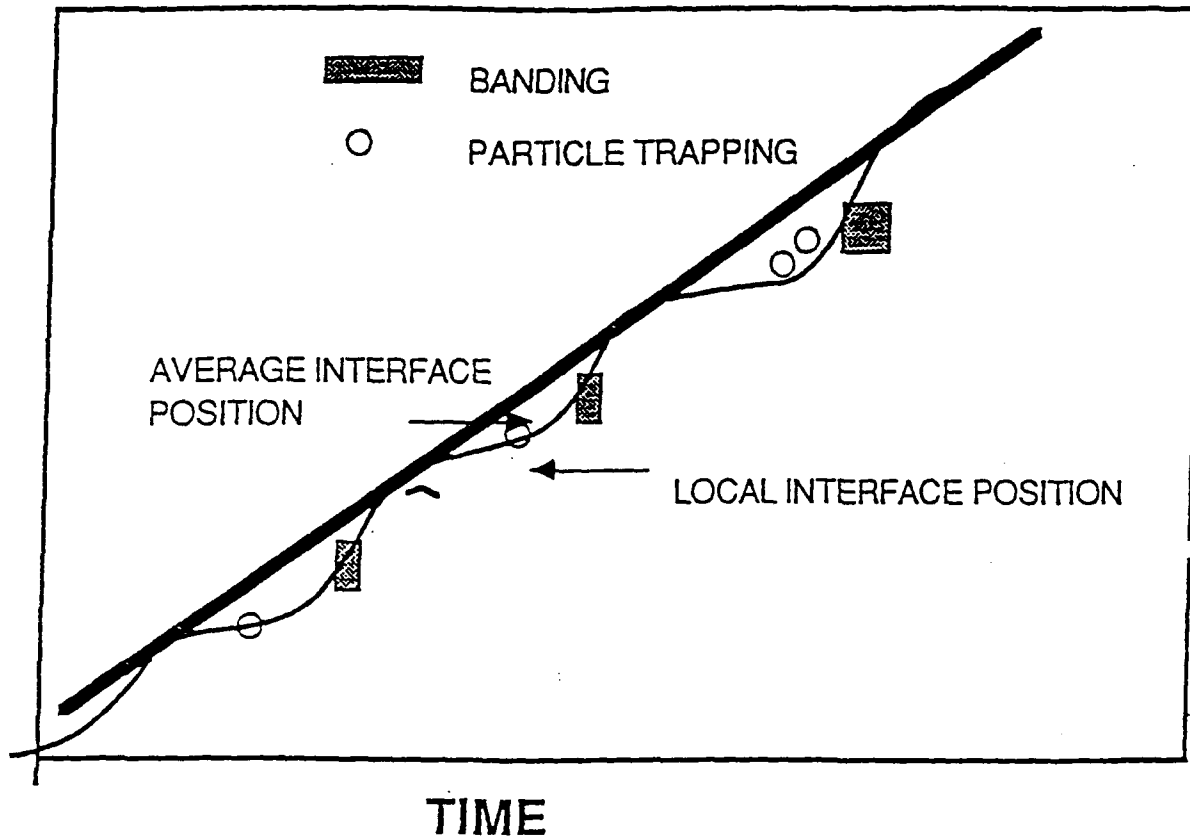


Figure 40. An illustration of the average and local interface position as a function of the distance solidified for a typical experiment involving the growth of a solidification interface in the presence of particles. The slope of the curve will give the average and local interface velocities.

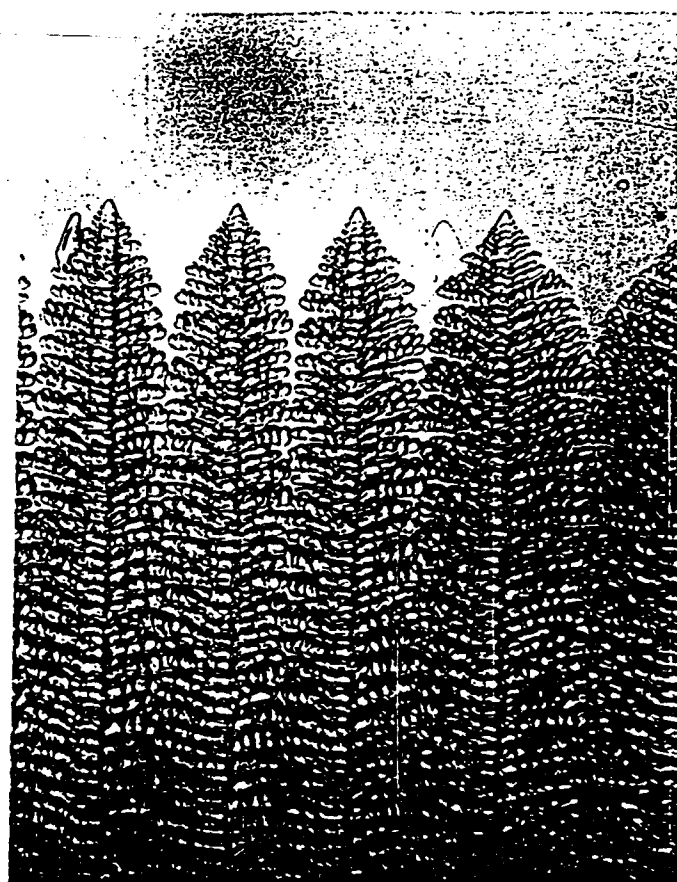


Figure 41. A typical solidification pattern in a SCN-4% acetone system illustrating the rapid growth of secondary dendrites not far behind the primary dendrite tip.

Mechanisms of Trapping of Particles by Dendrites

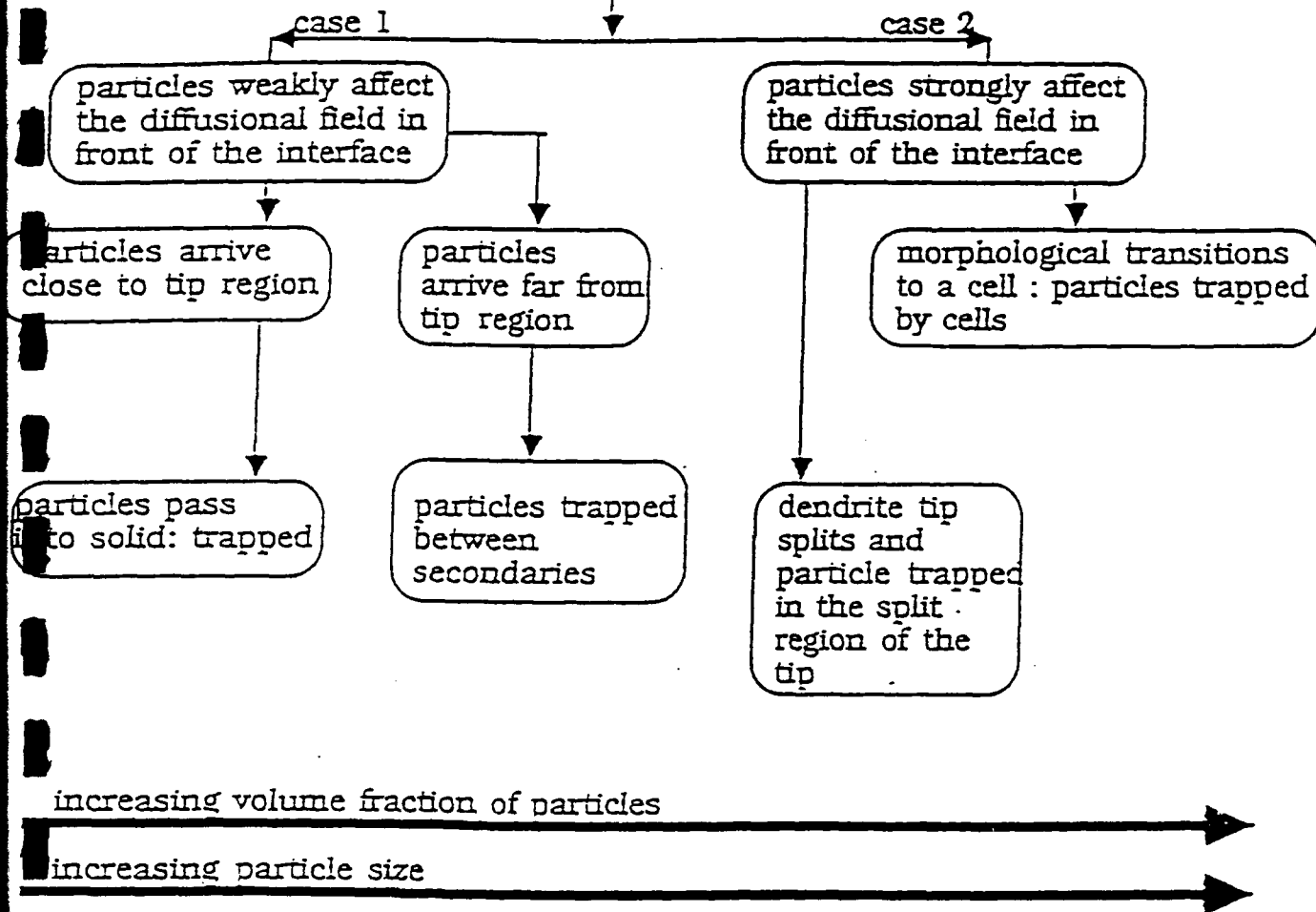


Figure 42. Possible trapping mechanisms by a dendritic interface.

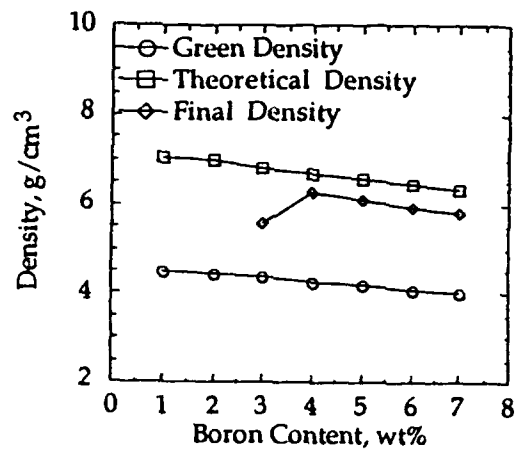


Figure 43. The calculated theoretical density, measured green density and final fired density for the 7 different compositions. Note that the compositions of 1 and 2% B did not ignite. The theoretical density is calculated on the basis of unrelated constituents.

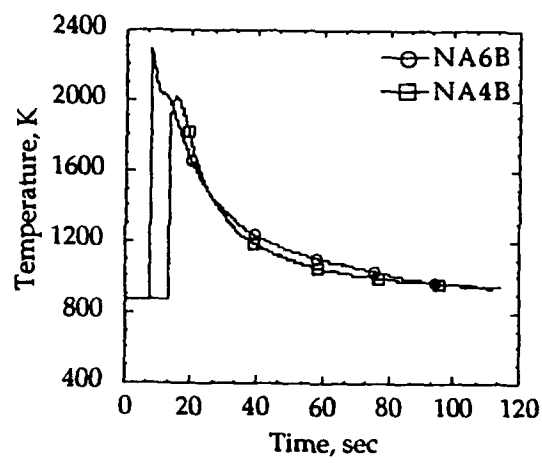


Figure 44. The combustion temperature profiles for alloys NA4B and NA6B.

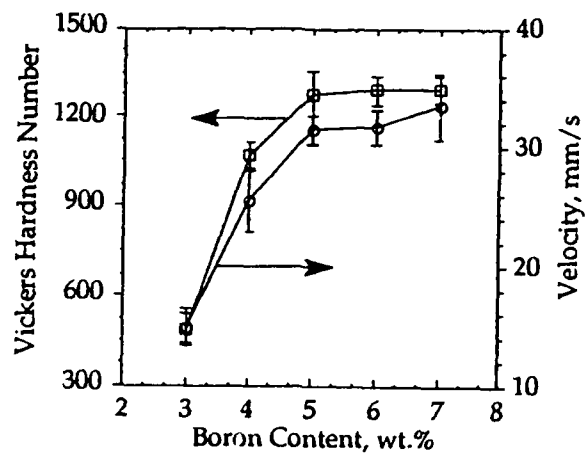


Figure 45. The Vickers hardness number and the combustion velocities for 5 different boron contents.

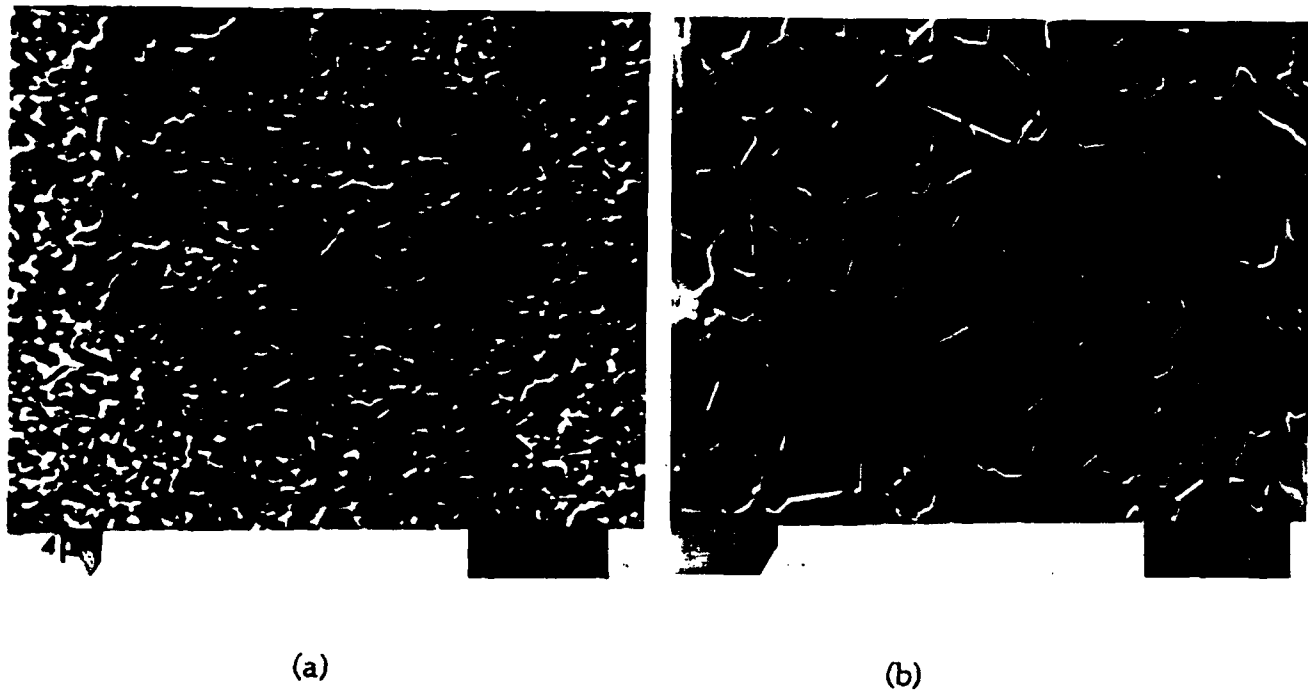


Figure 46. The SEM microstructures of the composites for the alloys (a) NA4B and (b) NA7B.

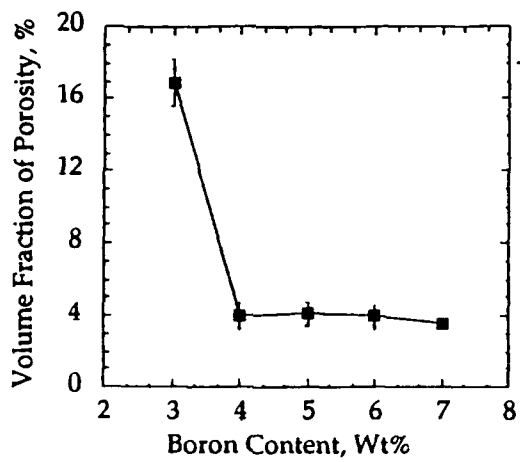


Figure 47. The variation of volume fraction of porosity for 5 different compositions.

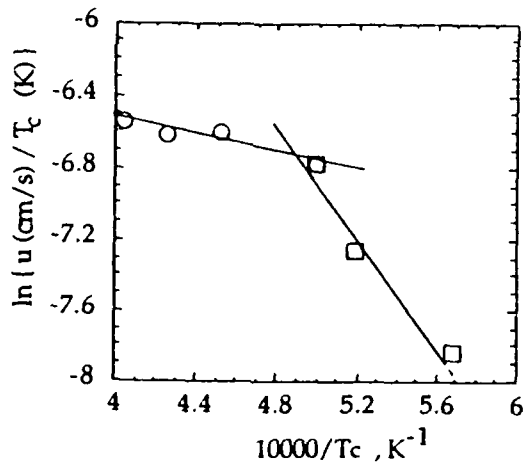


Figure 48. The correlation between the combustion temperatures and the combustion velocities.

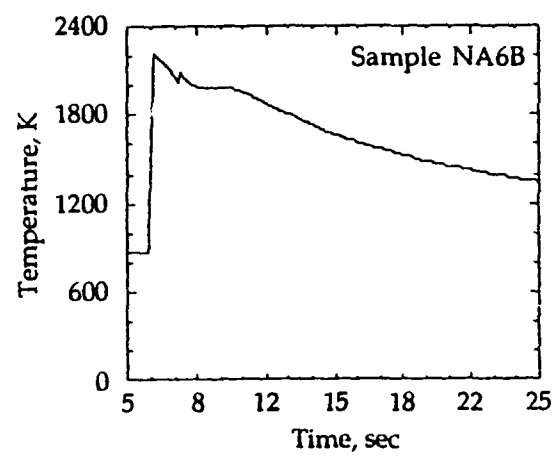


Figure 49. The secondary combustion peak noted in the alloy NA6B.



Figure 50. Typical facet interface configuration and cracking phenomenon noted during the bridgeman type growth of a transparent material Salol.

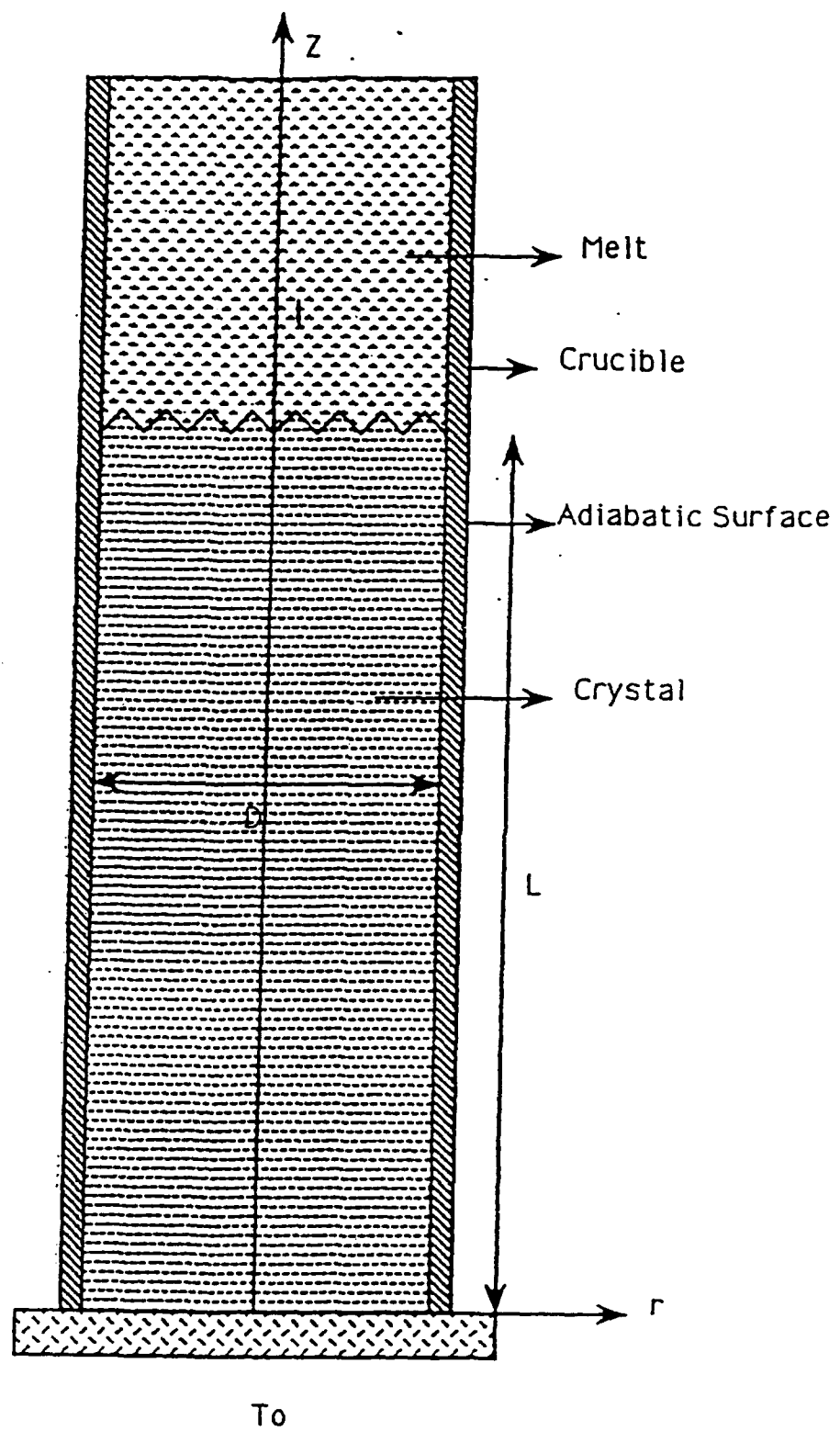


Figure 51. A schematic of the interface configuration and the system.
 $D = 5 \text{ cm}$ and $L = 3D$.

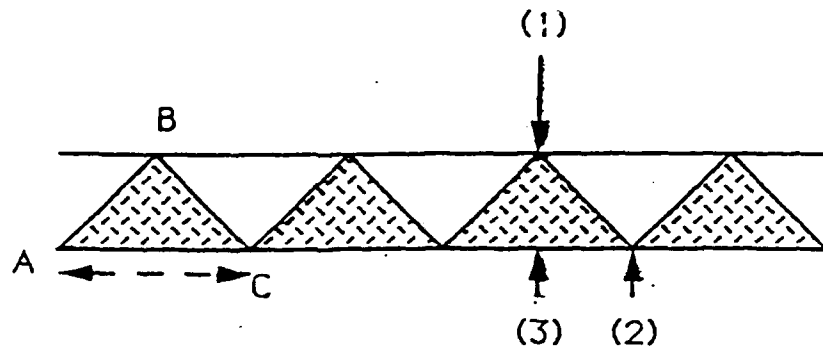
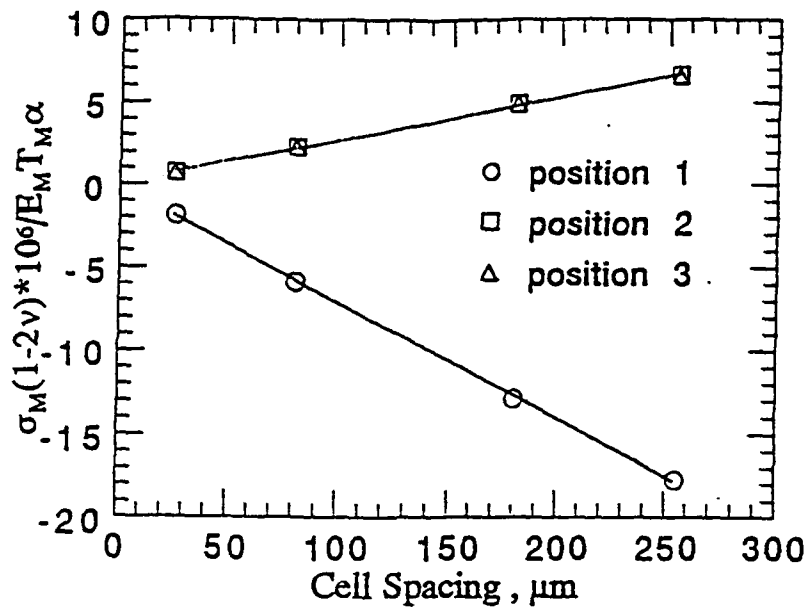
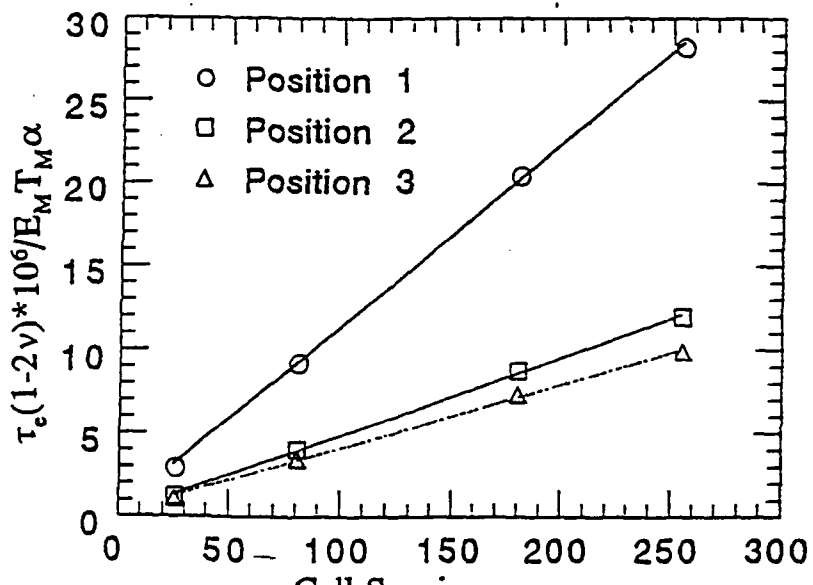


Figure 52. Magnified portion of the solid liquid interface. Distance between point 'A' and 'C' is the steady state cell spacing and the angle ABC is always constant for a particular direction of growth of the crystal, which in this model has been considered to be the $\langle 111 \rangle$ direction. Positions (1), (2) and (3) are the positions at which the stress calculations will be presented.

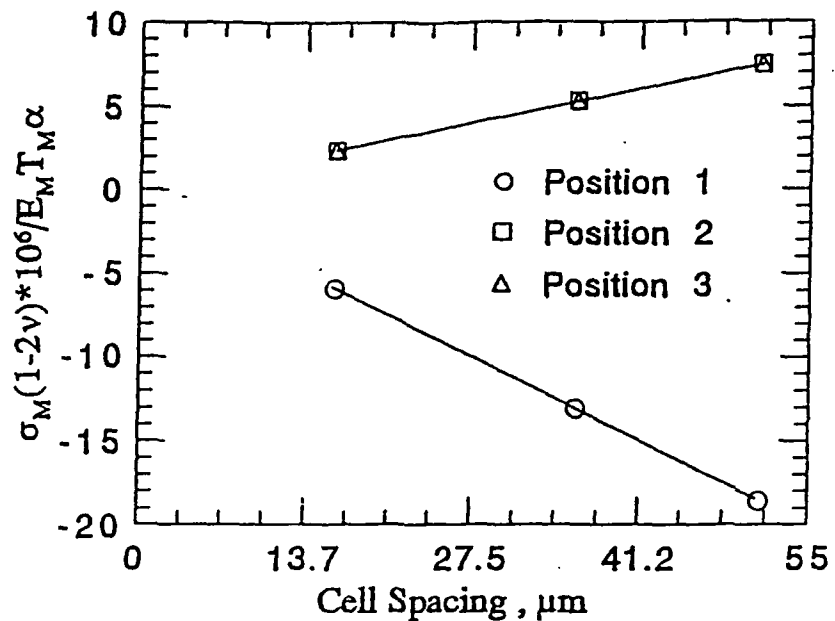


(a)

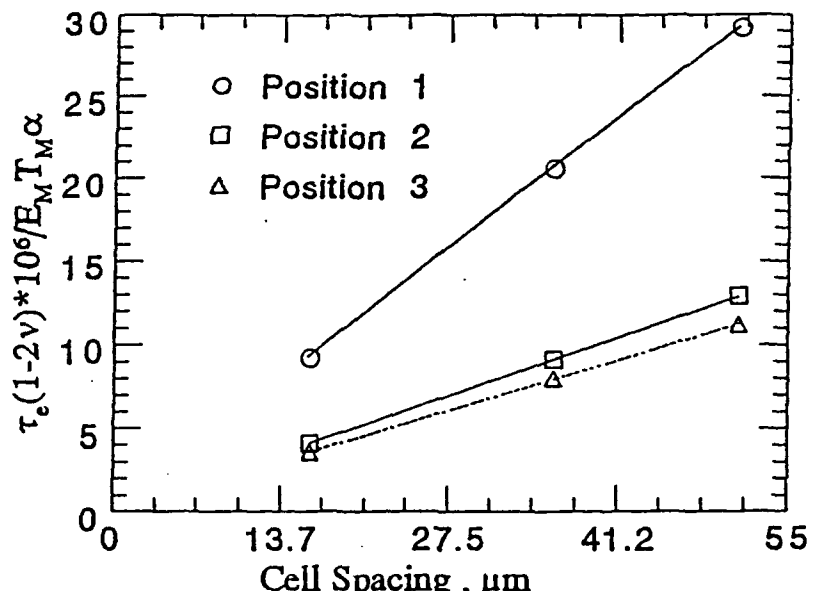


(b)

Figure 53. Plots of (a) normalized mean hydrostatic stress, σ_m , and (b) normalized equivalent shear stress, τ_e , at various positions defined in figure 52 as a function of cell spacing for a constant average axial temperature gradient of 1.0 K/mm (average local radial temperature gradient is 0.29 K/mm and average local axial temperature gradient is 2.9 K/mm near the interface).

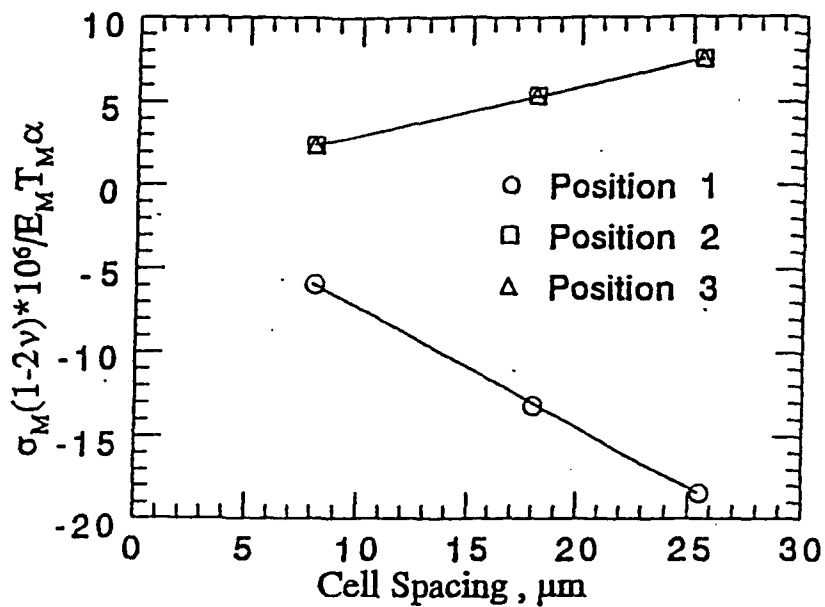


(a)

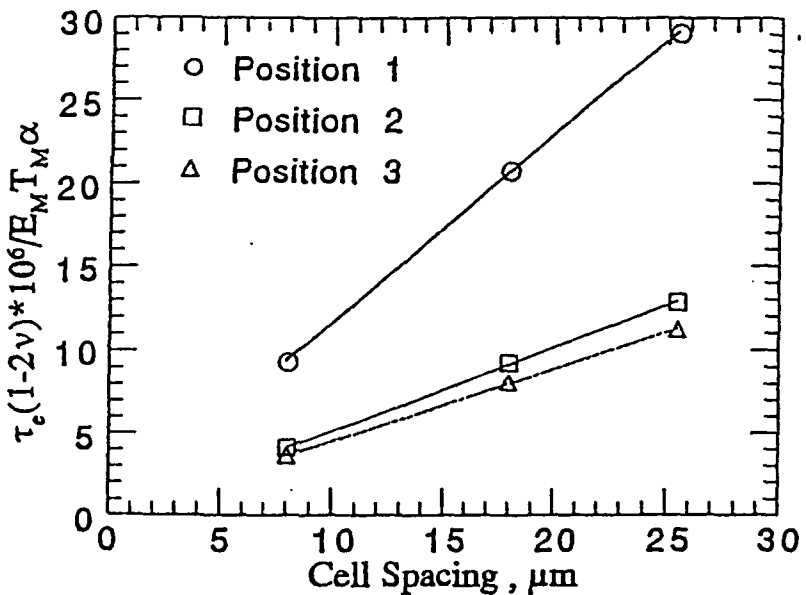


(b)

Figure 54. Plots of (a) normalized mean hydrostatic stress, σ_m , and (b) normalized equivalent shear stress, τ_e , at various positions defined in figure 52 as a function of cell spacing for a constant average axial temperature gradient of 5.0 K/mm (average local radial temperature gradient is 1.52 K/mm and average local axial temperature gradient is 14.9 K/mm near the interface).



(a)



(b)

Figure 55. Plots of (a) normalized mean hydrostatic stress, σ_m , and (b) normalized equivalent shear stress, τ_e , at various positions defined in figure 52 as a function of cell spacing for a constant average axial temperature gradient of 10.0 K/mm (average local radial temperature gradient is 3.09 K/mm and average local axial temperature gradient is 29.9 K/mm near the interface).

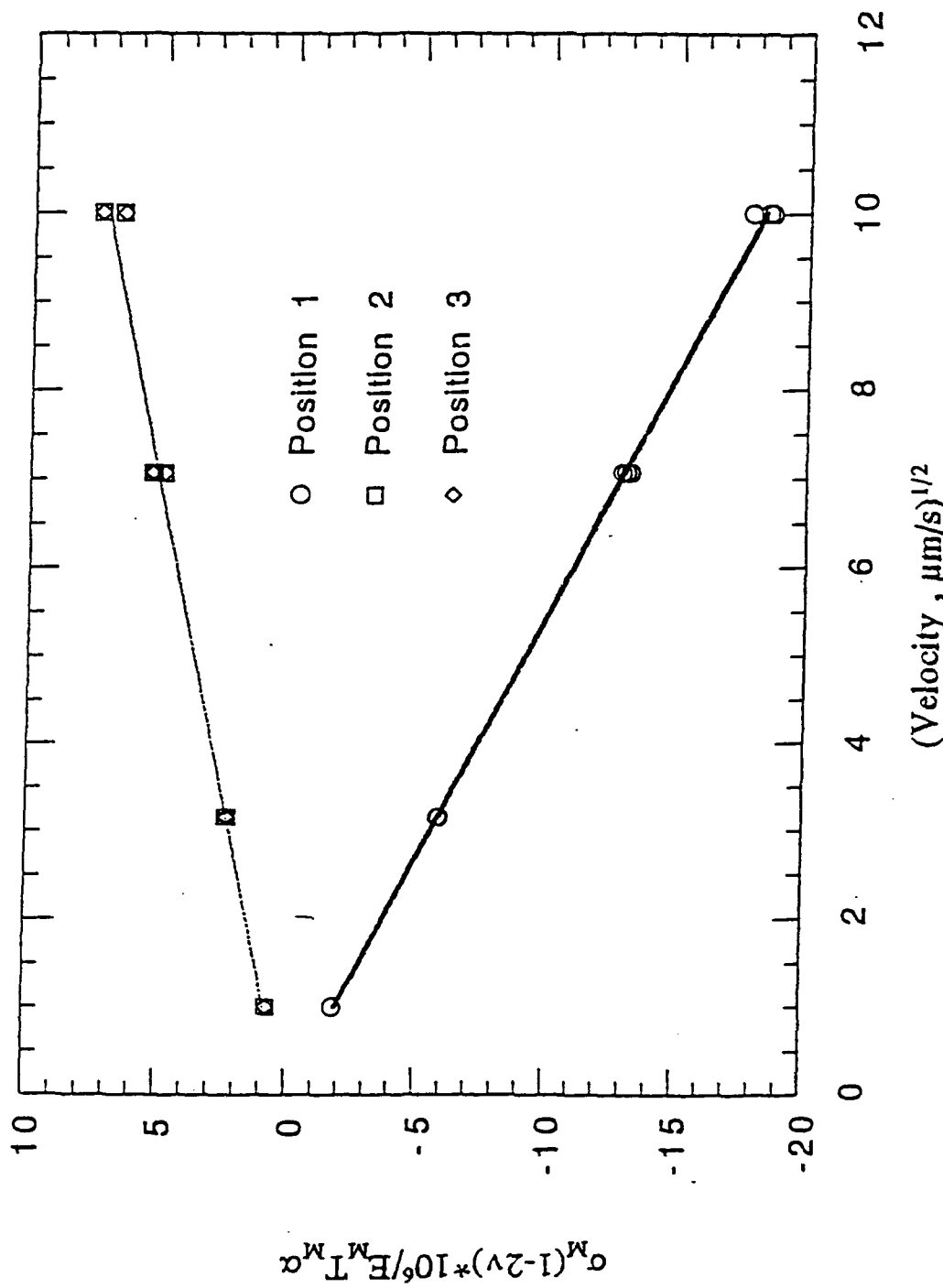


Figure 56. Normalized mean hydrostatic stress, σ_m , at various positions defined in figure 52 as a function of square root of interface growth velocity, $(V, \mu\text{m/s})^{1/2}$.

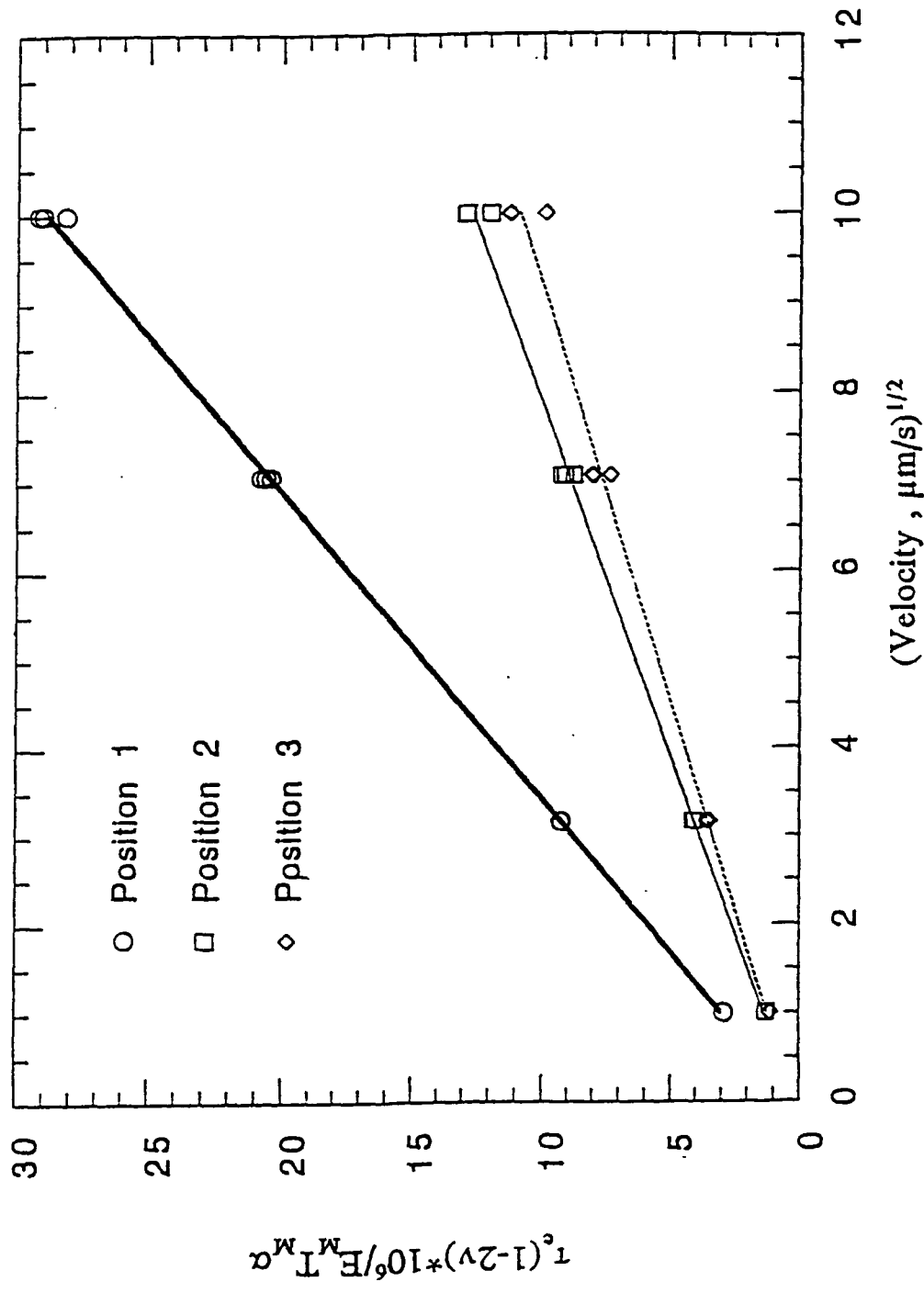
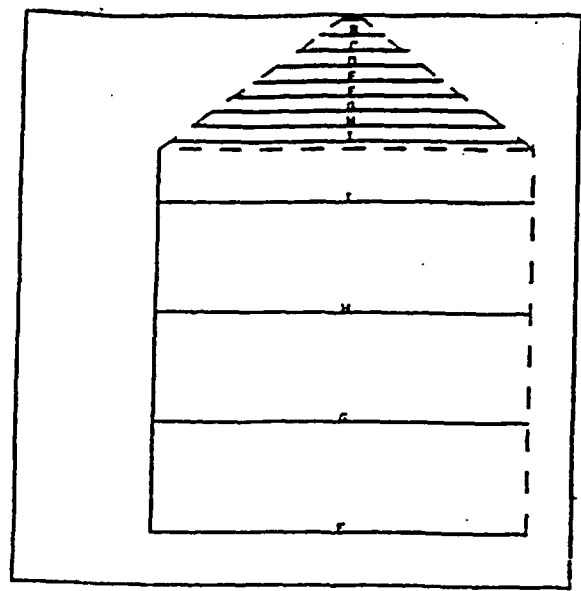
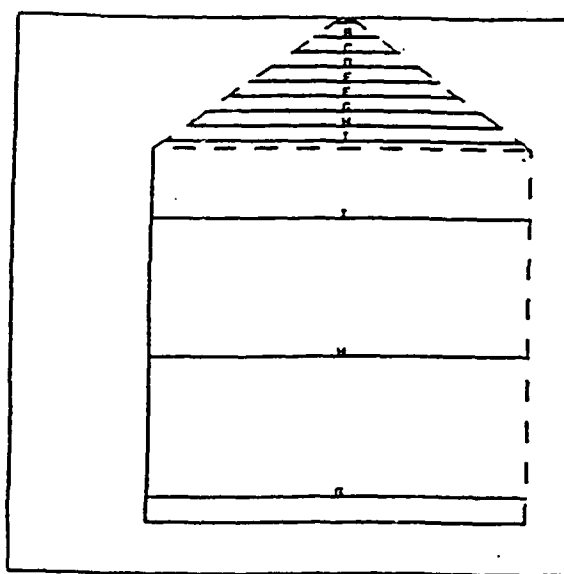


Figure 57. Normalized equivalent shear stress, τ_e , at various positions defined in figure 52 as a function of square root of interface growth

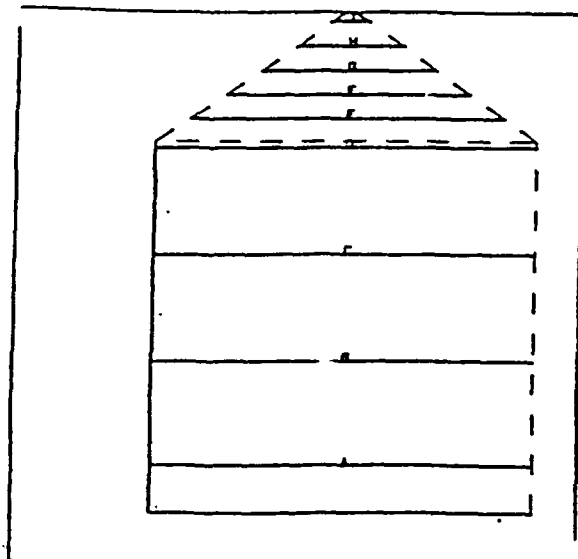


(a)

Figure 58. Contours of (a) radial stress, σ_{rr} , (b) hoop stress, $\sigma_{\phi\phi}$, and (c) equivalent shear stress, τ_e , on a growing facet (which is 0.5^*R away from the center of the crystal) when the cell spacing is $80.69 \mu\text{m}$ and average axial temperature gradient is 1 K/mm . All the stresses are normalized with respect to the $E_M T_{M\alpha} / (1-2\nu) * 10^6$.

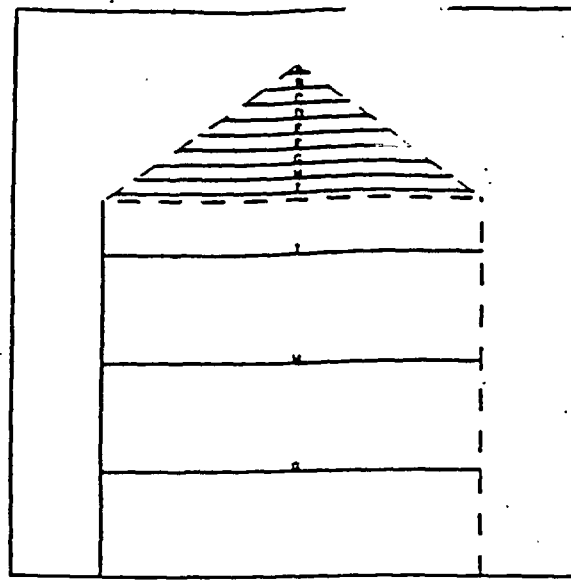


(b)



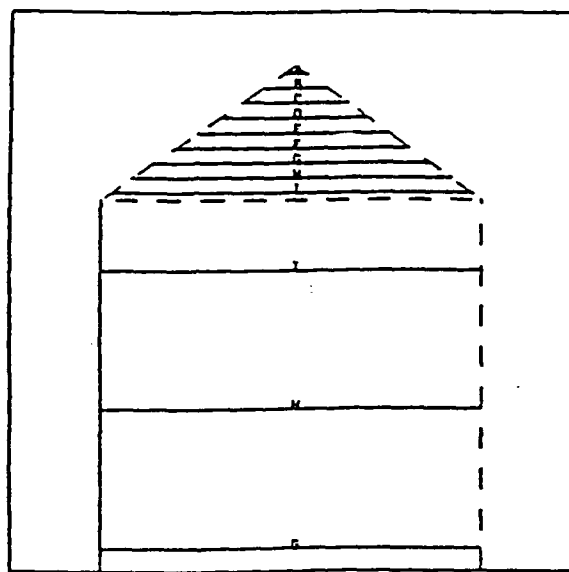
(c)

Figure 59. Contours of
 (a) radial stress,
 σ_{rr} , (b) hoop stress,
 $\sigma_{\phi\phi}$, and (c) equivalent
 shear stress, τ_e , on a
 growing facet (which
 is $0.5R$ away from the
 center of the crystal)
 when the cell spacing
 is $80.69 \mu\text{m}$ and average
 axial temperature
 gradient is 10 K/mm .
 All the stresses are
 normalized with respect
 to the $E_M T_M \alpha / (1-2\nu) \times 10^6$.



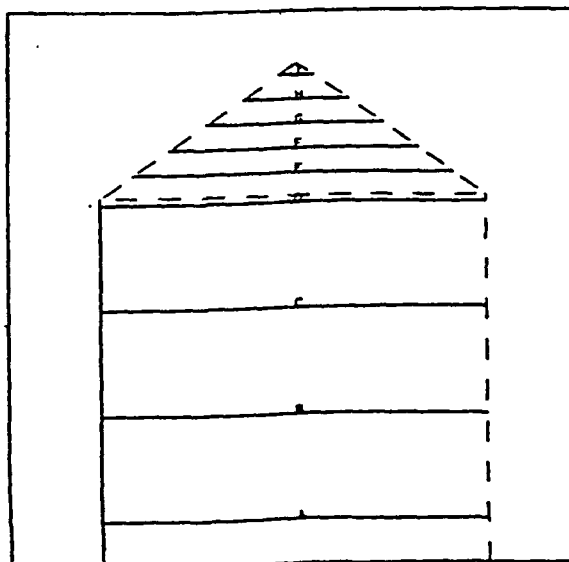
(a)

A = -65.0
B = -54.0
C = -42.0
D = -30.0
E = -18.0
F = - 6.0
G = 5.0
H = 17.0
I = 29.0



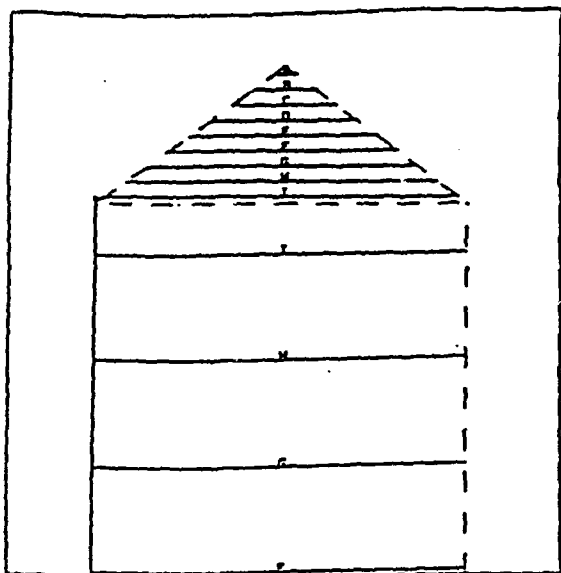
(b)

A = -96.0
B = -81.0
C = -65.0
D = -50.0
E = -34.0
F = -19.0
G = - 4.0
H = 19.0
I = 27.0



(c)

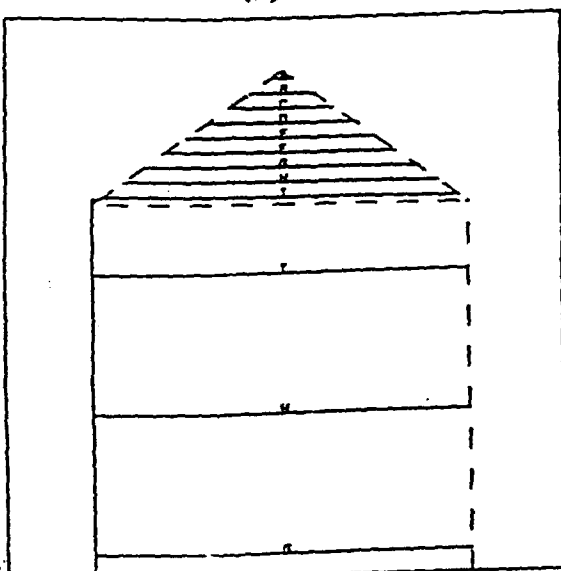
A = 11.0
B = 21.0
C = 30.0
D = 40.0
E = 49.0
F = 59.0
G = 68.0
H = 77.0
I = 87.0



(a)

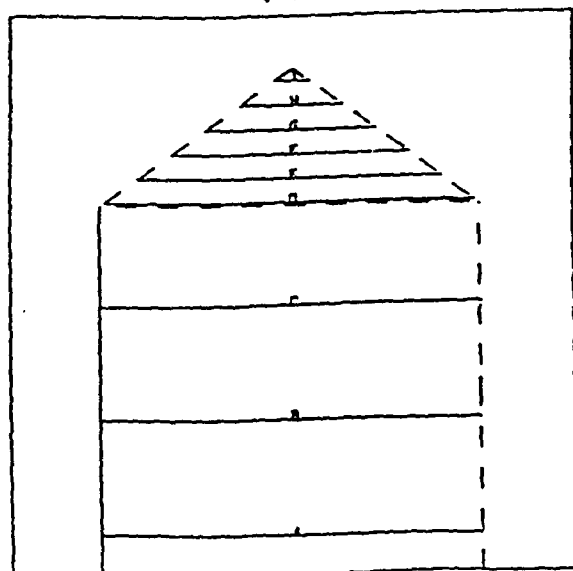
A = -20.0
B = -16.0
C = -13.0
D = - 9.0
E = - 6.0
F = - 2.0
G = 1.0
H = 5.0
I = 8.0

Figure 60. Contours of
(a) radial stress,
 σ_{rr} , (b) hoop stress,
 $\sigma_{\phi\phi}$, and (c) equivalent
shear stress, τ_e , on a
growing facet (which
is 0.5^*R away from the
center of the crystal)
when the cell spacing
is $255.2 \mu\text{m}$ and average
axial temperature
gradient is 1 K/mm .
All the stresses are
normalized with respect
to the $E_M T_M \alpha / (1-2\nu) * 10^6$.



(b)

A = -30.0
B = -25.0
C = -20.0
D = -16.0
E = -11.0
F = - 6.0
G = - 2.0
H = 3.0
I = 8.0



(c)

A = 4.0
B = 7.0
C = 10.0
D = 12.0
E = 15.0
F = 18.0
G = 21.0
H = 24.0
I = 27.0



Figure 61. The interface shape of the material salol during a imposed growth velocity of $0.1 \mu\text{m/s}$ and in the presence of a positive temperature gradient of 3 K/mm .

HD-11257 636

MICROSTRUCTURE EVOLUTION IN THE PRESENCE OF CONSTRAINTS 37-3
AND IMPLICATIONS D. (U) CINCINNATI UNIV OH DEPT OF
MATERIALS SCIENCE AND ENGINEERING J A SEKHAR ET AL.

UNCLASSIFIED

30 MAY 91 AFOSR-TR-93-0495

NL



END
FILED

DTIC

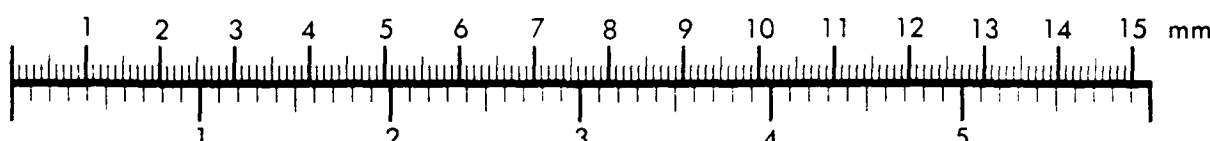


AIIM

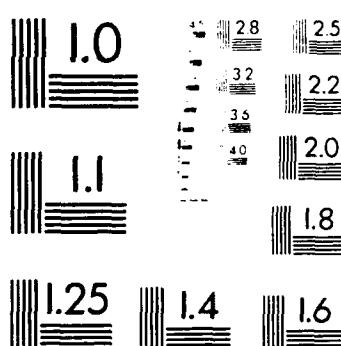
Association for Information and Image Management

1100 Wayne Avenue, Suite 1100
Silver Spring, Maryland 20910
(301) 587-8202

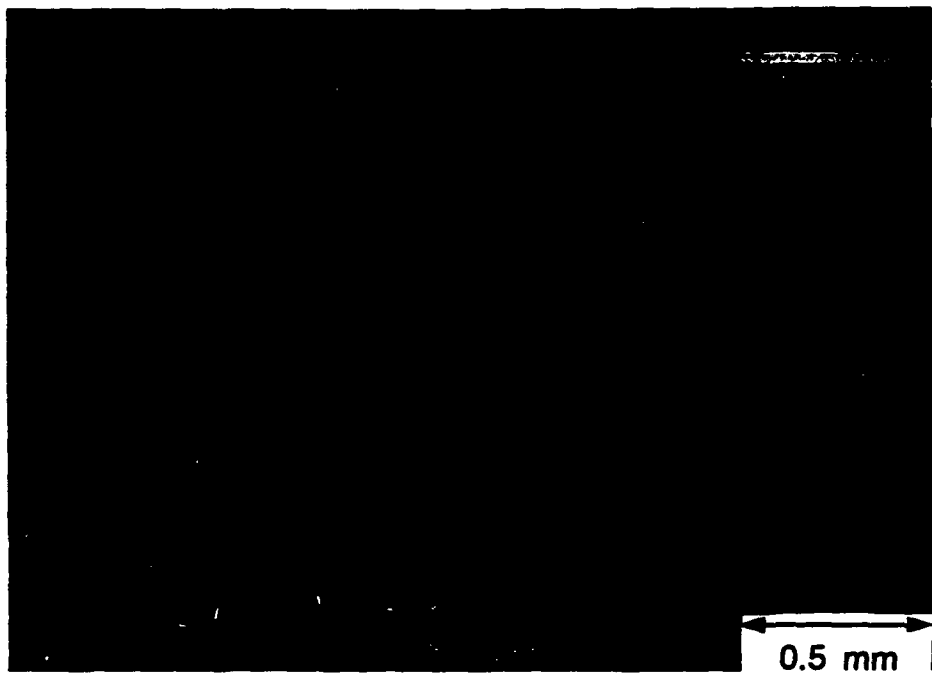
Centimeter



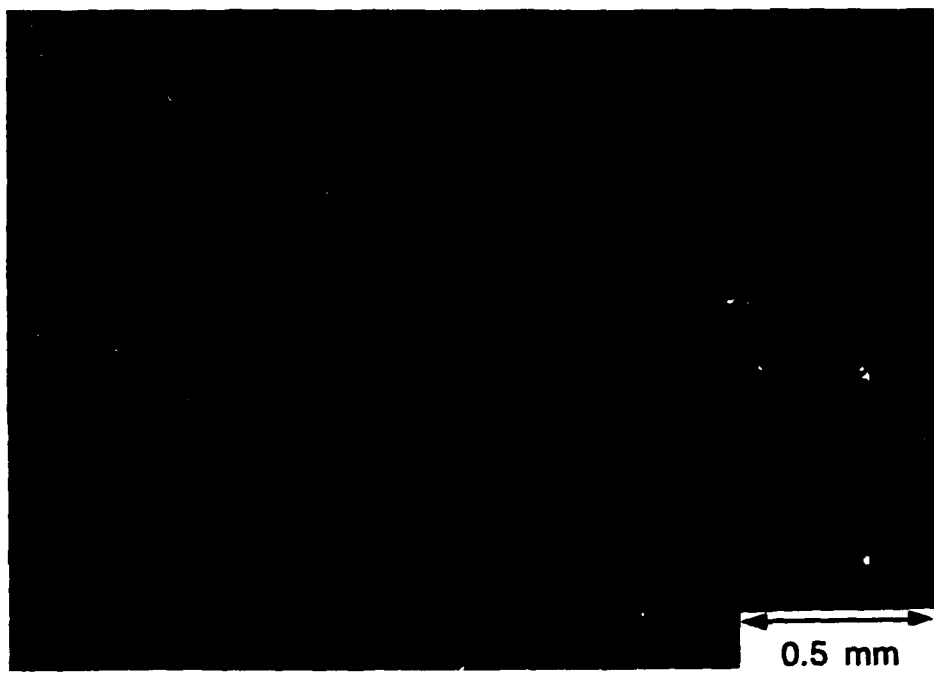
Inches



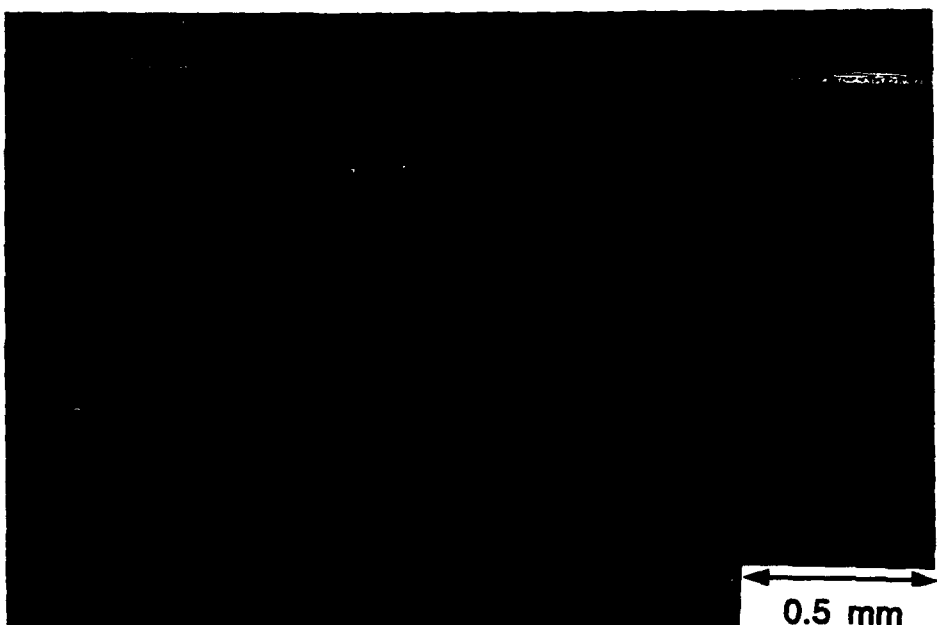
**MANUFACTURED TO AIIM STANDARDS
BY APPLIED IMAGE, INC.**



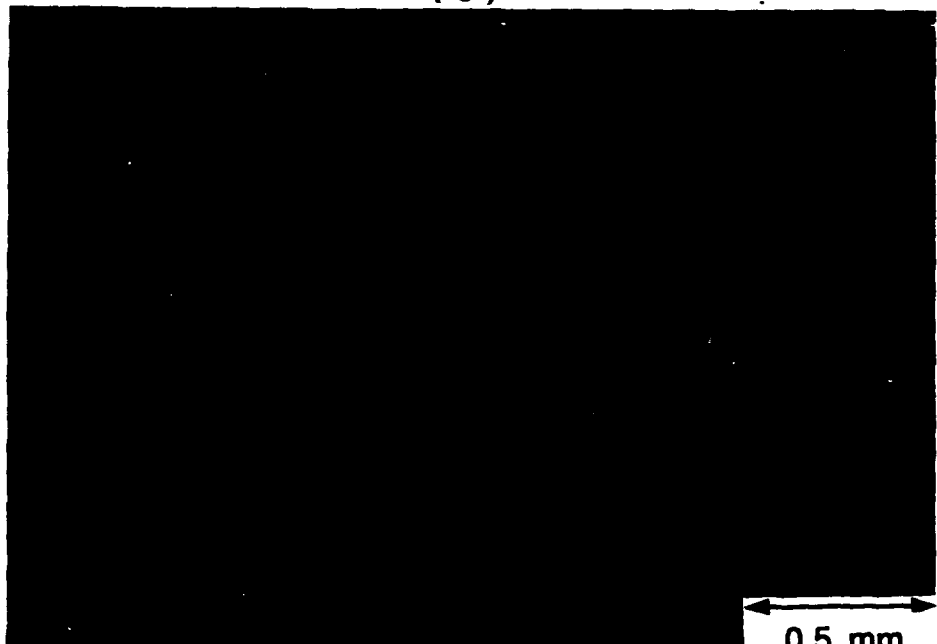
(a)



(b)

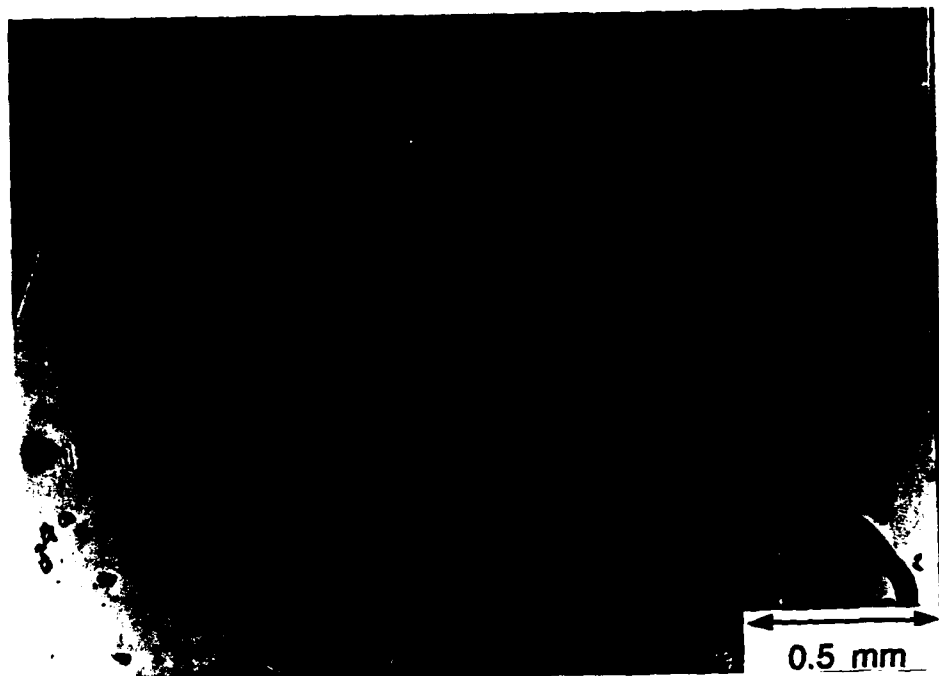


(c)



(d)

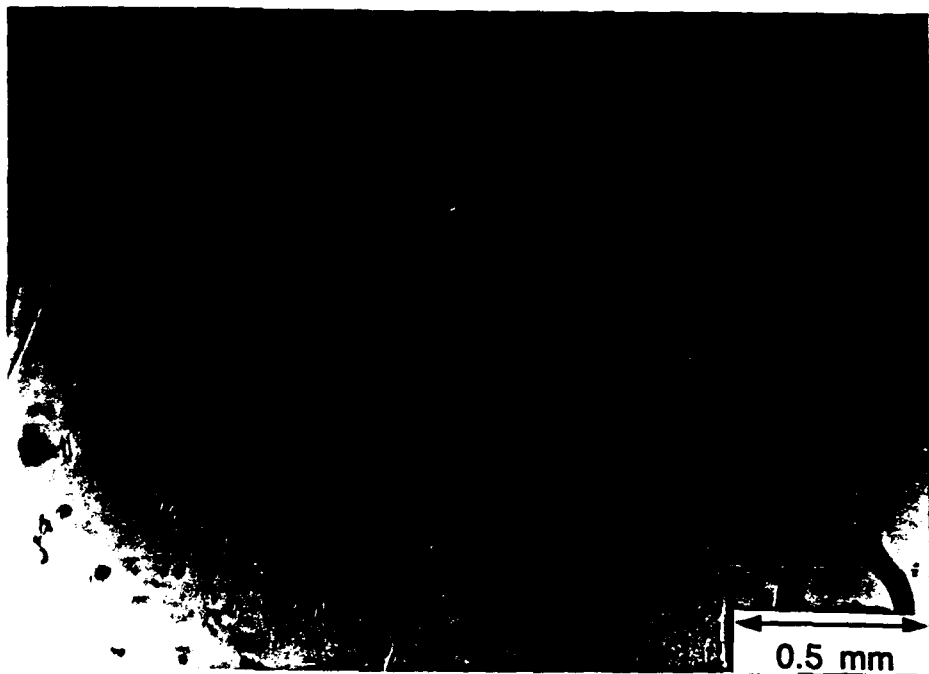
Figure 62. Shows the time sequence of events occurring on a single facet during a imposed growth velocity of $5.0 \mu\text{m/s}$ and in the presence of a positive temperature gradient of 3 K/mm . The photographs are taken 5 sec. apart during the growth. (a) Shows a facet with no apparent cracks near the interface. (b) Shows the formation of a sudden crack in a location between the tip and root. (c) Shows the crack being left behind in the crystal during subsequent growth. (d) Shows a fresh crystal facet growing on the cracked face.



(a)



(b)

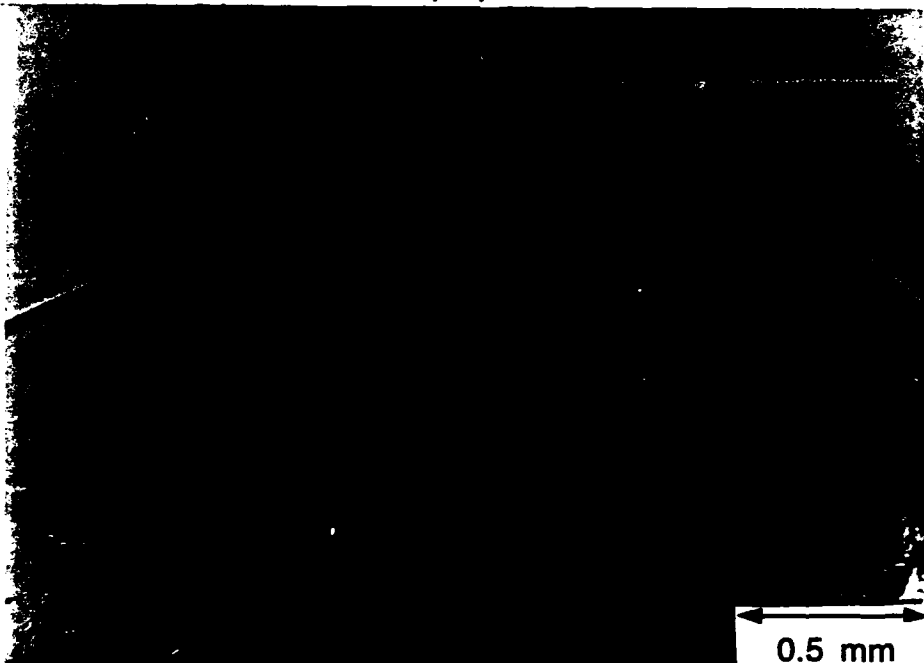


(c)

Figure 63. Shows the time sequence of events occurring on a single facet during a imposed growth velocity of $5.0 \mu\text{m/s}$ and in the presence of a positive temperature gradient of 3 K/mm . The photographs are taken 5 sec. apart during the growth. (a) Shows a facet with a freshly formed crack. (b) and (c) show crack continually propagating with the interface.



(a)



(b)

Figure 64. Shows the growth of two macroscopic facets during a imposed growth velocity of $5.0 \mu\text{m/s}$ and in the presence of a positive temperature gradient of 3 K/mm . The photographs are taken 5 sec. apart during the growth. (a) Shows tip splitting occurring on the right facet. (b) Shows crack appearing near the tip (at the new root location) of the right facet.

END
FILMED

DATE:

8-93

DTIC